Fall 2019

Characterization of Argon and Ar/Cl$_2$ Plasmas Used for the Processing of Niobium Superconducting Radio-Frequency Cavities

Jeremy J. Peshl
Old Dominion University, jjpeshl@gmail.com

Recommended Citation

CHARACTERIZATION OF ARGON AND Ar/Cl$_2$ PLASMAS USED FOR THE PROCESSING OF NIOBIUM SUPERCONDUCTING RADIO-FREQUENCY CAVITIES

by

Jeremy J. Peshl
B.S. May 2013, Grand Valley State University
M.S. Aug 2015, Old Dominion University

A Dissertation Submitted to the Faculty of the Department of Physics
Old Dominion University in Partial Fulfillment of the
Requirements for the Degree of

DOCTOR IN PHILOSOPHY

PHYSICS

OLD DOMINION UNIVERSITY
December 2019

Approved by:

Leposava Vušković (Director)

Gail Dodge (Member)

Alexander L. Godunov (Member)

Gianluigi Ciovati (Member)

Mileta Tomovic (Member)

ABSTRACT

CHARACTERIZATION OF ARGON AND Ar/Cl$_2$ PLASMAS USED FOR THE PROCESSING OF NIOBIUM SUPERCONDUCTING RADIO-FREQUENCY CAVITIES

Jeremy J. Peshl
Old Dominion University, 2019
Director: Dr. Leposava Vušković

The plasma processing of superconducting radio-frequency (SRF) cavities has shown significant promise as a complementary or possible replacement for the current wet etch processes. Empirical relationships between the user-controlled external parameters and the effectiveness of Reactive Ion Etching (RIE) for the removal of surface layers of bulk niobium have been previously established [1]. However, a lack of a physical description of the etching discharge, particularly as the external parameters are varied, limits the development of this technology. A full understanding of how these external parameters affect both the amount of material removed and the physical properties of the plasma would aid researchers in the development of a controllable and customizable cavity processing technique. While the RIE of integrated circuits on semiconductor wafers has been studied extensively, the unique properties of the discharge with the application of RIE to a complex 3-D metallic waveguide make comparisons difficult. Thus, electrical probe and spectroscopy techniques were applied to a coaxial cylindrical capacitively coupled plasma designed for the plasma processing of SRF cavities with the intention of finding pertinent relationships between the external parameters and the important plasma parameters.

A comparative analysis of two popular spectroscopy techniques was conducted in this aim. The density of the metastable and resonant levels in Ar was measured in both Ar and Ar/Cl$_2$ discharges to properly characterize the unique discharge system and aid in the development of a cavity etching routine. The first method, deemed the "branching fraction method", utilizes the sensitivity of photon reabsorption of radiative decay to measure the lower state (metastable and resonant) densities by taking ratios of spectral lines with a common upper level. This method has been gaining popularity as it does not require any *a priori* knowledge about the electron energy distribution. The second method is a tunable diode laser absorption spectroscopy technique that measures the thermal Doppler broadening of spectral lines,

from which the neutral gas temperature and lower state density of the transition can be evaluated. The two methods were conducted in tandem while external parameters that were empirically determined to be important to the etching mechanism of SRF cavities were varied. Relationships between the excited state densities and the external parameters are presented for both spectroscopy methods. In particular, the relationship between the first four excited state densities and the added DC bias indicate an increase in the plasma density and excited state ionization. The results found from the spectroscopic studies were applied to a collisional radiative model (CRM) to determine quantities related to the electron energy distribution. This is because electrons facilitate the vast majority of the collisional processes in the plasma bulk, leading to ionization and excitation. Results from the CRM were compared to Langmuir probe measurements assuming a Maxwellian distribution.

As an extension to the previous empirical investigation, niobium samples were plasma etched to study the roughness profile of the final surface as a function of external parameters. In particular, the positive DC bias and surface temperature were given significant attention as they are directly related to the physical and chemical etching mechanisms, respectively. As an unexpected consequence, a great deal of qualitative information regarding the construction and material limitations of the reactor were found. The highly reactive Ar/Cl_2 gas used for processing can have detrimental effects to the health of the experimental apparatus, as well as introduce impurities to the system through reactions with the necessary vacuum chamber and sealing materials. Suggestions for material improvements to the plasma reactor are given based on physical observations and surface profile results.

"I don't do magic, Morty, I do science. One takes brains, the other takes dark eyeliner."
-Pickle Rick, *Rick and Morty*

ACKNOWLEDGMENTS

As I come to the end of my graduate school journey, I find that my success was dependent on a great deal of people who not only supported me throughout, but endured the process by my side. I owe many of these people a debt I cannot expect to repay, but at the very least I would like to express my gratitude. I first have to thank my advisor Dr. Vušković for her everlasting encouragement, support, energy, and most importantly, belief in me. In those moments of my highest doubt in myself she was always the first voice of encouragement. Her efforts made me a scientist rather than just a researcher, and for that I am incredibly grateful. I must of course also thank my 'pseudo-advisor' Dr. Popović for all of his help throughout this work. Not even a brain tumor stopped him from making me a priority in his life, which is awe-inspiring and only one example of his commitment to science and his students. I would also like to thank Dr. Sukenik for his continued help and encouragement throughout this work. I leaned on Dr. Sukenik for a great deal, both experimentally and personally, and his desire to see students succeed is evident in all of his pursuits. A special thank you is due for Justin Mason who has allowed me to bother him and steal his equipment without a second thought. He is also a great friend, and someone who I admire dearly. Thank you to Ms. Lisa Okun for her support, patience, and grace in constantly dealing with my equipment orders, problems, travel, and so much more. Much of the success of this work is also due to the contribution by Roderick McNeill in his short time working in the lab with me. Besides being a talented researcher and clever thinker, while he was certainly a source of snide comments, he was also a constant source of encouragement in moments of doubt and I would not be here without him. Thanks is also due to Dr. Valente-Feliciano and Dr. Palczewski for their help with materials and services performed at JLab, and to Olga Trofimova for her patience and help with the surface studies.

I also could not have gotten to this point without the support of my amazing friends and family throughout the years. Thank you to Robert Fields for being one of very few sources of encouragement and hope through the first few years of graduate school, and for being a great friend to me since the day we met. I must also thank Torri Jeske, Tyler Viducic, Dr. Grady White, Lindsay Thornton, and Josh Carter for their friendship and mental support through this experience. It is also important to include Borjo coffeehouse, in which I anticipate I have spent $\approx 5\%$ of my total gross

salary while being in graduate school. I regret none of it, and their coffee fueled this dissertation. To my friends from Michigan, I don't know how I could be so lucky to have such an amazing group of people in my life. The support I receive from them on a daily basis is astonishing, let alone the various visits, trips, DoTA games, phone calls, and messages that I've received over the years in my most difficult moments. To Courtney Miller, who lived the struggle with me, thank you for your love and support for all of those years. Lastly, I must thank my parents Ron and Kathy, and my brother Darren, for their constant love and support. I could not ask for better people in my life.

TABLE OF CONTENTS

LIST OF TABLES

LIST OF FIGURES

CHAPTER 1

INTRODUCTION

The development and use of particle accelerator systems are highly instrumental in the discovery and understanding of the fundamental particles. It should not be surprising then that an immense amount of attention is placed on the construction, development, and advancement of particle accelerator technology. In particular, Superconducting Radio Frequency (SRF) cavity technology is a popular choice in many laboratories. Particles are accelerated in SRF cavities when high frequency electromagnetic fields are produced within the cavities, commonly made from bulk niobium (Nb). Since these cavities must be superconducting, a great deal of attention must be given to their construction and maintenance. Barring the consideration of doping effects or thin film deposition, the cavities must be of pure grade Nb with minimal impurities and deformities on the SRF cavity surface. These cavities have been successfully engineered to accelerate particles to velocities near the speed of light, but the required shape of the cavity is a complicated elliptical structure. To create a SRF cavity in the desired resonant shape, pieces of bulk niobium must be welded and formed by tools and machinery that introduce impurities and surface discontinuities. The resulting impurities, defects, pits, and surface discontinuities from the manufacturing and handling of the cavities have detrimental effects on the superconducting properties, so it should be no surprise that their elimination is extremely important.

Various solutions regarding the surface processing of these cavities have been developed to specifically address surface purity, smoothness, and cleanliness. The most common processing practices include Buffer Chemical Processing (BCP), Electro Polishing (EP), and Centrifugal Barrel Polishing (CBP). These processes have proven successful in attaining acceptable superconducting properties in SRF cavities, but they are not without their issues and limitations. One issue regarding these processes is personnel and environmental safety as these processes require the use of dangerous and corrosive chemicals such as hydrofluoric acid (HF), sulfuric acid (H_2SO_4), and phosphoric acid (H_3PO_4). Great care must be taken when using and disposing of these chemicals, and the safety procedures put in place must be quite rigorous. Scientifically, these wet chemical processes do not allow for a great deal of

control over the final surface of the SRF cavity. While machines and routines can be developed for efficient processing of these cavities, each SRF cavity will have unique surface properties that cannot be fully addressed using the wet etch processes.

An alternative method for SRF cavity processing is in development and has shown encouraging results to replace or complement these chemical processes. This approach, called Reactive Ion Etching (RIE) or sometimes Ion Assisted Reactive Ion Etching (IARIE), is a technology developed primarily for the semiconductor industry in the fabrication of integrated circuit products.[1] IARIE is a dry etch process that uses a reactive plasma to facilitate chemical reactions on a material surface. This is done by introducing a reactive gas, usually a halogen gas or a halogen/inert gas mixture, to an electromagnetic field inside a vacuum chamber. This is typically done by placing the substrate on one of two parallel plates and applying a strong radio-frequency (RF) electromagnetic field between the two plates. The ions created from the heating of the gas are accelerated into the substrate with high enough energy to react. This is advantageous as the substrate remains close to room temperature, while the same processes if done chemically would require the substrate to be heated to very high temperatures. Additionally, IARIE allows for a great deal of control in the removal of material surface layers as the process can be chemically selective, removing the desired material and leaving other materials unaffected [2]. IARIE can also be done isotropically where the plasma etches the material without discretion, or anisotropically where the plasma only etches material in a specific location of the material [2].

This makes IARIE an intriguing avenue for SRF cavity processing, but naturally implementation of IARIE to SRF cavities is not without its challenges. In the semiconductor industry the desired amount of surface material removal is on the nm scale, whereas for SRF cavities removal on the order of microns is desired. The difference in materials is significant as well, with polysilicon and Nb having very different surface and material properties. In addition, the semiconductor industry works on flat samples called "wafers" which are essentially 2D flat surfaces. Conversely, SRF cavities are 3D cylinders with a varying elliptical geometry. Therefore, in order to extend plasma etching technology into SRF cavity processing, a creative solution is required to overcome this geometrical challenge.

---

[1]Reactive Ion Etching processes are also typically referred to as plasma etching. For all intents and purposes of this dissertation, these terms are equivalent.

Previous studies have made significant progress in the application of reactive ion etching to bulk Nb and SRF cavity structures [1]. The vast majority of that work was done to establish an effective etching apparatus and investigate the relationship between the user controlled external parameters (such as pressure, temperature, power sources, and experiment construction) and the rate/amount of material removal. The experimental apparatus was explicitly constructed to be modular and geometrically modifiable to approximate SRF cavity structures. This allows for the establishment of the empirical relationships between external parameters and etching on Nb samples rather than full SRF cavities. While this setup is experimentally and financially advantageous, the vacuum components are made out of various materials that can chemically react or be etched and create a dirty processing environment. The mitigation of these unwanted reactions and subsequent impurities remains a significant limitation of the technology.

A significant goal of this work is to continue the development of this method by establishing relationships between these same external parameters and the figures of merit that describe an RIE plasma discharge[2]. In order to create an effective, consistent, and controllable process, knowledge about how the reactive plasma changes with the etching parameters is imperative. These plasma parameters consist of information that describe the physical processes and energy distribution in the etching discharge. The plasma parameters can then be used as inputs for computational models that can fully describe the plasma reactor. This model would aid in the development of customizable etching routines and increase the effectiveness of the etching process while avoiding the need for extensive trial and error experimentation.

There are a great deal of plasma parameters of importance, but information about the kinetic processes of the electrons within the plasma have significant value. Electrons are the most mobile and energetic species in the discharge due to their low mass compared to the various atomic species in the plasma. For this reason, electrons are primarily responsible for ionization and excitation of the atomic species, which is of the utmost importance to surface processing. The measurement and understanding of these plasma parameters are particularly important because of the unique geometry and application. In order to etch the inner surface of an SRF cavity, the plasma must be created within the cavity, meaning that a powered electrode must

---

[2]Throughout this dissertation the terms "plasma" and "discharge"/ "gas discharge" are used interchangeably. This is commonplace in the field, particularly in regards to low temperature plasmas, where the two terms mean essentially the same thing (a partially ionized gas).

be placed in the center. This type of configuration creates a coaxial plasma instead of a flat parallel plate plasma commonly used in industrial applications. This offers the opportunity to study the physics of a plasma configuration of which very little is known. Additionally, plasma etching requires both physical (or kinetic) and chemical processes in order to remove the surface layers of impurities and oxides that limit the superconducting properties of Nb. As previously discussed, this is not uncommon in plasma etching and halogen gases are used to encourage the chemical reaction. In our case, Cl_2 is added to Argon to facilitate the creation of a volatile product that can be removed through vacuum systems. However, the addition of Cl_2 greatly complicates the physical description of the plasma. Chlorine atoms can be both positively and negatively ionized as opposed to Argon which only produces positive ions. These heavy negative ions have a significant effect on the plasma distribution and energy and must be included in the mathematical models used to find the important physical quantities.

As mentioned above, plasma etching is advantageous because it allows one to have more control over the final surface properties of the processed material. Therefore, as a second goal of this work, the effect of different external parameters on the surface properties of plasma etched Nb was investigated. Among the various external parameters there are two that have a significant effect on the profile of the final surface. These parameters, the substrate temperature and electrode DC bias, directly influence the chemical and physical mechanisms of the etching process, respectively. To understand the individual and combined effects these parameters have on the surface roughness, small Nb coupons were plasma etched in a modular discharge cavity approximately the dimensions of a singe cell SRF cavity for different combinations of these parameters. The range of these quantities was based on what is known about the etching chemistry. As an unexpected consequence of this study, a great deal was learned about additional engineering and material science challenges that have to be addressed in order for this technique to be a viable alternative to the wet etch processes. Specifically, it has been found that the choice of corrosion resistant materials used in the apparatus is much more important than previously thought. This is particularly true for pieces of equipment that have prolonged exposure to the discharge at high temperatures, such as the internal gas feed, the RF power feedthrough system, and the gaskets used for sealing the vacuum chamber. These materials are not only damaged in the plasma etch process, but they create

unwanted byproducts in the system that can severely hinder the effectiveness of the etching process. Qualitative conclusions of more appropriate materials to use for these purposes have been established, but this investigation is currently incomplete and requires further attention from a future researcher.

The combination of the studies described above would ideally provide a more complete description of the etching process, therefore allowing for customizable recipes based on the physical needs of each individual cavity or application. A detailed summary of these investigations is presented within, and the dissertation is structured as follows. Chapter 2 provides a basic introduction to plasma discharges, particularly pertaining to the discharge source used in this work. A brief summary of superconductivity and SRF cavities is given in Chapter 3. Chapter 4 presents a summary of the previous work establishing the relationships between external parameters and etching results. Chapter 5 outlines the diagnostic methods employed to study the physics of the discharge. These diagnostics include optical emission spectroscopy, laser absorption spectroscopy, and Langmuir Probe analysis. Chapter 6 is a description of the experimental setups of the modular discharge apparatus and all diagnostic methods. Chapter 7 presents the results of the densities of the first four excited states of Argon in both Argon and Ar/Cl_2 discharges. Applying the results from Chapter 7 in a collisional radiative model, Chapter 8 presents the results pertaining to the description of the electron kinetics of the discharge. Chapter 9 is a summary of the investigation of external parameters on the final surface roughness of niobium, along with qualitative observations about engineering challenges and material limitations found throughout. Finally, Chapter 10 provides a short conclusion and suggestions for future work.

CHAPTER 2

BASICS OF PLASMA DISCHARGES

Plasma is comprised of ions, electrons, neutral species, and excited radicals. Plasmas are created when enough energy from heating and/or strong electromagnetic fields is transferred to a gas to facilitate ionization. Because of the number of charge carriers inside a plasma, it is susceptible to electric and magnetic fields, much like a fluid dielectric. Therefore, plasma systems can be very complicated and hard to model based on the environment in which the plasma is created. For example, while both the sun and neon lights are both technically plasmas, they must be treated very differently theoretically. Plasmas are often classified by the degree of ionization from 1 (fully ionized) to $10^{-4} - 10^{-6}$ (partially ionized). As one can imagine, plasmas that have a higher ionization degree are systems with high temperature, such as fusion reactors. Those plasmas that are partially ionized, especially those that are used for many commercial applications such as electronics and material processing, are considered low temperature plasmas. The plasma utilized for this work is a low temperature partially ionized gas discharge, and therefore the theoretical treatment presented within this dissertation is limited to this scope.

An important distinction in characterizing plasmas is the thermal distribution of the particles. If all of the species have equal temperatures (energy) then the plasma is said to be in thermal equilibrium (TE). These plasmas are typically those with high temperature, pressure, and density (electrons and ions) as these conditions facilitate efficient high energy transfer between particles. Oftentimes, the TE condition is not fulfilled throughout the entire volume, but is valid in local regions. This is referred to as a local thermal equilibrium (LTE) plasma. Furthermore, if the temperatures of the species vary throughout the plasma, it is classified as a non-LTE plasma. These non-LTE plasmas have electrons with temperatures much higher than the heavier species due to much smaller mass, and therefore velocity, of the electron. Electrons in the plasma are therefore the biggest source of energy delivery to the heavier particles and heavier particle collisions become less important [2]. This is particularly true at lower pressures (≤ 1 Torr) when collisions are less frequent and energy transfer is less efficient.

These low pressure discharges are often used for material processing applications due to the large difference in temperatures between electrons ($> 10,000$ K) and the heavy particles (≈ 300 K) which allow for reaction pathways that are unobtainable or reasonably unfeasible to achieve chemically [3]. Low pressure discharges therefore have many uses, among which are thin film deposition, material etching (removal), material cleaning, energy efficient lighting, and wound sterilization [3].

The work outlined in this dissertation was performed with the aim to further understand a low temperature, low pressure discharge used for the plasma etching of Nb SRF cavities. As stated above, plasma etching is a common use for these discharge types, however this is typically limited to applications in the semiconductor processing industry. The extension of plasma etching to Nb SRF cavities is rather new, and has shown significant success as a feasible alternative or addition to current chemical "wet" etch processes [1]. Missing from that study, is an investigation of the discharge parameters under various etching conditions, making the design of effective and controllable plasma etching applications for these cavities quite difficult.

This chapter is meant to introduce a simple theoretical treatment of plasma physics and the figures of merit that are used to describe low temperature plasma discharges. As one can imagine, this is not a simple or succinct subject matter, so many details about derivations of important quantities will be omitted, and only those characteristics that are important to the understanding of this study are given significant attention. For a more complete description of low temperature discharges, particularly as it pertains to the etching of bulk Nb, the reader is suggested to review the works of Nikolič and Upadhyay [1, 4].

2.1 THE QUASINEUTRALITY CONDITION

Arguably, the most important defining characteristic of plasmas is the quasineutrality condition. That is, in a macroscopic view of the plasma volume there is an equal number of positive and negative species. This is often also referred to as the plasma approximation, and is the foundation for much of the developed plasma theory [2] . However, while the plasma must remain neutral in a macroscopic view, this does not prevent the formation of electrically charged local distributions within the discharge. These localized collections of charged particles eventually create steady state forms of the discharge, which can then be used to facilitate the chemical and physical reactions required for the desired process.

2.1.1 ELECTROPOSITIVE DISCHARGE

Electropositive discharges typically contain only one positive species (ions) and one negative species (electrons). These are made from inert gases (Ar, Ne, Xe) that are typically used as a carrier gas for etching processes. The quasineutrality condition is simply

$$n_i = n_e. \tag{1}$$

Electrons within this discharge are going to have a much higher energy than the heavy ions/neutral species, so electronic collisions with these atoms are the dominant ionization and excitation channels. Recombination of electrons and ions is not typically considered in particle balance and transport treatments, particularly at lower pressures [2]. Additionally, at low pressures (also called the Langmuir regime) the ion transport through the plasma can be considered collisionless and therefore the ion kinetic energy into the wall/substrate is conserved.

2.1.2 ELECTRONEGATIVE DISCHARGE

Electronegative discharges are created when an additional negative species, typically negative ions (cations), are created within the plasma. These discharges typically contain halogen gases (Cl_2, O_2, F_2), which are often used for etching processes. This naturally changes the quasineutrality condition to

$$n_i^+ = n_e + n_i^-. \tag{2}$$

While it may not seem obvious at first, the additional negatively charged species greatly complicates the dynamics. This is particularly true when the heavy negative species is a significant fraction of the total negatively charged particles in the discharge. The kinetics of electrons is greatly affected by a slow, heavy negative species and thus the energy and particle balance equations are coupled. This makes for a complicated set of coupled differential equations that require significant assumptions in order to find analytical solutions [2]. Additionally, recombination of positive and negative ions cannot be ignored as these processes have a large rate constant [2]. Additional collisional processes must also be considered due to interactions between the inert and the halogen gas (Ar and Cl_2 in this work). Particularly, Cl_2 has a significant quenching effect on the population of excited states of Ar, which is important as it greatly affects the energy distribution in the discharge. This effect will be discussed in further detail in Chapter 7.

Due to the complicated nature of electronegative discharges, many realistic models and diagnostic methods use the electropositive discharge as a benchmark, and then gauge the change in physical parameters (typically the electron energy distribution function) when the halogen gas is included. This is particularly true for optical emission spectroscopy techniques, and this work is no exception. Therefore, much of the theoretical treatment of this chapter will be in regards to electropositive discharges with important extensions to electronegative discharges as needed.

2.2 PLASMA SOURCES

Low temperature plasma discharges that are created in laboratory settings are typically created using different sources of electromagnetic power and experimental configurations. The most common discharge power sources include direct current (DC), microwave (MW), and radio frequency (RF). As one can imagine, each one of these plasma types has unique conditions in which a plasma can be created, as well as specific properties that make each plasma useful for various purposes. This gives the experimenter options based on the physics being studied and/or the application. This section explicitly outlines the properties of an RF discharge as it is the power source utilized in this work. For more information regarding the properties of different plasma sources, the reader is referred to the pertinent references [1, 2, 4].

2.2.1 RF PLASMA

The type of plasma one uses for processing is very important and depends on the type of processing to be performed. For the purposes of this research, an RF plasma operating at 13.56 MHz, the commercial standard, is used. An RF plasma has distinct advantages for the purposes of etching and is commonly used in the semiconductor industry. The supplied RF power is an oscillatory field, which has a high energy transfer efficiency compared to DC discharges. This additional energy largely affects the electron population in the plasma leading to a higher level of ionization [2]. A sufficiently high amount of ionization is necessary as the reactive ion etching of materials is possible due to the formation of positively charged ion "sheaths" at the walls. These sheaths create local electric fields at those surfaces, which then accelerate ions that enter the sheath into the wall with high enough energy to chemically react. For a more thorough explanation of the choice of power source, the reader is referred to the doctoral dissertation of Upadhyay [1].

There are two different types of RF discharges that depend on how the power is provided to the system. One is the capacitively coupled plasma (CCP) where the discharge is driven by power provided between two electrodes, typically in a parallel plate type configuration. The second is the inductively coupled plasma (ICP) in which a coil is used to provide RF power to the discharge through time varying magnetic fields. Typically, ICP's have a higher plasma density than CCP's due to more efficient energy delivery to the gas [2]. However, using an ICP for SRF cavity processing would be very difficult due to the size and cylindrical geometry of the cavity. Therefore, a coaxial CCP system was designed due to its flexibility in geometry.

When a RF CCP is created, the geometry of the experimental setup is important. If the areas of the powered and grounded electrodes are the same, a symmetric plasma is created. Conversely, if the areas are different then an asymmetric plasma is created. A symmetric plasma has the unique property that sheath voltages on both electrodes are equal, meaning that both surfaces have equal ion bombardment. In an asymmetric plasma the sheath voltages are different with the grounded electrode having a lower sheath voltage compared to the powered electrode. This effect is shown in Figure 1 and can be derived mathematically as given by Koenig and Maissel [5].
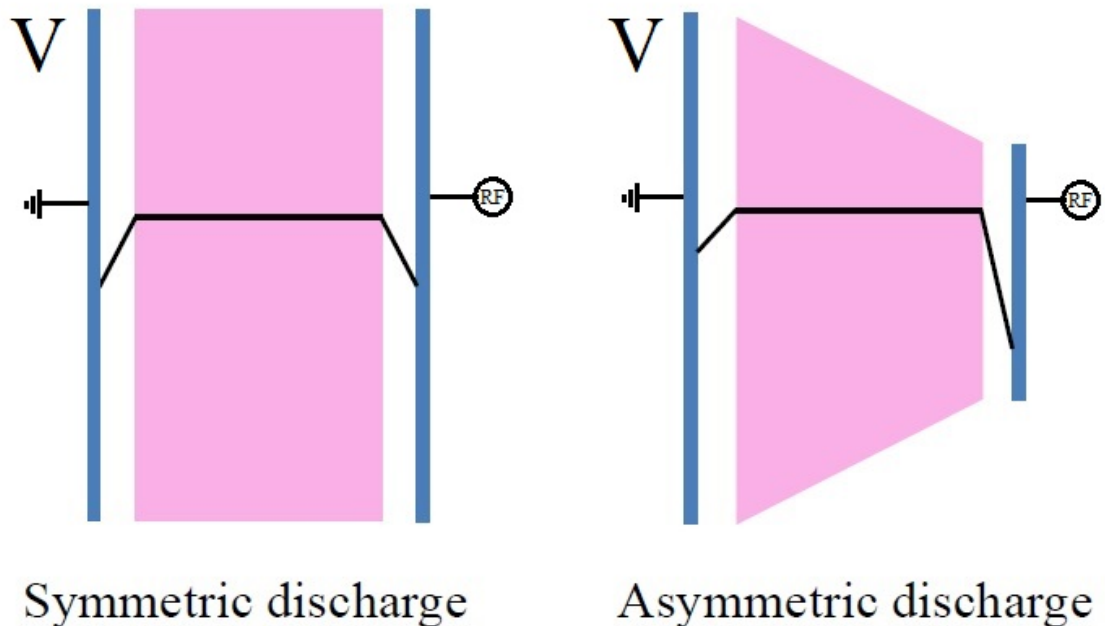
Figure 1: A simple drawing of the voltage distribution in a symmetric discharge (left) and an asymmetric discharge (right).

Considering two electrodes with areas A_1 and A_2 with sheath voltages V_1 and V_2 and thicknesses D_1 and D_2, the current density for each wall can be expressed using (collisionless) Child's Law,

$$J_i = \frac{KV^{3/2}}{m_i^{1/2}D^2}, \tag{3}$$

where K is a constant, m_i is the ion mass, V is the voltage and D is the sheath thickness. The current densities of positive ions at both electrodes are equal, so we can write

$$\frac{V_1^{3/2}}{D_1^2} = \frac{V_2^{3/2}}{D_2^2}. \tag{4}$$

The sheath that is formed around each electrode has a capacitance, and can be expressed as

$$C \propto A/D \propto 1/V, \tag{5}$$

which leads to the expression

$$\frac{V_1}{V_2} = \frac{A_2 D_1}{D_2 A_1}. \tag{6}$$

Substituting Eq. 6 into Eq. 4, we arrive at

$$\left(\frac{V_1}{V_2}\right)^{3/2} = \left(\frac{A_1 V_1}{A_2 V_2}\right)^2, \tag{7}$$

or

$$\frac{V_1}{V_2} = \left(\frac{A_2}{A_1}\right)^4. \tag{8}$$

This result suggests that there is a larger voltage drop at the smaller electrode and that the respective voltages can be altered by changing the area of the electrodes. The sheath voltage is what provides the ions with the bombardment energy to etch the substance on one of the electrodes. Therefore, it shouldn't be a surprise that the manipulation of this property is important to plasma etching processes. In fact, the manipulation of this property is what makes plasma etching of SRF cavities possible and will be explored further in the next subsection.

2.2.2 DC SELF-BIAS

Due to the large (negative) voltage drop at the smaller electrode, the ion bombardment is much larger and more energetic than at the larger electrode. For industrial applications this is oftentimes preferable as the material can simply be placed on the smaller electrode. Unfortunately, this is simply not possible in this work due to the

3D cylindrical geometry of SRF cavities. Therefore, in order ensure that there is enough ion bombardment to etch the niobium surface, the plasma asymmetry (Figure 1) must be reversed. This can be done by increasing the area of the smaller inner electrode (Eq. (8)), and/or by providing a positive external DC bias directly to the powered electrode.
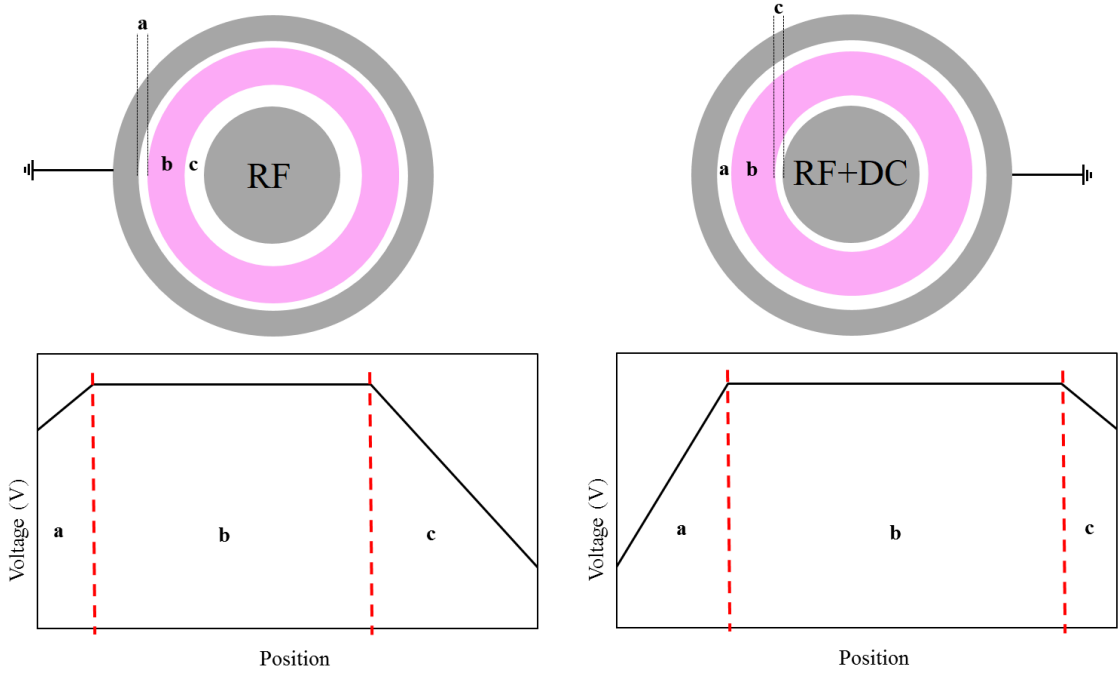
Figure 2: Illustration of the plasma asymmetry reversal in a coaxial CCP. Left: The electric potential distribution of a normal asymmetric discharge. Right: The electric potential distribution with the asymmetry reversed. Regions **a**, **b**, and **c** indicate the cavity sheath, the bulk plasma, and the powered electrode sheath, respectively.

With a large enough change to the potential of the powered electrode, the grounded electrode will eventually have a lower comparative voltage and become the more heavily bombarded surface. This asymmetry reversal is shown in Figure 2. A great deal of work has been done to accomplish this by varying both DC bias and the electrode area, and has proven to be a very important parameter in the etching of Nb [6–9]. More details about the DC self-bias and the plasma asymmetry reversal can be found in Sections 4.1.2 and 4.2.

2.3 PLASMA PARAMETERS AND CHARACTERISTICS

There is a large number of important quantities that are used to physically describe and characterize RF discharges, with all having varying degree of uses and significance. A brief description of those parameters that are of particular importance to this work are described in the following section.

2.3.1 SHEATH

In a plasma the charge carriers are moving rapidly and chaotically in the confined space in which it is held, but the thermal velocity of electrons is ≈ 100 times larger than the ion thermal velocity due to the large difference in the mass of these two particles [2]. When a CCP is created between two electrodes, the fast moving electrons are quickly lost to these surfaces. Due to this, the two walls quickly gain a net negative electric charge, which attracts the local positive ions in the plasma. The result, due to electrostatic screening, is a thin net positive ion sheath from the wall to a distance d. The formation of the sheath creates a voltage drop between the sheath and the wall (Figure 1), and therefore creates an electric field pointing from the sheath to the wall. This electric field then naturally repels the electrons traveling towards the surface ($\vec{F} = -e\vec{E}$), but any positive ion that has enough energy to enter the sheath will be accelerated towards the wall. This electric field and subsequent ion acceleration into the wall is the fundamental basis for plasma processing. The introduction of the positive ion or radical to the surface of the substrate provides the vehicle for processing, whether it is by kinetic means, chemical reactions, or a combination of both. Ions with enough energy to enter the sheath will do so with a velocity of

$$u_B = \sqrt{qk_BT_e/M}, \tag{9}$$

called the Bohm velocity. Here, q is the charge of the ion, k_B is the Boltzmann constant, T_e is the electron temperature, and M is the ion mass. The ion current J_i is then

$$J_i = qn_{is}u_B, \tag{10}$$

where n_{is} is the ion density at the sheath edge.

2.3.2 DEBYE LENGTH

The Debye length is the characteristic length of the plasma, defined by the electric

potential profile of the discharge and the electron density distribution. Considering the same parallel plate configuration as the previous section, both the plasma potential and the electron density are constant in the plasma bulk, but drop rapidly through the sheath. We show this by first using Poisson's equation in one dimension

$$\frac{d^2\Phi}{dx^2} = -\frac{e}{\mathcal{E}_0}(n_i - n_e), \tag{11}$$

where $\mathcal{E}_0$ is the permittivity of free space and Φ is the electric potential. The electron density is given by the Boltzmann relation

$$n_e = n_0 e^{(e\Phi/k_B T_e)}, \tag{12}$$

where n_0 is the electron density at $\Phi = 0$. This relationship is determined from the balancing of electrostatic forces in the discharge (see Ref. [2]). Plugging Eq. (12) into Eq. (11), we find

$$\frac{d^2\Phi}{dx^2} = \frac{en_0}{\mathcal{E}_0}\left(e^{\Phi/k_B T_e} - 1\right), \tag{13}$$

with $n_i = n_e = n_0$ due to the quasineutrality condition. The electron temperature is much higher than the plasma potential, so the exponential term can be simplified using a Taylor expansion

$$\frac{d^2\Phi}{dx^2} = \frac{en_0}{\mathcal{E}_0}\frac{\Phi}{k_B T_e}. \tag{14}$$

The potential must go to 0 as x approaches $\pm\infty$, so the solution to Eq. (14) is

$$\Phi = \Phi_0 \exp^{-|x|/\lambda_d}, \tag{15}$$

with

$$\lambda_d = \sqrt{\frac{\mathcal{E}_0 k_B T_e}{n_0 e^2}}. \tag{16}$$

This characteristic length can be used to define the size of regions within the discharge, and is the distance scale in which large charge densities can exist. That is to say, in spaces larger than a Debye length, the plasma is typically neutral [2].

2.3.3 PLASMA POTENTIAL

The rapid depletion of electrons to the walls in a plasma quickly creates a net positive charge in the bulk of the plasma. Once the sheath is established, it becomes difficult for electrons to escape the bulk plasma and a steady state is quickly developed. When this steady state is established, the loss of ions and electrons to the walls

are equal due to current conservation. The potential created within the plasma is called the space potential or plasma potential (V_s). Due to the formation of sheaths at each wall, the plasma potential is always the highest (positive) potential in the system.

2.3.4 THE ELECTRON ENERGY DISTRIBUTION FUNCTION

Arguably, the electron energy distribution function (EEDF) is the most important plasma characteristic to measure in a low temperature partially ionized discharge. This is especially true for discharges being used for plasma processing/etching as electron collisions are the primary energy transfer processes. Essentially, the EEDF can provide a good profile of the energy distribution within the plasma, and knowing how the EEDF changes with external parameters can be used to develop a more robust etching technique.

Since the EEDF ($F(\mathcal{E})$) is the functional representation of the energy distribution of electrons, it follows that the density of electrons (n_e) and the average energy ($\langle\mathcal{E}\rangle$) can be calculated as

$$n_e = \int_0^\infty F(\mathcal{E})\mathrm{d}\mathcal{E}, \tag{17}$$

and

$$\langle\mathcal{E}\rangle = \frac{1}{n_e}\int_0^\infty \mathcal{E}F(\mathcal{E})\mathrm{d}\mathcal{E}. \tag{18}$$

The most probable distribution for a population in thermal equilibrium is the Maxwell-Boltzmann (Maxwellian) distribution

$$F(\mathcal{E}) = \frac{2}{\sqrt{\pi}}T_e^{-3/2}\sqrt{\mathcal{E}}e^{-\mathcal{E}/T_e}. \tag{19}$$

Here, $T_e = \frac{2}{3}\langle\mathcal{E}\rangle$ is the effective electron temperature (henceforth simply called the electron temperature) and $\mathcal{E}$ is the electron energy (both in eV)[1]. Naturally, not all low temperature discharges follow a simple Maxwellian distribution. Oftentimes, the discharge can be characterized by a bi-Maxwellian distribution that has two distinct regions of low temperature electrons in the plasma bulk, and high temperature electrons at the tail of the distribution characterized by two distinct electron temperatures [10]. Considerations also must be made for non-Maxwellian distributions

---

[1]Until this point, the electron temperature T_e has been in units of Kelvin. In plasma physics, it is typically advantageous to redefine the electron temperature in electron-volts with the definition $T_e = k_B T_e(K)/e$. For the remainder of this dissertation, the unit of T_e is eV.

as well, and the following two-term EEDF is widely used [11–13]

$$F(\mathcal{E}) = C_1 T_x^{-3/2} \sqrt{\mathcal{E}} e^{-C_2(\mathcal{E}/T_x)^x}. \tag{20}$$

Here, the value of x determines the form of the EEDF, T_x is the electron temperature and C_1 and C_2 are constants dependent on x with the form

$$C_1 = x \left(\frac{2}{3}\right)^{3/2} \frac{\left[\Gamma(\frac{5}{2x})\right]^{3/2}}{\left[\Gamma(\frac{3}{2x})\right]^{5/2}}, \tag{21}$$

$$C_2 = \left(\frac{2}{3}\right)^x \left[\frac{\Gamma(\frac{5}{2x})}{\Gamma(\frac{3}{2x})}\right]^x. \tag{22}$$

This two term form of the EEDF reduces to a Maxwellian with $x = 1$. Comparative plots for three different EEDF types is shown in Figure 3.
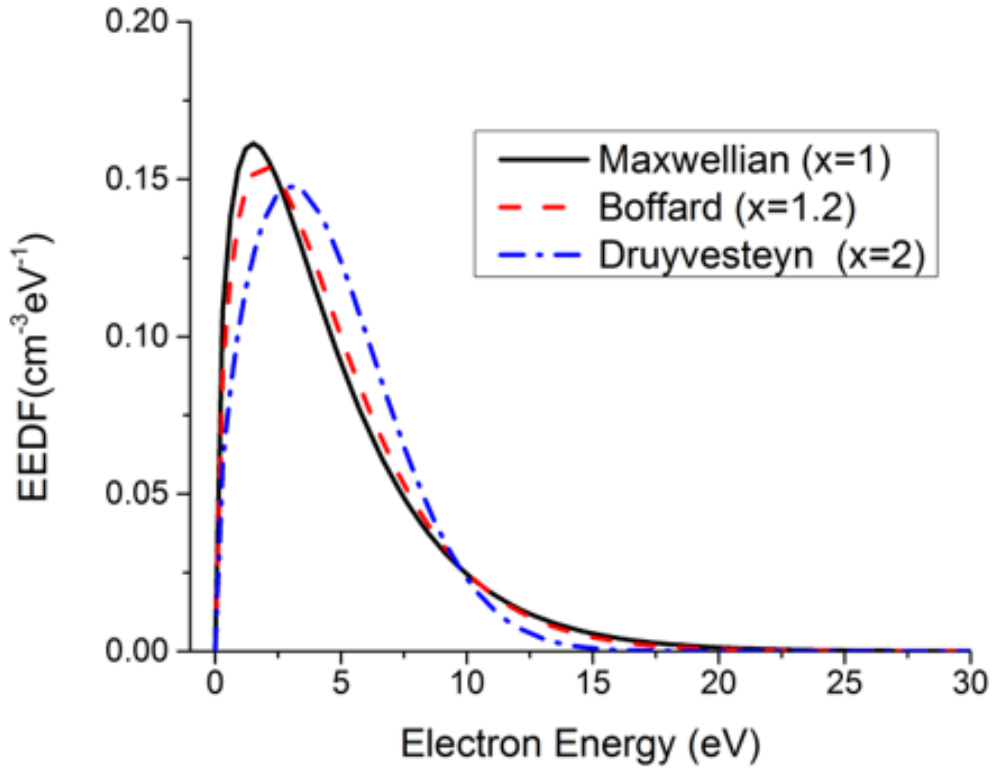
Figure 3: Example of different EEDF forms found in the literature. Each EEDF is plotted with $T_e = 3$ eV.

The three values for x are values found widely used in literature. Druyvesteyn and Penning found in 1940 that many low temperature discharges are more properly

characterized by a distribution with $x = 2$, while recently Boffard *et al.* has found that a value of $x = 1.2$ is more appropriate for a low temperature ICP discharge (in Argon) [11, 13]. In the case of this work, a Maxwellian distribution was used for the EEDF. Although this is most likely not a true representation of the discharge, it remains a reasonable approximation. It also greatly simplifies some of the diagnostic treatments outlined in Chapter 5.

The EEDF can be used to define the collision frequency of electrons with other species within the discharge. This is very useful when employing collisional radiative models (CRMs) that use particle balancing to find information about the various heavy atomic species (ions, excited neutrals, etc.). As will be shown in Chapter 5, CRMs are also commonly used to find the electron temperature and density. The rate coefficient for electron-atom collisions is defined as

$$Q_{e \rightarrow atom} = \left(\frac{2e}{m_e} \right)^{\frac{1}{2}} \int \sigma(\mathcal{E}) F(\mathcal{E}) \sqrt{\mathcal{E}} d\mathcal{E}, \tag{23}$$

where $\sigma(\mathcal{E})$ is the collisional cross section of the particular electronic interaction. The collisional cross section is essentially the probability of that transition occurring within the discharge, so it naturally is of high importance to these quantities. Indeed, there has been a great deal of work in experimentally measuring, and theoretically calculating these cross sections for various conditions [14–21]. While these works have certainly advanced the field, applying these cross sections is no simple task. All low temperature discharges are going to have shared characteristics and approximations, but cross sections must be applied with care based on the type of discharge in which they were measured or modeled. Furthermore, discrepancies of collisional cross section results still exist, even among studies considering similar discharges both experimentally or theoretically [16, 19–21]. More details about collisional cross sections and how they relate to this work can be found in Section 5.2.3.

CHAPTER 3

SRF CAVITY ACCELERATORS

Superconducting radio-frequency cavities at Jefferson National Laboratory are used to accelerate charged particles at high energy in modern particle accelerators. Collisional energy in the GeV range allows for the study of the most basic building blocks of the universe. This is possible because of the unique properties of super-conductivity and the propagation of electromagnetic fields through resonant cavity structures. The simplest case of a resonant rf cavity is a "pill-box" cavity in which a cylindrical waveguide is shorted by metal plates a certain distance l. This is the simplest case because the eigenvalue equation that describes the rf fields inside the cavity can be solved analytically. This eigenvalue equation is found from Maxwell's equations and has the form

$$\left(\nabla^2 - \frac{1}{c^2}\frac{\partial^2}{\partial t^2}\right)\left\{\begin{matrix}\vec{\mathbf{E}}\\\vec{\mathbf{B}}\end{matrix}\right\} = 0, \tag{24}$$

with the boundary conditions

$$\hat{n} \times \vec{\mathbf{E}} = 0, \qquad \hat{n} \cdot \vec{\mathbf{H}} = 0, \tag{25}$$

where c is the speed of light, $\vec{\mathbf{E}}$ is the electric field, $\vec{\mathbf{H}}$ is the magnetic field and $\hat{n}$ is the unit vector normal to the surface of the cavity. The solution of Eq. (24) yields a number of different possible modes within the cavity classified by two distinct groups. One group being the transverse magnetic (TM) modes where the magnetic field is created transverse to the waveguide symmetry axis. The other being the transverse electric (TE) modes in which the electric field is then transverse to the symmetry axis [22]. The TM_{010} mode is used for particle accelerators as it has a purely longitudinal (parallel to the symmetry axis) electric field, eliminates the angular dependence of $\vec{\mathbf{E}}$ and $\vec{\mathbf{H}}$ fields, and the frequency only has radial dependence.

In reality, the shape of the cavities are much more complicated than a simple "pill box" and have different shapes dependent on the application. The geometry of the resonant cavities of interest to this work is shown in Figure 4. Resonant cavities are divided into three different categories hallmarked by the value $\beta = v/c$, where v is the
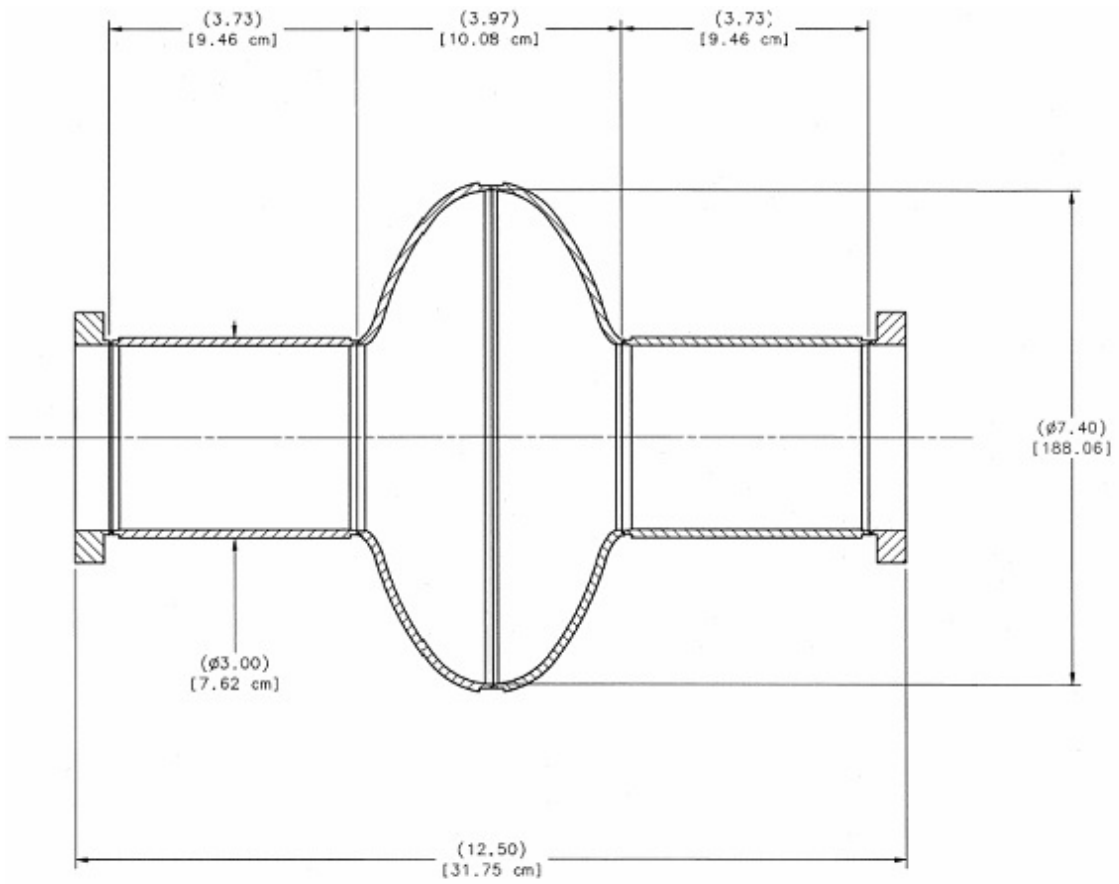
Figure 4: Geometry of an SRF cavity commonly used in particle accelerators today [22].

speed of the particle [23]. The cavities of interest here are those with high β values in which the particle beam is traveling near the speed of light. Figure 5 shows a 9-cell TESLA cavity with $\beta \approx 1$ used in superconducting particle accelerators today to primarily accelerate electrons, positrons, and high energy protons [23].

Figure 5: A 1.3 GHz 9-cell SRF cavity developed by the TESLA collaboration in 2000 [24]. This design is still widely used in accelerator facilities around the world.

Throughout this dissertation any mention of SRF cavities, beyond the theoretical treatments of this chapter, is referring to a 1.3 GHz single cell cavity (one cell in Figure 5). As will be shown in the following sections, these cavities are not without both physical and theoretical limitations that create a ceiling of effectiveness for these devices. Improving the performance of these cavities is the motivation for a great deal of scientific research, including the work described here.

3.1 CAVITY PERFORMANCE FIGURES OF MERIT

Consider a particle traveling through a cavity with a speed $v \cong c$ ($\beta \cong 1$). If the cavity is tuned to the driving frequency of the supplied RF power a standing wave of the electric field is developed inside the cavity. For the particle to receive the maximum acceleration gain it must enter the cavity with the electric field pointing in the same direction as the traveling particle, and exit the cavity when the electric field changes sign(*ie.* reverses direction). The time the particle spends in the cavity must then be equal to one half of the rf period and can be given by

$$T = \frac{\pi}{\omega_0} = \frac{L}{c},$$ (26)

with ω_0 being the angular frequency of the driving mode, and L the length of the cavity. The standing wave properties can be utilized further if the resonant structure is repeated, as in Figure 5. In this case, as is shown in Figure 6, when the particle

is exiting the first half wave resonator the standing wave changes sign, repeating this process and accelerating the particle further. Theoretically this can be done indefinitely, but of course in practicality there are physical limitations [24].

With the appropriate length of the cavity determined from Eq. (26), the electronic figures of merit can be established. The accelerating voltage of the particle V_{acc} is the maximum energy gain possible from the cavity divided by the particles charge. This can be written as

$$V_{acc} = \left| \int_0^L E_z(r = 0, z) e^{i\omega_0 z/c} dz \right|, \tag{27}$$

which leads to an average accelerating electric field with the value

$$E_{acc} = \frac{V_{acc}}{L}. \tag{28}$$

3.1.1 THE QUALITY FACTOR, GEOMETRY FACTOR, AND SHUNT IMPEDANCE

A significant figure of merit, appropriately called the quality factor (Q_0), is the ratio of the stored energy within the cavity (U) and the power dissipated through the cavity walls (P_c)

$$Q_0 = \frac{\omega_0 U}{P_c} = \frac{\omega_0 \mu_0 \int_V |\vec{\mathbf{H}}(\vec{\mathbf{r}})|^2 dV}{R_s \oint_A |\vec{\mathbf{H}}(\vec{\mathbf{r}})|^2 dA}. \tag{29}$$

Here, R_s is the surface resistance, V is the cavity volume and A is the cavity area. Essentially, the quality factor can be interpreted as the number of rf cycles required to deplete the stored energy of the cavity [23]. Another figure of merit can be defined, called the geometry factor

$$G = Q_0 R_s, \tag{30}$$

which is strictly determined by the shape of the cavity.

Limitations within the cavity can also be expressed by the shunt impedance

$$R_{sh} = \frac{V_{acc}^2}{P_c}, \tag{31}$$

which is a measure of how strong the rf field interacts with the traveling particle. The ratio of the shunt impedance and the quality factor yields

$$\frac{R_{sh}}{Q_0} = \frac{V_{acc}^2}{\omega_0 U}, \tag{32}$$
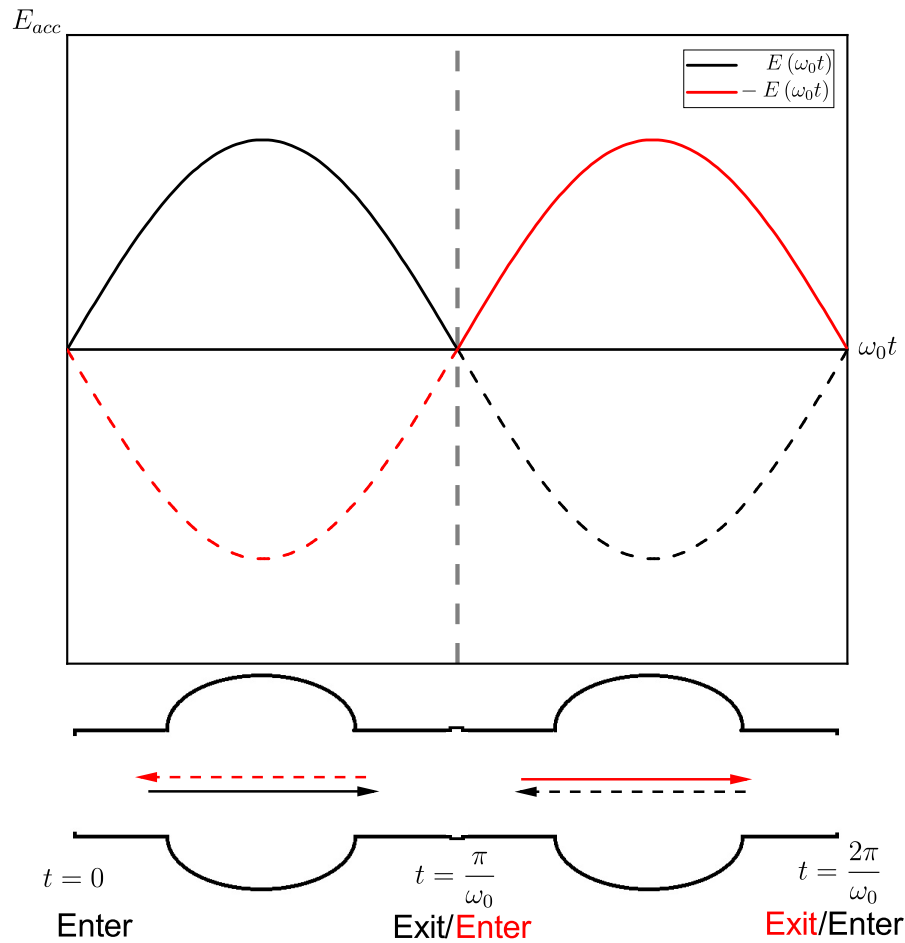
Figure 6: Scheme of the acceleration of a particle through SRF cavities. The particle enters the first cavity at $T = 0$ and exits at $T = \frac{\pi}{\omega_0}$ to receive the maximum accelerating field (black curve). As the particle exits the first resonator and enters the second, the time varying field has changed sign (red curve) and the process is repeated. It is for this reason there is an odd number of resonators in accelerating cavities (Figure 5).

which is both a material and shape independent quantity. In designing cavities, the aim is to maximize the quality factor and shunt impedance while minimizing the geometry factor. In reality, this is of course no easy feat, and compromises must be made to make realistic SRF cavities.

3.2 SUPERCONDUCTIVITY

Certain materials can exhibit a behavior of near zero electrical resistance allowing for current to flow through the object with no electrical power loss. This occurs at an object's critical temperature T_C, where two defining characteristics of superconductors occur. The first is the zero DC resistance of the material, and the second is perfect diamagnetism, where the material perfectly expels any applied magnetic field within the surface of the material. These two effects were found by Kammerlingh-Onnes and Meissner, respectively, but they are not mutually exclusive [25, 26]. A list of common superconducting materials and their critical temperatures can be found in Table 1.

Table 1: Short list of common superconducting materials and their respective critical temperatures.

Material	T_C (K)
Al	1.2
In	3.4
Sn	3.7
Hg	4.2
Ta	4.5
Pb	7.2
Nb	9.3
NbN	16
Nb_3Sn	18

The perfect diamagnetism, or Meissner effect, occurs due to surface or "screening currents" that act like induced "eddy currents" that never decay [22]. These surface currents create an equal and opposite magnetic field when placed in an external magnetic field, but there is a limit to this external field at which the Meissner effect breaks down. This critical magnetic field (H_C) has the form

$$H_C(T) = H_0(0) \left[1 - \left(\frac{T}{T_C} \right)^2 \right], \tag{33}$$

where H_0 is the maximum external magnetic field at absolute zero and T is the temperature. This relationship shows that the superconducting critical field is a thermodynamic entity, rather than being a direct consequence of zero electric resistance. The first model to successfully derive an electrodynamic relationship that explains both perfect conductivity and diamagnetism was found by London and London in 1935 when they successfully applied a two fluid electron model proposed by Gorter and Casimir a year prior [27, 28]. This two fluid model considered two different current states of electrons, with one superfluid current with density n_s and velocity v_s and one normal current with density n_n and velocity v_n. By considering two different currents through the material, one that encounters surface resistance and one that does not, Maxwell's equations can be applied to obtain

$$\nabla^2 \vec{\mathbf{B}} = \frac{1}{\lambda_L^2} \vec{\mathbf{B}}, \tag{34}$$

which shows that the applied magnetic field decreases exponentially inside the superconductor with the solution

$$B(x) = B(0)e^{-x/\lambda_L}. \tag{35}$$

The quantity λ_L is called the London penetration depth and represents the distance in which the external magnetic field drops by $1/e$ in the material. It is also representative of the location of the supercurrent and magnetic fields created within the material to oppose this external field. The London penetration depth is given as

$$\lambda_L = \left[\frac{m}{\mu_0 n_s e^2} \right]^2, \tag{36}$$

where m is the electron mass, μ_0 is the vacuum permeability, and e is the electron charge. The two fluid model allows for a comparison of the superconducting electron density to the normal electron density with the relationship

$$\frac{n_s}{n_n} = 1 - \left[\frac{T}{T_C} \right]^4, \tag{37}$$

which then leads to the following temperature dependence of the London penetration depth

$$\lambda_L(T) = \frac{\lambda_L(0)}{\sqrt{1 - \left[\frac{T}{T_C} \right]^4}}. \tag{38}$$

Initially, it was found that there exists a fundamental discrepancy between the experimental and theoretical values of the London penetration depth. This was addressed by Pippard by introducing a coherence length ξ_0 [29], which is analogous to the mean free path in the treatment of normal conducting metals [22] . This coherence length is estimated to be

$$\xi_0 = a\frac{\hbar\nu_F}{k_B T_C},\tag{39}$$

according to the uncertainty principle, where a is a constant (a=0.15 based on experimental fits), and ν_F is the Fermi velocity.

An alternative theory of superconductivity was proposed by Ginzburg and Landau in 1950 [30]. This was a more quantum mechanical approach as the superconducting electron density was described using a pseudowavefunction $\psi(\vec{r}) = |\psi(\vec{r})| \exp^{i\phi(r)}$ with $|\psi(\vec{r})|^2$ representing the local density of superconducting electrons [22]. The details of this treatment can be found elsewhere [22, 30], but it leads to a general classification of superconductors based the Ginsberg-Landau parameter $\kappa = \frac{\lambda_L}{\xi}$ with

- Type I superconductor: $\kappa = \frac{\lambda_L}{\xi} < \frac{1}{\sqrt{2}}$

- Type II superconductor: $\kappa = \frac{\lambda_L}{\xi} > \frac{1}{\sqrt{2}}$.

The major distinction between the two superconducting types is the emergence of a second critical field in type II superconductors. This means there exists a range where the type II superconducting material is limited by the development of magnetic flux through so-called "vortices" that develop on the surface [31].

However, as the treatments by London-London and Ginzberg-Landau were developed phenomenologically based on experimental observations, a full theoretical treatment of superconductivity was still needed. The work of Bardeen, Cooper and Schrieffer filled this gap in 1957 with their BCS theory and the discovery of the so-called Cooper pair [32]. Cooper pairs are developed through the interaction between two electrons in the lattice structure of the material. At absolute zero, interactions between two electrons (assuming interactions with other electrons does not occur) are facilitated by phonon exchange inside the lattice structure. Through this exchange it surprisingly becomes energetically favorable for the electrons to have an attraction and move through the material together. As a classical explanation, an electron passing as a free particle through a metal will attract positive ions in the lattice structure and repel other close electrons. The attraction of the ions to the

electron in the lattice perturb the structure and increases the positive charge of the local region. This positive region will attract other electrons, and at long distances (Cooper pairs can have a separation of hundreds of nanometers) the two electrons will travel as a pair through the material. To achieve the lowest energy state between two interacting electrons, the two electrons should have equal and opposite momentum. This maximizes the attraction of the second electron to the local positive charge region, therefore *increasing* the amount of scattering processes. The equal and opposite momentum of the two electrons minimizes the energy of the pair (average momentum is zero) and the center of mass of the pair is stationary with respect to the lattice. Additionally, the two electrons must have opposite spins as the singlet state is the lowest electron interaction state [22]. Cooper pairs become energetically favorable below T_C with all electrons becoming pairs at absolute zero ($T{=}0$) [23].

3.3 LOSSES IN SRF CAVITIES

It should be no surprise that limitations in superconducting materials arise from an increase in the surface resistance. When considering radio-frequency cavities where the current through the cavity is time varying (AC), a non-zero surface resistance can arise. In the DC case, there must be no electric field as this would continuously accelerate the superelectrons, and the superconducting current would increase indefinitely. The lack of electric field means that the normal electrons do not flow. In the AC case, the supercurrent can lag behind the change in the field due to the inertial mass of the electrons. This lag creates an electric field within the material that can drive the normal electrons. Therefore, there exists a nonzero resistance that can be developed from the BCS theory. Theoretically this would be the only source of dissipation in the material, but experimentally this is far from the truth. The total surface resistance R_s of a superconductor with an AC current can be stated as

$$R_s = R_{BCS} + R_{res}, \tag{40}$$

where R_{BCS} is the surface resistance found from the BCS theory and R_{res} is the residual resistance from outside sources like impurities, hydrides, oxides, residual dc magnetic fields, and chemical residues from processing, among others. It should be no surprise that the elimination of the residual resistance and its sources is of the utmost importance for the construction and processing of SRF cavities.

3.3.1 RESIDUAL LOSSES

The residual resistance in Eq. (40) is a temperature dependent quantity and is the primary source of power losses at lower temperatures. There are a number of sources for these losses that often manifest from the construction and preparation of the cavity. A significant source of residual resistance is from the formation of hydrides on the surface during the cryogenic cooling of the cavity to the critical temperature (< 10 K). This loss, called "Q disease", is dependent on a number of factors including the amount of dissolved hydrogen, the cooling process (particularly around 100 K), and impurities [23]. Furthermore, the BCP process used for surface material removal can increase the dissolved hydrogen in the material if the process occurs at too high a temperature ($> 15^oC$) [23]. The typical remedy for Q disease is to bake the cavity at high temperatures ($\approx 800^oC$) to degas the material.

Oxide layers are naturally developed on the surface of Nb and can lead to significant residual losses. The dielectric properties of the oxide layer can contribute to losses, but is negligible in most cases of Nb cavities. However, these oxide layers can trap other gases (including hydrogen, contributing to Q disease) at the oxide-Nb interface, particularly at grain boundaries, causing non-negligible losses [22]. These losses are typically alleviated by baking the cavity at high temperatures under vacuum to allow the oxide layer to disappear, and then introduce oxygen to the furnace for a controlled dry oxidation on the surface [22].

The strong rf fields within the cavity can accelerate particles to speeds close to the speed of light, so it is important to consider the effects these fields have on the surface electrons of the cavity. At small regions within the cavity that have high transverse magnetic fields, electrons can be emitted from the surface. These emitted electrons travel in a circular orbit and return to the cavity surface in the same location. The collision with the surface can generate a secondary electron that travels a similar orbit [33]. This effect, called multipacting (multiple impact electron excitation), can cause significant losses in the cavity through heating from the electron-wall collisions. Multipacting is typically alleviated from improved cavity shapes (pill-box cavities have more multipacting issues than elliptical cavities) and thorough cleaning of the cavity surface.

Among the sources of residual resistance, the most challenging to overcome is the field emission of electrons. In the presence of a high electric field, electrons in the cavity material have a higher probability of tunneling into the vacuum space

through the reduction of the work function at the surface [34]. Therefore, specific locations of extremely high electric fields in the cavity emit a great deal of heating electrons and x-rays through bremsstrahlung radiation [22]. Field emission naturally becomes particularly influential at high E_{acc}. The reduction of field emission is usually facilitated by ensuring the cavity is exceptionally clean. Furthermore, plasma processing has shown reduction of field emission in an SRF cavity [1].

3.4 CAVITY PROCESSING

As it is clear from the previous section, it is imperative that impurities and surface defects are eliminated from the surface of the cavity. This is currently done through a series of wet chemical etch processes and extensive cleaning procedures. A number of these techniques are described in the following subsections.

3.4.1 BUFFER CHEMICAL POLISHING

Buffer chemical polishing (BCP) is a popular wet chemical etch process due its effectiveness in removing surface layers of Nb. This process typically has a removal rate of 1 micron/minute [22]. The BCP process consists of filling the cavity with nitric, hydrofluoric and phosphoric acids in a ratio of 1:1:1 or 1:1:2. The nitric acid starts the process by oxidizing the surface of Nb, then the hydrofluoric acid removes the oxide layer. The phosphoric acid acts as a buffer since the previous two processes are highly exothermic and remove too much material on their own. The chemical reactions with niobium are given by

$$6\text{Nb} + 10\text{HNO}_3 \rightarrow 3\text{Nb}_2\text{O}_5 + 10\text{NO} \uparrow + 5\text{H}_2\text{O} \tag{41}$$

and

$$\text{Nb}_2\text{O}_5 + 10\text{HF} \rightarrow 2\text{NbF}_5 + 5\text{H}_2\text{O}. \tag{42}$$

The etch rate for BCP can change depending on the temperature of the acid, the amount of dissolved Nb, and agitation. The chemicals used for BCP are very dangerous and pose serious health and safety risks if not properly handled and/or disposed. After the BCP process, the cavity must be thoroughly rinsed to eliminate residue left by the acid. While BCP is a rather simple and straightforward process, it can create "steps" around grain boundaries because the local etch rate can vary depending on the orientation of the niobium grains [23]. This typically causes significant issues above $E_{acc} = 20$ MV/m, so other methods must be employed for higher Q cavities.

3.4.2 ELECTROPOLISHING

Electropolishing (EP) is another chemical based process that can alleviate the limitations of BCP for high Q cavities. This is accomplished by partially filling a cavity with hydrofluoric and sulfuric acid and inserting a high purity aluminum cathode ($-$) to provide electric current to the electrolytic mixture. The cavity then acts as the anode ($+$) in an electrolytic cell where it absorbs electrons and oxygen to make niobium pentoxide, which is then dissolved by the hydrofluoric acid [33]. The acid mixture is a 1:9 ratio of sulfuric to hydrofluoric acid and the chemical processes are governed by

$$2Nb + 5SO_4^{--} + 5H_2O \rightarrow Nb_2O_5 + 10H^+ + 5SO_4^{--} + 10e^- \tag{43}$$

and

$$Nb_2O_5 + 10HF \rightarrow 2NbF_5 + H_2O. \tag{44}$$
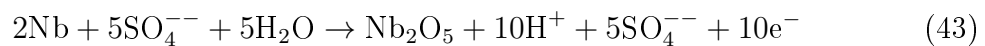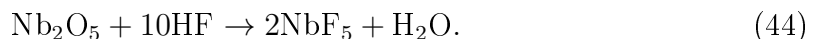
The process is conducted with a constant flow of acid while the cavity is rotated to avoid gas trapping at the surface of the cavity. The etch rate of EP is approximately 0.3 microns/minute. While the full understanding as to why EP is more effective than BCP is not complete, it is seen that EP leaves a smoother (<0.5 micron), shiny surface compared to BCP [1]. While this does not fully explain the phenomenon, it is generally considered a significant contributing factor. After the EP process, the cavity must be high pressure water rinsed to remove the dangerous and hydrogen trapping film left on the surface.

3.4.3 CENTRIFUGAL BARREL POLISHING

Centrifugal barrel polishing (CBP) is not always used for cavity processing, but it is useful when cavities have high initial surface roughness. CBP is simply a mechanical smoothing process where the cavity is filled with a solid material (typically ceramics or wood) and rotated. This tumbling process is quite effective at removing surface irregularities like scratches and pits, and smooths the weld locations [35]. The final surface can have low surface roughness, on the order of nanometers, but this does not correlate to better performance [23]. Chemical etching is almost always required after CBP to remove the abrasive material that gets embedded in the surface [23].

3.4.4 ULTRASONIC CLEANING AND HIGH PRESSURE WATER RINSING

Among the cleaning and surface processing procedures, ultrasonic cleaning and high pressure water rinsing are the simplest and very common techniques used in science in general. Ultrasonic cleaning, or sonication as it is commonly referred, is the process of using sound waves to agitate the surface of a material submerged in a liquid cleaning solution. This is effective in removing grease and oils from the surface. High pressure water rinsing is conducted by shooting a jet of water pressurized at roughly 80 bar through a nozzle. The nozzle is programmed to run along the length of the cavity as it is rotated to ensure the entire cavity is thoroughly rinsed.

CHAPTER 4

PLASMA PROCESSING AND ITS APPLICATION TO SRF CAVITIES

Plasma etching and processing has been a part of the semiconductor industry for a large part of the last century, but extending this technology to accelerator cavities is no simple task. While the basic concepts may remain similar, the vast differences in target material, geometry, amount of removal, and desired final surface require an in depth study into the feasibility of this technology for this application. Because of this, a great deal of work was done by Upadhyay [1] to engineer and develop an etching experiment to prove the practicality of plasma etching for SRF cavities. Throughout this study, not only was he successful in the removal of surface layers on Nb samples, but empirical relationships between externally controlled experimental parameters and final etch rate/material removal were established [1].

This chapter serves to summarize the work by Upadhyay [1] that established the empirical relationships between the external parameters and the etch rate. All of the figures in this chapter were reproduced with permission from the author's work and publications [1, 6–9, 36–38].

4.1 THE Nb RING SAMPLE EXPERIMENT

The cylindrical geometry of SRF cavities presents a number of challenges in the plasma processing of its inner surface. The two most significant issues are the uniform etching of a 3-D cylindrical surface, and the necessary reversal of the plasma asymmetry to etch the inner surface of the cavity (the grounded electrode). Both of these issues are related, so the systematic study of both in tandem was paramount. Therefore, etching experiments were conducted in a simple cylindrical geometry with Nb ring type samples placed on the inner surface of the vacuum chamber. Examples of the ring samples can be seen in Figure 7.
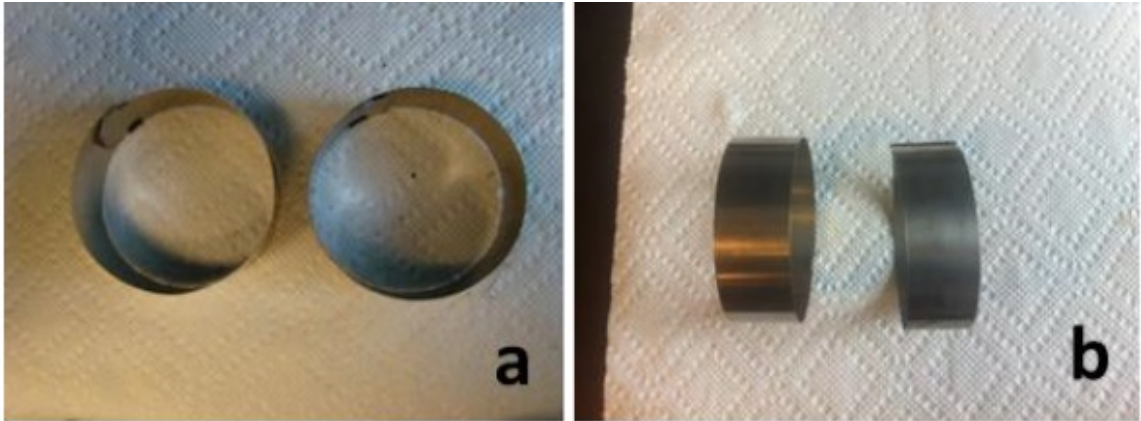
Figure 7: Photos of the niobium ring samples with a width of 2.5 cm and diameter of 7.2 cm. The diameter is comparable to the diameter of an SRF cavity beamtube. (a) Top view (b) Side view [36].

The ring samples were employed in two specific configurations. The first is to simply measure the etch rate as a function of the various external parameters, mostly in the region of the discharge that corresponds to the highest ion energy. The second was to measure the etch rate uniformity at different locations along the chamber length, with one sample closer to the gas flow input. Although these studies are presented separately in the literature, results from these studies are presented together throughout this chapter for brevity [7, 36].

4.1.1 THE REQUIREMENTS FOR ION ASSISTED REACTIVE ION ETCHING

Ion Assisted Reactive Ion Etching requires both chemical and physical processes to achieve bulk removal of surface layers of a material. As will be shown later in this chapter, it was found that the etching rate of Nb indeed has a significant dependence on the gas composition and ion energy into the surface. However, these conclusions were shown explicitly and simply by conducting etching experiments with these parameters studied independently of one another. As is shown in Figure 8, one can see that the IARIE of Nb requires that both chemical and physical components are required for *any* removal of surface layers.
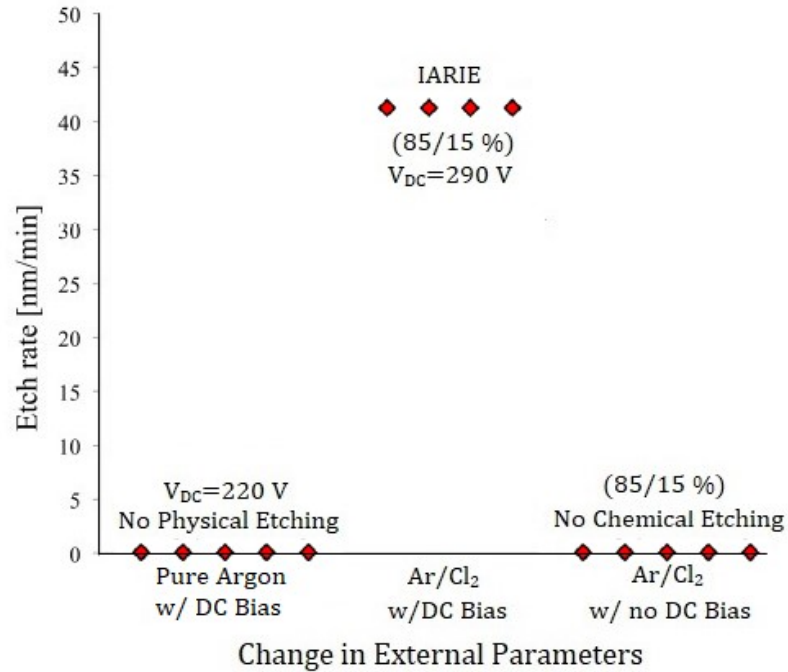
Figure 8: Etch rate dependence on the combination of DC bias and gas composition. Conditions were as follows: RF power = 150 W, pressure = 150 mTorr, electrode diameter = 5.08 cm, chamber temperature = 422 K [7].

It is important to point out that the addition of a positive DC bias is necessary for etching as the natural potential difference between the plasma potential and the cavity wall is not sufficient. The large negative self bias on the powered electrode, and therefore the sheath, is simply too large so that all of the ions are accelerated into the wrong target. This distinction is important as most RIE processes done in a parallel plate configuration treat this natural self bias as a boon and simply place the target substrate on the powered electrode. Therefore, studies involving the manipulation of bias on the powered electrode are typically done by increasing the *negative* bias [39–42]. While limiting, this allows for a unique study of the effects of positive DC bias on the discharge parameters. This exploration was a significant motivation of this dissertation and the results of this study can be found in Chapters 7 and 8.

4.1.2 DRIVEN ELECTRODE DC BIAS

The importance of positively biasing the driven electrode was shown in the previous section, but there is also a significant quantitative relationship between etch rate and DC bias. This relationship can be seen clearly in Figure 9.
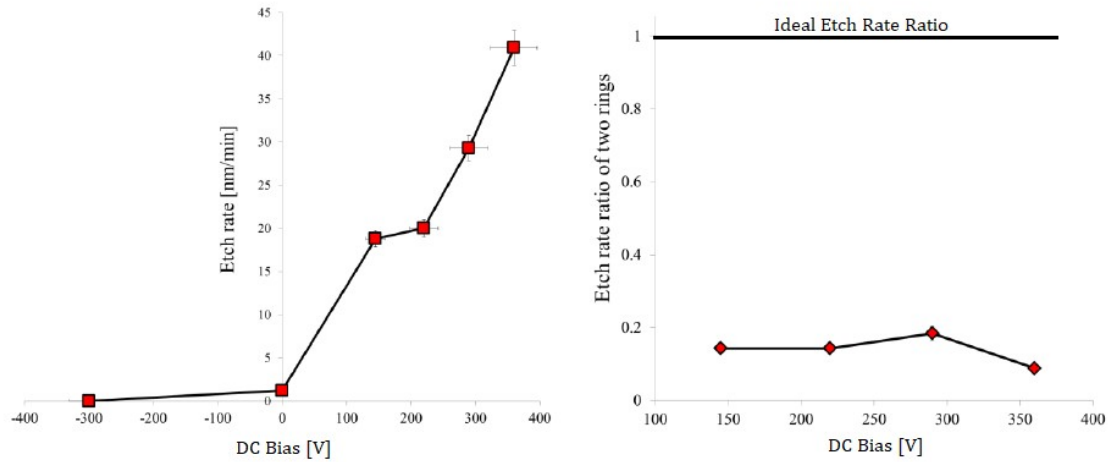
Figure 9: Left: Etch rate of ring sample vs. DC bias. Right: Etch rate ratio of two ring samples vs. DC bias. Conditions were as follows: RF power = 150 W, pressure = 150 mTorr, electrode diameter = 5.08 cm, chamber temperature = 422 K, gas composition = 85/15 % Ar/Cl$_2$ [7].

As was shown in sections 2.2.1 and 2.2.2, a negative self-bias voltage is developed on the smaller driven electrode due to the high mobility of the electrons. Electrons are also lost to other surfaces, but these surfaces are (typically) electrically grounded. This leads to the formation of a positively charged ion sheath along the surfaces. The sheath on the driven electrode is naturally bigger due to the high negative voltage, and therefore the ion energy into the driven electrode is much higher. In order to increase the ion bombardment and energy on the chamber surface, the potential profile inside the discharge must be modified to make this surface the energetically favorable target. Essentially, the potential difference between the plasma bulk (plasma potential V_p) and the chamber wall (V=0) must be larger than the potential difference between the bulk and the driven electrode (V_{DC}). Therefore, the potential on the driven electrode has to exceed 0 V (see Figure 2). As V_{DC} is increased and approaches V_p, the bulk potential must also increase to maintain it's distinctive property that it is the highest (positive) potential in the system. This is an effective way

to increase the ion energy/bombardment on the grounded surface as it's potential remains constant.

This concept is confirmed by Figure 9 as no etching occurs without a net positive DC bias on the driven electrode. This also confirms that an increasing positive V_{DC} increases the ion energy/bombardment on the grounded target surface. The 'knee' in the curve could be indicative of two energy thresholds for ion etching related to the positive Ar and Cl ions, and the other related to the Cl_2 ions [7, 43].

The right side of Figure 9 shows a consistent low etch rate uniformity with the increase in bias. This indicates that the DC bias is not a good control parameter for uniformity, and therefore other parameters are better suited in this aim.

4.1.3 Cl_2 CONCENTRATION

In order for plasma etching to be effective, surface impurities, contaminants, oxides, and layers of bulk surface material need to be removed from the target. It is also imperative that these materials are volatile enough to be quickly and efficiently removed from the system. As shown in the previous section, simple physical sputtering cannot effectively remove surface layers, so a mixture of halogen and inert gases are used to facilitate both physical and chemical processes. To this end, industrial plasma etching applications typically use fluorine or chlorine as the chemically reactive halogen gas and oxygen or argon as the carrier gas. While the use of fluorine based mixtures was explored, it was found that an Ar/Cl_2 mixture was more advantageous [44]. This mixture is useful as chlorine forms a volatile product with niobium (Nb_5Cl) according to Eq. (45) that can be pumped out of the system

$$2Nb_{(s)} + 5Cl_{2(g)} \rightarrow 2NbCl_{5(g)}. \tag{45}$$
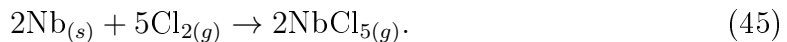
The boiling point of Nb_5Cl is ≈ 250 ^oC so the internal substrate temperature is important, as will be shown in 4.1.4.

Argon is a well studied inert gas used for plasma etching and processing. Argon also has well defined and easily measurable atomic energy transitions that are useful in characterizing the discharge physics. Additionally, chlorine poses a smaller health risk compared to Florine and can be more safely handled in a university laboratory environment.

With the processing gases established, the appropriate concentration of the gases to effectively etch must be found. It was established that both physical and chemical

etching mechanisms must be present in order to remove layers from bulk Nb, so it is important to ensure there is enough of each process to facilitate desired results [7].
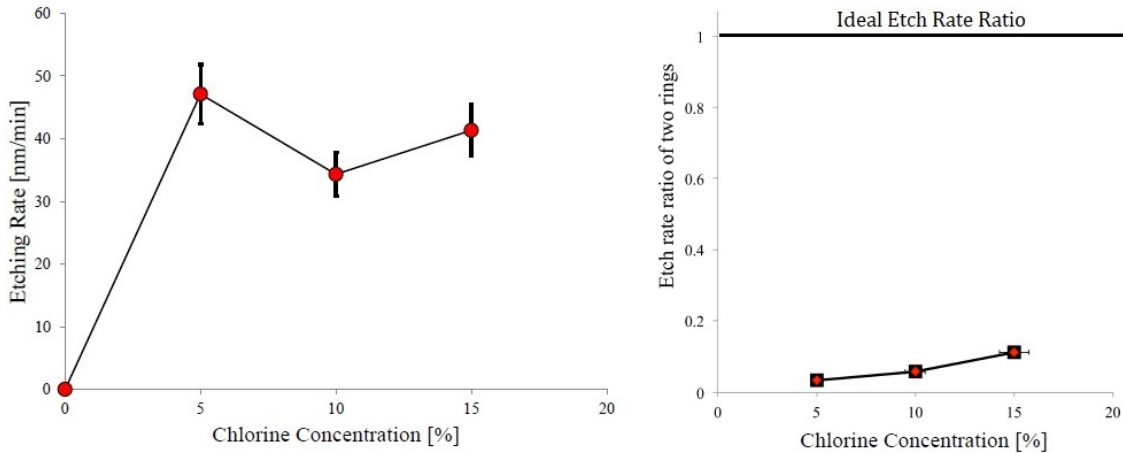
Figure 10: Left: Etch rate of ring sample vs. Cl_2 concentration [36]. Right: Etch rate ratio of two ring samples vs. Cl_2 concentration [7]. Conditions were as follows: RF power = 150 W, pressure = 150 mTorr, electrode diameter = 5.08 cm, chamber temperature = 422 K, positive DC bias = 290 V.

It was found, as shown in Figure 10 that the difference in etch rates between a 5-15% concentration of Cl_2 in Ar were within error. However, Figure 10 also shows a higher etch rate uniformity in ring samples located in different locations of the chamber for a higher concentration [7, 36]. The reason for the apparent saturation effect with Cl_2 concentration is not completely clear, but it is most likely due to a short residence time of Cl_2 in the chamber and a lack of Cl_2 consumption in the surface reactions. The latter of these two possible sources has been seen previously in Ar/Cl_2 discharges [45]. The increase in uniformity with increasing Cl_2 concentration suggests that the radical density is an important constraint [1].

4.1.4 SUBSTRATE SURFACE TEMPERATURE

The relationship between the etch rate and surface temperature of the substrate is an important indicator of etching mechanisms. Surface temperature is directly related to the chemical etching mechanism and normally exhibits an Arrhenius relationship with etch rate [7]. As shown in Figure 11, this is indeed the case for our discharge.
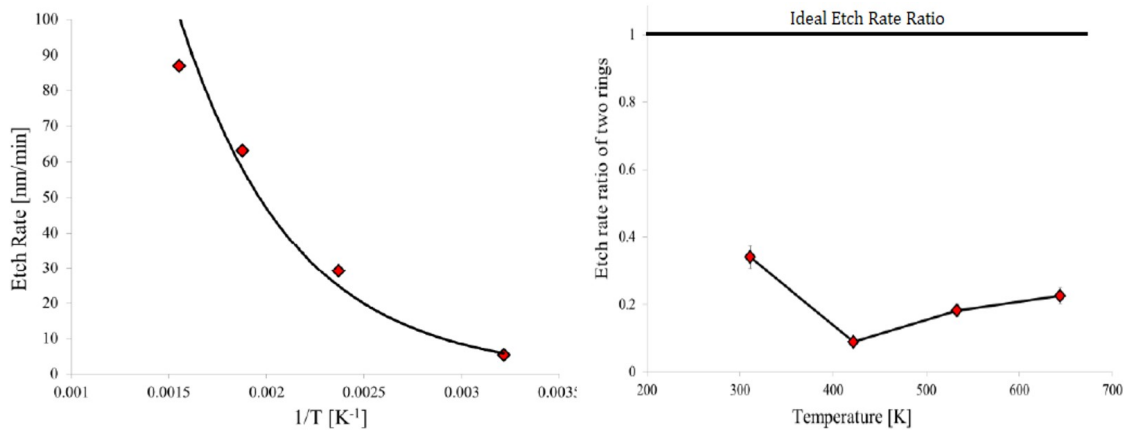
Figure 11: Left: Etch rate of ring sample vs. substrate temperature. Right: Etch rate ratio of two ring samples vs. surface temperature. Conditions were as follows: RF power = 150 W, pressure = 150 mTorr, electrode diameter = 5.08 cm, positive DC bias = 290 V, gas composition = 85/15 % Ar/Cl$_2$ [7].

This Arrhenius relationship confirms that the Nb etching process has a strong chemical component. The exponential fit to the data yields an estimated activation energy of 0.15 eV. It has been shown that a higher temperature improves the morphology of the surface, especially in conjunction with increased power density [46, 47]. Exploring these surface effects as a function of substrate temperature is very important as the smooth surface of SRF cavities is paramount. This study was a part of the work presented in this dissertation and the details can be found in Chapter 9.

Figure 11 also shows the relationship, or lack thereof, between the substrate temperature and etch rate uniformity. The slight benefit of a lower temperature to etch rate uniformity is greatly outweighed by the benefits of increasing temperature outlined previously. It was deemed that temperature is not an effective control parameter for etch rate uniformity [7].

4.1.5 RF POWER

The relationship between RF power and etching rate is rather straightforward. An increase in RF power leads to an increase in the plasma density, or rather the density of ions and electrons, in the discharge. Therefore, it should be no surprise that the etch rate increases as a function of RF power as shown in Figure 12.
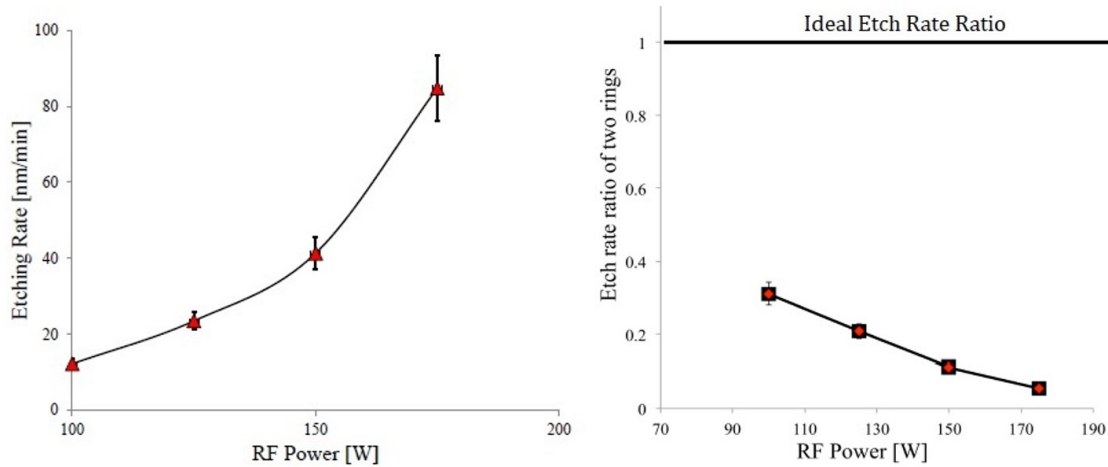
Figure 12: Left: Etch rate of ring sample vs. RF power. Right: Etch rate ratio of two ring samples vs. RF power. Conditions were as follows: pressure = 150 mTorr, electrode diameter = 5.08 cm, chamber temperature = 422 K, positive DC bias = 290 V, gas composition = 85/15 % Ar/Cl$_2$ [7].

It is important to emphasize that increasing RF power in this case is has different consequences than the typical parallel plate reactor. In the parallel plate case, the substrate is placed on the powered electrode and an increase in RF power also increases the negative self bias on this electrode. The increase in self bias increases the ion energy into the substrate, thus increasing the etch rate further. In the coaxial reactor, the necessity of a positive DC bias on the powered electrode stifles this effect as the DC bias voltage is held constant.

The right side of Figure 12 clearly shows a decrease of etch rate uniformity as RF power is increased. While an increase in RF power indeed leads to a generally higher etch rate, the increase in power facilitates a higher creation of reactive ions in the region closer to the gas delivery. Thus, there are less radicals and ions that can be used to etch the sample downstream.

4.1.6 PRESSURE

The relationship between the etch rate and pressure can be indicative of the etching mechanism of the discharge. The pressure is increased in the chamber simply by the increase of the flow of gas into the volume. Not surprisingly, this leads to an increase in the concentration of the reactive species in the discharge. However, the concentration of reactive Cl ions depends on the delivered RF power and the

electronegativity degree of the plasma. Additionally, an increase in pressure leads to a lower mean free path of the particles/molecules in the discharge. The increase in collisions quenches radical production as the electron temperature, or average electron energy, is decreased. From this perspective it stands to reason that if the etch rate increases with pressure, the etching mechanism is more chemical in nature, while a decrease indicates a RIE process as the ion concentration and energy have increased significance. Indeed, Figure 13 shows a decrease in etch rate as the pressure is increased, providing additional confirmation that the etching process is RIE.
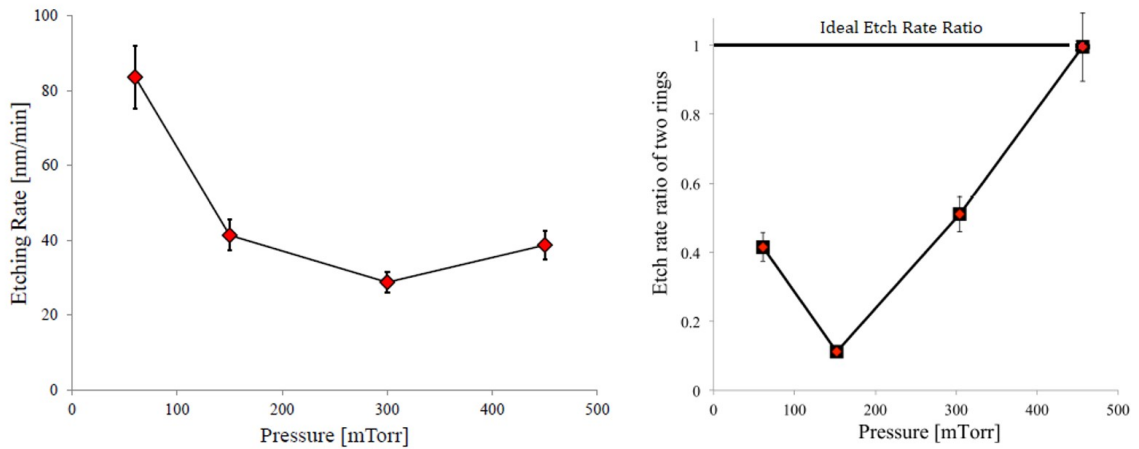
Figure 13: Left: Etch rate of ring sample vs. pressure. Right: Etch rate ratio of two ring samples vs. pressure. Conditions were as follows: RF power = 150 W, electrode diameter = 5.08 cm, chamber temperature = 422 K, positive DC bias = 290 V, gas composition = 85/15 % Ar/Cl$_2$ [7].

The right side of Figure 13 shows that a significant increase in pressure leads to a better etch rate uniformity. This is simply due to the increase of the plasma volume as more gas is pushed through the chamber at a higher rate.

4.2 DRIVEN ELECTRODE GEOMETRY AND THE MODIFICATION OF THE PLASMA ASYMMETRY

The significant dependence of the etch rate on the driven electrode DC bias shown in Figure 9 outlines the importance of this parameter in the success of IARIE processing of SRF cavities. The asymmetry of the plasma due to the difference in electrode areas (see Section 2.2.1) leads to the highly negative self-bias voltage that develops on the driven electrode. Equation 8 shows the explicit theoretical

relationship between the electrode areas and the voltage asymmetry of the discharge. In reality, experimental observations show that the relationship varies from Eq. (8), but only in the exponential factor [2]. Thus, a better representation of this effect is given by

$$\frac{V_1}{V_2} = \left(\frac{A_2}{A_1}\right)^q \tag{46}$$

with $q \lesssim 2.5$. Regardless, the area of the two electrodes is directly related to the asymmetry of the plasma and can therefore be used to modify the potential distribution. If the area of the driven electrode is increased, the degree of asymmetry of the discharge will decrease, leading to a more positive self-bias. This is advantageous as it decreases the amount of added DC bias required to reverse the asymmetry and make the grounded electrode the favorable ion bombardment target. It was therefore pertinent to study the direct effect that changing the driven electrode geometry has on the self-bias voltage, the etch rate, and the current required to raise the electrode DC bias to $\approx 0V$.

4.2.1 ELECTRODE GEOMETRY

The simplest way to modify the surface area of the driven electrode is to change the diameter. Unfortunately, this modification is limited as the chamber's diameter remains constant and the driven electrode can only be made so large until the plasma volume becomes too small to be effective. However, it is not required that the driven electrode remain a continuous smooth cylinder and the surface area can be increased by making trench like modifications to the shape. These geometrical alterations can be seen in Figure 14.
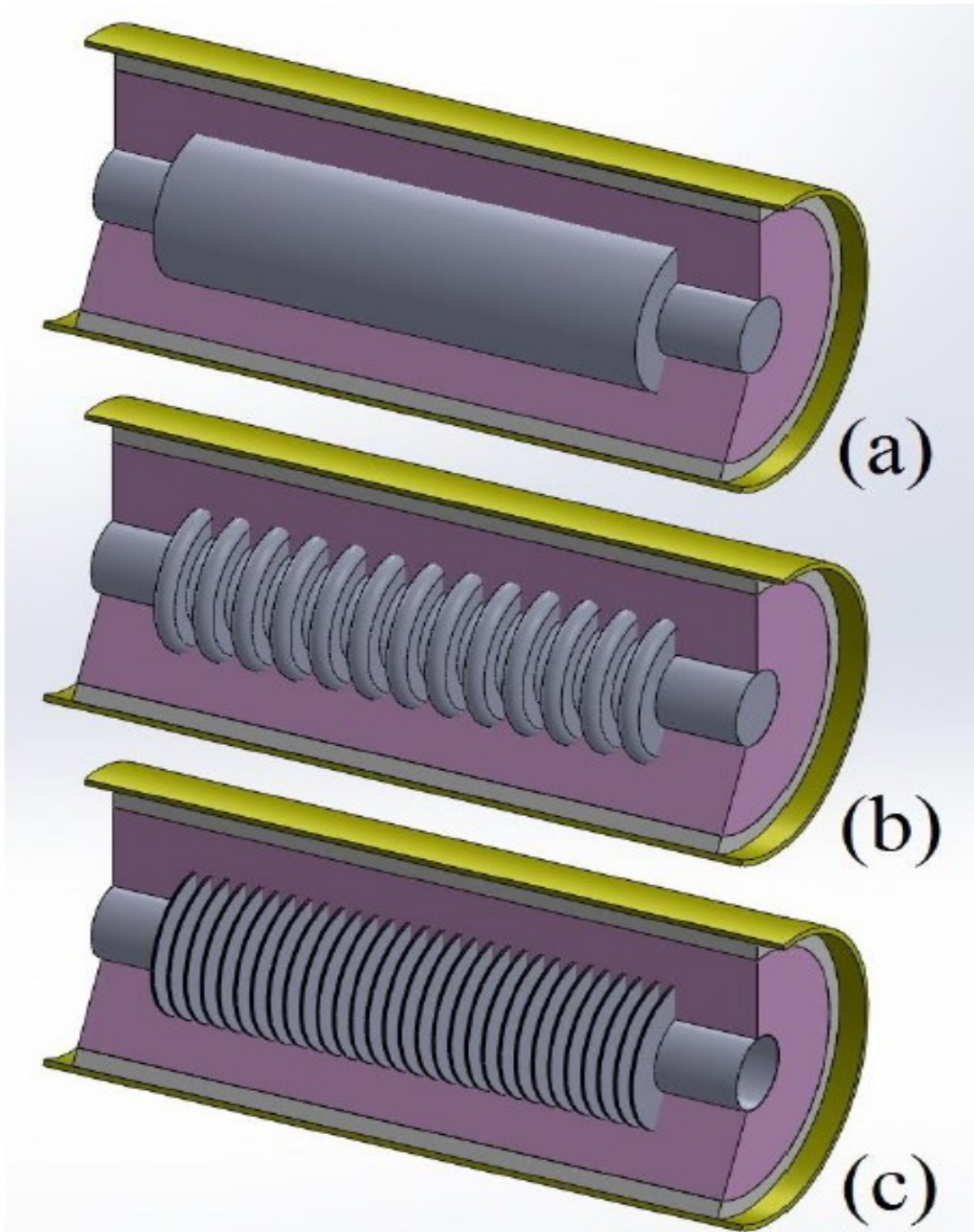
Figure 14: Illustration of various structures used for the study of the modification of plasma asymmetry, listed in increasing order of surface area [8]. (a) 5.0 cm diameter smooth straight tube, (b) large pitch bellows with 3.8 cm inner diameter and 4.8 cm outer diameter, (c) Disk-loaded corrugated structure with 5.0 cm outer diameter and 2.5 cm inner diameter. Each disk is 1.0 mm thick and separated by 3.0 mm.

The relationship between self-bias and different external parameters was studied for each of these geometries and compared and can be found in Ref. [8]. However, here we only present those results that are particularly significant.

4.2.2 SELF-BIAS VOLTAGE

While the relationship between the self-bias voltage and each external parameter is important, the relationship with RF power as shown in Figure 15 is particularly enlightening.
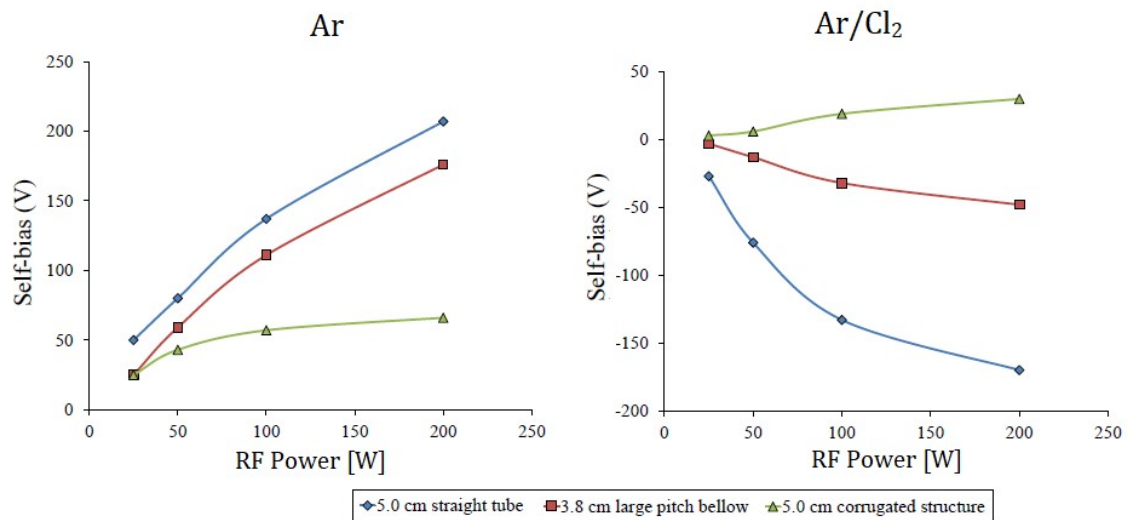
Figure 15: Left: Self-bias voltage vs. RF power in a pure Argon discharge. The self-bias voltage is negative for each geometry, but is presented as positive for clarity. Right: Self-bias vs. RF power in an Ar/Cl$_2$ (85/15 %) discharge [8]. The pressure is 450 mTorr in both cases.

It is expected that the self-bias on the driven electrode will become more negative as the RF power is increased due to the increase in the plasma density. In the case of a pure Argon discharge, the magnitude of the self-bias voltage shows a significant decrease as the surface area is increased. The corrugated structure shows a much smaller change in self-bias as RF power is increased. In the Ar/Cl$_2$ case, a similar trend is expected, but to a lesser extent as the electronegative Ar/Cl$_2$ discharge has a much lower electron density. The straight tube and bellow type electrodes show the expected trend as the self-bias becomes more negative with RF power. However, the corrugated structure shows a complete reversal of the plasma asymmetry as the

self-bias actually increases in the *positive* direction. This result shows the significant benefit of increasing the driven electrode surface area as much less, or potentially zero, additional DC bias is required to reverse the asymmetry and etch the grounded electrode surface. Figure 16 shows this more explicitly as the DC current required to bring V_{DC} to 0 is plotted as a function of RF power.
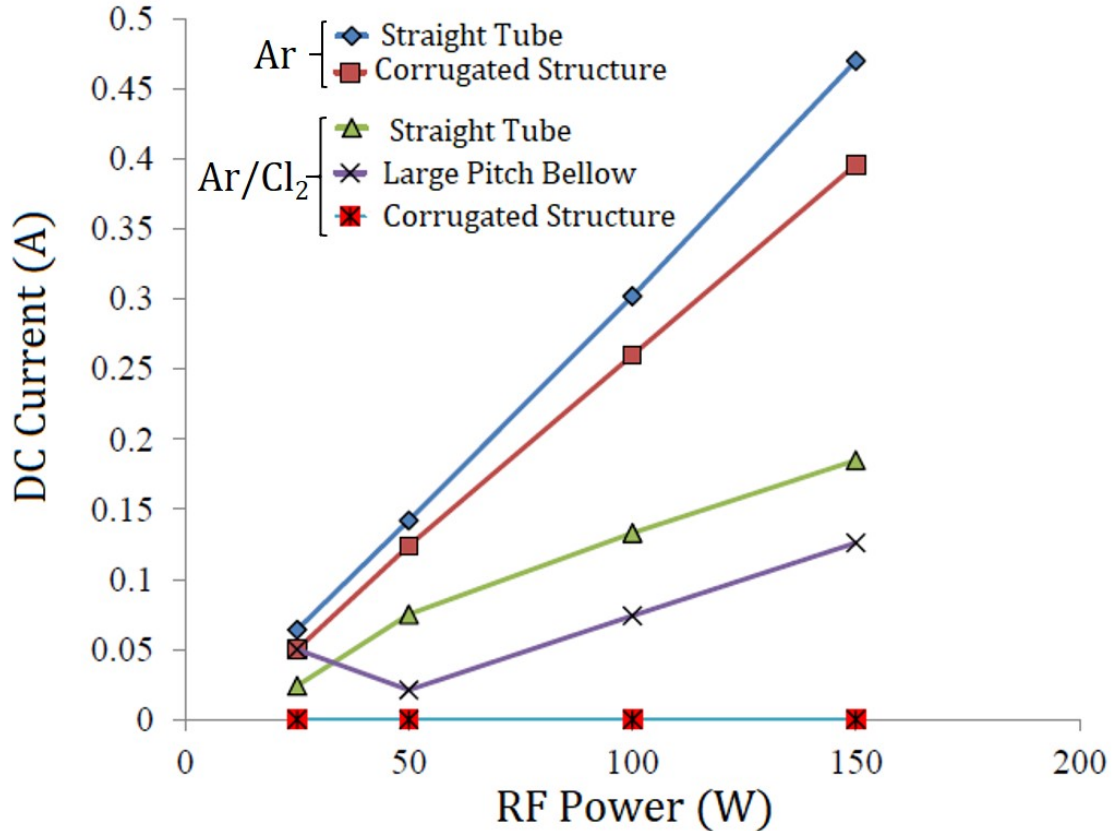
Figure 16: DC Current vs. RF power for different electrode geometries in both Ar and Ar/Cl$_2$ discharges [8]. The pressure is 450 mTorr in both cases.

The corrugated structure does not require any external current source at this pressure due to the reversal of the asymmetry.

Each of the electrode geometries were extended to Nb ring sample etching experiments. As seen in Figure 17, the corrugated electrode greatly outperformed the other structures, with a 4× increase in etch rate compared to the straight tube.
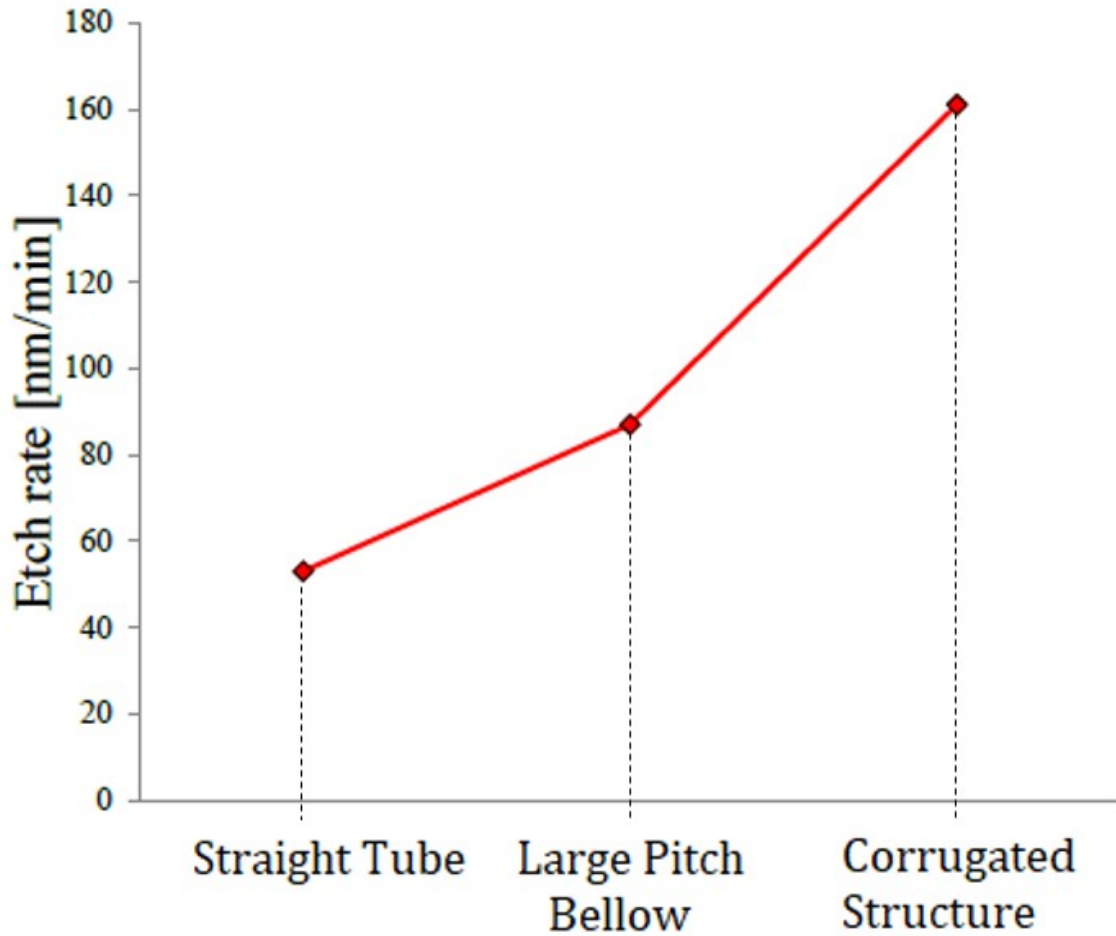
Figure 17: Nb etch rate vs. electrode geometry [8]. The discharge conditions were as follows: RF power = 150 W, Pressure = 60 mTorr, V_{DC} = 290 V, Surface Temperature = 422 K.

These results show that there is a significant benefit to increasing the surface area of the electrode with no particular downside. For this reason, the corrugated electrode was explicitly used for the work of this dissertation.

From this point, the rest of the dissertation describes the work done to continue the development of this technology after Upadhyay's departure from the project. This was done by establishing experimental relationships between the external parameters and the plasma parameters to aid in the creation of a theoretical discharge model. Various measurement techniques utilizing both electrical probe and spectroscopic techniques were used to directly measure specific plasma parameters, which were subsequently used to find valuable information about the electrons in the discharge.

Additionally, the direct effect of the substrate temperature and driven electrode DC bias on the surface properties of plasma etched Nb. The etch rate, surface roughness, and surface impurities were among the most important quantities to measure as a function of these external parameters. The following chapters describe the pertinent details of these experimental investigations and their results.

4.3 CRYOGENIC RF TEST OF THE FIRST SRF CAVITY ETCHED WITH AN Ar/Cl$_2$ PLASMA

As the relationships between etch rate and external parameters were established, the next step was to plasma etch a 1.5 GHz single cell SRF cavity. A freshly made cavity was processed using centrifugal barrel polishing and buffer chemical polishing (see Section 3.4) and placed in the plasma etching apparatus seen in Figure 18. Both the driven electrode and the gas flow system were mounted on linear translation systems to simultaneously move the two systems through the cavity.
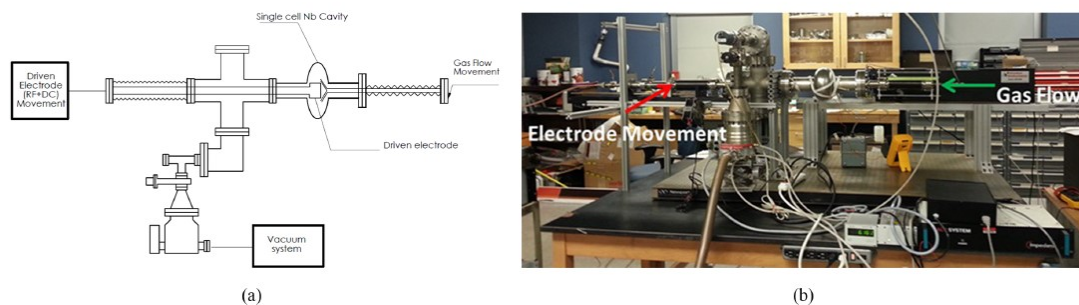
Figure 18: (a) Schematic diagram of the experimental setup of the single cell cavity etching system. (b) Photo of the cavity etching system. The direction of the electrode and gas feed movement are highlighted [38].

The translation of the electrode and gas system is important to ensure the entire cavity is processed and increase etch rate uniformity. The reader is referred to Ref. [38] for the specific details of the experiment. The rf performance of the plasma etched cavity was tested at various stages of the experiment and is shown in Figure 19.
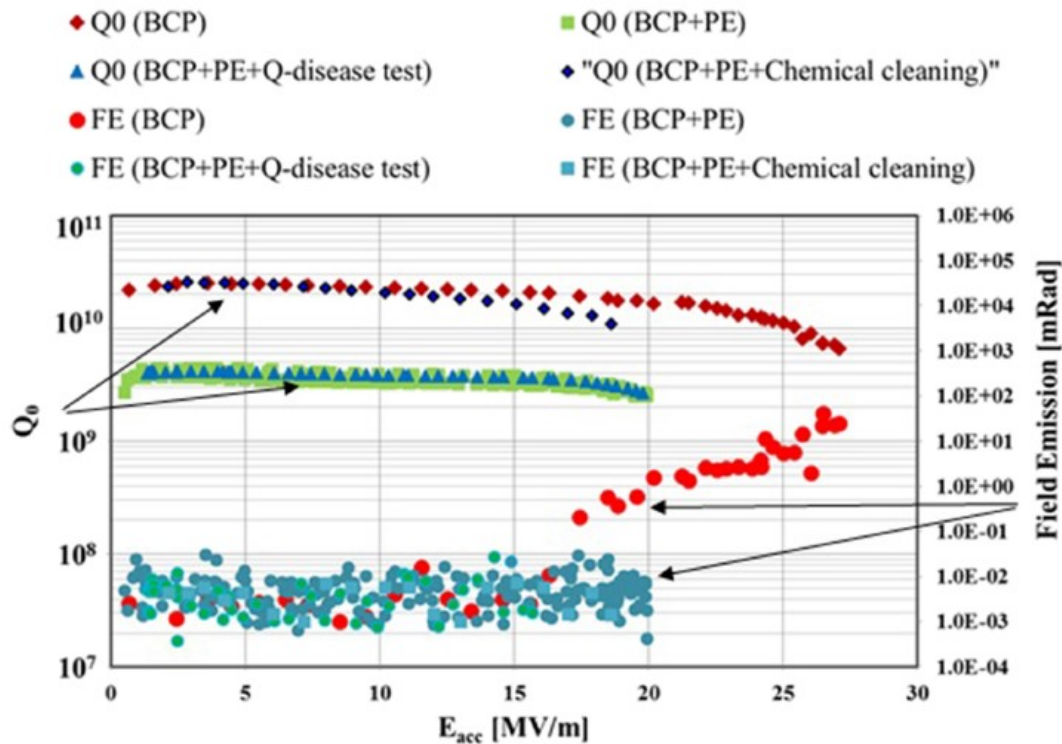
Figure 19: The rf performance test results of the plasma etched SRF cavity at 1.8 K [38]. The quality factor Q_0 and field emission are presented in tandem.

While it seems that there was no benefit in terms of the quality factor as the accelerating field is increased, there was a significant decrease in field emission. As discussed in Section 3.3, field emission is a significant source of losses in SRF cavities. These results show that IARIE can, at the very least, assist in the reduction of losses in SRF cavities.

This experiment also illuminated some of the more significant material limitations of the process. The final surface of the cavity after plasma etching was covered with black residue caused by the etching and deposition of the stainless steel components. This was confirmed by the surface analysis of this residue as shown in Figure 20.
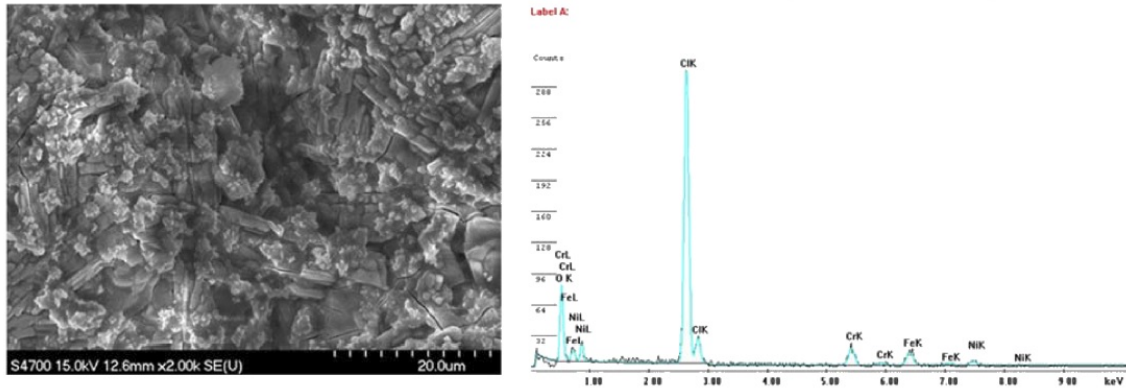
Figure 20: The surface analysis (left) and elemental composition (right) of the residue on the surface of the cavity after plasma etching [38].

The residual analysis shows that the residue is composed of iron, nickel, chromium and Cl_2. The reduction of field emission shown in Figure 19 was only found after the cavity was high pressure water rinsed and cleaned with both phosphoric acid and an aqua regia solution. It is important to point out that HF was not used on the cavity to avoid any chemical etch processes. The exploration of these material limitations in cavity processing is among the motivations of this work as is presented in Chapter 9.

CHAPTER 5

PLASMA DIAGNOSTIC METHODS

There are a number of different diagnostic methods available for the measurement of plasma parameters. However, the most common tool, the Langmuir Probe, is an electrical probe that requires direct contact with the discharge. While it allows for quick measurements of the plasma parameters, the introduction of the probe into the system inherently changes the distribution and physics of the plasma. Thus, it is often more desirable, as is the case of this work, to use spectroscopic measurements that are non-intrusive. The following chapter outlines the different methods used in this work, which consists of the Langmuir probe and two different spectroscopy techniques.

5.1 LANGMUIR PROBES

In the 1920's Irving Langmuir and H.M. Mott-Smith developed the first successful theory of electric probe collectors in a gas discharge [48]. This theory and the corresponding probe, commonly referred to now as the Langmuir probe, is the most popular diagnostic technique in the study of gas discharges. This is the case for a number of reasons, but chief among them is the ability to simultaneously measure many different plasma parameters (eg. T_e, n_e, the EEDF etc.) rather quickly. The technological advances of the past century has aided the Langmuir Probes' popularity as commercial probes and computer software allow for instantaneous measurements. Like any diagnostic technique, the Langmuir probe is not without its limitations. Probe geometry, plasma field oscillations, scan frequency, and probe contamination are among the most common significant sources of error in probe measurements. Furthermore, the introduction of the probe into the discharge can actively change the local distribution of charged species. Therefore, a great deal of work has been done to address the many issues of this measurement technique as can be seen in the topical review by Godyak and Demidov [49]. Additionally, the original Orbital Motion Limited (OML) probe theory is not applicable to all discharges as the deviation from a Maxwellian distribution will yield spurious results [10]. Thus, various models have

been developed to account for these discrepancies based on different kinetic processes involved in the collection of charge carriers [50–52]. These models were considered for the analysis of Langmuir probe scans in this work, but experimental limitations and negative scan artifacts greatly limited their applicability. These shortcomings are explained in further detail in Chapter 8. Therefore, the original OML theory assuming a Maxwellian distribution is used to measure approximate values for T_e and n_e for comparison to the other diagnostic techniques. A short description of the theory is given here as it pertains to this work.

5.1.1 THE PROBE I-V CHARACTERISTIC

The probe is used to measure the I-V characteristic of a ramping negative to positive voltage source in a localized area within the discharge. The theoretical shape of a scan is shown in Figure 21.
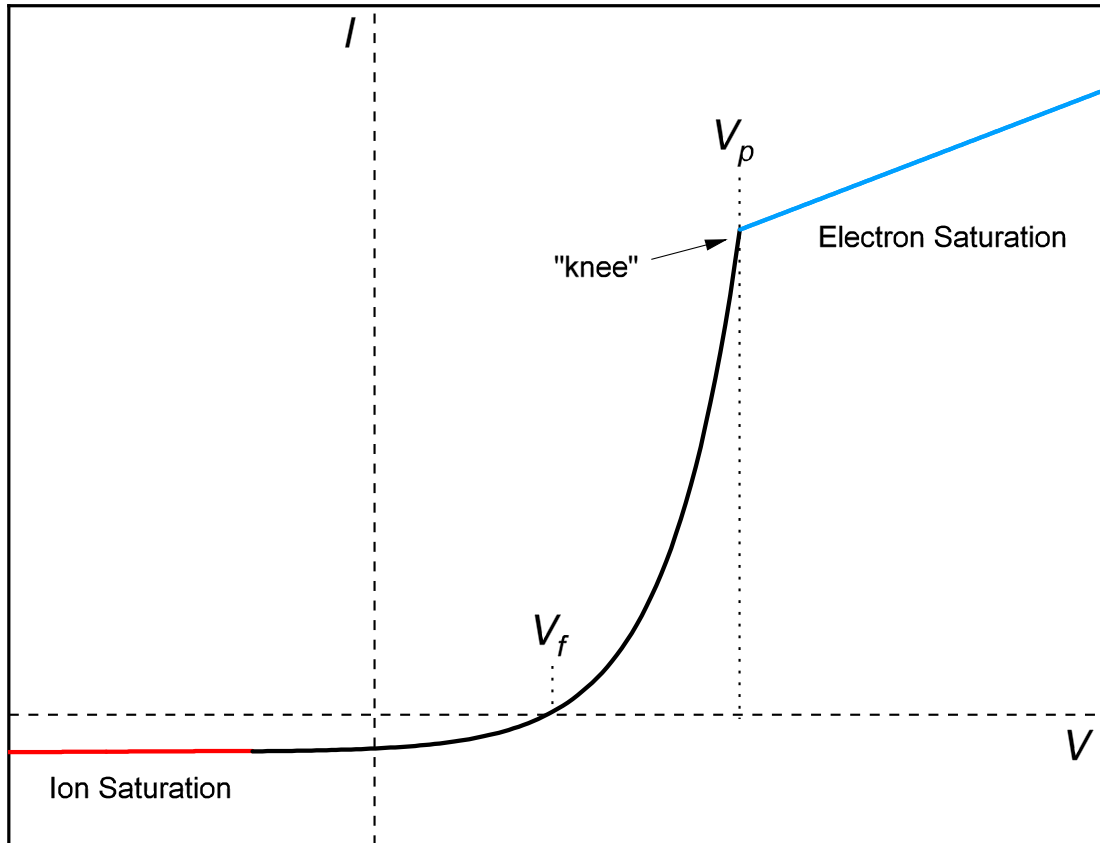
Figure 21: A theoretical I-V characteristic. This figure follows the common practice of plotting the characteristic with the electron current as positive and the ion current as negative.

The scan can be segmented into regions of particular importance due to the physical response of the discharge with the introduction of the probe. The leftmost region is the ion saturation current (I_i) region where the negative voltage attracts positive ions to the probe surface. As the voltage crosses the origin from negative to positive, ions become repelled and electrons are collected. At $I = 0$ the ion and electron currents are equal $(I_i = I_e)$ and the net current is zero. The corresponding voltage is called the floating potential V_f, as this is the potential that an insulated probe could not draw any current and would therefore float [2]. The exponential region about the floating potential is the electron current or transition region, which holds a great deal of the important information as this is representative of Maxwellian electrons. As the probe potential V increases, the electron current begins to saturate as it approaches the plasma potential V_p. At $V = V_p$, the probe is at the same

potential as the plasma and draws a great deal of current from faster, more mobile electrons [2]. This point is distinguished by a sudden change in slope, or "knee" in the I-V characteristic. Once the probe voltage passes the plasma potential, the electron current begins to saturate due to the expansion of the localized sheath around the probe. The same electrostatic screening process occurs as explained in Section 2.3.1. Theoretically the electron saturation region should be flat, but the effective collection area can increase depending on the probe geometry [2]. Each of these regions are important in different ways to the calculation of plasma parameters.

For a Maxwellian distribution, the electron current has the form

$$I - I_i = I_e = I_{es}e^{(V-V_p)/T_e}, \tag{47}$$

where A is the area of the probe tip, and T_e is the electron temperature in units of eV. The electron saturation current I_{es} is the value of the electron current I_e when $V = V_p$, given by

$$I_{es} = en_eA\left(\frac{eT_e}{2\pi m_e}\right)^{1/2}. \tag{48}$$

The electron temperature is found by plotting the electron current (Eq. (47)) semi-logarithmically vs. the probe voltage. The electron current region will therefore be linear as shown in Figure 22 with the inverse slope of this line as T_e. A longer linear region indicates that the electrons are highly Maxwellian.
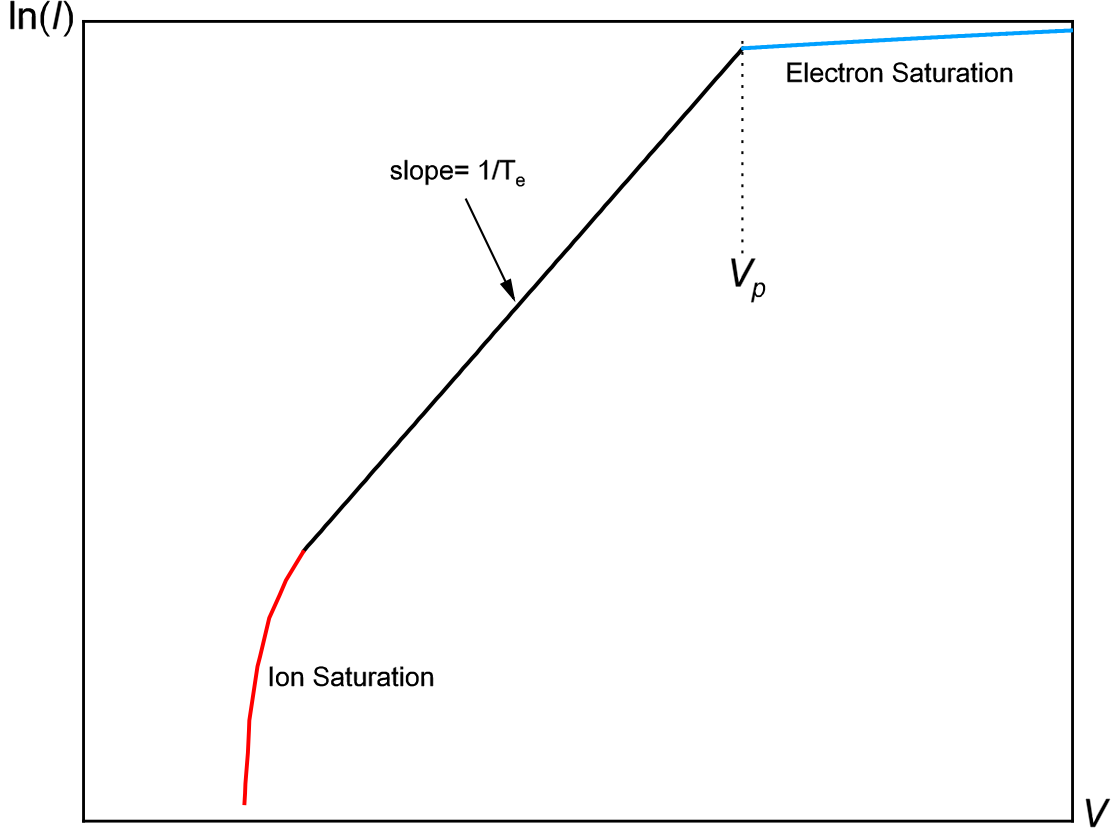
Figure 22: A semilog plot of the I-V characteristic. The electron temperature can be found by fitting the linear region and calculating the slope.

Once T_e is found from the log-linear plot, the electron density can be calculated by rearranging Eq. (48). The ion current region can be estimated by the Bohm current

$$I_i = \alpha e n A \left(\frac{e T_e}{M} \right)^{1/2},$$ (49)

where α is the ratio of the plasma density at the sheath edge to the bulk plasma (the theoretical value is $\alpha = 0.61$), and M is the mass of the ion [2, 50]. The Bohm velocity, or the speed needed for ions to enter the probe sheath, is given by $(eT_e/M)^{1/2}$ in Eq. (49). This expression can also be used to estimate the plasma density n ($n \approx n_i \approx n_e$ due to quasineutrality) once T_e is found. The electron and ion currents are equal at the floating potential V_f. Thus setting Eqns. (47) and (49) equal to one another yields

$$V_f = V_s - \frac{T_e}{2} \ln \left(\frac{2M}{\pi m_e} \right).$$ (50)

This equation is a useful relationship as it connects the floating potential, the plasma potential, and the electron temperature.

The EEDF can be ascertained from the I-V characteristic by applying the Druyvesteyn method, which is applicable for any functional form of the EEDF. For a generic EEDF $F(\mathcal{E})$ the electron current has the form

$$I_e = \frac{e^2 A}{2\sqrt{2m_e}} \int_V^\infty \left(\frac{\mathcal{E}}{e} - V\right) \frac{F(\mathcal{E})}{\sqrt{\mathcal{E}}} \mathrm{d}\mathcal{E}, \tag{51}$$

with V being the probe potential [49]. The second derivative of Eq. (51) with respect to V gives the Druyvesteyn formula [53]

$$\frac{\mathrm{d}^2 I_e}{\mathrm{d}V^2} = -\frac{e^2 A}{4} \sqrt{\frac{2e}{m_e V}} F(\mathcal{E}). \tag{52}$$

Given a "well-behaved" I-V characteristic Eq. (52) can directly give the EEDF. Additionally, measuring I'' can give the electron density and temperature according to

$$n_e = \int_0^\infty F(\mathcal{E}) \mathrm{d}\mathcal{E}, \tag{53}$$

and

$$T_e = \frac{2}{3}\langle \mathcal{E} \rangle = \frac{2}{3}\frac{1}{n_e} \int_0^\infty \mathcal{E} F(\mathcal{E}) \mathrm{d}\mathcal{E}, \tag{54}$$

as was shown in Section 2.3.4.

5.2 OPTICAL EMISSION SPECTROSCOPY

To avoid the limitations of the Langmuir Probe, the use of an optical emission spectroscopy (OES) system was implemented. Using OES, the light radiation emitted by the plasma is collected and measured in a spectrometer completely outside of the plasma reactor. Spectral lines corresponding to atomic excitation within the plasma can then be examined, compared, and manipulated to calculate plasma parameters. OES offers a great deal of benefits as a diagnostic technique compared to the Langmuir probe. Firstly, and most importantly, OES is a completely external measurement system that has no effects on the nature of the plasma. OES also allows for a very robust analysis depending on the desired quantity. Both neutral and ion excitation lines can be measured, and with the help of kinetic models and balance equations, can be used to find a great deal of plasma parameters.

Metastable and resonant states of excited Ar atoms play an indirect, but important role in the interaction of rf discharges with solid surfaces. One aspect of this

interaction, in general, is the direct or indirect role in the ion assisted reactive ion etching (IARIE) of metallic surfaces in increasing the population of both assisting and reactive ions, modification of the electron energy distribution function (EEDF), and in the chemical kinetics of the etching process [5, 54]. Ionized mixtures of reactive and noble gases are the natural medium for IARIE, and their application to chemical kinetics is not very well documented. This situation affects the understanding of surface phenomena of practical interest in processing of large metallic surfaces, such as the rate of material removal, surface roughness, and electron field emission from nano-scale particulates.

This work uses optical absorption and emission spectroscopy to measure plasma properties of the discharge. Quantities like the electron density, electron temperature, ion and neutral densities can be evaluated from the recorded spectra. The densities of Argon's first four excited states in Ar and Ar/Cl_2 discharges are among those with particular importance. These include the two resonant ($1s_2$ and $1s_4$, in Paschen notation) and two metastable ($1s_3$ and $1s_5$) levels. The two long-lived metastable levels, with a relatively large stored energy, have a strong influence on the excitation and chemical processes. It was a significant goal of this work to inspect a possible influence of these states on the etching chemistry.

5.2.1 THE FIRST 14 EXCITED STATES OF ARGON

As stated in Chapter 4, Argon is a popular inert carrier gas used in plasma discharges and material processing recipes. There are many reasons for this, but chief among them is because the first 14 excited levels of Argon in an external electric field are very important to the ion and electron energy distributions in the discharge [11]. These transitions can be used to gain information about both hot and cold electrons within the discharge as the energy threshold from the ground state is ≈ 12 eV for each level, and the energy difference between decay channels is $\approx 1 - 3$ eV. Specific details about each level is presented in Table 2.

Table 2: The first fourteen levels of excited Argon. Levels are labeled in Paschen notation.

Energy Level	J (2L+1)	Degeneracy g	Energy (eV)
G.S.	0	1	–
$1s_5$	2	5	11.55
$1s_4$	1	3	11.62
$1s_3$	0	1	11.72
$1s_2$	1	3	11.83
$2p_{10}$	3	3	12.91
$2p_9$	0	1	13.27
$2p_8$	3	7	13.08
$2p_7$	2	5	13.10
$2p_6$	1	3	13.15
$2p_5$	2	5	13.17
$2p_4$	1	3	13.28
$2p_3$	2	5	13.30
$2p_2$	1	3	13.33
$2p_1$	0	1	13.48

Perhaps the most useful aspect of these levels is that the natural decay channels from the 2p levels to the 1s levels emit photons mostly in the visible spectrum between 600-1100 nm. These transitions are easily measured using basic spectroscopy equipment, making Argon a well studied and modeled discharge gas. A depiction of the possible decay channels for the 2p levels is shown in Figure 23. As will be made clear in Section 5.2.4, a great deal of information about the physics of the discharge can be attained by utilizing the relationships between these 14 levels.
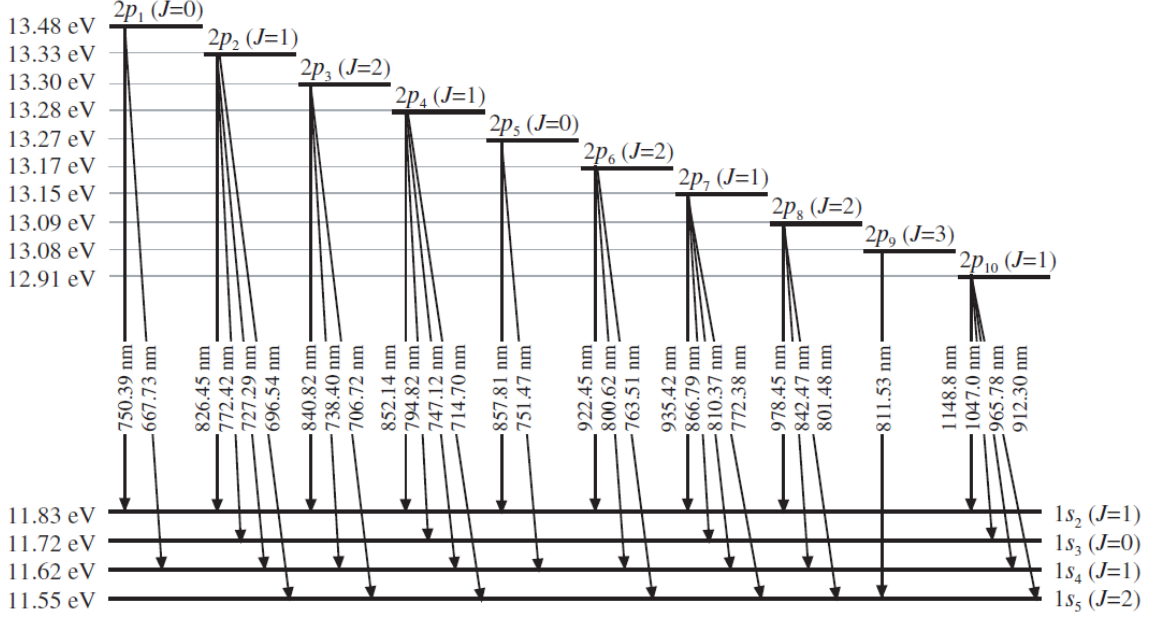
Figure 23: The possible 2p → 1s transitions for Argon [11].

From this point, the individual levels will be referred to by their Paschen notation label seen in the first column of Table 2. The first excited configuration denoted by 1s contains 4 levels while the second configuration, denoted by 2p, contains 10 levels. Among the first four 1s levels there are two levels, $1s_2$ and $1s_4$, with total angular momentum J=1. Due to electric dipole selection rules ($\Delta J = \pm 1$) these two levels decay into the ground state (J=0) very quickly (on the nanosecond scale) and are therefore referred to as resonant levels. These resonant transitions emit VUV light (≈ 100 nm) which can be measured, but requires specialized spectroscopy equipment. The other two levels, $1s_3$ and $1s_5$ (J=0 and J=2), cannot decay to the ground state due to the same selection rules, and are therefore called metastable levels because of their much longer lifetimes. These levels require collisional processes to eventually reach the ground state.

While Figure 23 outlines the physically possible transition channels of these Argon levels, the probability of these transitions is of particular importance. The probability of spontaneous emission of an excited atom is governed by Fermi's golden rule, which describes the transition between energy eigenstates of a discrete energy system in a time dependent perturbation [55]. The rate of spontaneous emission for a particular $i \rightarrow j$ transition is given as

$$A_{i \rightarrow j} = \frac{1}{\tau} \tag{55}$$

where τ is the radiative lifetime, or how long it takes for the excited states to decay to $1/e$ (37 %) of its original value. This quantity (A), also known as the Einstein coefficient, can be used to define the probability of each possible emission channel out of an excited state. This is called the branching fraction, and is defined as

$$\Gamma_{i \to j} = \frac{A_{i \to j}}{\sum_l A_{i \to l}}, \tag{56}$$

where l represents the possible lower levels. The branching fraction is very useful in spectroscopy techniques and can be used to identify "strong" or "weak" transitions in an excited atomic medium. The theoretical values of the Einstein coefficient and branching fraction for each 2p $\to$ 1s transition (see Figure 23) is tabulated below.

Table 3: The Einstein coefficient and branching fraction for the optically allowed 2p
→ 1s transitions [56].

Transition	λ (nm)	$A_{i\to j}$	$\Gamma_{i\to j}$
2p1→1s2	750.39	4.45E+07	0.995
2p1→1s4	667.73	2.36E+05	0.005
2p2→1s2	826.45	1.57E+07	0.434
2p2→1s3	772.42	1.17E+07	0.332
2p2→1s4	727.29	1.83E+06	0.052
2p2→1s5	696.54	6.39E+06	0.181
2p3→1s2	840.82	2.23E+07	0.645
2p3→1s4	738.4	8.47E+06	0.245
2p3→1s5	706.72	3.80E+06	0.11
2p4→1s2	852.14	1.39E+07	0.419
2p4→1s3	794.82	1.86E+07	0.561
2p4→1s4	747.12	2.20E+04	0.001
2p4→1s5	714.7	6.25E+05	0.019
2p5→1s4	751.47	4.00E+07	1
2p6→1s2	922.45	5.03E+06	0.146
2p6→1s4	800.62	4.90E+06	0.142
2p6→1s5	763.51	2.45E+07	0.712
2p7→1s2	935.42	1.06E+07	0.031
2p7→1s3	866.79	2.43E+06	0.072
2p7→1s4	810.37	2.50E+07	0.743
2p7→1s5	772.38	5.18E+06	0.154
2p8→1s2	978.45	1.47E+06	0.046
2p8→1s4	842.46	2.15E+07	0.667
2p8→1s5	801.48	9.28E+06	0.288
2p9→1s5	811.53	3.31E+07	1
2p10→1s2	1148.8	1.90E+05	0.007
2p10→1s3	1047	9.80E+05	0.038
2p10→1s4	965.78	5.43E+06	0.213
2p10→1s5	912.3	1.89E+07	0.741

Experimentally, the branching fraction can be found from measuring the intensity of spectral lines originating from the same upper level

$$\Gamma_{i \to j} = \frac{\Phi_{i \to j}}{\sum_l \Phi_{i \to l}}. \tag{57}$$

Measuring the difference between the theoretical and experimental branching fractions can be used to deduce how experimental parameters are affecting the emitting source (plasma). This concept is the backbone of much of the optical emission spectroscopy techniques used in this work, as will become evident in Section 5.2.4. One of the main sources of branching fraction modification is radiation trapping, which is explained in detail in the next subsection.

5.2.2 RADIATION TRAPPING

Radiation trapping occurs when the plasma is "thick" enough so that emitted photons do not escape the plasma volume before they are reabsorbed. The reabsorption can lead to incomplete measurements of the strength of spectral lines because it is not guaranteed that an excited atom will decay in the same process and/or emit a photon in the same direction. This process is shown in Figure 24.
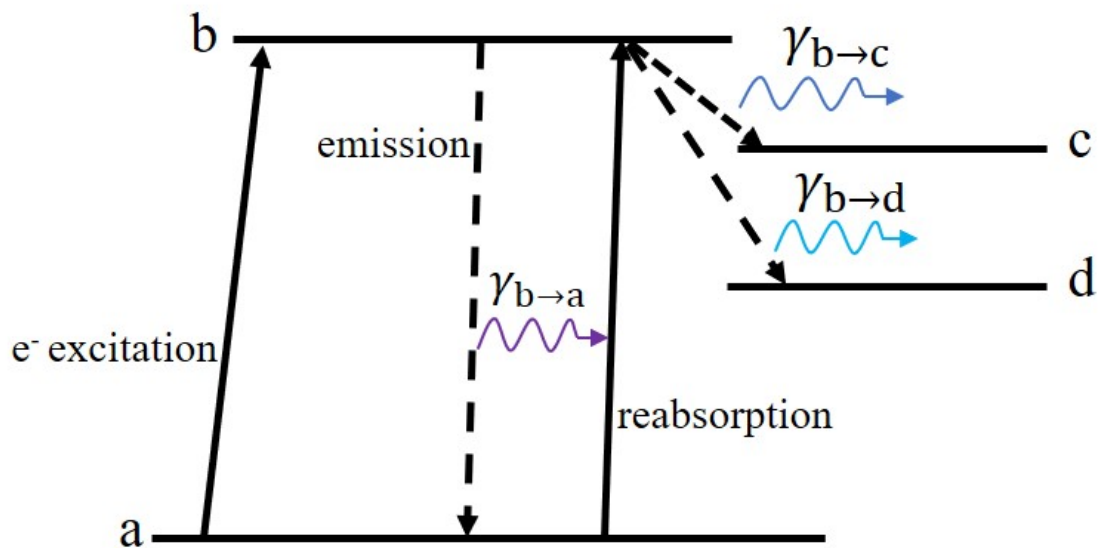
Figure 24: Resonant radiation reabsorption, or radiation trapping. Level b is optically coupled to the lower level a, while c and d are not. Photons emitted in the b-a transition can re-excite atoms back to level b, allowing for the radiation decay to levels c or d.

Since the optical thickness of the plasma is pressure dependent, the branching fraction, and therefore the optical emission cross section, are also pressure dependent [18]. Radiation trapping can occur with any optically allowed transition given that the population density of the absorber is high enough. Thus, the populations of 2p levels can be affected by cascade effects from the higher lying levels in the same way [18].

Radiation trapping effects can be included in OES techniques either through the use of pressure dependent collisional cross sections, or by using a quantity called the photon escape factor, which acts as a scaling factor based on a quantifiable optical thickness. The two approaches are further explained in the next two subsections, but for reasons that will become clear, only the second approach involving the photon escape factor was applied.

5.2.3 THE APPARENT CROSS-SECTION

Consider a transition from an initial level l into an arbitrary $2p$ level i with an apparent cross section $Q_{l \to i}^{app}(\mathcal{E})$. This cross section is defined as the sum of the optical cross sections out of the $2p$ level (decays) to lower levels j as well as the sum of the direct cross section and the cascade contributions from higher lying levels.

$$Q_{l \to i}^{app}(\mathcal{E}) = \sum_{j < i} Q_{ij}^{opt} = Q_{l \to i}^{dir} + \sum_{k > i} Q_{ki}^{opt}, \tag{58}$$

The lower level of origin l can be the ground state or one of the 4 $1s$ levels (for excitation into the $2p$ levels). The optical cross section for a specific transition is defined as

$$Q_{ij}^{l} = Q_{l \to i}^{app} \Gamma_{ij}, \tag{59}$$

where Γ_{ij} is the branching fraction for that transition defined as

$$\Gamma_{ij} = \frac{A_{ij}}{\sum_l A_{il}}. \tag{60}$$

The optical cross section is the probability that an electron impact excitation from a lower level l will end in that particular transition. Since the apparent cross section contains all significant contributions to a species population, the apparent cross section can be used to calculate the transmission coefficients (see Section 2.3.4). The apparent cross sections for the transitions used in this work are measured and

fitted to analytical functions in the work by Boffard, however, these are only fitted up to 5 mTorr [16]. As the pressures in this work are upwards of 100 mTorr, using these cross sections in the analysis would be seemingly inaccurate. Additionally, while the study by Boffard was most certainly robust, the collection of apparent cross sections is not complete.

Due to the complications associated with using the apparent cross sections, this treatment was abandoned. However, the second treatment is a rather new OES technique that is able to achieve the same goal without needing any *a priori* knowledge about the discharge. This is very useful as no information about the EEDF needs to be known, so fewer assumptions about collisional processes need to be made.

5.2.4 OES-BRANCHING FRACTION METHOD

Since using the apparent cross sections in the traditional formality proved unsuccessful, significant work was done to implement the spectroscopic technique now known as the optical emission spectroscopy-branching fraction method (OES-BFM) [57–61]. This technique uses the intensities of partially self-absorbed spectral emission lines from 2p→1s transitions to determine the amount of reabsorbed photons (the photon escape factor). This optical emission spectroscopy technique is essentially nonintrusive and dependent on the distribution of the lower state density of the transition. A set of simultaneously recorded line intensity pairs is chosen so that they involve densities of all 1s states from a single broad range calibrated spectrum. Ratios of the escape factors (or modified branching fractions) of those lines with densities as free parameters are adjusted to the ratios of recorded spectral lines. Thus the whole set of 1s densities at a particular location is obtained from a single emission spectrum in the 650-1000 nm range.

Assuming a homogeneous distribution of excited atoms and excitation sources in the bulk of the cylindrical capacitive discharge, the spectral line intensity of a transition i→j as recorded with a detector can be expressed as

$$\bar{I}_{ij} = c\gamma_{ij}(n_j)A_{ij}n_i, \tag{61}$$

where $\bar{I}_{ij}$ is the line of sight averaged spectral line irradiance from a given observation column, c is a constant which defines the geometry of the observation column, $\gamma_{ij}(n_j)$ is the radiation-reducing Holstein's [62] escape factor, n_j is the average density of atoms in the lower, 1s state, A_{ij} is the transition probability, and n_i is the density of

atoms in the upper, 2p state. The use of the line irradiance from rf discharges avoids the effect of Doppler, instrumental, and Stark broadening. The irradiance depends on the densities of both states in the transition and increases with the density of emitters, n_i (2p state), and decreases with the density of absorbers, n_j (1s state). Therefore, there are two unknown variables in the nonlinear Eq. (61) for every 2p→1s transition. In the branching fraction method, the irradiances from a pair of 2p→1s transitions with the same upper level are divided to eliminate the density of the 2p state and the geometric factor. This leads to [57–59]

$$\frac{\bar{I}_{ij} A_{ik}}{\bar{I}_{ik} A_{ij}} - \frac{\gamma_{ij}(n_j)}{\gamma_{ik}(n_k)} = 0, \tag{62}$$

where the ratio of irradiances is measured, the ratio of transition probabilities are known, and the ratio of escape factors depends on the unknown densities of the corresponding two 1s states, which have to satisfy Eq. (62). The escape factor in its most accurate form is evaluated from the integral of the photon transmission coefficient over the plasma volume, and is dependent on the distribution of emitters and absorbers along the observation column [62–64]. A more complete investigation of the photon escape factor and its application to low temperature plasmas can be seen in the work by Zhu *et al.* [65]. There are, however, several approximations that can be used in measurements with various level of accuracy [59, 61, 62, 66, 67]. For this work, we follow the case of a homogeneous distribution of emitters and absorbers proposed by Mewe [66, 67]

$$\gamma_{ij} = \frac{2 - \exp(-\tau_{ij}/1000)}{1 + \tau_{ij}}; \qquad \tau_{ij} = k_{ij}l, \tag{63}$$

where τ_{ij} is the optical thickness of the observed plasma column at the center of the spectral line corresponding the i→j transition [67]. The value l is the effective plasma length defined as the radius of the cylindrical plasma for a volume averaged escape factor [65]. In this work, this is equivalent to the radius of the discharge chamber. The reabsorption coefficient $k_{ij}(n_j)$ is given by

$$k_{ij}(n_j) = \frac{\lambda_{ij}^3}{8\pi^{3/2}} \frac{g_i}{g_j} A_{ij} n_j \sqrt{\frac{M}{2k_B T_g}} = \alpha_{ij} n_j, \tag{64}$$

where λ_{ij} is the center wavelength of the transition, g_i and g_j are the statistical weights of the the upper and lower states respectively, M is the atomic mass, k_B is

the Boltzmann constant, and T_g is the gas temperature. All known quantities are grouped in α_{ij}, which is calculated for every measured spectral line.

For the range of densities found in capacitive discharges an even more simplified version of the escape factor was used [59]

$$\gamma_{ij} \approx \frac{1}{1 + \tau_{ij}}. \tag{65}$$

Figure 25 shows the escape factor values evaluated from Refs. [59, 62, 66, 67] plotted against the optical thickness corresponding to the lower state density range of 10^{15}-10^{18} m^{-3}. The escape factor values are distributed over two orders of magnitude, depending on the approximation. The difference between Eq. (63) and Eq. (65) is negligible in the optical thickness range of this work as outlined by Figure 25. Within the conditions of this experiment we have deemed that Eq. (65) is sufficient for our purposes.
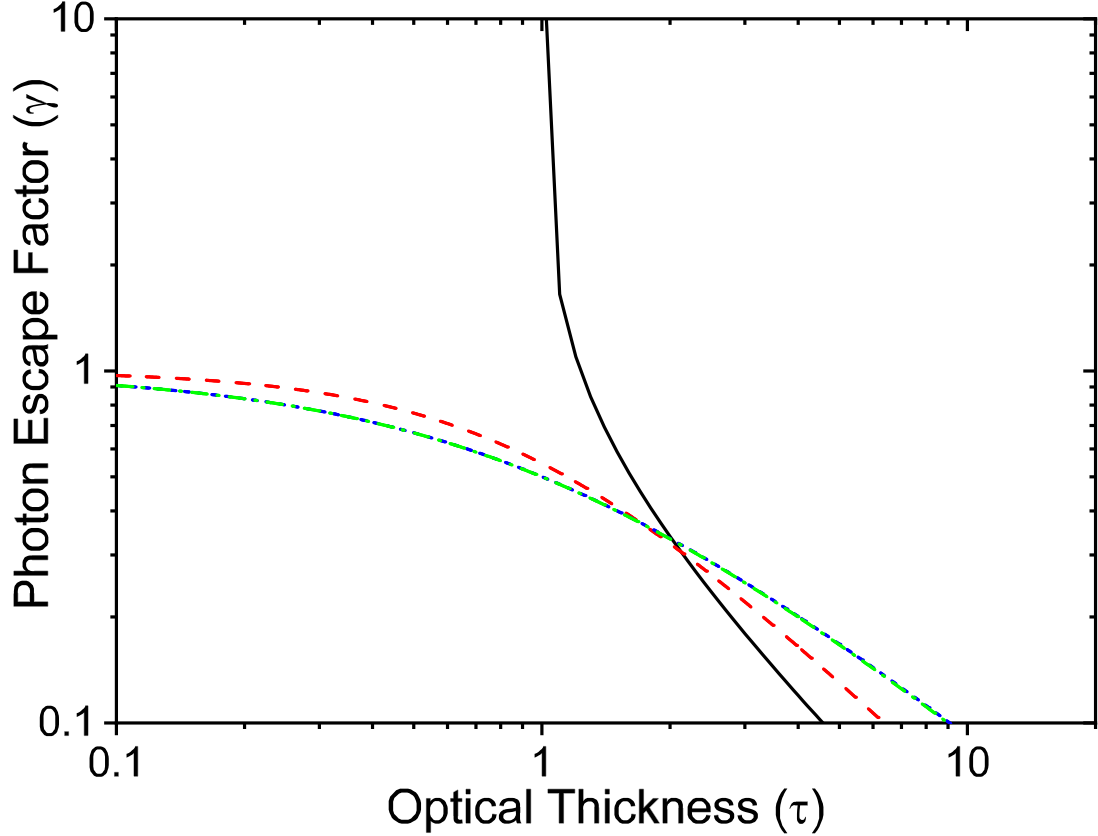
Figure 25: Various forms of the photon escape factor as a function of optical thickness found in literature. Solid black line: [62], Red dashed line: [67], Blue dashed line: Eq. 63, Green dash-dot line: Eq. 65.

Densities of the four Ar 1s states can be evaluated using Eq. (62). The density of atoms at each level was calculated using a nonlinear least square method to minimize the sum of a set of five transition pairs

$$\sum_{m=1}^{5} \left[\left(\frac{I_1 A_2}{I_2 A_1} \right)_m - \left(\frac{\gamma_1}{\gamma_2} \right)_m \right]^2. \tag{66}$$

The Ar 1s densities (and therefore the photon escape factors) were iteratively adjusted so that the above sum is minimized below 1%. With four unknowns (the 1s state densities), five density pairs are used as in Ref. [57] to over-constrain the system and reduce error.

5.3 COLLISIONAL RADIATIVE MODEL

Collisional Radiative Models (CRMs) are widely used in low temperature plasma physics to study the numerous kinetic processes within. CRMs are able to predict excited state densities through a balancing of population and depopulation processes. These include collision, radiation, absorption, and diffusive processes [68]. Using OES, relationships between the emission intensity of spectral lines and the plasma parameters can be established, particularly, information about the EEDF can be readily found. In the case of Argon discharges, the balancing of the 1s and 2p level populations are often used. This choice is easily made due to the strong optical transitions between these levels, and the significant effect the 1s levels have on the chemical processes in the discharge due to their large densities and high excitation energies [69, 70]. However, CRMs require the use of excitation/quenching rate coefficients (see Section 2.3) that are difficult to calculate as they are dependent on experimental parameters. The rate coefficients are calculated from the integration of the product of the electron velocity and collisional cross section over the velocity distribution function of the discharge [68]. As shown in the previous section, the experimental effect on the collisional cross sections is significant, so great care must be taken with their application. For this reason, there has been a great deal of work to calculate these cross sections both experimentally [14, 16, 18, 21, 71] and theoretically [19, 20, 72, 73].

Depending on the experimental parameters, the number of excitation/quenching processes to include in the CRM varies. As mentioned in Chapter 2, plasmas can be categorized based on the ionization degree and thermal equilibrium properties. Proper classification of a discharge allows one to quickly eliminate processes that are negligible in the CRM. Low temperature discharges have been studied extensively because of their applications, so there exists a great deal of developed CRMs in the literature [68, 69, 72, 74, 75]. While these models contain most of the same important processes, the lack of a consistent model for a wider group of experimental parameters is a detriment. Specifically, many of these models only work within specific pressure regimes, which makes experiments conducted over a significant pressure range quite difficult to model. However, Zhu *et al.* has made considerable progress in this aim by developing simple Arrhenius forms of many excitation and quenching rate coefficients that are applicable over a large pressure range (1-10^5 Pa) [68, 69, 75, 76]. While some properties of the discharge must be generalized (most significantly the

EEDF is assumed Maxwellian), this is extremely convenient as the effects of varying pressure on the cross sections (eg. radiation trapping) are more easily included in the model. Furthermore, the "gray area" between pressure regimes has been defined more explicitly, thus making the choice of processes to include much simpler [69, 76].

The classifications outlined by Zhu are primarily defined by a discharges ionization degree (n_e/n_g) and pressure. There are five main regimes, with some containing 'sub-regimes' based on additional important processes. The five main regimes are the corona (C-regime), low pressure (L-regime), medium pressure (M-regime), high pressure (H-regime), and Saha (S-regime) [69]. Each of these and their sub-regimes are described in detail in [69, 76]. According to the parameters of this work, the coaxial CCP is firmly in the L-regime. Thus, the dominant excitation and quenching process of the 2p levels are

1. Electron excitation from the ground state

$$e + Ar \rightarrow e + Ar(2p_x) \tag{67}$$

2. Electron excitation from the metastable and resonant levels

$$e + Ar(1s_x) \rightarrow e + Ar(2p_x) \tag{68}$$
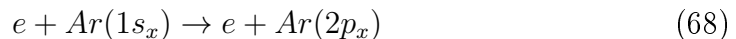
3. Radiative transitions to metastable and resonant levels

$$Ar(2p_x) \rightarrow Ar(1s_x) + h\nu. \tag{69}$$
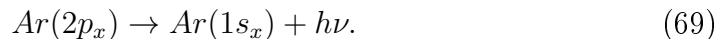
As one can see, any of those processes that involve ionization, recombination, atom-atom collisions, and cascade contributions from higher lying levels are ignored. The ionization and recombination processes have small rate coefficients, so the ionization degree must be large for these processes to be significant. Heavy atomic collisions are ignored due to the low pressure range of the discharge. The transitions from higher levels can be ignored as the amount of electrons with enough energy to excite atoms to these levels is negligible.

The effects of radiation trapping are included in the model through the use of the volume averaged photon escape factor (see previous section) included in the 2p radiative transitions. The inclusion of the radiation trapping effects are imperative to the success of the model due to the known pressure dependent effects of the collisional

cross sections [16, 18, 71]. The result is the following steady state balance equation for the 2p excited states

$$n_{2pi} \sum_{j=2}^{5} \gamma_{2pi \to 1sj} A_{2pi \to 1sj} = n_e n_g Q_{g \to 2pi}(T_e) + n_e \sum_{j=2}^{5} n_{1sj} Q_{1sj \to 2pi}(T_e), \qquad (70)$$

where n_{2pi} is the density of the upper 2p state, $\gamma_{2pi \to 1sj}$ is the volume averaged photon escape factor, $A_{2pi \to 1sj}$ is the Einstein coefficient, n_e is the electron density, n_g is the ground state density, and Q is the rate coefficient for a particular excitation channel. The ground state density is calculated from the pressure according to the ideal gas law

$$n_g = \frac{p(\text{Pa})}{k_B T_g}, \qquad (71)$$

where p is the pressure in Pascals. To reiterate, the photon escape factor is essentially a measure of how many photons escape the plasma volume without being reabsorbed based on the distribution of emitters and absorbers in the discharge. As in Section 5.2.4, the simplified expression assuming a homogeneous distribution proposed by Mewe, Eq. (65) is used in Eq. (70).

5.3.1 LINE-RATIO TECHNIQUE

Electron Temperature

By using OES-BFM to find the 1s densities, the only unknowns in Eq. (70) are the electron temperature (T_e) and electron density (n_e). Since Eq. (70) represents the balance equation for any 2p level, a ratio of two different 2p levels can be utilized to find T_e

$$\frac{n_{2px} \sum_{j=2}^{5} \gamma_{2px \to 1sj} A_{2px \to 1sj}}{n_{2py} \sum_{j=2}^{5} \gamma_{2py \to 1sj} A_{2py \to 1sj}} = \frac{n_g Q_{g \to 2px}(T_e) + \sum_{j=2}^{5} n_{1sj} Q_{1sj \to 2px}(T_e)}{n_g Q_{g \to 2py}(T_e) + \sum_{j=2}^{5} n_{1sj} Q_{1sj \to 2py}(T_e)}, \qquad (72)$$

where x and y represent two different 2p levels ($x \neq y$). This ratio essentially has one unknown (T_e), but the result strongly depends on the accuracy of γ_{ij}, and therefore the 1s densities. The 2p densities can be calculated from the measured spectral lines by

$$n_{2px} = \frac{I_{2px \to 1sj}}{hc\gamma_{2px \to 1sj}A_{2px \to 1sj}} = \frac{\Phi_{2px \to 1sj}}{\gamma_{2px \to 1sj}A_{2px \to 1sj}}, \tag{73}$$

where $I_{2px \to 1sj}$ is the spectral radiance of the transition, h is the Planck's constant, and c is the speed of light. The spectral intensities are calibrated to absolute spectral radiance (W/m^2) so approximate values of the absolute 2p densities can be calculated as compared to using relative spectral intensities.

Theoretically, transitions from any two different 2p levels can be used in Eq. (72) and only one ratio is required to find T_e. In reality, it is of course more prudent to use multiple spectral lines and ratios to reduce error and validate results. Additionally, using a specific and consistent transition in the denominator can be advantageous. Particularly, the 750.39 nm (2p$_1 \to$ 1s$_2$) and the 751.47 nm (2p$_5 \to$ 1s$_4$) lines are natural choices. Both of these transitions dominate the decay channels (in this model) for their respective upper levels, essentially meaning that their branching fractions are 1, and the uncertainty of other transitions from that level do not have to be considered [58]. Additionally, the 2p$_1$ and 2p$_5$ levels are primarily dominated by ground state transitions, which mitigates the effects of radiation trapping [14, 58, 77]. In this work, the 751.47 nm line was used exclusively as the denominator in all ratios. Therefore, Eq. (72) can be simplified to the following form

$$\frac{\Phi_{2px \to 1sj}}{\Phi_{2p5 \to 1s4}} = \frac{\Gamma'_{2px \to 1sj}}{\Gamma'_{2p5 \to 1s4}} \left[\frac{\sum_l n_l Q_{l \to 2px}}{\sum_l n_l Q_{l \to 2p5}} \right], \tag{74}$$

where Γ' is the effective branching fraction, and l indicates the lower levels in the transitions (ground, 1s levels). The effective branching fraction is defined as [58]

$$\Gamma'_{2px \to 1sj} = \frac{\gamma_{2px \to 1sj}A_{2px \to 1sj}}{\sum_{j=2}^{5} \gamma_{2px \to 1sj}A_{2px \to 1sj}}, \tag{75}$$

and is a measure of the transition probability with the inclusion of reabsorption.

Of course, T_e cannot be found without knowing the rate coefficients for the excitation channels. The rate coefficient is obtained from the following expression

$$Q_{i \to j} = \sqrt{\frac{2}{m_e}} \int_0^\infty \sigma_{i \to j}(\mathcal{E}) f_e(\mathcal{E}) \sqrt{\mathcal{E}} d\mathcal{E}, \tag{76}$$

where $\sigma_{i \to j}(\mathcal{E})$ is the electron collision cross section, $f_e(\mathcal{E})$ is the EEDF, and $\mathcal{E}$ is the electron energy. We use the familiar Maxwellian form of the EEDF (see Section 2.3.4)

$$f_e(\mathcal{E}) = \frac{2}{\sqrt{\pi}} T_e^{-3/2} \sqrt{\mathcal{E}} e^{-E/T_e}, \tag{77}$$

where

$$\int_0^\infty f_e(\mathcal{E})d\mathcal{E} = n_e. \tag{78}$$

While it is likely that the EEDF is in fact slightly non-Maxwellian based on comparative works, the low energy region is expected to follow a Maxwell-Boltzmann distribution, and the use of this distribution is a reliable approximation [11, 74, 78]. Zhu *et al.* has done an extensive investigation of CRMs used for Argon discharges, and has compared a number of collisional cross section data from a number of sources in the field [68]. Through this extensive investigation, the rate coefficients for 1s $\rightarrow$ 2p transitions have been simplified to a convenient Arrhenius form for T_e in the range of $1 - 5$ eV

$$Q_{i\rightarrow j} = Q_0 \cdot \exp\left(-\frac{E_a}{T_e}\right)\left(\frac{T_e}{E_a}\right)^b, \tag{79}$$

where Q_0 is a rate constant, E_a is activation energy, and b is a constant fitting parameter. The values for Q_0 and b are given in Ref. [68] for four different cross section measurements/calculations available in the literature. These parameters are fit with an activation energy E_a set to 2 eV for all transitions. Among the four techniques, we have elected to use the values that correspond to the measurements using combined diagnostics in the afterglow period of a pulsed capacitive plasma (referred to as CDAP), and the calculations by Zatsarinny and Bartschat which use a large-scale R-matrix (referred to as LRM) to calculate the collisional cross sections [20, 79, 80]. The values for CDAP are used as a first choice, while the values for LRM are used for the cases where values for CDAP are not listed.

Table 4: The rate constants Q_0 and fitting parameter b used in this work. Values taken from Refs. [68, 69].

	Q_0 $(10^{-14}$ m^3/s$)$					b				
	$2p_1$	$2p_2$	$2p_3$	$2p_4$	$2p_5$	$2p_1$	$2p_2$	$2p_3$	$2p_4$	$2p_5$
g.s	0.22	0.07	1.3	0.1	0.1	13.9	13.8	13.7	14	13.6
$1s_2$	7.22	15.3	22.3	11	0.52	0.2	0	-0.9	0.4	-1
$1s_3$	0.94	18.2	1.67	28.5	0.77	-0.8	0	-0.7	0	-0.9
$1s_4$	0.36	2.12	5.11	1.33	4.95	-0.8	0	0.5	-0.6	0.3
$1s_5$	0.18	1.83	2.67	1.13	0.53	-0.6	0.3	0	0	-0.6

The rate coefficients pertaining to transitions from the ground state have a similar,

yet simpler, Arrhenius form [69]

$$Q_{gs \to 2p} = Q_0 \cdot \exp\left(-\frac{b}{T_e}\right). \tag{80}$$

A summary of the values used for this work can be seen in Table 4, and the full comprised list of values can be found in Ref. [68, 69]. From here, Eq. (74) can be used to find T_e by minimizing

$$\left(\frac{\Phi_{2px \to 1sj}}{\Phi_{2p5 \to 1s4}} - \frac{\Gamma'_{2px \to 1sj}}{\Gamma'_{2p5 \to 1s4}}\left[\frac{\sum_l n_l Q_{l \to 2px}}{\sum_l n_l Q_{l \to 2p5}}\right]\right)^2 \to 0, \tag{81}$$

for each spectral line. The final value is then the average of all the T_e's calculated using Eq. (81).

Electron Density

Once the electron temperature is found using the line ratio technique in the previous subsection, we can return to Eq. (70) and solve for n_e by

$$n_e = \frac{\Phi_{2px \to 1sj}}{\Gamma_{2px \to 1sj} \sum_l n_l Q_{l \to 2px}}. \tag{82}$$

In a similar fashion as for T_e, a value for n_e can be found for each spectral line, and the final value is the average of these values.

While calculation of the electron density from Eq. (82) is consistent with the outlined CRM, Li *et al.* formulated a simple relationship between the ratio of $1s_5$ and $1s_4$ densities and the plasma parameters T_e and n_e given by [61, 81]

$$\frac{n_{s5}}{n_{s4}} = \frac{g_{s5}}{g_{s4}}\left(1 + \frac{\gamma_{s4 \to gs}}{5n_e}\frac{A_{s4 \to gs}}{Q_{s4 \to s5}(T_e)}\right). \tag{83}$$

This relationship was developed through the implementation of a more robust CRM for a low temperature ICP and parallel plate CCP Argon discharge in a comparable pressure regime. This expression is particularly convenient because it provides an additional avenue for n_e calculation in which results from *all* diagnostic techniques can be implemented. The excited state densities from TDLAS or OES-BFM can be used on the r.h.s. of Eq. (83), while T_e or n_e from the CRM or the Langmuir Probe can used on the l.h.s. Therefore, values for n_e and T_e can be compared for a number of different analysis methods. The consistency of the results will determine the confidence in each method in respect to the external parameters.

Equation 83 is strictly dependent on the transition from the $1s_4$ state to the ground state, and the collisional decay of the $1s_4$ state to the $1s_5$ state. The photon escape factor for the $1s_4 \to$ g.s. transition is calculated from Eq. (63) with n_g as the lower state density. This particular form of the escape factor is used as this transition has an optical thickness $\tau > 100$, outside of the valid range of Eq. (65). The rate coefficient of the $1s_4$ to $1s_5$ transition has a similar form as those in Eq. (79), and is calculated from the reverse process ($1s_5 \to 1s_4$ excitation) through the principle of detailed balancing [2, 61, 81]. Thus, $Q_{s4 \to s5}$ has the form

$$Q_{s4 \to s5} = Q_{s5 \to s4} \frac{g_{s5}}{g_{s4}} e^{-E_a/T_e}, \tag{84}$$

with

$$Q_{s5 \to s4} = Q_0 \left(\frac{T_e}{E_a} \right)^b, \tag{85}$$

where $E_a = 0.07$ eV is the activation energy, and $Q_0 = 6.4 \times 10^{-14}$ m^{3}s^{-1} and $b = -0.6$ are fit parameters according to the work by Zhu [68].

5.4 TUNABLE DIODE LASER ABSORPTION SPECTROSCOPY

Depending on the physical conditions of the discharge or emitting body, the spectral line profiles of radiative transitions can be broadened or widened [62]. In this case, these lines are dominated by Doppler broadening due to the kinetic motion of absorbers. Much like the electrons within the discharge, the neutral atoms have a distribution of velocities based on the gas temperature (T_g). Thus, when excited atoms emit photons through the allowed radiation channels (for example, see Figure 23) the wavelength is Doppler shifted based on the relative velocity of the atom as seen by the observer. Therefore, as spectral lines are measured their line profiles will become wider as the gas becomes hotter. A simple depiction of this phenomenon can be seen in Figure 26.The typical broadening of a line profile is 800 to 900 MHz, or roughly 10^{-3} nm in the conditions of this work. While significant, most modern spectrometers don't have the resolution to detect the changes in the spectral line as the temperature is varied. However, this process works exactly the same in reverse through absorption rather than emission.
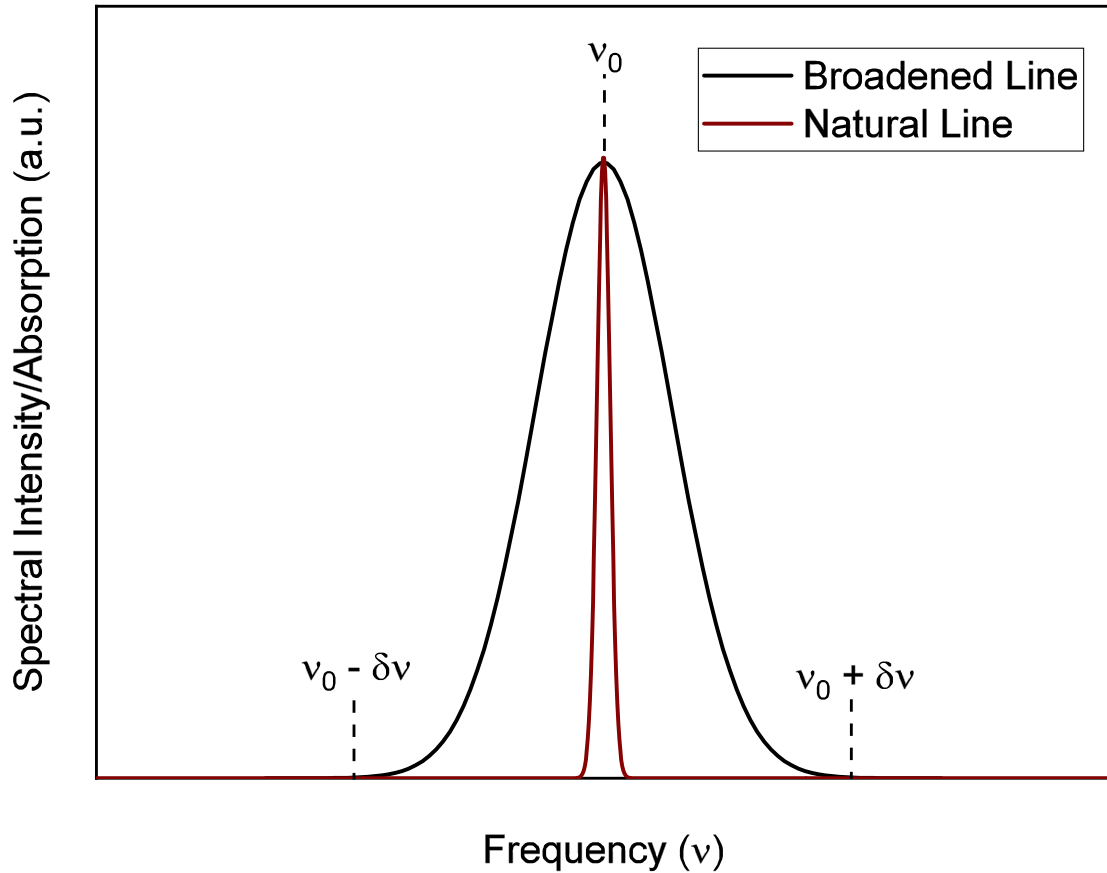
Figure 26: Depiction of a Doppler broadened spectral line/absorption profile. In the reference frame of the observer, fast moving atoms emit/absorb photons at a frequency shifted off resonance (ν_0) based on their velocity. More details can be found in the text.

Consider a beam of light traveling through a volume of dense atoms. For the sake of clarity, let us assume that the atoms can only travel in one dimension parallel to the path of the beam. If the beam is tuned to an energy ($E = h\nu_0$) equal to an atomic resonant transition, the "stationary" atoms absorb the photon and are excited to a higher energy state. However, the atoms with a significant nonzero velocity will see this light as off resonance, shifted by some frequency $\delta\nu$ in their reference frame. Those atoms that are traveling towards the light source (opposite direction of light propagation) will see blue-shifted light ($+\delta\nu$), while the atoms traveling away from the light source will see red-shifted light ($-\delta\nu$). Thus, in order for these "hot" atoms to be excited, the beam frequency must be shifted by $\delta\nu$ depending on the direction of travel. Therefore, atoms traveling towards the beam source will accept photons with

an energy shift of $\delta E = -h\delta\nu$ (red-shifted light in the observer frame) and atoms moving away will accept photons with a shift $\delta E = h\delta\nu$ (blue-shifted in observer frame). A basic portrayal of this process is shown in Figure 27.
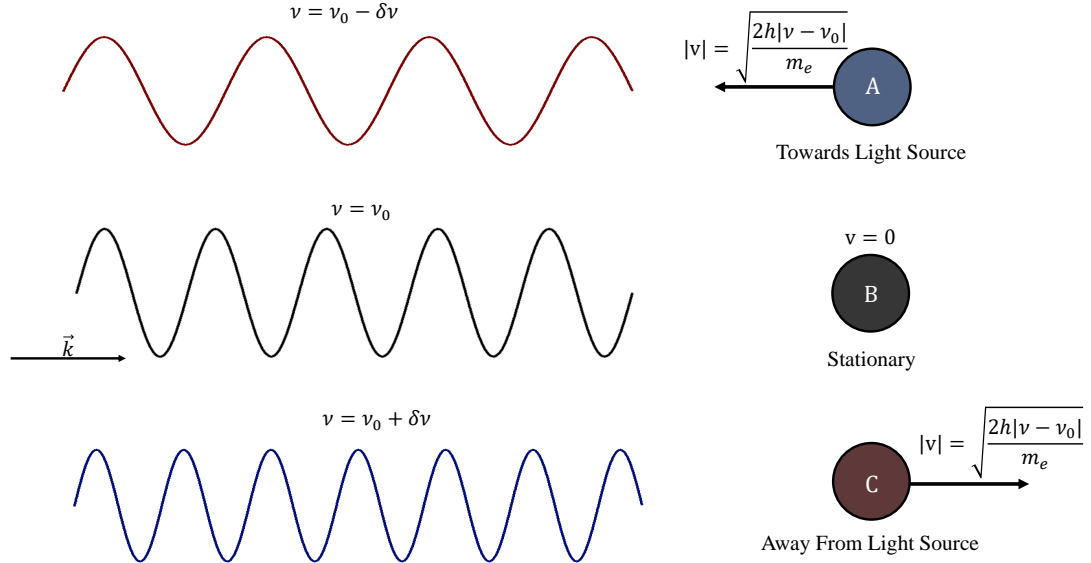
Figure 27: A basic 1-D model of absorption in a Doppler broadened medium drawn in the reference frame of the observer (same frame as the stationary atom). Atoms A, B, and C will all accept the incoming photon and be excited. This is because in the reference frames of each individual atom, the frequency of incoming light is equal to ν_0, the resonant frequency of the transition. More details can be found in the text.

If the beam frequency is continuously swept between $\nu - \delta\nu$ and $\nu + \delta\nu$ the distribution of atom velocities within this range can be measured by the absorption signal of the beam as it exits the volume. The amount of absorption at a shifted frequency is directly related to the amount of atoms at a particular velocity, given by

$$|v| = \sqrt{\frac{2h|\nu - \nu_0|}{m_e}},$$
(86)

with the distribution centered about the resonant frequency ν_0. In reality, the atoms are moving in 3 dimensions, but only the vector component $\vec{v} = |v|\hat{k}$ affects the absorption of off-resonant photons.

We can therefore use an external light source swept about a wavelength of a $2\mathrm{p}_i \to 1\mathrm{s}_j$ transition to determine the velocity distribution of the $1\mathrm{s}_j$ state. This can be further applied to calculate the gas temperature and the excited state density. Provided that the absorbers are uniformly distributed in the discharge, the intensity of transmitted light is described by the Beer-Lambert law as

$$I(\nu) = I_0(\nu)e^{-k_{ij}(n_j)l}, \tag{87}$$

where ν is the frequency of transmitted light, $I(\nu)$ is the intensity of the incident light, l is the length of the observation column (equal to diameter of the plasma cylinder), and $k_{ij}(n_j)$ is the absorption coefficient of the $2\mathrm{p}_i \to 1\mathrm{s}_j$ transition. As defined in Eq. (63), $k_{ij}(n_j)l = \tau_{ij}(\nu)$ is the optical thickness. Frequency and wavelength domains are conveniently interchanged in the case of narrow incident light and a narrow line profile, which is interrogated by scanning the incident light about the line center in the frequency domain and recording the transmitted intensity. Incident light was provided by a laser diode tunable around the center of the absorption line. The transmitted and incident intensities are defined by four distinct measurements, required for each scan:

$$I(\nu) = L(\nu) - P(\nu), \tag{88a}$$

$$I_0(\nu) = L_0(\nu) - B(\nu), \tag{88b}$$

where $L(\nu)$ is the detected intensity when both the discharge and laser is on; $P(\nu)$ is the detected intensity when the discharge is on and the laser is off; $L_0(\nu)$ is the detected intensity when the discharge is off and the laser is on, and $B(\nu)$ is the detected intensity when both the discharge and laser are off.

The absorption coefficient has the general form [57, 58, 60, 62, 82–84]

$$k_{ij}(\Delta\nu) = \frac{\lambda_{ij}^2}{8\pi}P_{ij}(\Delta\nu)\frac{g_i}{g_j}n_j A_{ij}, \tag{89}$$

where $\Delta\nu = \nu - \nu_0$ and ν_0 is the central frequency of the transition line, and $P_{ij}(\Delta\nu)$ is the Doppler broadened (Gaussian) line profile [57, 60, 62]

$$P_{ij}(\Delta\nu) = P_0(\lambda_{ij})e^{-[P_0(\lambda_{ij})\Delta\nu]^2} \tag{90a}$$

$$P_0(\lambda_{ij}) = \lambda_{ij}\sqrt{\frac{M}{2\pi k_B T_g}}. \tag{90b}$$

In the first step of this method the full width of the scanned absorption profile at half maximum, $\Delta\nu$(FWHM), is measured and the gas temperature is evaluated from [60, 82–84]

$$T_g = \frac{M}{2k_B \ln(2)} \left(\frac{\lambda_{ij}\Delta\nu_D(FWHM)}{2}\right)^2. \tag{91}$$

In the second step, the lower state density n_j is evaluated by using Beer-Lambert's law from the full absorption coefficient of the state j: [60, 82, 83]

$$\int_0^\infty \ln\left(\frac{I_0(\nu)}{I(\nu)}\right) d\nu = S = \frac{\lambda_{ij}^3 A_{ij} n_j}{8\pi^{3/2}} \frac{g_i}{g_j} l \sqrt{\frac{M}{2k_B T_g}} \tag{92}$$

where S is the area of the Gaussian spectral profile.

CHAPTER 6

EXPERIMENTAL SETUP

Due to the unique geometry required to process a 3D cylindrical structure, the discharge chamber must be designed to not only properly etch a cavity, but also to include access for diagnostic equipment. Fortunately, much of these issues were addressed by Upadhyay [1] in his work to establish the etching routine, but a great deal was done in this work to improve those designs and implementations. Much of the modifications to the existing design were to improve the pumping conductance, power delivery, gas delivery, and optical observation channels. A general description of the discharge reactor and the subsequent diagnostic materials will be outlined in this chapter, with particular emphasis on the improvements of the design laid out by Upadhyay [1].

6.1 MODULAR DISCHARGE REACTOR

The front view of the active discharge reactor can be seen in Figure 28. The strength of this experimental apparatus as a robust tool lies in the modular nature of the entire setup. As can be seen in Figure 28, and as will become more clear throughout the chapter, many of the pieces of the apparatus can be removed and replaced. This is advantageous for a number of experimental reasons, but particularly because it allows for the experiment to be modified and designed for specific investigations, like changes in geometry for example, without the need for complicated additions. For the purposes of this work, the customization of the apparatus was used primarily for diagnostic purposes by allowing for multiple significant locations for optical measurements.
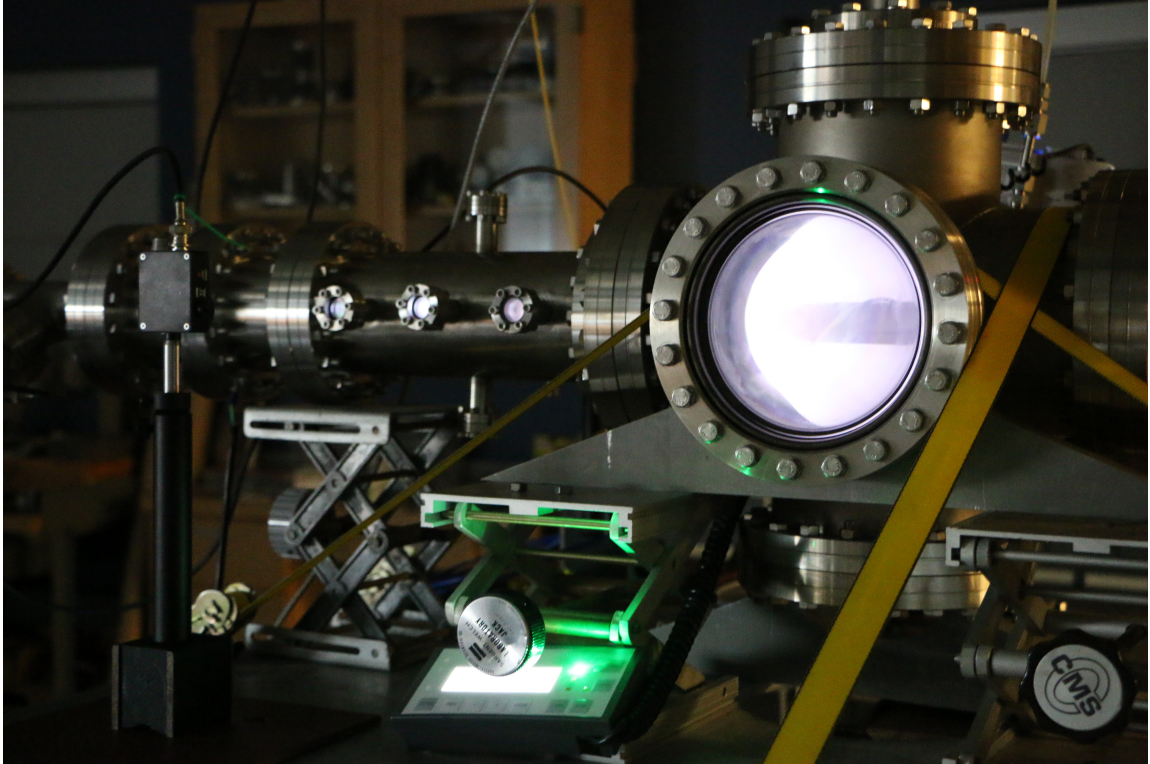
Figure 28: The active plasma discharge chamber.

The cavity is a stainless steel cylinder with eight mini-conflat ports extending from the sides. A 3-D wire diagram of the processing cavity region of the apparatus is shown in Figure 29. The cavity has a length of 26.5 cm ($\approx$ 10.4") and a diameter of 10.0 cm ($\approx$3.9"). The powered electrode has a corrugated structure and is made of niobium with a length of 8.2 cm ($\approx$ 3.2") and a diameter of 5.1 cm ($\approx$ 2.0") [8]. The corrugated structure is used to increase the surface area and help with the reversal of the plasma asymmetry (see Section 4.2) [8]. The electrode is constructed of niobium to eliminate stainless steel impurities that can be introduced in the system from the etching of the driven electrode.

6.1.1 POWER DELIVERY AND PUMPING SYSTEMS

The discharge is powered by a 13.56 MHz RF power supply connected to an electronic matching network which works to reduce the amount of reflected power through the transmission line by matching the impedance of the circuit with the discharge. The matching network is further equipped with an input that allows the connection of an external DC power supply to add the positive bias required for the
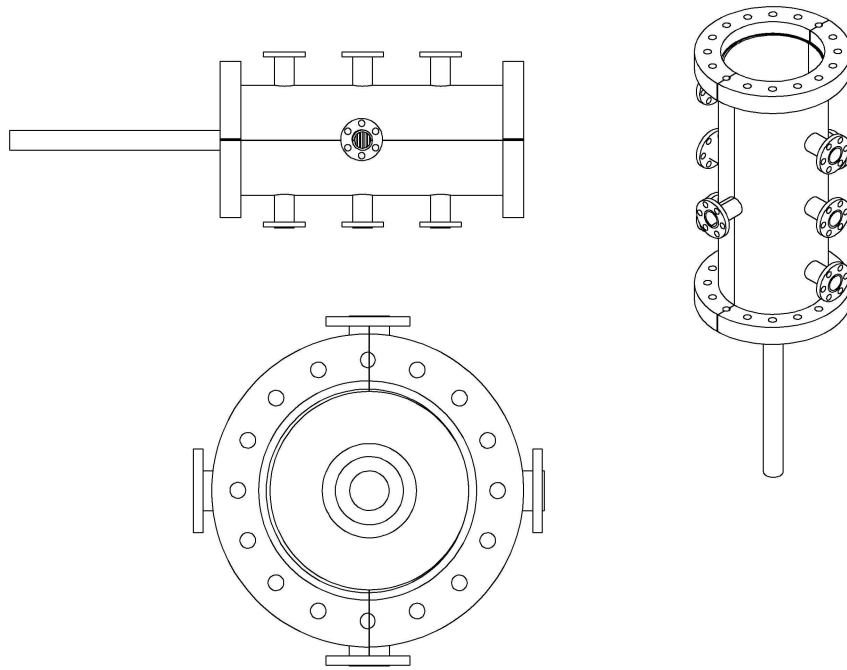
Figure 29: A wire diagram showing different perspectives of the coaxial electrode setup.

reversal of the plasma asymmetry (see Section 6.1.1). The plasma chamber is evac-uated using a combination of a Pfeiffer/Adixen ATH-500MT turbomolecular pump and a Leybold Trivac D65 BCS PFPE rough pump. The inclusion of the Adixen turbomolecular pump was imperative due to the highly corrosive nature of the re-active gas. This particular pump is magnetically levitated to eliminate the reliance on mechanical bearings. While the previous experimental design indeed used "cor-rosive resistant" pumps, the highly reactive process still caused severe damage to the pump bearings with continued use, leading to their eventual destruction. The ATH-500MT is designed specifically for reactive gas etching processes, and therefore greatly improved the longevity and effectiveness of the pumping system. It is im-portant to note that while a high pump speed is useful for the removal of volatile products, the more important pump figure of merit is the gas throughput, or rather the amount of gas that can effectively flow through the pump. This is because the products being removed are not only plentiful, they are also heavy, which requires a pump able to continuously move heavier products and sustain the resulting increase in heat throughout the pump. Since the apparatus is so large and long, the pressure is monitored by two Agilent FRG-700 Pirani gauges at either end of the experiment when applicable. Otherwise, a single Pirani gauge was used in a location downstream from the gas flow and processing area.

The RF power is delivered to the powered electrode through an atmospheric coaxial power feedthrough, and is electrically insulated from the rest of the system by a ceramic break.
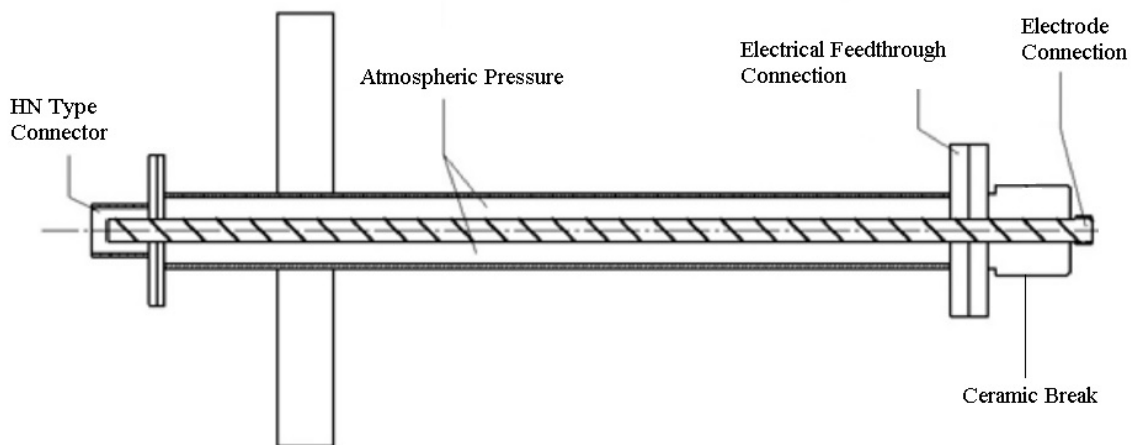
Figure 30: Schematic of atmospheric pressure power feedthrough system [1].

The atmospheric feedthrough, shown in Figure 30, was designed to help ensure that the discharge remained in the correct processing region of the cavity, especially in the case of a leak through the feedthrough. This feedthrough system is among the modular pieces of the apparatus, so the length can be adapted to fit many different sizes of discharge chambers.
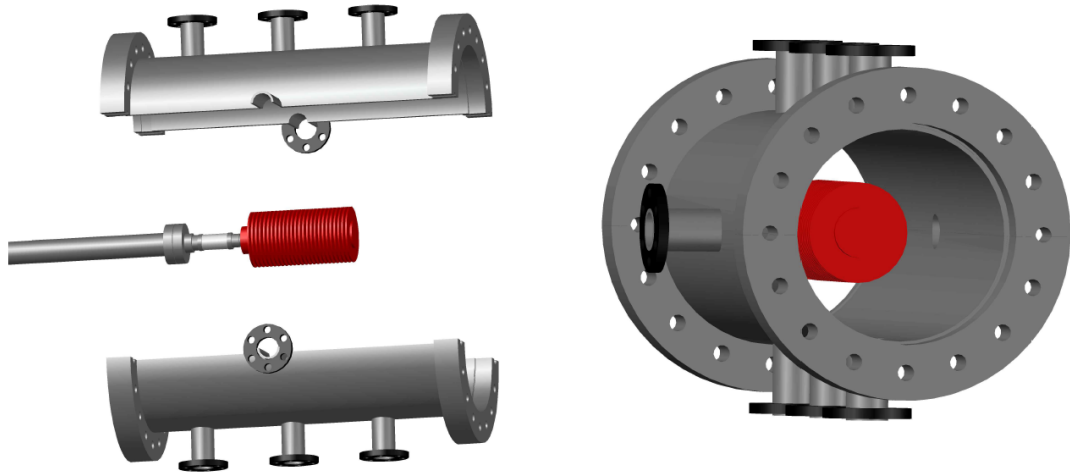
Figure 31: Left: A 3-D split-axis depiction of the coaxial electrode region of the apparatus. Right: An end-on view of the coaxial setup. The corrugated powered electrode is shown in red and the optical viewports used for diagnostic methods are in black.

The powered electrode is then held suspended inside the processing chamber in a coaxial configuration. This can be seen more clearly in Figure 31.

6.1.2 GAS DELIVERY

Proper delivery of the reactive gas into the chamber was a major focus of the study conducted by Upadhyay [1, 9, 37]. This is because of an apparent loading effect, where the reactive species are produced and used at locations surrounding the powered electrode that are closer to the source of gas delivery. Additionally, the turbulent flow of the gas through the chamber led to non-uniform etch rates at locations that are symmetrically identical, ie. the Nb on one side of the powered electrode would be etched more than the other side. This was explicitly seen in experiments conducted for ring like samples placed in various locations along the chamber length [1]. This leads to significant etch rate uniformity issues along the cavity length. To alleviate this issue, a nesting conical gas inlet was designed so that

the gas feed and powered electrode could be moved along the symmetry axis of the cavity. Rather than try to overcome the loading effect, it can be utilized as the local region of high radicals can traverse the length of the cavity. The implementation of this gas feed in a pill-box type cavity experiment can be seen in Figure 32.
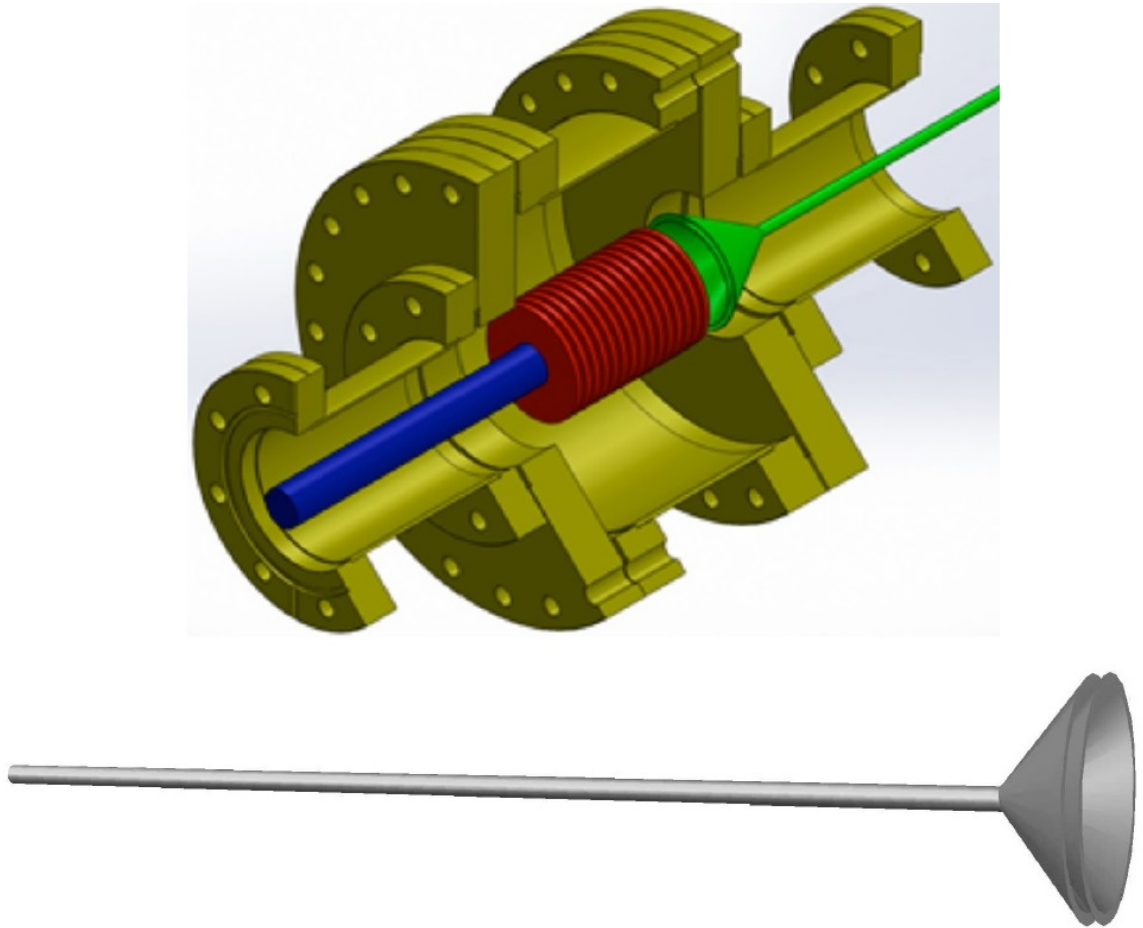
Figure 32: Top: The power feed (red) and gas delivery inlet (green) for a pill-box type cavity experiment found in the work of Ref. [1]. Bottom: A close up depiction of the conical gas inlet.

While this was a novel idea, when implemented the gas feed was destroyed by the reactive ion etching process. This occurred because the gas inlet was electrically connected to the rest of the etching chamber, that is to say that the inlet was attracting ion bombardment in the same way as the cavity, except it was directly exposed to the most dense region of reactive radicals. Additionally, the gas feed was made of stainless steel which subsequently created a great deal of impurities that settled on the cavity walls. To overcome these challenges, two significant changes were made to the

gas feed system. First, gas delivery to the chamber was redesigned to allow positive DC biasing on the inlet (much like the powered electrode) to prevent significant ion bombardment. This was done by flowing the gas through a alumina ceramic break before it reaches the inlet, thus electrically insulating the part from the rest of the chamber. The second improvement was constructing the inlet out of pure niobium to prevent the addition of stainless steel based contaminants in the still likely case that the gas feed becomes etched.

The conical design was used for the majority of the work in this dissertation, but a second design of the gas inlet was constructed due to the destruction of the inlet after a great deal of use. This second inlet was designed to more completely provide a continuous and evenly distributed flow of gas into the chamber. The design was inspired by a combination of the typical showerhead design in semiconductor etching and common popular demonstrations of laminar flow. This is accomplished by constricting the flow through a collection of tubes or metal "straws" inside a pipe. This design can be seen in Figures 33 and 34. This gas feed will be referred to as the laminar showerhead (or just showerhead) for the rest of this dissertation.
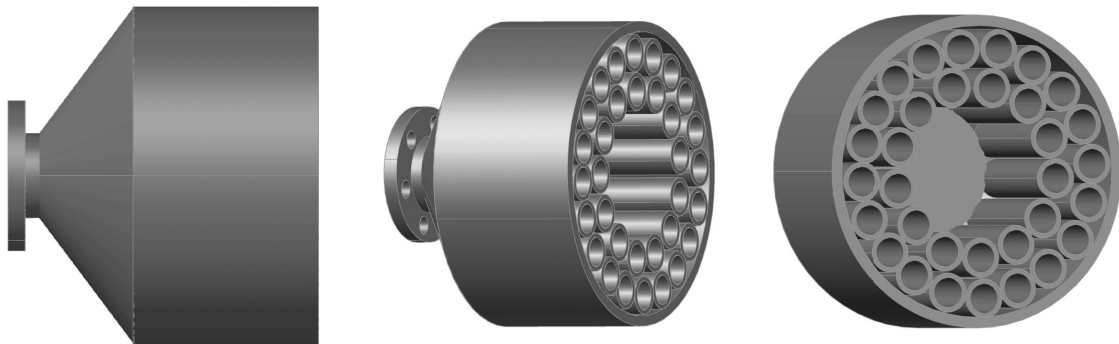
Figure 33: A multi-view depiction of the laminar showerhead. More information about the design and effectiveness can be found in Chapter 9.
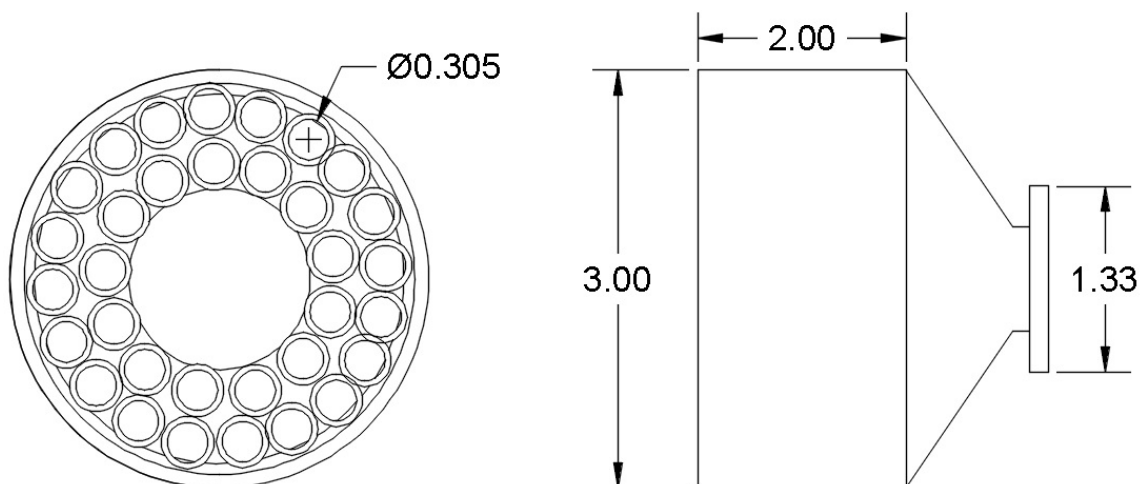
Figure 34: Schematic of the laminar showerhead. All dimensions are shown in inches.

The form of gas delivery is not the only difference between the two designs. The laminar showerhead is much larger with an outer diameter of 3" (7.62 cm) and total body length of approximately 3". Each individual tube is 2" long with an outer diameter of 3/8" and inner diameter of 0.305". The center of the showerhead was blocked off to further encourage flow to the walls of the chamber where the etching targets are located. Otherwise, much of the gas would simply flow through the middle of the showerhead providing no benefit compared to a simple tube. The gas enters the showerhead through a DN16 (1.33") flange welded to the funnel region. In the same way as the conical inlet, the showerhead was electrically separated from the rest of the chamber by a DN16 alumina ceramic break allowing for a positive DC bias to be applied. The tubes and their respective housing are made from nickel Alloy 600, commonly called Inconel, while the center block, the funnel region, and the flange are made of stainless steel. This nickel alloy was chosen for the construction due its substantially corrosive resistance compared to stainless steel and other common alloys. More information about this material and the showerhead's construction can be found in Chapter 9 as it is directly related to the material studies outlined therein.

6.2 OPTICAL EMISSION SPECTROSCOPY

The emission spectra are measured using an Ocean Optics HR4000CG-UV-NIR spectrometer, capable of measuring spectral lines from 200-1100 nm in a single scan

with a 1 nm resolution. A 600 micron fiber (OceanOptics P600-5-VIS-NIR) was used for each measurement along with a 3D printed aperture seen in Figure 35 to limit the acceptance angle of the fiber optic, as well as ensure the fiber took measurements in a consistent line of sight through the plasma chamber. The configuration of the fiber optic system during measurements can be seen in Figure 42. The fiber optic has a natural acceptance angle of 15° in all directions and the aperture limits this acceptance angle to $\approx 5°$, allowing for a more accurate line of sight measurement.
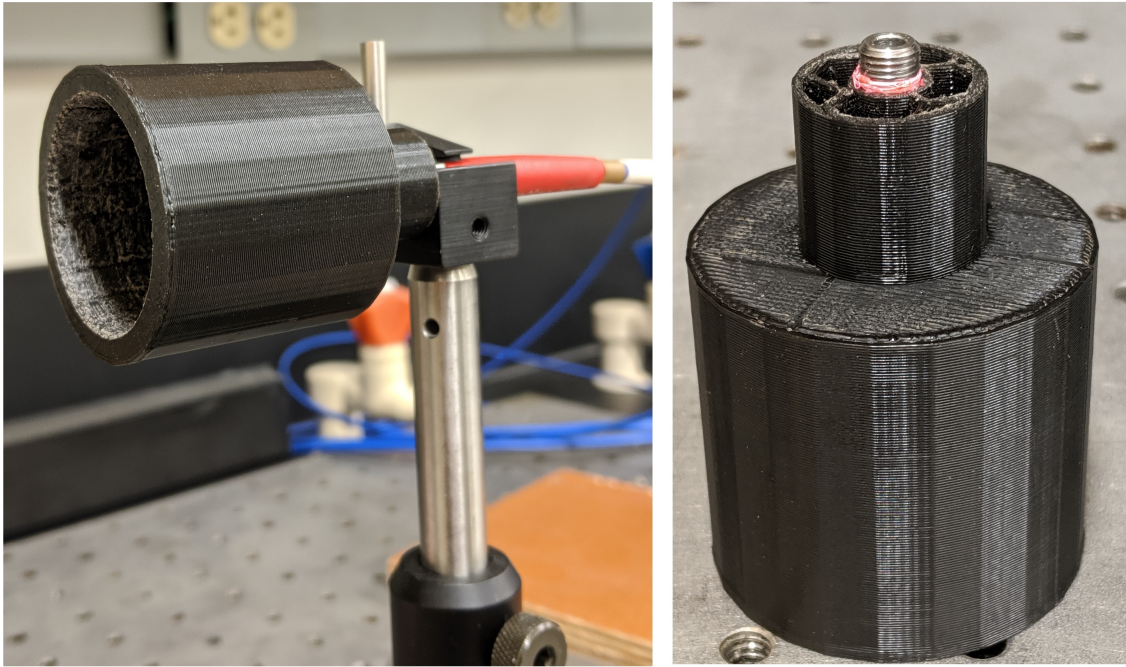
Figure 35: The 3-D printed fiber optic aperture. The piece fits over a DN16 conflat flange and holds the fiber optic in the center. The smaller cylinder is solid plastic with a small hole where the fiber is mounted. This effectively decreased the acceptance angle of the fiber to $\approx 5°$.

While larger CCD camera spectrometers have a much better resolution capable of measuring spectral lines well within a nm, the speed and convenience of the low resolution spectrometer is a significant advantage, especially when using OES-BFM. In fact, OES-BFM was designed with these types of spectrometers in mind as they are widely available in both laboratory and commercial settings. Using a higher resolution system would make this technique, especially for a robust study, unfeasible simply due to the amount of time required to measure each spectral line.

6.2.1 SPECTROMETER INTENSITY CALIBRATION

The spectrometer was calibrated using an Oriel Quartz-Tungsten Halogen black-body lamp source (Model no. 63358). This lamp is pre-calibrated by the manufacturer and has a predefined relationship between the spectral irradiance of the lamp I in units of mW/m$^2 \cdot$ nm^{-1} and the wavelength λ (nm). This relationship is given by

$$I = \lambda^{-5} e^{A + \frac{B}{\lambda}} \left(C + \frac{D}{\lambda} + \frac{E}{\lambda^2} + \frac{F}{\lambda^3} + \frac{G}{\lambda^4} \right), \tag{93}$$

where the coefficients are provided by Newport

$$A = 41.4853757741901$$
$$B = -4899.97859767823$$
$$C = 0.821306420331086$$
$$D = 428.610013779585$$
$$E = -317020.290823792$$
$$F = 85820275.9042372$$
$$G = -8493841443.25665.$$

The spectral irradiance represents the electromagnetic power radiation per unit area incident on a surface at a particular wavelength. The blackbody lamp's spectral irradiance is plotted in Figure 36.
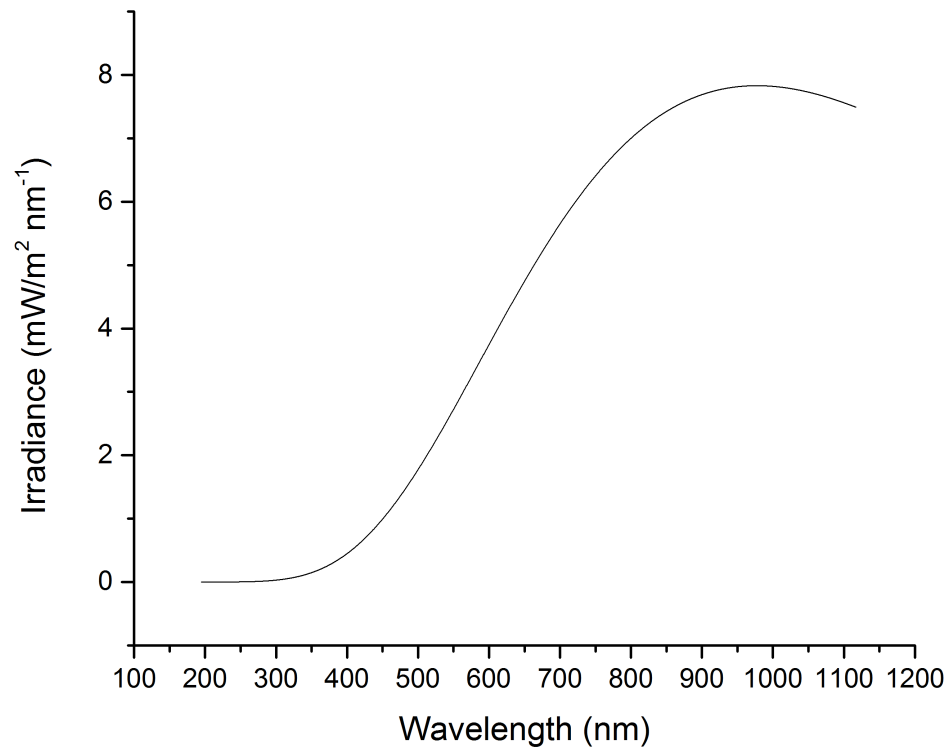
Figure 36: Irradiance as a function of wavelength for the Newport/Oriel Tungsten Halogen blackbody source as given by Eq. (93).

For each spectrometer, the blackbody source is measured from a distance of half a meter, as recommended by the manufacturer. This yields a blackbody curve as defined by the resolution and accuracy of the spectrometer shown in Figure ??.
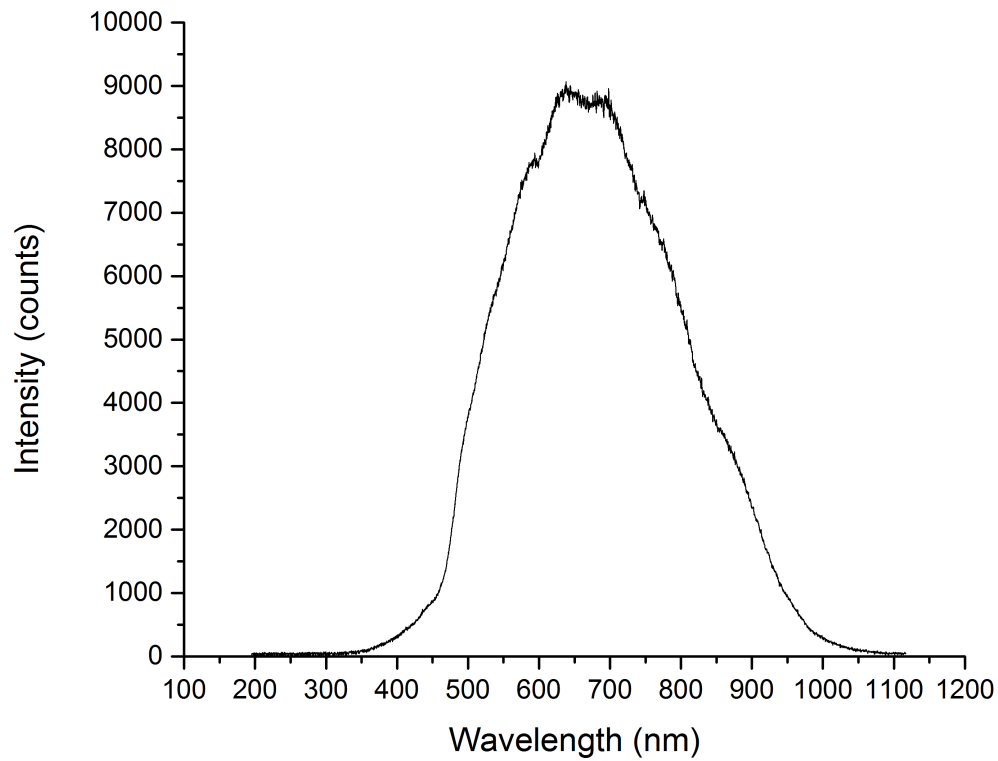
Figure 37: Intensity as a function of wavelength for the blackbody source as measured by the OceanOptics fiber optic spectroscopy system.

The irradiance of the source is then divided by the intensity to yield an irradiance/count value for each wavelength. These values are then used to calibrate the signal the spectrometer measures from the plasma. Each raw spectral measurement is multiplied by the irradiance/count for each wavelength. This yields a true irradiance of the measured signal from the plasma as shown in Figure 38.
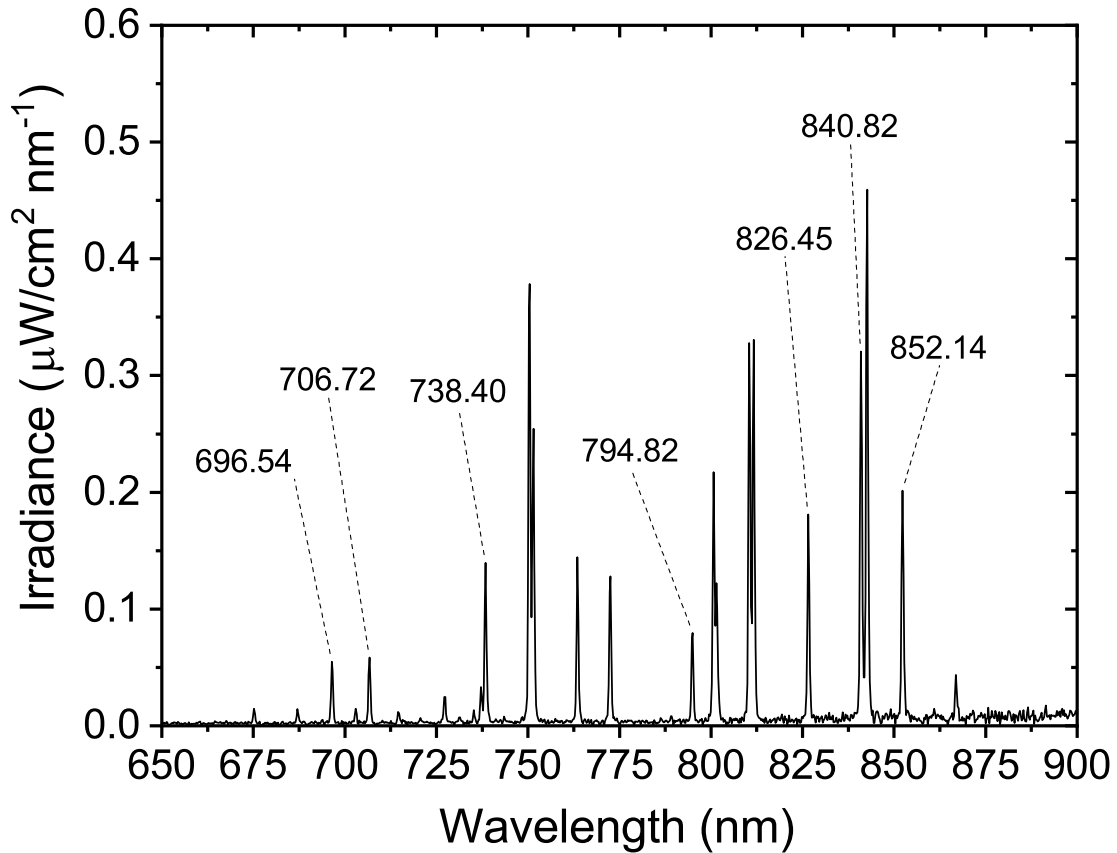
Figure 38: Example spectral irradiance of an Argon plasma using the OceanOptics system. Spectral lines pertinent to the OES methods outlined in Chapter 5 are emphasized. The limitations of the spectrometer can be seen as some lines are not distinct and may overlap.

Once the spectral lines are measured, they are fit to a Gaussian and integrated using Origin fitting software. The resulting integrated value for each peak, which is in units of Radiance (μW/cm^2), is used for the solution of Eq. (66). The expected and calculated error for OES-BFM is higher due to the low resolution of the spectrometer, the extended calibration required, and the acceptance angle of the fiber. The error for each measurement was calculated from standard error calculations of two sets of measurements taken on separate days under the same conditions. Data points that do not have multiple measurements for those specific conditions due to experimental error are given a statistical error of 30% as a default.

6.3 TUNABLE DIODE LASER

An external cavity diode laser was built using a 150 mW Sanyo semiconductor diode with a nominal free running wavelength of 808 nm in a Littman-Metcalf configuration [85]. A picture and schematic of the tabletop laser setup can be seen in Figs. 40 and 41. This laser was capable of scanning both the 810.37 nm and 811.53 nm transition lines after proper tuning to measure the gas temperature and the $1s_4$ resonant and $1s_5$ metastable level densities. The laser can be tuned to a transition by a coarse adjustment of the grating in the cavity, along with temperature and current adjustments. Once the laser is tuned to a transition, a piezoelectric device is used to change incident angle of the laser light by slight adjustments of the mirror mount. This changes the frequency of the light according to

$$\frac{d\nu}{d\theta} = -\frac{2ac}{\lambda^2}\cos\theta, \tag{94}$$

where θ is the incident angle and a is the grating spacing [86]. At the same time, a change in the length of the diode laser cavity, or the distance between the diode and the grating, will cause a frequency shift of

$$\frac{d\nu}{dl} = -\frac{c}{\lambda l}. \tag{95}$$

Oftentimes, a single piezoelectric changing θ is sufficient to scan a few GHz in a single longitudinal cavity mode. However, if the change in angle is too large it will change the effective cavity length and cause a mode-hop. In our case, the piezoelectric could only achieve approximately 1 GHz of mode-hop free tuning, which is smaller than the absorption frequency profile. To address this, one can either add a second piezoelectric to change the cavity length in sync with the incident angle, or the frequency of the light can be adjusted to compensate for this change in cavity length. For the second option, the frequency can be tuned by changing the injection current (I_{LD}) to the diode. This second option was implemented through the use of a feed forward circuit, which allows for the simultaneous adjustment of the current and piezoelectric voltage. In essence, the piezoelectric voltage ramp is used as a time varying addition to the injection current with the form

$$\Delta V_{piezo} = \Omega \Delta I_{LD}, \tag{96}$$

where V_{piezo} is the driving voltage of the piezo, and Ω is the circuit resistance in which the frequency change from the piezo is equal to the change from the current adjustment, or $\Delta\nu_{piezo} = \Delta\nu_{current}$.

The feed-forward circuit was built based on a simpler version of the design by Doret *et al.* and can be seen in Figure 39 [86]. The combination of the piezoelectric and feed-forward allowed for a mode-hop free scan of 4 GHz. Absorption profiles were typically $\approx$ 3 GHz.
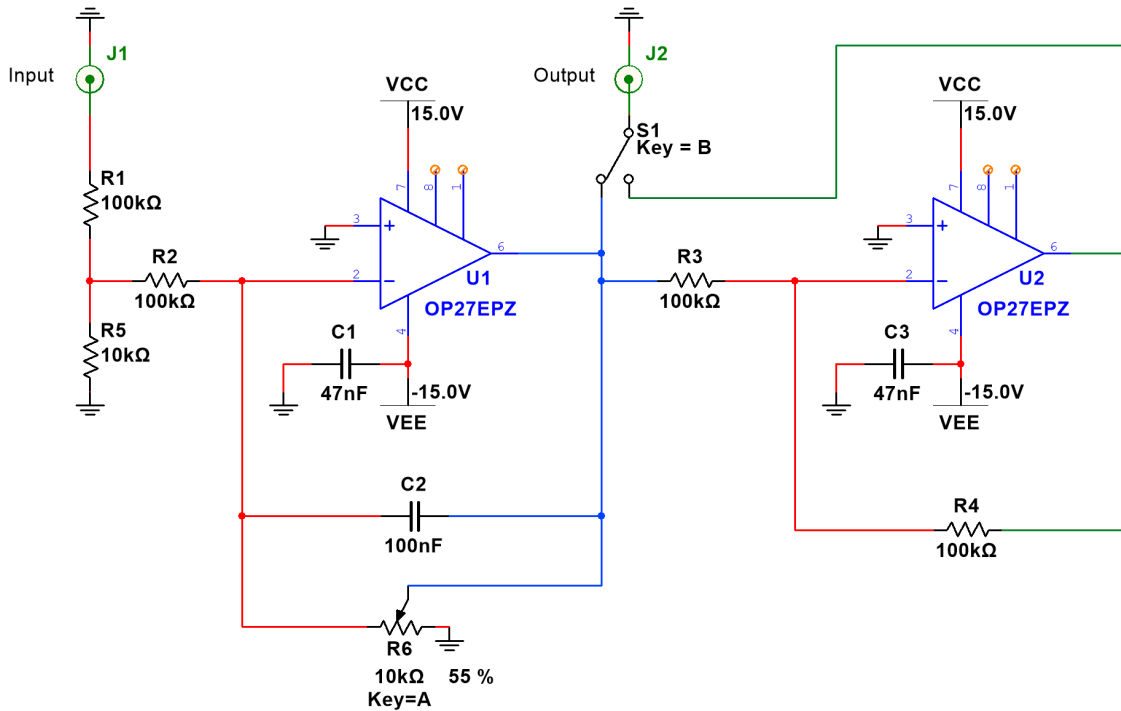
Figure 39: The feed forward circuit schematic. The second stage on the right is a unity gain low pass filter that is only necessary if the signal needs to be inverted.

The feed forward takes the high voltage output from the piezoelectric and yields a proportional output with an adjustable gain from the potentiometer (R6 in Figure 39). The output signal is adjusted so that $\Delta I_{LD} = 0$ at the middle point of the piezo's voltage range ($\Delta V_{piezo}/2$). The value for Ω, and therefore the highest frequency sweep range, is found by tuning the potentiometer. More details about the feed forward circuit can be found in Ref. [86].

The laser is guided through an optical isolator into a beam splitter that allows a portion of the beam to be sent to two different Fabry-Perot Interferometers (FPI). One is a ThorLabs SA200-7A with 1.5 GHz Free Spectral Range (FSR), and the other is a homemade low finesse parallel mirror interferometer with a calibrated FSR of 303 MHz. Due to the piezoelectric and feed-forward circuit required to get the laser to sweep over a large enough frequency range, the resulting scan signal has a nonlinear
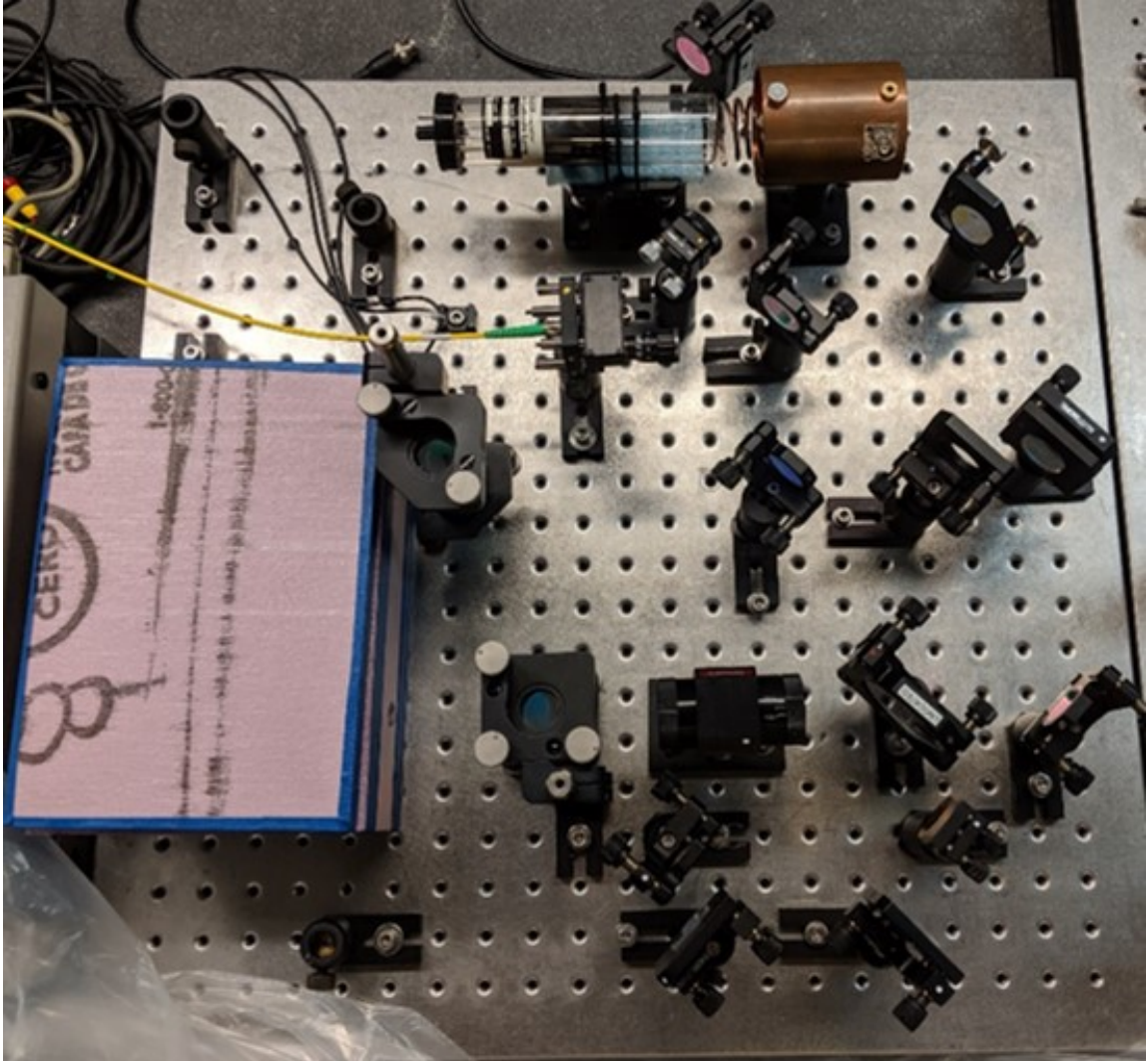
Figure 40: The experimental TDLAS setup (without the FPI systems).

scan rate that propagates throughout the scan. Since the laser can only scan 4 GHz mode-hop free, the 1.5 GHz FSR of the ThorLabs is too large to properly detect and account for this nonlinearity. The lower FSR of the homemade interferometer allows for this nonlinearity to be seen over the length of the scan, and the scan can be calibrated accordingly. The other half of the beam is then split again to be sent
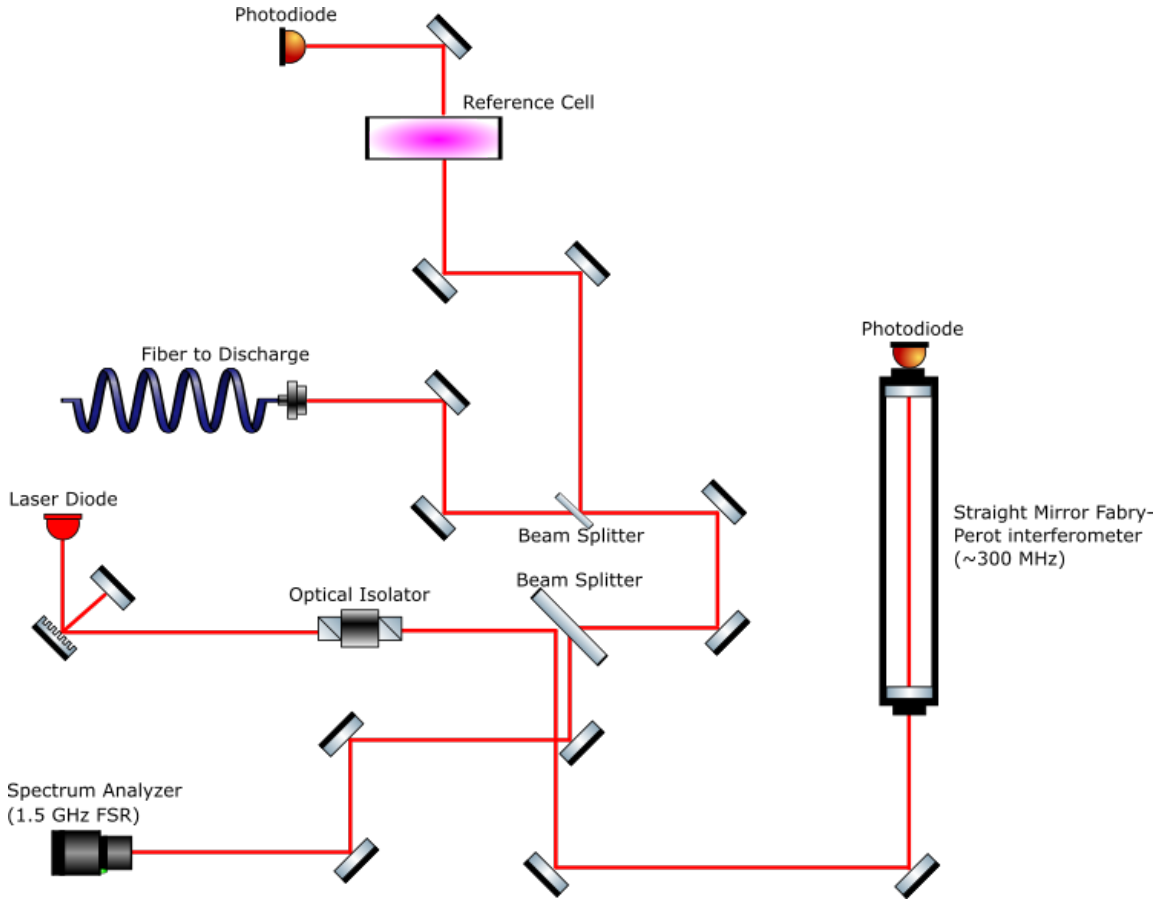
Figure 41: Schematic of the TDLAS tabletop setup.

to a low pressure Ar reference discharge cell for wavelength confirmation and laser tuning. The other part of the beam is sent to a flip mount that can either send the beam to a Burleigh WA-20VIS wavemeter or to a fiber launcher which sends the beam to the plasma chamber.

The laser is sent through an unobstructed area of the plasma chamber in front of the powered electrode by passing through two mini-conflat ports as seen in Figure 42.
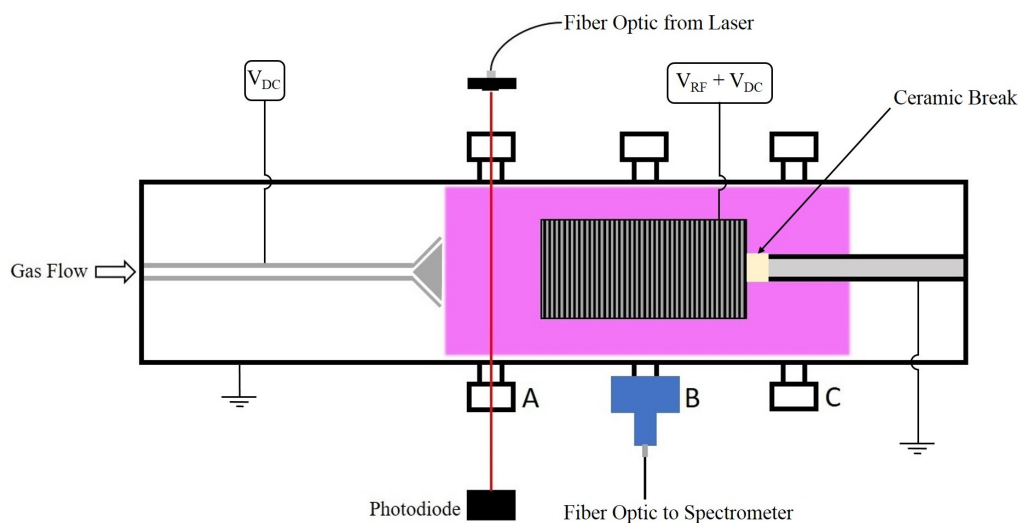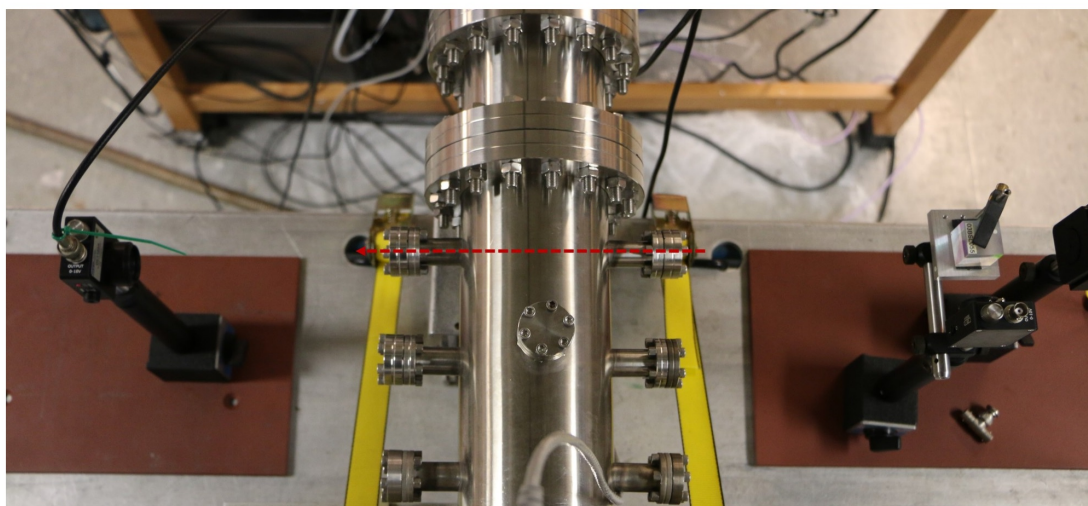
Figure 42: Top: The laser path through the plasma chamber. The laser exits the fiber launcher on the right and passes through a non-polarizing beamsplitter cube before entering the discharge through the viewport. The laser (minus absorption) exits the chamber and is collected by the photodiode on the left. Bottom: A cartoon schematic of the discharge and location of the diagnostic tools. While the laser can only travel unobstructed through viewport A, the fiber optic can be placed at A, B, or C. However, location A was strictly used for both methods to ensure a more direct comparison of results.

The beam is collected on the other side of the chamber by a ThorLabs DET100A photodiode and sent to a 4-channel oscilloscope that measures the laser absorption, the two FPIs, and the piezoelectric voltage signal (which shows the bounds of the

scan). Using the Beer-Lambert law, the absorption signal is converted into the signal shown in Figure 43 and fit to a Gaussian. The resulting Gaussian fit yields all the pertinent information to calculate the gas temperature and density. Each
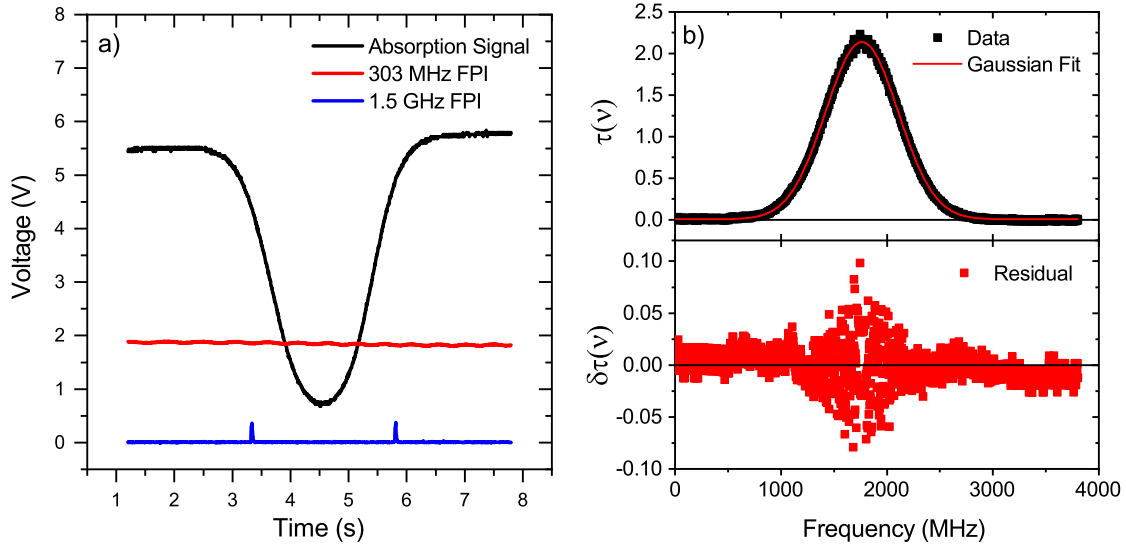
Figure 43: Example of laser absorption measurement using TDLAS: a) Laser absorption and two Fabry-Pérot Interferometer signals (the piezo voltage signal is not pictured); b) The processed signal along with residual plot.

measurement consisted of three scans, which were fit and then averaged, to ensure that the scans are consistent and reliable. The error in TDLAS measurements is calculated from a combination of the error in the Gaussian fits of the profile and the frequency calibration. The error in these measurements is very small compared to OES-BFM with an average error of $\pm$ 3%.

6.3.1 LASER SCAN FREQUENCY CALIBRATION

The nonlinear jitter caused by the combination of the feed-forward circuit and the piezoelectric used for the frequency sweeping of the laser requires proper calibration, without which the final fit can be off by over 100 MHz. The home-built parallel mirror FPI has a very low finesse and has the form of a cosine wave, but the accompanying low FSR allows for the measurement and fitting of the nonlinear jitter over the scan length. The 1.5 GHz FSR Thorlabs FPI has a very high finesse and a very low frequency error, about 3 MHz as stated by the manufacturer. The high FSR is too large compared to the scan size (approximately 4 GHz) to calibrate the signal for

the jitter, but it can be used to properly calibrate the parallel plate FPI and provide consistency across all measurements. The calibration process works as follows. A measurement of the two FPIs is taken under typical conditions for a laser absorption experiment. The signal from the home-built FPI is imported into the Origin data manipulation and fitting software where the background noise is subtracted and the data is smoothed, yielding a signal that has the form of a cosine function with a time dependent phase.
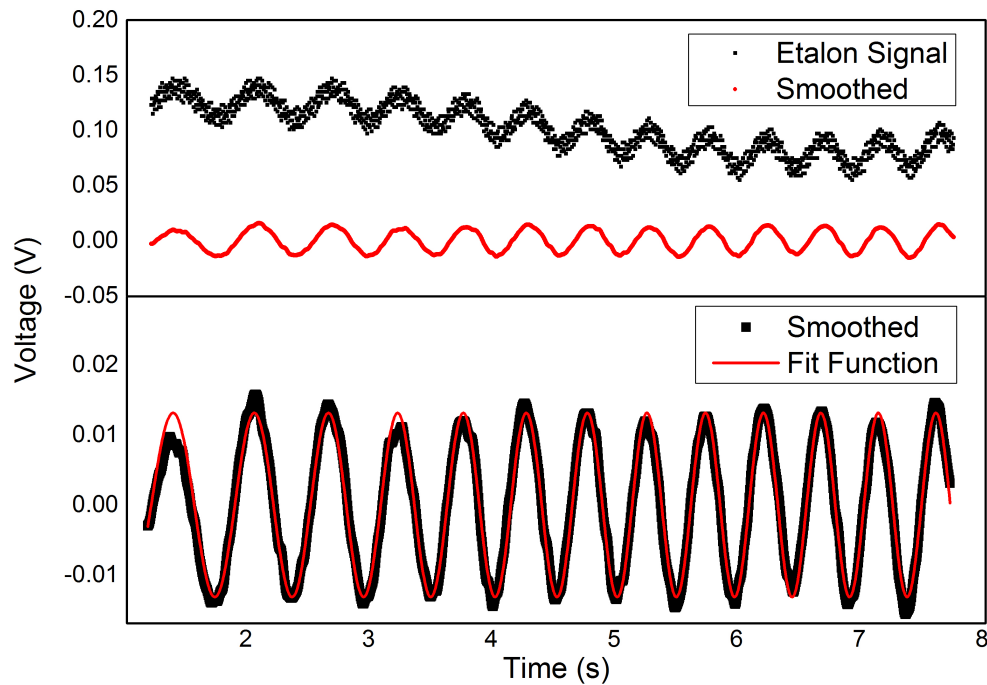
Figure 44: Top: The raw home-built etalon signal and the processed signal. Bottom: The time-varying phase cosine function fit to the smoothed data.

This signal is then fit according to the following function

$$V = B\cos((E + Dx + Fx^2)x + p) = B\cos(k(x)x + p), \tag{97}$$

with final values

$$B = 0.01316$$
$$E = 6.34076$$
$$D = 1.0376$$
$$F = -0.05061$$
$$p = 1.74223,$$

where E, D, F and p are all defined by the fit. It is important to point out that the values B and p don't matter for the overall calibration of the signal. In fact, the signal from the etalon is different every scan, and one would think that each scan would need to be calibrated. However, as long as the *change in phase* is consistent between scans, the same calibration can be used for every scan. That is to say that the value of $E + Dx + Fx^2$ must remain the same for every scan. This is done by setting and not adjusting the piezo voltage, feed-forward, and oscilloscope range. This is not ideal as it does not allow for adjustment if the system requires it, but this worked sufficiently well for our purposes.

Equation 97 can now be used in conjunction with the ThorLabs FPI to calculate the FSR of the parallel mirror etalon. The total phase change of the cosine function as measured between the two sharp peaks of the ThorLabs FPI will correspond to 1.5 GHz (the FSR of the FPI). This phase change will then correspond to a specific number of wavelengths between the two ThorLabs etalon peaks. The number of wavelengths is then used to calculate the FSR of the parallel mirror FPI according to

$$FSR = \frac{1.5\text{GHz}}{N} \approx 303 \text{ MHz}. \tag{98}$$

With the FSR in hand, the change in frequency as a function of phase can be calculated by

$$f = \frac{k(x)}{2\pi} \cdot 303 \text{ MHz} \tag{99}$$

for each value of x. This array of frequency values can then be used to replace the arbitrary x axis as measured by the oscilloscope and used for the analysis. The frequency calibration can easily be checked for each scan by plotting the ThorLabs

etalon signal vs. the new frequency axis and measuring the FSR compared to the known 1.5 GHz value as seen in Figure 45. Each scan was within 30 MHz of 1.5 GHz, while most were within 15 MHz. This error is quite small when compared to the typical 800-900 MHz FWHM of a laser absorption scan. This error, along with error from the fit shown in Figure 44 is propagated through the calculations of the gas temperatures and the population densities found using laser absorption spectroscopy.
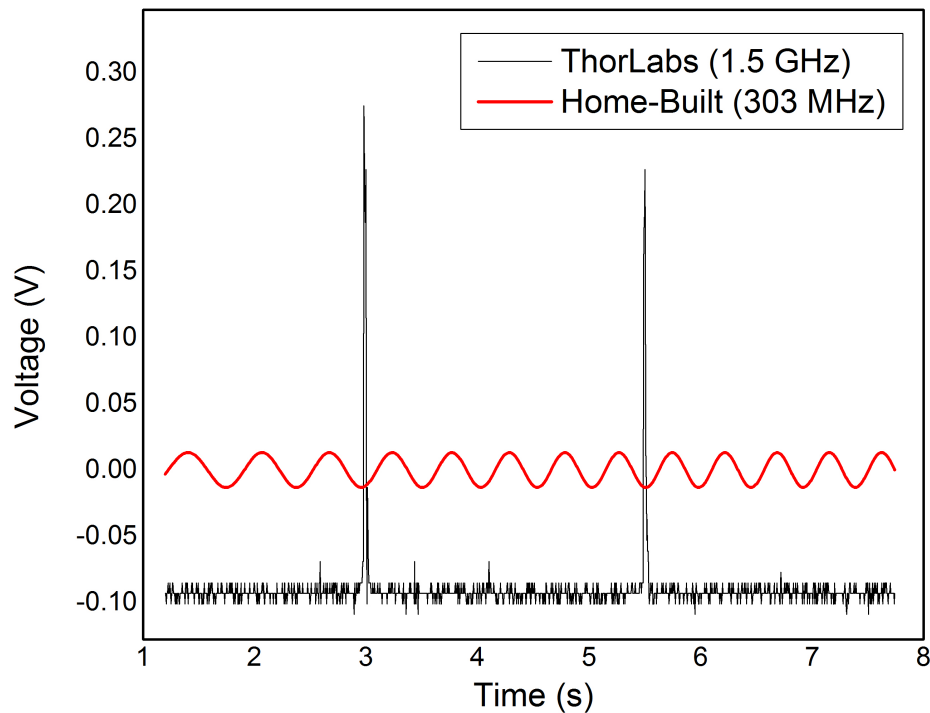
Figure 45: The ThorLabs etalon and final fit for the Home-Built etalon. One can see that there are 4.95 wavelengths between the two sharp peaks.

6.4 LANGMUIR PROBE

A single tipped Tungsten Langmuir probe was placed in the discharge to measure T_e and n_e independent of purely optical methods. The probe was originally made by Impedans as an all-in-one measurement device. However, the probe design was ill-suited for this particular application due to an outdated design in the electrical

circuit related to the rf filtering and compensation. More about these particular issues are discussed in the following paragraph. As it provided no discernible benefit, and a possible source of error, this circuitry was removed from the original probe. The probe tip is held by an alumina coated metal rod mounted to a mechanical bellow system seen in Figure 46 that allows the probe to be actively moved (linearly) in the chamber.
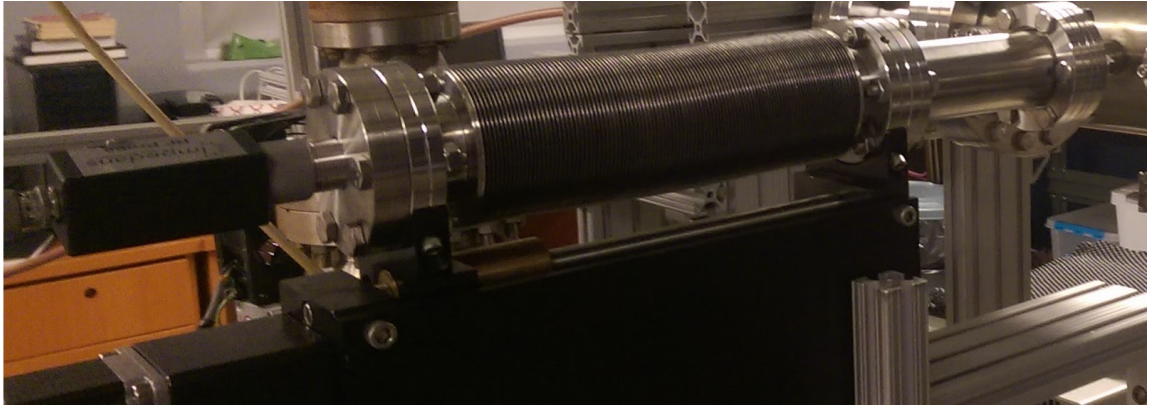
Figure 46: The Langmuir probe housing and linear translation stage.

The probe was inserted at the same location in the chamber as the OES and laser absorption measurements (see Figure 42). The cylindrical probe tip had a length of 5 mm and a radius of 0.2 mm. While scans were attempted at various radial locations, the close proximity of the probe to the powered electrode and gas feed made most locations unusable. This is especially true in those cases in which positive DC bias was added to the gas feed and/or powered electrode. Regardless of probe position, the additional DC bias caused the I-V characteristics to be completely unusable. The most effective probe location was in the radial "gap" between the inner and outer electrodes, and thus all presented results were conducted at this position. A picture of the Langmuir probe in the discharge reactor can be seen in Figure 47. The probe scans were still measured using the provided software from Impedans, but the analysis was done independently as the software could not properly characterize the unfiltered and uncompensated probe. More details about the independent analysis procedure can be found in Chapter 8.
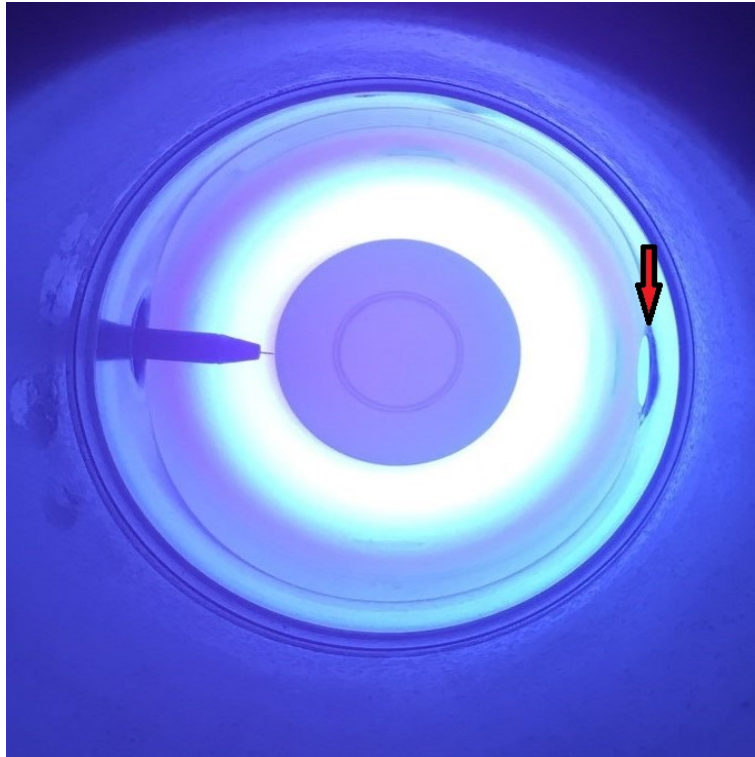
Figure 47: An end-on photo of the plasma reactor with the Langmuir probe inserted. A sample for the surface roughness characterization experiment can be seen mounted in the viewport opposite the probe (red arrow).

As mentioned previously, the probe is limited in its capabilities due to the properties of the experiment and the initial construction of the probe. The most significant limitation of the probe arises from the insufficient grounding of the surrounding discharge about the probe. This is typically done with a second probe tip which measures the change in the plasma potential (V_p) with the probe potential (V) and subtracts this voltage shift from the scan. Without this grounding, V_p can increase with V, meaning that the probe is directly changing the dynamics of the discharge at large [87]. This effect is called plasma pulling, and it can make analyzing Langmuir Probe scans very difficult as the exponential region of the scan is "pulled" toward the x-axis, therefore flattening the electron current and making the transition region difficult to discern. While this does make the scan difficult to analyze, it does not make the scan unusable. Potential pulling occurs because the electron current is large enough to change the potential of the bulk plasma if it is not appropriately grounded, or if this change in V_p as V is increased is not measured and removed from the scan. However, by setting a current limit purposely lower than the maximum range, the

exponential region is pulled less due to the limiting of the electron saturation current. This essentially shortens the amount of time the scan spends in the electron saturation region, and thus has a smaller effect on the variance of V_p. If the probe draws electron saturation current for too long, the probe tip can be heated to the point of emission, which is not only detrimental to the scan, but also the health of the probe [87].

A comparison of scans with different current limits and examples of plasma pulling in an Argon discharge is shown in Figure 48. While evidence of plasma pulling can
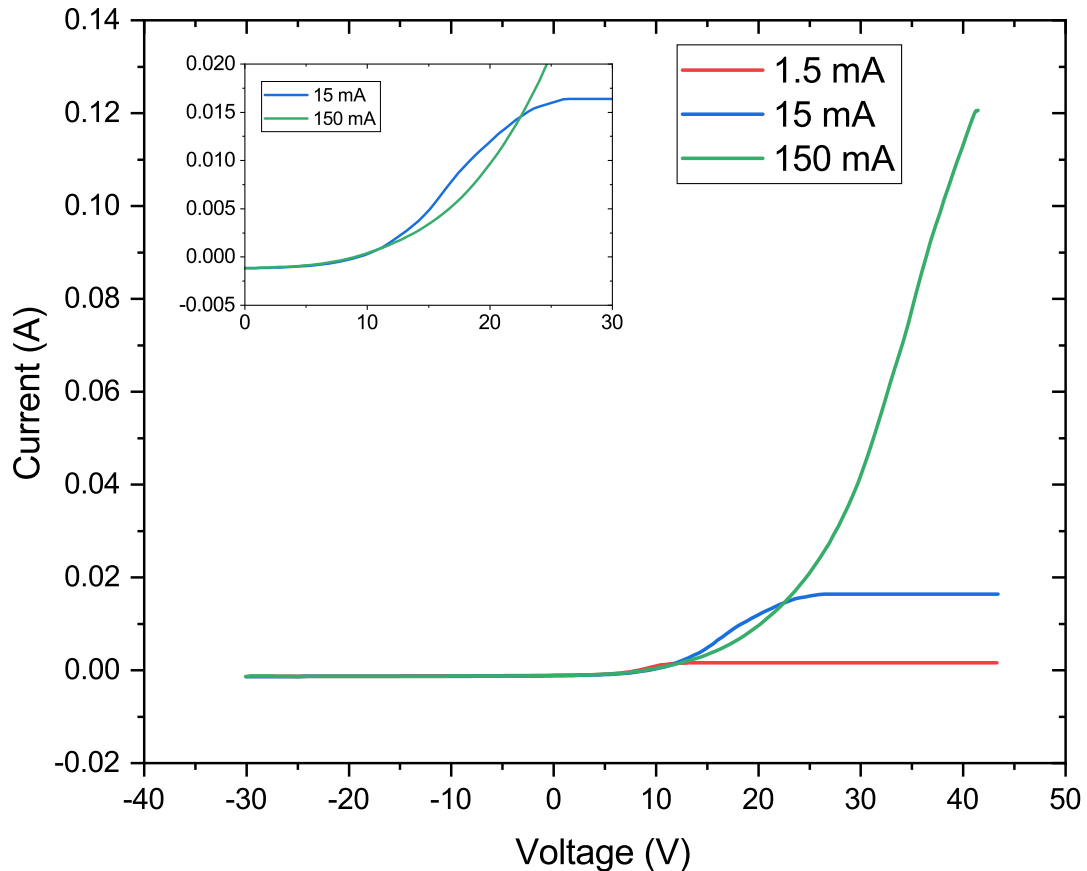
Figure 48: Example of I-V characteristics for different current ranges allowed by the software. A close up of two of the scans in the region in which they start to deviate is shown in the upper left corner.

be seen in all scans, it is most evident and problematic for those with a large current range. All scans share common features in the exponential region of the electron current, but quickly deviate after the floating potential. The lower current limited scans have a much better defined exponential region making T_e much easier to discern

and less ambiguous as the linear region of the $\ln(I) - V$ is more clear. Unfortunately, there is no way to mathematically correct the effects of plasma pulling on the scans without the measurement of $V_p - V$, so using traditional methods to find the EEDF and V_p (see the Druyvesteyn method in Section 5.1) are not feasible. Therefore, the use of the scans is limited to calculating T_e and n_e under the strict assumption of a Maxwellian EEDF and using the basic Orbital Motion Limited (OML) theory outlined in Chapter 5. While this is not ideal, the main purpose of the probe is to compare the results from the CRM to a more widely used measurement method.These scans are deemed satisfactory for this aim.

In an RF discharge, the harmonics of the RF field can cause interference in the probe scan as the probe effectively acts as an antenna. Thus, RF filtering is considered imperative for a complete and accurate measurement of the discharge EEDF [49]. However, since plasma pulling has already rendered this outcome impossible, the importance of RF filtering is minimized. As we are assuming a Maxwellian distribution and specifically intend on finding T_e and n_e, only the linearity of the semilog I-V characteristic is necessary for this analysis. Indeed, there are a number of works in which this is explored, and the reader is referred to Refs. [88, 89]. The direct effects of removing the RF filtering circuitry were negligible to the scan at large, with the only noticeable change being in the ion current region. A small oscillation can be seen at a very small scale, but for all intents and purposes this effect is averaged out when the ion saturation current region is fit linearly. This is discussed further in Chapter 8.

6.5 Nb SAMPLE SURFACE ROUGHNESS EXPERIMENT

niobium samples were produced to study the effect of surface temperature and electrode positive DC bias on the final surface roughness profile of plasma etched niobium at different locations in the reactor. The samples were water jet cut from a sheet of cavity grade Nb provided by Jefferson National Lab. Water jet cutting was used to eliminate the embedding of silicon and metal impurities from other cutting techniques. Each sample was diamond paste polished with a Dremel tool so the samples have as similar a roughness profile as possible. Diamond paste was used to avoid silicon based polishing methods. Each sample was polished with a series of pastes with decreasing coarseness down to 1 micron. Most samples were polished to this 1 micron level, while a small amount were polished to 0.1 microns for post-etch

comparison (see Chapter 9). A close up photo of a polished sample before plasma processing can be seen in Figure 49.

Figure 49: A picture of a Nb coupon sample polished to 1 micron surface roughness. A mirror-like surface can be seen, along with surface defects like pits and trenches.

These circular "coupon" type samples were made with the specific intention to be inserted into the chamber through the DN16 conflat viewports. The samples are then held suspended by a threaded rod in the back of the sample that is connected to the center of a blank DN16 flange. The length of the rod is such that the sample is flush with the chamber wall. An example of how the sample is placed in the reactor can be seen in the right hand side of Figure 47 (red arrow) and a close up of a mounted sample can be seen in 50. The substrate temperature is measured for each sample through a type k thermocouple mounted on a vacuum electronic feedthrough. Four samples were mounted for each experimental run at consistent locations corresponding to different local discharge regions of the coaxial plasma reactor. These locations are shown in Figure 51. The samples that were polished to 0.1 microns were placed in the sample 4 position in Figure 51. This was done for comparison as it is expected that samples 2 and 4 will have similar etch profiles since
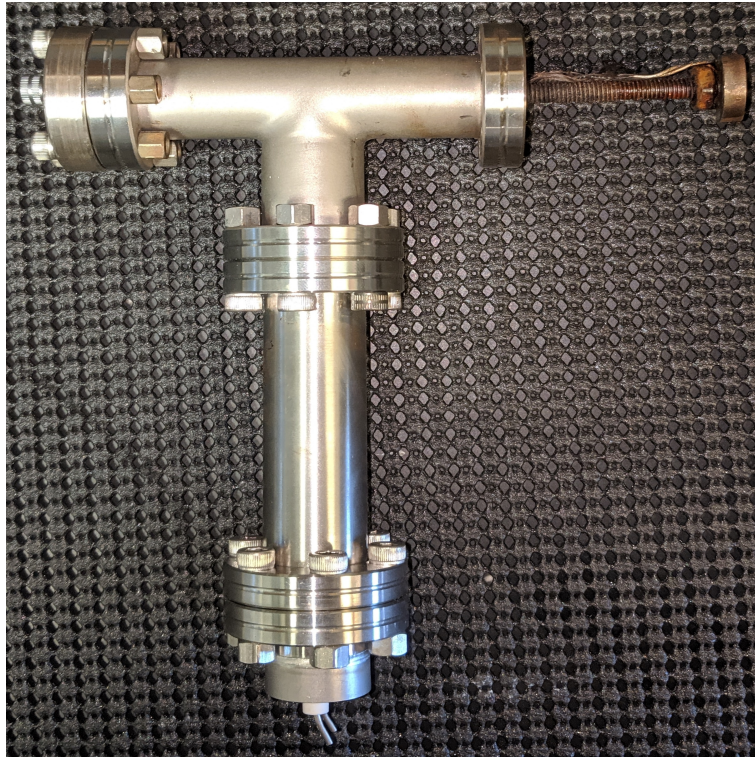
Figure 50: The sample mounting and thermocouple setup. The sample is suspended flush to the chamber wall by the threaded rod. The thermocouple is wired along the rod and compression fit against the back of the sample.

they are in symmetric locations in the chamber.

The substrate temperature was modified externally by wrapping the chamber first with conductive heating tape, and then covered with aluminum foil. The tape was wrapped tightly around the chamber with particular emphasis on even temperature distribution. The temperature of the heating tape was controlled by variac transformers through the adjustment of the output voltage to the tape. However, maintaining consistent temperatures between all four samples simultaneously in this way is difficult. The various local regions of the plasma in the chamber have significant influence on the temperature distribution, so there is little control over the 'fine tuning' of temperatures at specific locations. The variation in temperature at each sample location was monitored throughout the experiment with the highest amount of fluctuations in the first hour of the etching experiment. After the first hour, the

temperature at each location remained consistent within $\approx$ 15 º C. Each thermo-couple was tested for consistency and found to be consistent within 2 $\approx$ º C of one another, so this error was ignored. The final value used for the analysis in Chapter 9 is the average value of temperature measurements taken at consistent time intervals (typically an hour). The error in temperature is therefore the standard error of the mean, and is presented as statistical error bars in Chapter 9. The DC bias is adjusted in the usual way of adding an external positive DC voltage to the powered electrode through the RF power matching network (see Section 6.1.1).
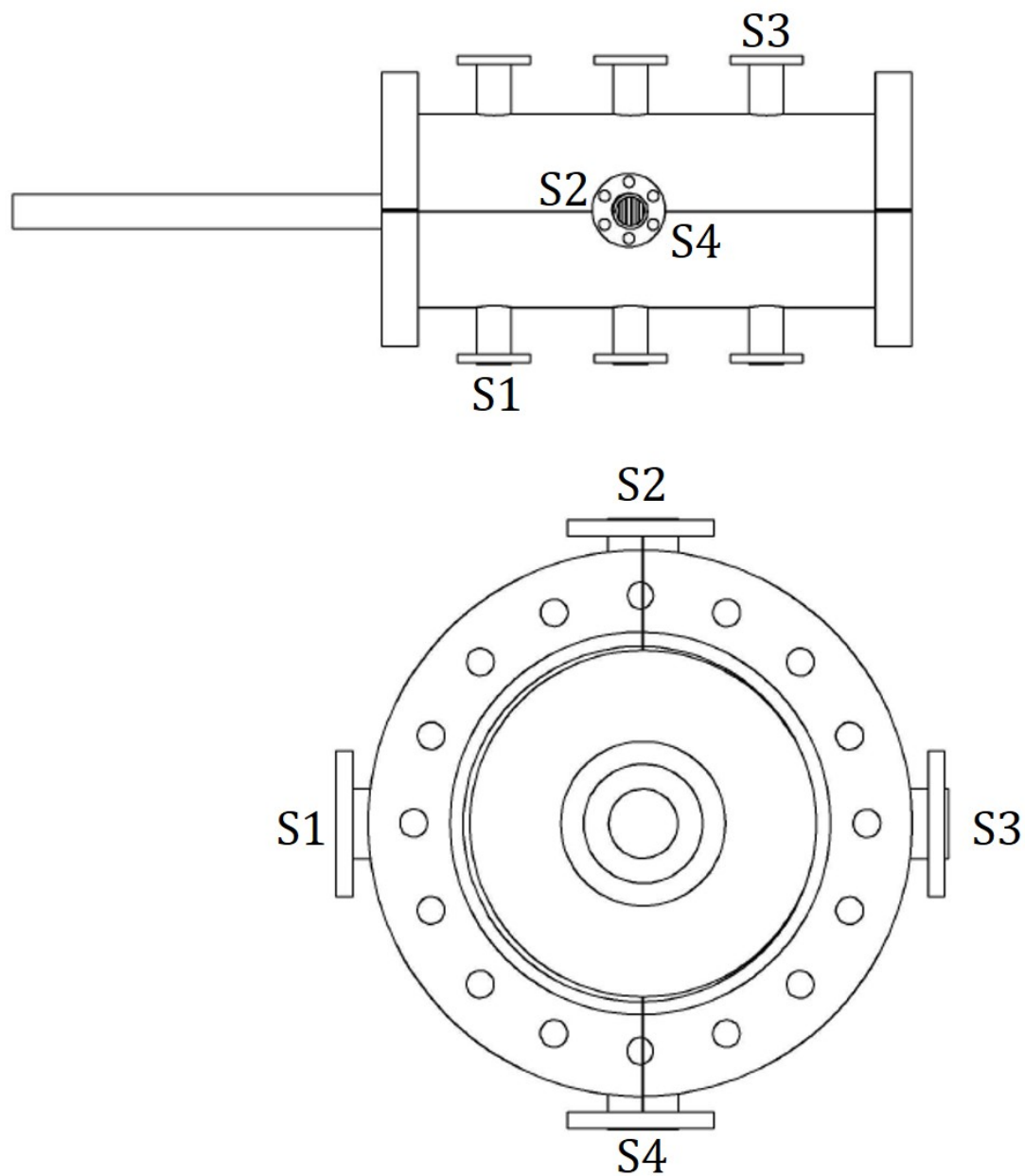
Figure 51: The sample mounting locations. Sample 1 is located at the 'rear' of the electrode. Samples 2 and 4 are located at the center of the corrugated electrode on opposite sides, and sample 3 is located at the front of the electrode. The chamber orientation was such that sample 2 is the top of the chamber and sample 4 is the bottom.

CHAPTER 7

DENSITIES OF ARGON EXCITED STATES VS. EXTERNAL PLASMA PARAMETERS

The following chapter presents results from the measurements taken by Tunable Diode Laser Absorption Spectroscopy (TDLAS) and the Branching Fraction Method (OES-BFM). In particular, the $1s_4$ and $1s_5$ levels are primarily discussed as these were measured by both methods and direct comparisons can be made. A comprehensive summary of the relationship between these densities and the plasma parameters is outlined, although not all of the data can be included for the sake of brevity. Pertinent trends, consistencies, and inconsistencies are examined for sets of data that illustrate effective points clearly and succinctly. Those data that are significantly different or particularly noteworthy are either addressed in the discussion or presented separately. Explanations of trends and phenomena are given with literature backing when available, otherwise educated speculation as to the effects of plasma parameters (ie. added DC bias voltage) is provided.

Table 5 outlines the external parameters covered in this study. These parameters are described more in depth in Chapter 2. Each external parameter was treated as a dependent variable while all other parameters were kept constant. This allows a full understanding of the effects of each of these external parameters on the measured and calculated plasma parameters. Combined effects of multiple external parameters can also be studied as data exists for each external parameter combination. The array of external parameters was empirically established in previous work for the best etching outcome, with the Nb etch rate between 60-200 nm/min for the range of these parameters in this work [6–8, 36, 38].

This chapter is organized as follows. Firstly, a comparison of the two diagnostic techniques, TDLAS and OES-BFM, are compared as they both have distinct advantages and disadvantages. This will allow a framework for which the study of the external parameters to be presented. Secondly, each external parameter will be considered separately as the effects of each on the resonant and metastable levels is studied independently. A separate description is presented for both Argon and

Table 5: The external parameters studied. The * indicates that these values are not present for all data sets due to experimental limitations.

Parameter	Value	Unit
pressure	10*, 25, 50, 75, 100*	mTorr
RF power	25, 50*, 75, 100*, 150	W
DC bias	self bias, 0, 50, 100	V
Cl_2 concentration	0, 1, 5, 10, 15*	%

Ar/Cl_2 discharges. While this chapter is set to only discuss the effects of the external parameters on the 1s densities, comments about the electron temperature, electron density, and EEDF are included when important to illuminate physical effects. Analysis of those particular plasma parameters are outlined in a later chapter. Lastly, a short discussion summarizing the important outcomes of the study as a whole is included.

7.1 TDLAS VS. OES-BFM

A significant motivation for this work is to validate the feasibility of using OES-BFM to accurately measure the Ar 1s densities in Ar and Ar/Cl_2 discharges. Based on published work there is no reason *a priori* as to why it couldn't be used in the cylindrical capacitively coupled plasma (CCP) discharge, but as this system is distinctly unique, and since there are no published works to directly compare, the OES-BFM results must be compared to a more accurate method of measurement. Therefore the densities evaluated from OES-BFM are compared to those measured from TDLAS. Since TDLAS has the distinct disadvantage of only being able to measure one transition at a time, and the need for a laser that can be tuned to particular wavelengths, only certain densities could be compared. However, the closeness of the 810.37 nm and 811.53 nm lines allow for a measurement of both the Ar $1s_4$ and $1s_5$ densities with the same tunable laser. OES-BFM has the advantage of being able to calculate all four lower level densities simultaneously by using an array of measured spectral lines from a low resolution, high speed spectrometer.

In general, a direct comparison of densities measured using TDLAS and OES-BFM shows consistency within a factor of eight, with the largest discrepancy stemming from the measurements conducted at lower pressures, most prominently those at 10 mTorr. At 25 mTorr and above, TDLAS and OES-BFM are consistent within a factor of three for all measured parameters, with a vast majority of those results well within a factor of two. Published work outlining OES-BFM in comparison to TDLAS or other experimentally measured results show consistency usually within a factor of two [58, 59]. Indeed, Li *et al.* has shown significant improvement of OES-BFM results with the use of a mono-directional escape factor instead of the volume averaged escape factor commonly associated with this method [61]. While this is a promising modification to the method, we have elected to remain consistent to the original technique and explore the use of a mono-directional escape factor in future work. As it stands, the results are sufficiently consistent to make significant qualitative observations, as both sets of measurements vary similarly as a function of external parameters. This is particularly true for results pertaining to the Ar $1s_5$ densities as they are more consistent than the $1s_4$ densities as a whole. These observations are pointed out throughout the analysis to provide an argument of OES-BFM as a reliable diagnostic technique.

While OES-BFM is a fast and convenient method, it has a number of limitations that are being discovered as attempts are made to extend this technique to different types of systems, particularly in mixed Ar discharges. It was the goal of this work to use OES-BFM in Ar/Cl_2 discharges, but there was little to no success. The limitations and proposed reasons why this technique is not effective in Ar/Cl_2 discharges is discussed in the next subsection.

7.2 LIMITATIONS OF OES-BFM

In principle, OES-BFM should work as long as there are enough metastable atoms to produce measurable changes in the effective branching fraction (for more information on the effective branching fraction, see Ref. [11]). With that being said, the method can fail if there are not enough metastables in the discharge or if the changes in the branching fractions due to reabsorption cannot be measured. In the case of this work, there is most likely a combination of both of these problems. Metastable level densities measured using TDLAS show a drop of upwards of two orders of magnitude when Cl_2 is added to the discharge, depending on the concentration. This

is not unexpected as the addition of another species, especially one that creates an electronegative discharge, would reduce the energy and collisions required to populate Ar metastables. In addition, the quenching rate of Ar metastables due to Cl_2 is rather high at $71 \times 10^{-17} m^3/s$ [90]. For context, this is about twenty times higher than N_2 and three times higher than O_2, two other common plasma discharge additives [90]. Wang *et al.* has shown that OES-BFM can be effective in a 15 mTorr Ar/O_2 inductively coupled plasma (ICP) discharge in concentrations up to 50% [77]. For our case, the partial pressure of Cl_2 in our discharge is comparable to Wang's for many of our measurements, particularly those that are closest to previously established etching conditions (15% Cl_2 at > 50mTorr). The combination of high partial pressures and the metastable-Cl_2 quenching rate makes OES-BFM a difficult measurement technique for the Ar/Cl_2 discharge. At those conditions in which the partial pressure was very small (1% concentration of Cl_2) OES-BFM managed to produce some reasonable results, but not enough to make clear conclusions.

The necessity of having enough metastable atoms to modify the effective branching fraction naturally leads to an investigation of the lower limit of the density in which OES-BFM can be useful. This is not easy to estimate, but the limitations can be illuminated by considering the form of the photon escape factors for the transitions used in the analysis. A plot of the photon escape factor for a number of spectral lines used in the analysis is shown in Figure 52.

Figure 52 shows that below 10^{16} m^{-3} the change in the photon escape factor for transitions involving the Ar $1s_5$ metastable level is quite small compared to the other transitions. Below 10^{15} m^{-3} the photon escape factor is approximately 1 for all transitions. In addition, it is pertinent to point out that for the conditions of this discharge the Ar $1s_5$ density is consistently the highest of the four 1s levels, sometimes by almost an order of magnitude. Therefore even if the Ar $1s_5$ density is in the low to mid 10^{16} m^{-3} the other densities may be so much lower that OES-BFM cannot properly work. The combination of these two issues nicely explains the reason why realistic results for Ar/Cl_2 discharges were seemingly unattainable.

7.3 GAS TEMPERATURE

The gas temperature is a necessary quantity for OES-BFM, and it was measured for the array of external parameters outlined in the beginning of the chapter. Overall,
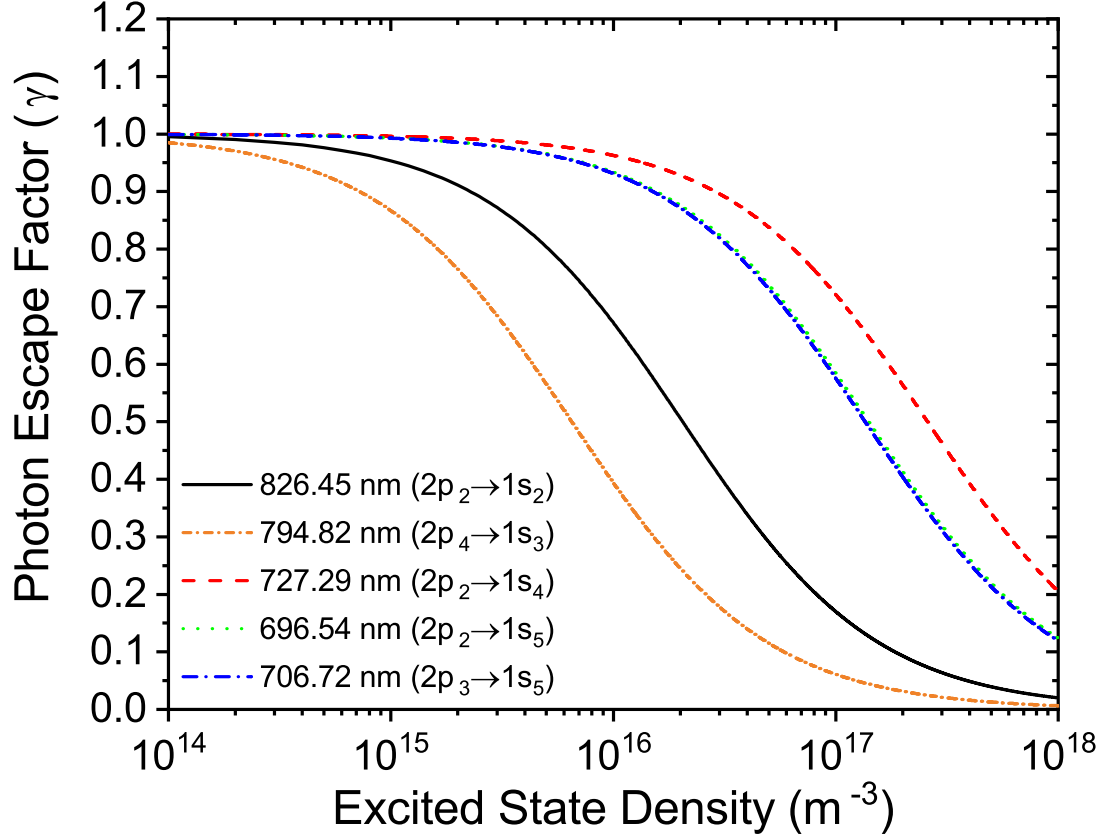
Figure 52: Calculated photon escape factors using Eq. (63) as a function of Ar 1s population density.

the gas temperature did not vary significantly as a function of the external parameters. In a pure Ar discharge the gas temperature is consistently in the 370-420 K range with only a few instances of T_g dropping below 370 K. The average gas temperature for the Ar discharge across all external parameters is 391 ($\pm$ 15) K, which was rounded up to 400 K for all calculations presented here. This value for T_g is lower than the temperature in analogous works, but those experimental configurations use inductively coupled plasmas in a much smaller configuration [57, 58, 82]. Sushkov *et al.* [59] conducted similar OES-BFM/TDLAS measurements in a parallel plate CCP and measured T_g in the range of 320-410 K, which closely matches the T_g range of this work and has the most similar experimental conditions [59].

The Ar/Cl$_2$ discharge has a larger range of measured values, but in general T_g remained between 350-450 K. Once again, for ease of use in the OES-BFM data

analysis program the gas temperature was approximated to 400 K since the average T_g across all external parameters is 423 ($\pm$ 24) K. The gas temperature has been measured previously for Cl_2 containing plasmas and typically show an increase in T_g as the RF power is increased [91]. However, this is once again an ICP reactor with much higher RF power upper limits, so we are confident that the values found for T_g in this work are appropriate.

7.4 RESULTS AND DISCUSSION

We present the $1s_4$ and $1s_5$ excited state densities of Ar in both Ar and Ar/Cl_2 discharges as a function of external parameters. As stated in Chapter 4, the range of external parameters is defined based on empirical results of previous etching experiments. Statistical error bars are included on all presented plots, however the error is oftentimes smaller than the plot symbol size. The $1s_2$ and $1s_3$ densities are not presented in the following section, but on average we have seen $n_{1s4} \approx 3n_{1s2}$ and $n_{1s5} \approx 6n_{1s3}$. Due to the limitations outlined in Section 7.2, all presented results involving Ar/Cl_2 discharges were measured using TDLAS.

7.4.1 PRESSURE

Ar Discharge

The effects of increasing pressure on the $1s_4$ and $1s_5$ levels is well established in literature, particularly for rf ICPs in pure Ar [57, 58, 82, 92]. In general, there is an initial increase in both density populations as pressure is increased, with an eventual plateau and decrease as pressure is increased further. This effect can be explained in terms of the dominant creation and loss mechanisms of the excited levels in the discharge. At lower pressures the metastable atoms are primarily lost to diffusive and collisional losses to the resonant levels, while the resonant density is mainly lost to radiative decay to the ground state. An increase in pressure facilitates an increase in the electron density, which leads to an increase in excited state density as more electron-atom excitation collisions take place. Eventually, the electron density reaches a point where decay from electron-atom collisions (of excited atoms) becomes significant enough to lead to a total decrease in the population density. While the effect can be seen for both populations, the $1s_4$ density typically shows the eventual decrease at a higher pressure due to the effects of radiation trapping. Since the only

radiative decay channel for resonant level atoms is to the ground state, the VUV (Vacuum Ultraviolet) light that is emitted for this transition is reabsorbed by ground state atoms, repopulating the resonant levels. The amount of ground state atoms increases with pressure, but eventually this radiation trapping reaches a saturation point, and the previously outlined quenching mechanisms take over [58].
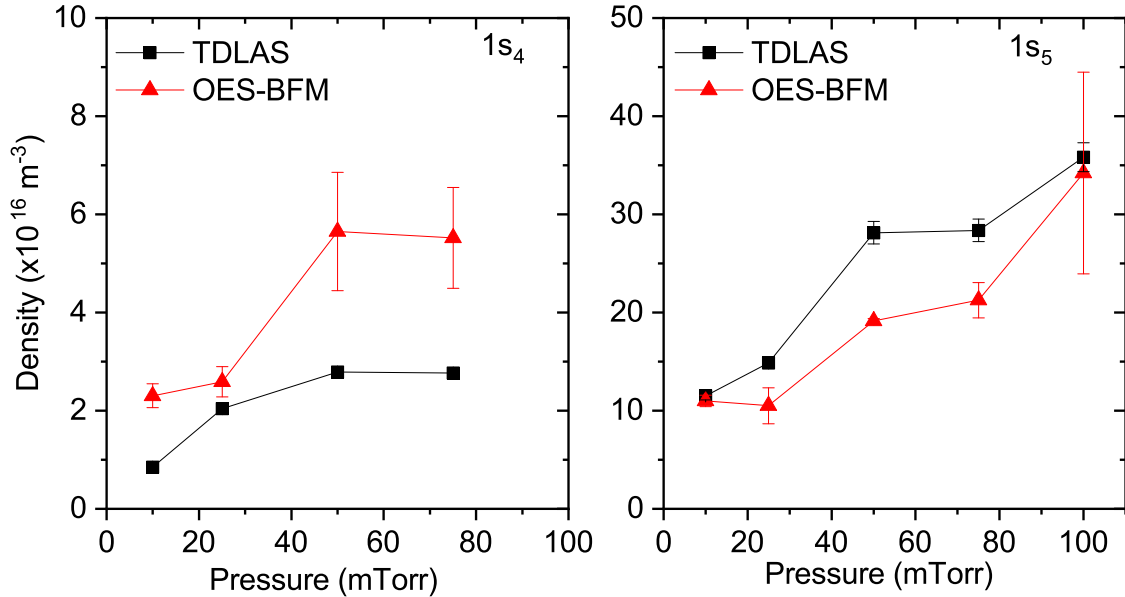
Figure 53: Density of Ar $1s_4$ and $1s_5$ states vs. pressure at 150 W and with no added bias. Solid lines are visual guidelines.

Results from TDLAS and OES-BFM in pure Ar, as shown in Figure 53, show the expected behavior as the discharge pressure is increased. Both measurement techniques show an increase in the $1s_4$ and $1s_5$ densities as a function of pressure up to 75 mTorr and begins to saturate. The $1s_5$ density shows a further increase beyond 75 mTorr. It is important to point out the differences in pressure ranges between this work and that of the known literature. Since most of the cited work operate in an ICP configuration, the pressure ranges are much lower, typically up to 25 mTorr to observe the full effect [11, 57, 58, 92]. However, the work done by Sushkov *et al.* in a parallel plate CCP has very similar experimental conditions [59]. Sushkov shows similar effects at comparable pressures to our work, with an extension that shows the decrease in both the $1s_4$ and $1s_5$ densities after 75-100 mTorr, the upper pressure limit of this work.

Ar/Cl$_2$ Discharge

The relationship between the Ar 1s$_5$ density and Cl$_2$ concentration is shown for different RF powers in Figure 54 as obtained by TDLAS measurements. An increase in concentration accelerates the expected trend of the initial rise, then fall of the density as pressure is increased. This is most evident in the comparison between the 1% and 10% concentrations, as the 1% shows a very similar result as the pure Ar discharge, while the 10% shows a maximum at 25 mTorr, and a decrease as pressure is increased. The results for 25 W power show a much more pronounced fall as pressure is increased past 25 mTorr. This could be due to an increase in the electron density as power is increased, leading to more electron-atom collisions that could sustain the production of metastables.
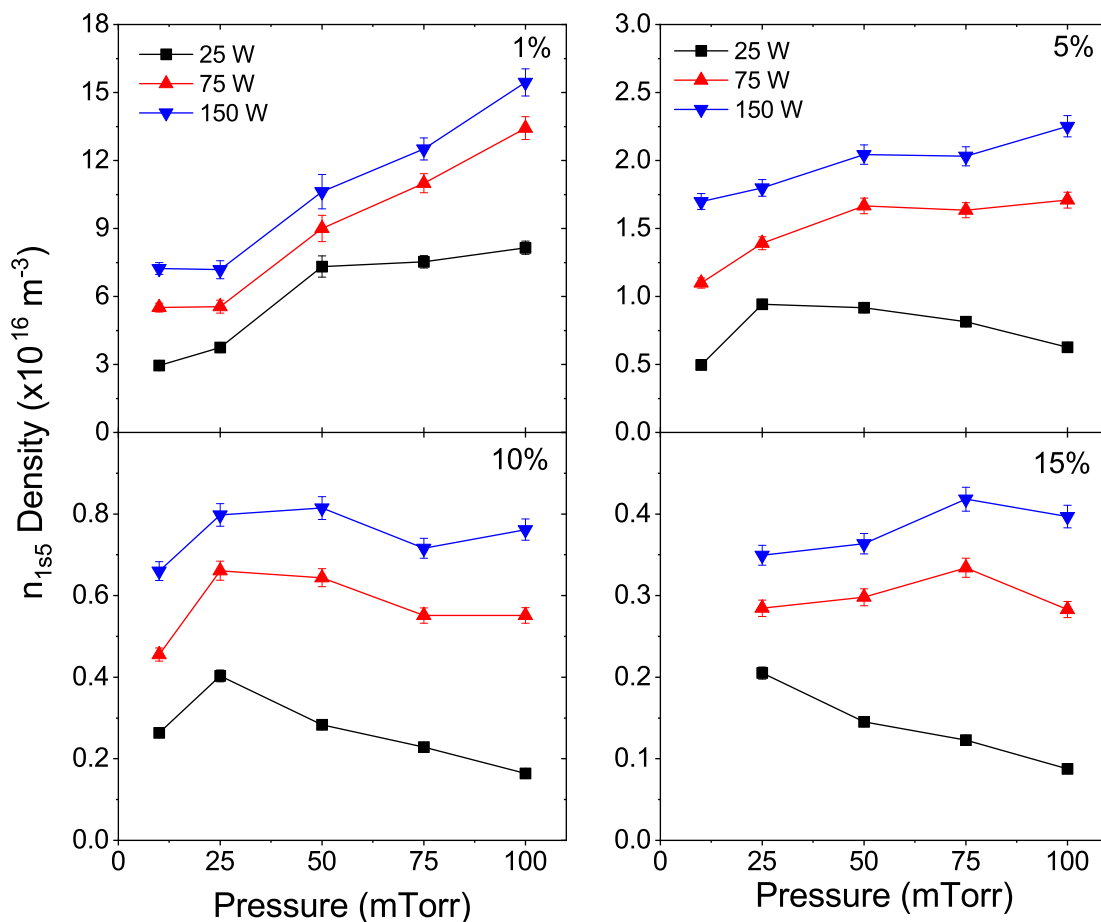
Figure 54: Ar 1s$_5$ density measured by TDLAS vs. pressure for different concentrations of Cl$_2$ in Ar with no added bias. Solid lines are visual guidelines.

7.4.2 RF POWER

Ar Discharge

An increase in RF power while the pressure remains constant serves to increase the plasma density [11]. While the plasma density, and therefore the electron density, is expected to increase, the electron temperature T_e is expected to remain roughly constant as the mean free path of the species in the plasma remains the same. This increase in plasma density facilitates an increase in the resonant level densities through electron-atom collisions from the ground state, and electron-atom collisions of the metastable levels, forcing a population transfer into the resonant levels. An increase in the metastable level density as a function of power can be expected for many of the same reasons, although to a much lesser extent. There is evidence of an increase of the $1s_5$ metastable level with power in the literature, but there are also cases where the density remains constant [11, 57, 59, 82]. The most analogous literature source to this work, Sushkov, shows an increase and then leveling off of the $1s_5$ and $1s_4$ densities, although the trend for the metastable level is much less pronounced [59].

In general, the $1s_4$ density increases with power at a constant pressure, while the $1s_5$ density typically initially increases, then decreases. This is particularly true at lower pressures where the effects of increased pressure, as outlined in the previous subsection, are not as prominent. Figure 55 shows the effect of increasing power on the $1s_4$ and $1s_5$ densities at 50 mTorr for both TDLAS and OES-BFM measurement techniques. There is very little change in the $1s_4$ and $1s_5$ densities as a function of rf power. The changes in the densities are not expected to be large, and the small range of studied powers does not allow for a highly detailed study.

Ar/Cl$_2$ Discharge

The addition of Cl_2 in the discharge is expected to show an increase in Ar metastable level density as RF power is increased [93]. When the RF power is increased the plasma density, and therefore the electron density, will increase, but not necessarily the negative ion density [93]. Low energy electrons are lost to negative ion formation in an Ar/Cl_2 discharge, while the electron density increases with power. The increase in electron density facilitates high energy electron collisions with ground state atoms to produce Ar metastables, while the decrease in low energy electrons reduces the amount of metastables that are lost to low energy electron mixing [92].
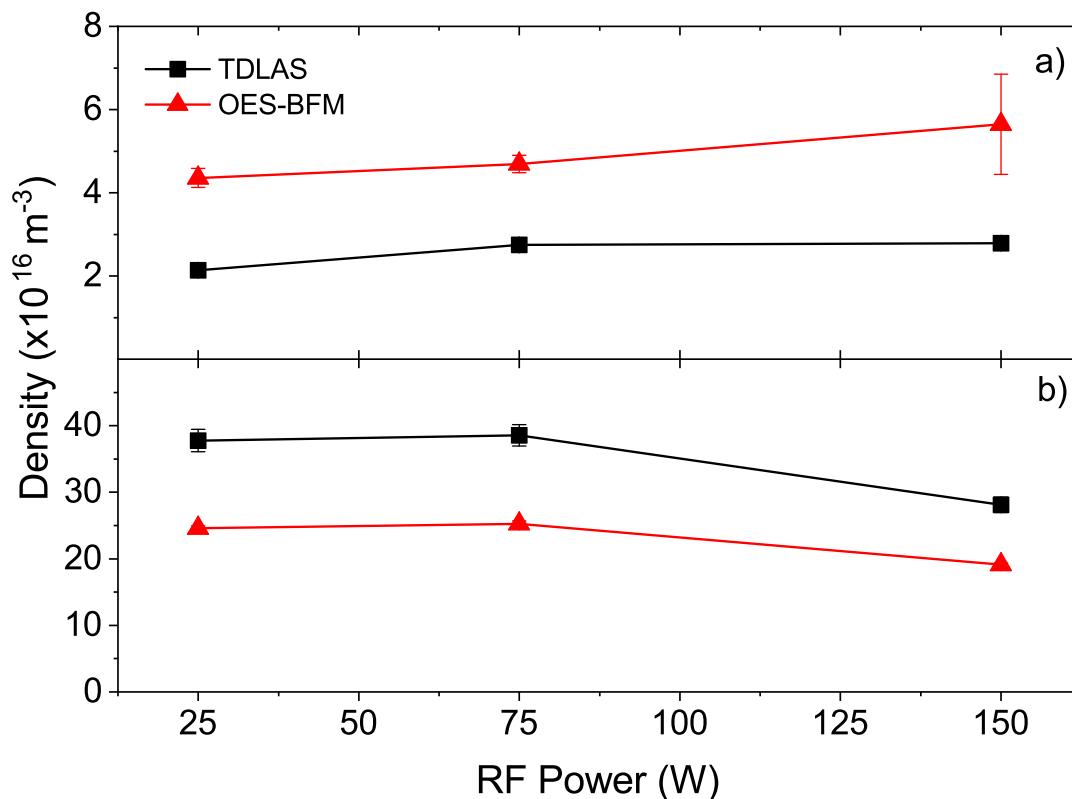
Figure 55: Density of Ar a) $1s_4$ and b) $1s_5$ densities vs. RF power measured with TDLAS and OES-BFM at 50 mTorr with no added bias. Solid lines are visual guidelines.

Indeed there is a general increase in Ar metastable density as RF power is increased for discharges without added DC bias as shown in Figure 56. The concentration of Cl_2 added to the discharge does not have a direct effect on the increasing trend of density with power, but it is important to keep in mind that the increase in concentration causes a drastic decrease in Ar 1s state population in general. As the Cl_2 concentration is increased the electron density will decrease to maintain quasineutrality. Increasing the concentration will also cause more low energy electrons to be lost to the creation of negative ions, although this will once again not increase as power is increased. Although data for only one pressure is shown here, the trend is consistent across the pressure range studied, with higher pressures typically having higher densities.
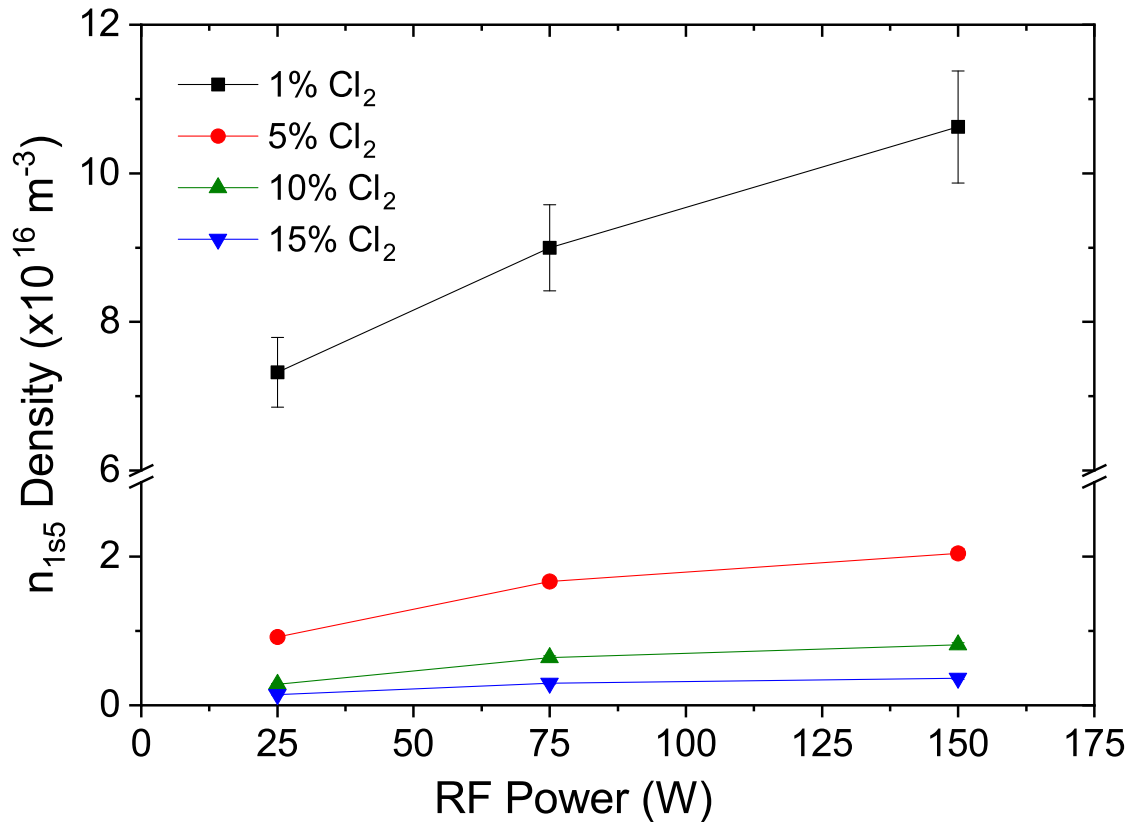
Figure 56: Ar $1s_5$ density measured by TDLAS vs. RF power for different concentrations of Cl_2 in an Ar/Cl_2 discharge at 50 mTorr with no added bias. Solid lines are visual guidelines.

7.4.3 DC BIAS

The negative dc self bias that forms on the powered electrode due to the blocking capacitor in the RF power circuit leads to a larger potential drop between the plasma bulk and the powered electrode across the corresponding sheath. In semiconductor processing, this can be an advantage as the substrate can be placed on the powered electrode to take advantage of the high ion acceleration energy. In our case however, the goal is to etch a large grounded outer surface. This is not possible without the use of a positive DC bias on the powered electrode due to the asymmetric discharge configuration [7]. The positive DC bias essentially serves to flip the discharge asymmetry that causes a larger voltage drop between the plasma bulk and the smaller

powered electrode, thus making the larger grounded electrode the surface with the largest voltage drop. This leads to larger ion energy and ion flux into the grounded surface and provides the physical energy component of IARIE. Further explanations of the effect of positive DC biasing on etching mechanisms and results can be found in previous work [7, 8, 36].

The effect of DC biasing on rf CCP etching reactors has been studied by a number of research groups, both experimentally and with particle-in-cell simulations [39–41, 94–96]. However, a majority of this work was done to study the addition of a *negative* added bias on either the powered or grounded electrodes, rather than a *positively* added bias. While these works are useful for gaining a general understanding of the effects of DC bias on the discharge, the complete picture for the purposes of SRF cavity etching remains incomplete. Understanding the relationship between the Ar 1s states, and later T_e and n_e, and total positive DC bias will provide better insight into the effect of DC bias on the plasma dynamics.

Ar Discharge

The effects of DC bias on the $1s_5$ densities can be seen in Figure 57. The introduction of a positive DC bias causes a decrease in the $1s_5$ density, with a larger drop as the pressure is increased. For most cases, increasing the bias has no significant effect on the density, with the exception being when the pressure is higher. Although an increase in $1s_5$ density with DC bias is seen for 100 mTorr, the overall increase is rather small. A subtle drop in density can been seen for 75 W and 150 W, particularly for the higher pressures, but the effect is essentially within statistical error.

A comparison of TDLAS and OES-BFM for the $1s_4$ densities (not shown) show similar trends as seen in Figure 57, and results from OES-BFM show an overall drop in density as positive DC bias is introduced for each 1s density (including the $1s_2$ and the $1s_3$ densities). Both measurement techniques show essentially the same trends, including the increase in density with DC bias at higher pressure.

The decrease in the 1s densities as positive bias is introduced could be due to an increase in ionization of these states and a total increase in the plasma density. Indeed, there are multiple studies that show an increase in ion/electron density as bias becomes more positive [95, 96]. As the powered electrode becomes positively biased the electron current increases through this surface with an increased energy.
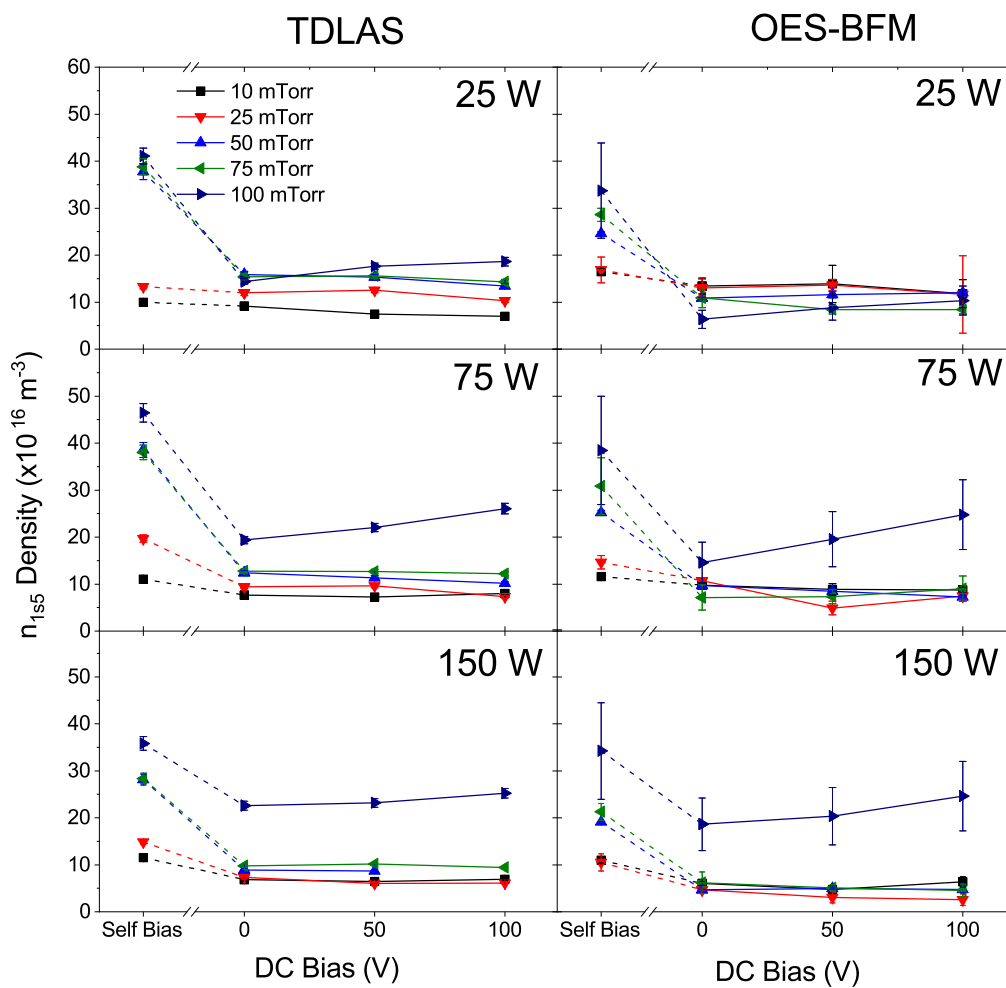
Figure 57: Ar $1s_5$ density vs. DC bias for 25, 75, 150 W power measured with TDLAS and OES-BFM. The dashed lines indicate the negative bias region outlined in Section 7.4.3.

This effect was recorded by measuring the current through the dc power supply that provides the positive bias. These electrons then cause high energy secondary electron emission from the powered electrode that can effectively ionize neutral atoms in the discharge. In addition, the larger electric fields in the rf sheath and the bulk result in more forced ionization processes [96]. Total positive DC biases serve to increase the plasma volume inside the discharge chamber, while total negative biases restrict the discharge to the smaller region between the two electrodes [96]. The positive bias effectively "pushes" the discharge throughout the chamber as the entire grounded surface (with a much larger surface area) becomes the most attractive surface for ions in the discharge, and the powered electrode becomes the least. This expansion of plasma volume is confirmed qualitatively by observation of the discharge as positive bias is added. In addition, a measured increase in electron current as positive DC bias is introduced and then increased means that an equal ion current must be flowing through the grounded surface due to conservation of current.

Ar/Cl$_2$ Discharge

In general, the behavior of the Ar 1s$_5$ density as a function of bias in Ar/Cl$_2$ discharges is similar to the relationship outlined in a pure Ar discharge. This is particularly interesting because of the large difference in the densities as the addition of Cl$_2$ reduces the density by two to three orders of magnitude. However, the relationship between density and DC bias changes as other external parameters, most particularly pressure and power, are varied.

Figure 58 shows the relative Ar 1s$_5$ density as a function of DC bias for 25 mTorr and 100 mTorr. The trends for the 25 mTorr set show very similar behavior as in pure Ar as the density drops when positive bias is introduced, and remains relatively constant as the bias is increased. For higher pressures. however, it seems that the increase in bias does much less to decrease the density, particularly for higher powers. In addition, the increase in bias also has an effect in increasing the Ar 1s$_5$ density, even to the point in which it surpasses the value for self bias. No explicit explanation for this behavior can be offered at this time, but forthcoming analysis of the electron temperature, electron density, and EEDF will serve to help provide answers.

7.4.4 CL$_2$ CONCENTRATION

The addition of Cl$_2$ in an Ar discharge adds a great deal of complexity to the
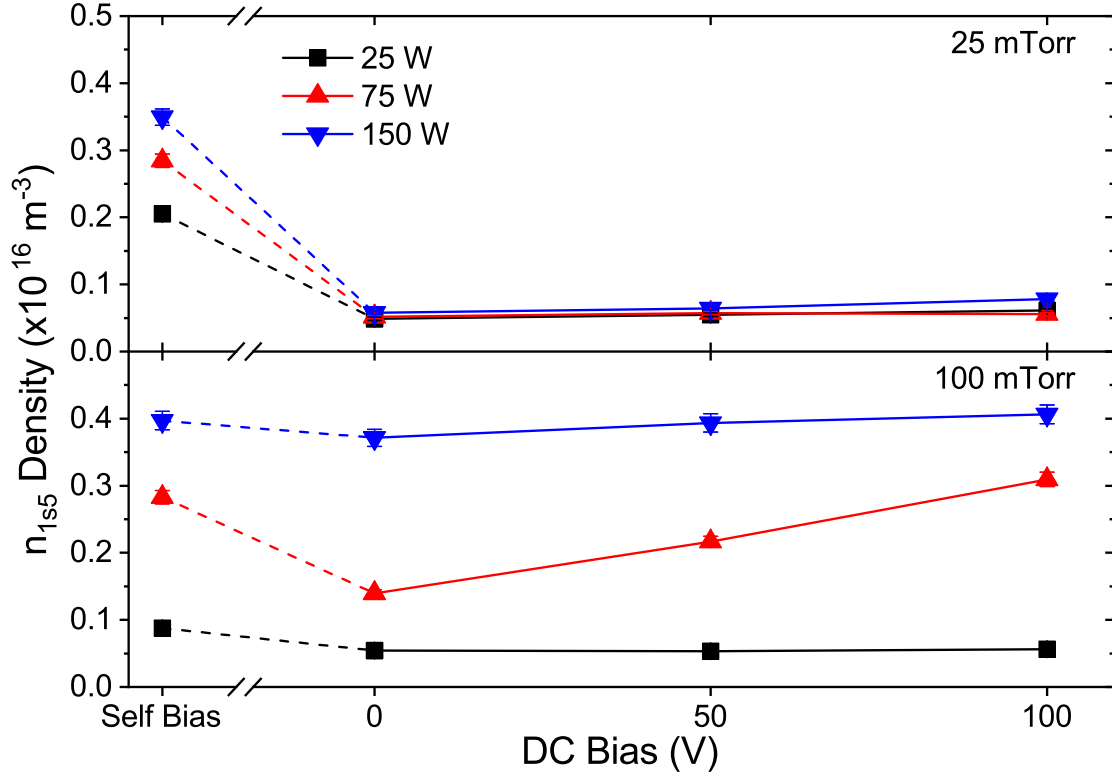
Figure 58: Ar $1s_5$ density measured by TDLAS vs. DC bias for 15% Cl_2 in an Ar/Cl_2 discharge. The dashed lines indicate the negative bias region outlined in Sec. 7.4.3. Solid/dashed lines are visual guidelines.

kinetics and charge particle balance of the plasma. An Ar/Cl_2 plasma is electronegative, which means there is an additional negatively charged species, namely negative Cl ions in this case, in the discharge. However, the quasineutrality condition does not change and the total amount of positive and negative species in the discharge (macroscopically) must be equal. With an additional negative species in the discharge, the amount of electrons will naturally decrease, and therefore the amount of electronic collisions will decrease. In addition, there are a number of new electronic excitation channels involving Cl_2, such as molecular and atomic ionization, dissociative attachment (Cl^- formation) and dissociation (molecular splitting) [54]. As previously mentioned in Section 7.2, the Cl collisional quenching rate of Ar metastable and resonant level densities is quite high compared to other commonly used molecular gases in discharges [90]. With all of these new processes in mind, it should not be surprising that the Ar $1s_4$ and $1s_5$ densities are expected to decrease as Cl_2 is added
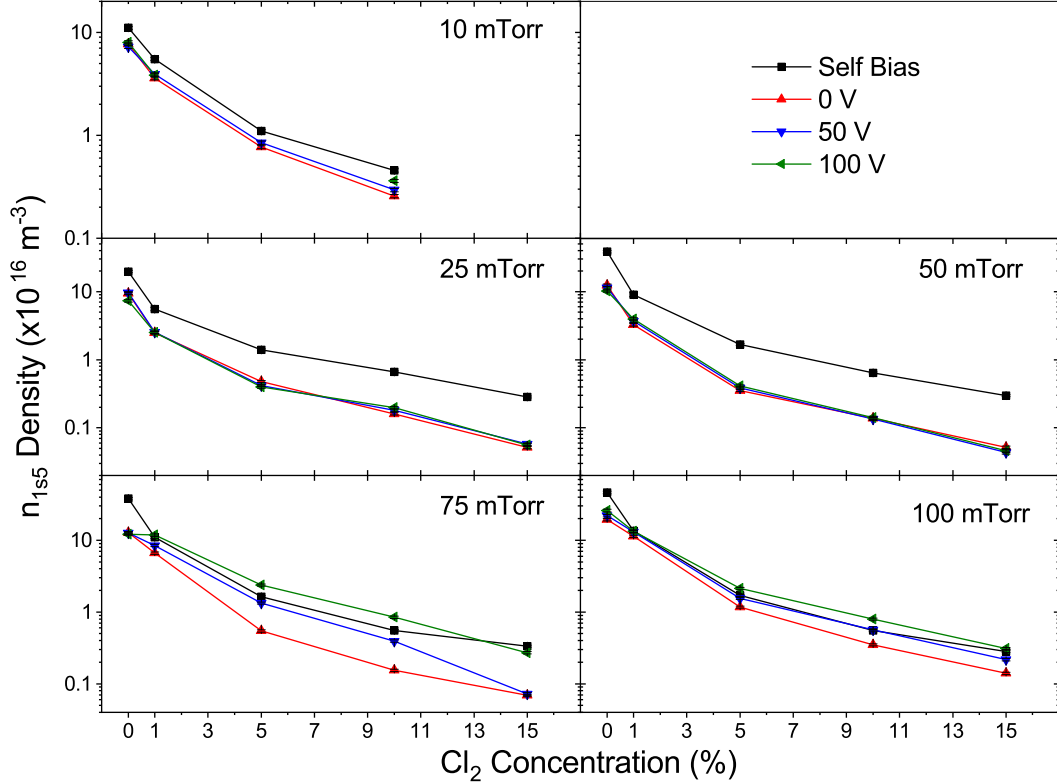
Figure 59: Ar 1s$_5$ density measured by TDLAS vs. Cl$_2$ concentration at 75 W. Solid lines are visual guidelines.

to the discharge. Indeed, there are a number of sources that have shown theoretically and experimentally that this is the case for different types of discharges [54, 92, 97]. While the general effect of Cl$_2$ concentration on the Ar 1s densities is known, the experimental confirmation between this work and outside sources is important. It is also pertinent to study the effects of Cl$_2$ concentration as it pertains to the other external parameters, particularly DC bias, for etching experiments.

The effect of increasing Cl$_2$ concentration on the Ar 1s$_5$ density for different pressures is shown in Figure 59. In all cases, just a 1% concentration of Cl$_2$ significantly decreases the Ar metastable density, with an eventual leveling off as the concentration is increased. This relationship matches very closely to previously published work involving the study of Ar metastable density and Cl$_2$ concentration, as well as relationships established with other molecular gases [60, 97]. The comparison to the work done by Scheller *et. al.* is quite intriguing, with the data trend being almost

identical [97]. However, Scheller does show an initial increase in Ar metastable density at very low concentrations of Cl_2 in Ar [97]. This increase was not seen for any of the measurements made in this work, but this is most likely due to experimental limitations as very low Cl_2 concentrations ($<1\%$) are required. Scheller explains that the initial increase in metastables at low Cl_2 concentrations is due to a decrease in metastable relaxation as low energy electrons are consumed by attachment processes of Cl_2 [97]. As the concentration increases, the collisional quenching processes quickly become dominant and the Ar $1s_5$ density decreases accordingly.

The amount of Ar metastables that are lost when Cl_2 is added is significant, with a typical drop of two orders of magnitude as the concentration is increased from 0% to 15%. This large drop in Ar metastable density as measured by TDLAS gives additional credence to the limitations of OES-BFM outlined in Sec. 7.2. Typical values of the Ar metastable density at concentrations above 5% are in the $10^{14} - 10^{16}$ m^{-3} range, with the larger values attributed to the self bias results.

7.4.5 CONCLUSIONS

Among the external parameters studied in this work, the external DC bias is arguably the most important as it is directly related to the effectiveness of the etching of niobium and SRF cavities. In many cases, a negative external bias is added to either electrode to increase the ion energy into that surface and to assist in etching. As the desired surface to be etched is the inside surface of a grounded cylinder, a positive DC bias is added to the powered electrode to flip the natural asymmetry caused by the unequal surface areas and force ions into the grounded surface. When positive DC bias is added to the powered electrode, the density of all 1s states drops significantly, but does not necessarily continue to change as bias is increased. Studies conducted on the effect of DC bias have shown that the plasma density increases as the DC bias on the powered electrode becomes more positive [40, 41, 95, 96]. A drop in Ar 1s densities as the plasma density increases is indicative of increased ionization of the 1s states and the 2p states that populate them.

Two different non-invasive spectroscopy techniques were used to measure the density of the first four excited states of Ar in a coaxial cylindrical rf CCP designed for the plasma processing of SRF cavities. These excited state densities were measured for both Ar and Ar/Cl_2 mixtures of varying concentrations as the Ar/Cl_2 mixture is necessary for etching of these cavities. The two measurement techniques, TDLAS

and OES-BFM, were conducted in tandem as pertinent external parameters were varied to develop a working model to describe this particular discharge. While TD-LAS is a much more accurate measurement technique, it requires the use of a tunable diode laser. In addition, TDLAS can only measure one density at a time as it requires the laser to be tuned to a specific atomic transition. OES-BFM has gained popularity since its introduction by Schulze and further implementation by Boffard [57, 58]. This optical method is advantageous due to its ability to measure all four Ar 1s state densities simultaneously using inexpensive low-resolution spectroscopy systems. Similar to the TDLAS method, OES-BFM avoids any requirement that knowledge of the EEDF must be known *a priori* as the method does not require the use of any collisional cross sections. However, this method is not nearly as accurate as TDLAS and the use of a low-resolution spectrometer in favor of speed can be a detriment when using a variety of strong and weak lines in the analysis. In addition, OES-BFM is limited in its ability to measure these densities for multi-gas discharges, especially when Cl_2 is involved, due to much lower excited state densities and much higher photon escape factors.

As a direct comparison, TDLAS is much more effective than OES-BFM at measuring the excited state density with accuracy and consistency. The results of this work show agreement between the two methods up to a factor of three for the vast majority of the external parameters studied, which is consistent with other studies [58–61]. At a minimum, OES-BFM is effective in modeling qualitative relationships between the excited state density and the external parameters, especially in regards to pressure and DC bias. This can be quite useful to gain a quick yet effective understanding of a discharge.

CHAPTER 8

EFFECTS OF EXTERNAL PARAMETERS ON THE

ELECTRON DISTRIBUTION

The study presented in the previous chapter outlined some very useful techniques to gain a better understanding of a low temperature discharge, but the full description is far from complete. Explicit information regarding the EEDF, particularly T_e and n_e, provide direct connections between the plasma parameters and the etching mechanisms. The electron temperature and density are related to both the physical and chemical etching components of IARIE as electrons are responsible for the vast majority of excitation and ionization processes. This information can be attained in a number of ways, but is commonly found through Collisional Radiative Models (CRMs) and electrical Langmuir Probes. Both of these methods are employed in this work, and the details of which are described in Sections 5.1, 6.4, and 5.3. Presented here are the results of applying those methods utilizing the results and observations from the spectroscopy diagnostics in the previous chapter. Results are presented first for pure Argon discharges, with a shorter section dedicated to Ar/Cl_2 discharges at the end of the chapter. Due to the experimental limitations of the OES-BFM technique, its direct application to Ar/Cl_2 discharges was not possible, and therefore similar limitations exist for the application of the CRM. Thus, the results for Ar/Cl_2 are incomplete and still require further work.

8.1 T_e AND n_e MEASUREMENT AND CALCULATION SOURCES

As outlined in Chapter 5, there are a number of different ways to measure the electron temperature and density. Furthermore, the use of Eq. (83) (Section 5.3) allows for an alternate calculation method in which measurements from multiple sources can be used in conjunction. This is particularly useful because the 1s state densities measured from TDLAS can be used in Eq. (83) to calculate n_e by using T_e measured from the CRM and Langmuir Probe (LP), allowing for direct comparisons of consistency between measurement channels. The CRM and LP can be used to calculate both T_e and n_e, although the LP can only do so in the case where there is

no added bias due to the limitations outlined in Section 6.4. The combinations for calculating n_e using Eq. (83) are presented in Table 6.

Table 6: The parameter combinations for calculating n_e using Eq. (83). N_R refers to the ratio of $1s_5/1s_4$. The LP results can only be used for discharge conditions without added DC bias.

Combined Methods for n_e	
N_R	T_e
OES-BFM	CRM
TDLAS	CRM
TDLAS	LP

8.2 LANGMUIR PROBE RESULTS

The Langmuir Probe scans were analyzed using the simple Orbital Motion Limited theoretical treatment presented in Section 5.1. An example of a typical Langmuir Probe scan is shown in Figure 60.
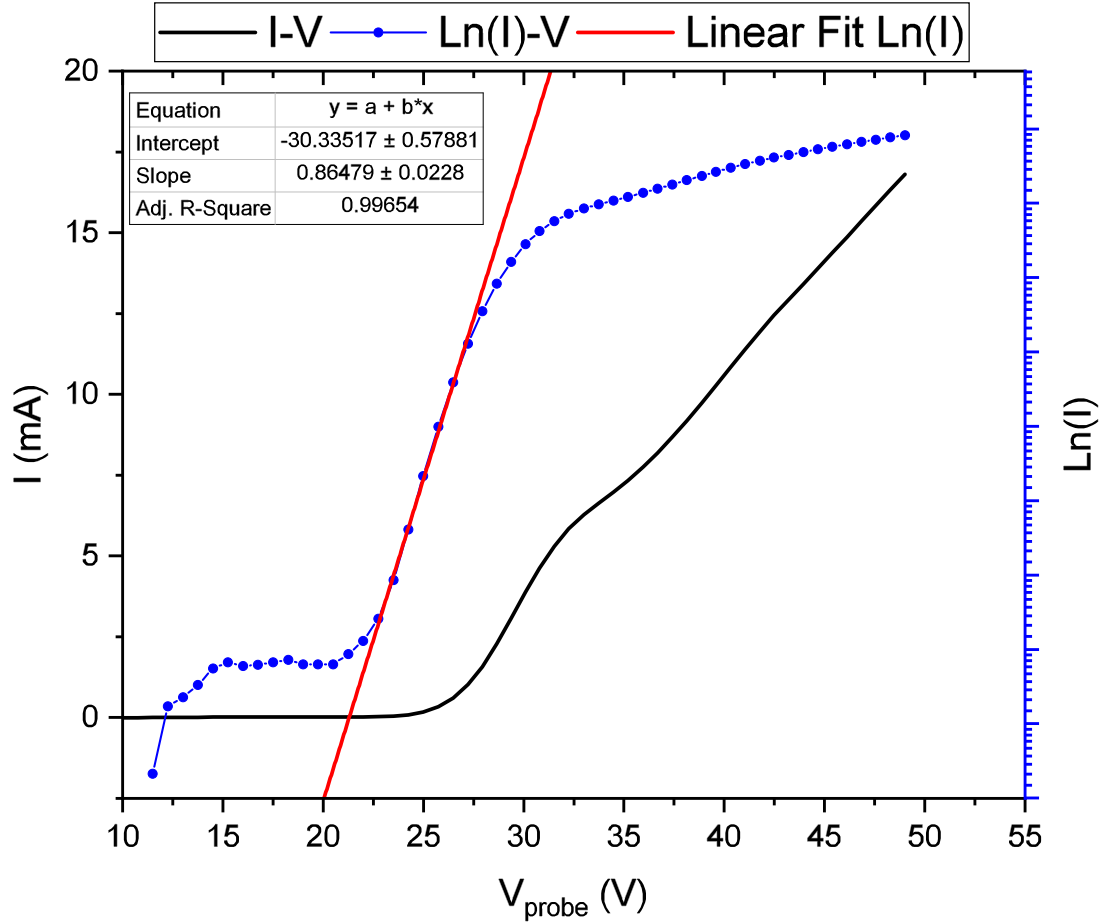
Figure 60: Example of a typical I-V characteristic and the Ln(I)-V curve for measuring T_e. The slope corresponds to a value of $T_e \approx 1.2$ eV. The pure Argon discharge conditions were 75 mTorr, 100 W, and no added bias.

This scan is a particularly good example with a definitive linear region to extract T_e. The linear region became more difficult to fit as the pressure and RF power increased, indicating a diversion from a purely Maxwellian electron energy distribution for these conditions. Due to the limitations caused by plasma pulling (Section 6.4), the electron density is calculated from the Bohm current through Eq. (49). As the plasma potential V_p cannot be reliably found using the scan, it is calculated using Eq. (50) with the experimental T_e and V_f as input parameters. The T_e and V_p results are summarized in Figure 61 with T_e results from the CRM for comparison.
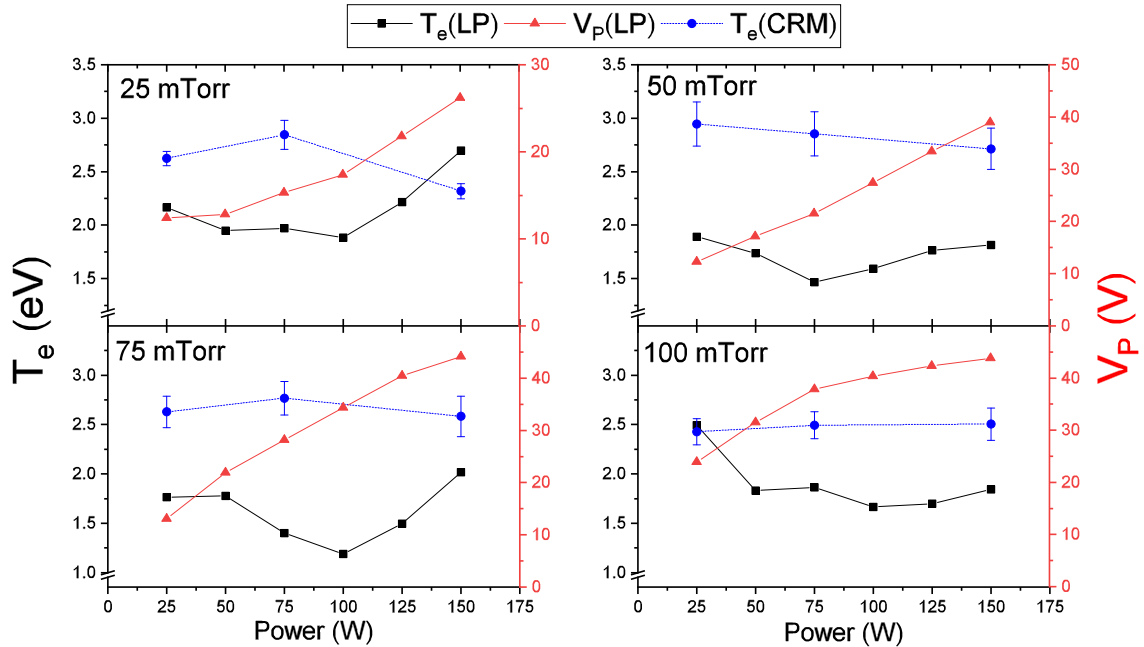
Figure 61: T_e (left axis) and V_p (right axis) as measured from the Langmuir Probe. The results from the CRM for similar discharge conditions are included for comparison.

In all cases, the Langmuir Probe underestimates T_e compared to the CRM, in some cases up to an eV. The plasma potential shows a steady increase with RF power as it should since the plasma potential is directly related to the amount of ions in the bulk of the discharge. Increasing RF power leads to an increase in the plasma density, therefore leading to an increase in V_p. Overall, the Langmuir Probe results are encouraging as T_e and n_e (presented later in the chapter) are within the expected range for this discharge. However, that is the extent of the usefulness of the probe results as the experimental limitations provides too much uncertainty in their validity. It is for this reason that these results are presented without error, as they serve to merely act as a comparison and confirmation of trends seen in the CRM. Additionally, the inability of the probe to work effectively with the inclusion of a positive DC bias on the driven electrode greatly limits the probes applicability.

8.3 CRM RESULTS AND SELF-CONSISTENCY

The electron temperature and density was calculated following the model outlined in Section 5.3, but it is pertinent to discuss how the final values were decided. As was

stated in 5.3, T_e and n_e were calculated independently for each spectral line using Eq. (81) and 82 respectively. The "final" value for each of these quantities is therefore the average of the individual calculations, with the error being the standard error of the mean. Table 7 shows a typical example of the final results calculated using the CRM.

Table 7: Results from the CRM for a pure Argon discharge at 50 mTorr, 150 W, and with no added DC bias.

Originating Level	2p$_2$		2p$_3$			2p$_4$	
Wavelength (nm)	826.45	696.54	840.82	738.40	706.72	852.14	794.82
T_e (eV)	2.76	2.76	2.20	2.20	2.20	3.44	3.44
n_e (10^{17} m^{-3})	7.78	7.78	21.0	21.0	21.0	3.21	3.21

It is plain to see that the results are consistent for lines that originate from the same upper level. Additionally, the relationship between results is consistent for all experimental conditions with the 2p$_4$ lines having the highest T_e (lowest n_e), the 2p$_3$ lines having the lowest T_e (highest n_e) and the 2p$_2$ lines being in the middle. The values in Table 7 are among those with the highest spread, while the majority of results are consistent well within 1 eV. When a positive DC bias is applied on the driven electrode, the same trend exists but with the spread being much smaller. The most likely explanation for this behavior lies in the uncertainty of the transmission rates Q used for each transition. As each 2p level is going to use the same rates in Eq. (81), it would follow that the results should be consistent for those lines originating from that level. Since this is indeed the case, it shows that the model is effective as the experimental values used in the left hand side of Eq. (81) are certainly different for each spectral line ratio. While the consistency within 2p levels is encouraging, the reason for the spread of the values as a whole remains unknown at the present time.

8.4 THE ELECTRON TEMPERATURE AND DENSITY AS A FUNCTION OF EXTERNAL PARAMETERS

In the following section, T_e and n_e results from the CRM are presented as a function of the external parameters found in Table 5. It is important to reiterate that these results assume a Maxwellian distribution for the electron energy. There exist several indicators that the EEDF diverges from this form under certain conditions,

which will be explained in the text. Once again, statistical error bars in the form of standard error are included for each plot, but the error bars may be smaller than the plot symbol size.

The electron temperature and density as a function of RF power for each pressure and bias configuration is shown in Figure 62.
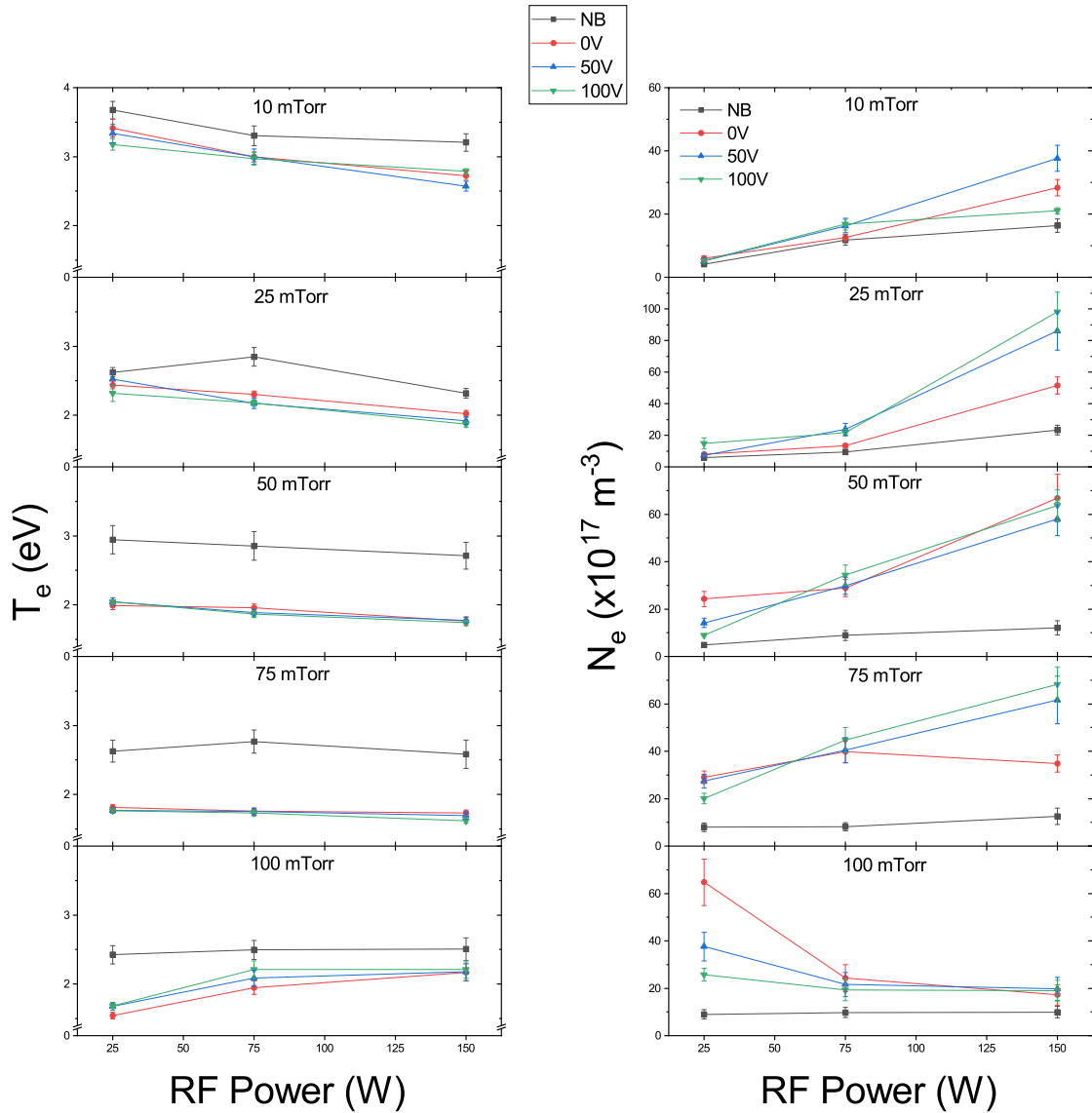
Figure 62: Electron Temperature (Left) and Density (Right) vs. RF power. Solid Lines are visual guidelines.

It is expected that there be little variation in T_e with RF power while n_e should increase, according to global particle and energy balance considerations respectively [2]. This is indeed the case for all conditions shown in Figure 62 except for those

results at 100 mTorr. For the results involving a positive DC bias, the expected trend seems to reverse course as T_e increases with increasing RF power and n_e sees an initial reduction, but little change with further increase in power. Without added DC bias, T_e and n_e remain essentially constant as a function of RF power. This seems to mark a transition region of the discharge to a non-Maxwellian distribution. As 100 mTorr was the upper pressure limit of this work, further investigation would be required to study this transition region fully.

The effects of pressure and DC bias can be seen in Figure 62, but plotting T_e and n_e as a function of the DC bias provides additional clarity as shown in Figure 63. It
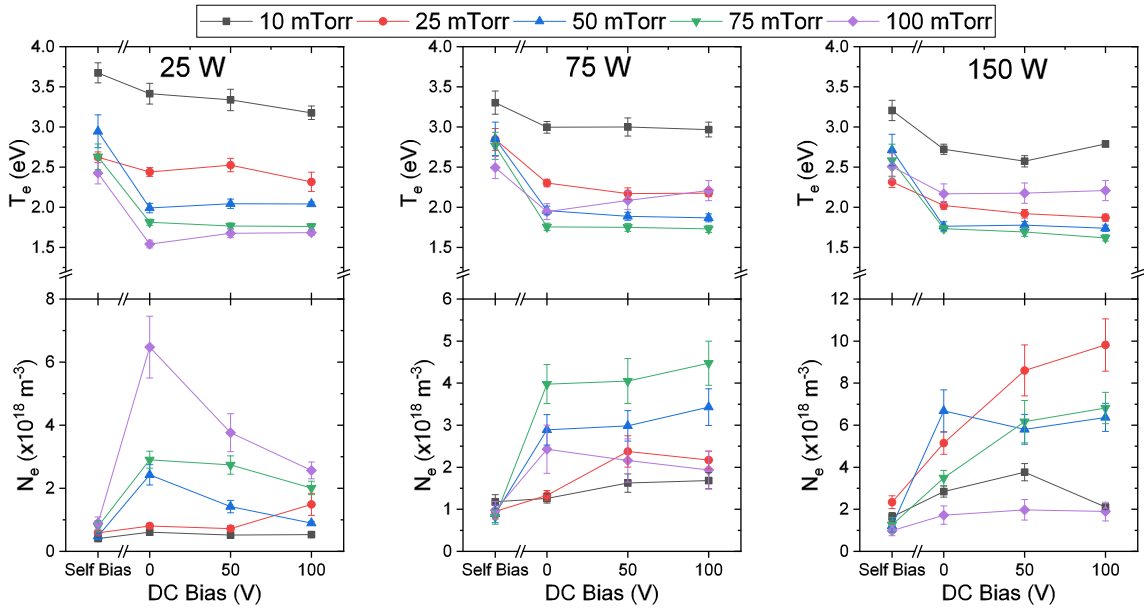
Figure 63: Electron Temperature and Density vs. DC bias for 25 W, 75 W and 150 W.

is evident that the addition of a positive DC bias on the powered electrode causes a decrease in the electron temperature and increase in the electron density. Indeed, this exact outcome was proposed in the previous chapter as the $1s_4$ and $1s_5$ densities also decreased with the addition of positive DC biasing. It is important to reiterate here that this is indicative of an increase in the ionization of the excited states as opposed to ground state atoms. Much like the 1s state densities, the transition from negative to positive bias voltage has a much larger effect on T_e and n_e than the further increase of the voltage in the net positive region. These results hold a striking similarity to those of Zuener $et\ al.$ in which the effects of a variable DC bias

(placed on the powered electrode) on the ion densities was studied in a parallel plate Argon CCP [96]. Their measurement of the ion density as a function of DC bias show a very similar increase and sharp plateau for a number of different discharge powers once the total DC bias crosses the positive axis. In the same study, the ion current into each electrode was measured as a function of DC bias. At the powered electrode, the ion current shows a similar increase and eventual plateau at $V_{DC} = 0$, while the ion current into the grounded electrode continues to increase slightly with increased positive bias [96]. These effects are attributed to the plasma adjusting to the most stable state as the plasma potential is changed. The plasma potential V_P is always the highest potential in the discharge (see Section 2.3) and thus must increase as the DC bias becomes more positive. The plasma compensates for this by confining electrons in the bulk to increase ionization processes, which are then emitted to the electrodes [96].

Additionally, there have been a number of theoretical studies of the effect of DC bias on the particle and energy distributions in a parallel plate CCP [41, 42, 94, 95]. While most of these primarily study the effect of adding a *negative* bias on one of the electrodes, they all confirm the results shown in Figure 63. Particularly, as the bias is used to *reverse* the asymmetry, the plasma density is increased in the bulk between the two electrodes and further confined. Additionally, the electron temperature decreases under the same effects, with a minimum at the location of the highest density (see Figs. 3 and 4 in Ref. [42]).

The effect of increasing the discharge pressure in the positive bias regime can also be seen in Figure 63. In the majority of cases, the electron temperature decreases with pressure, while the electron density increases. This is due to the increase in collisional processes in the discharge with higher pressure, therefore decreasing the average energy of the electrons. However, these respective effects become less prominent as a whole with an increase of the RF power, with the 100 mTorr set completely traversing the trend for both T_e and n_e. As mentioned above, this indicates a transition in the EEDF with the combination of high pressure, high power, and a total positive DC bias. Figure 63 provides additional evidence for this conclusion as no discernible trend between n_e and pressure can be seen for the highest RF power (Bottom right panel of Figure 63). As the effect of pressure for the non-biased results cannot be seen clearly in the above figures, these results are plotted by themselves in Figure 64.
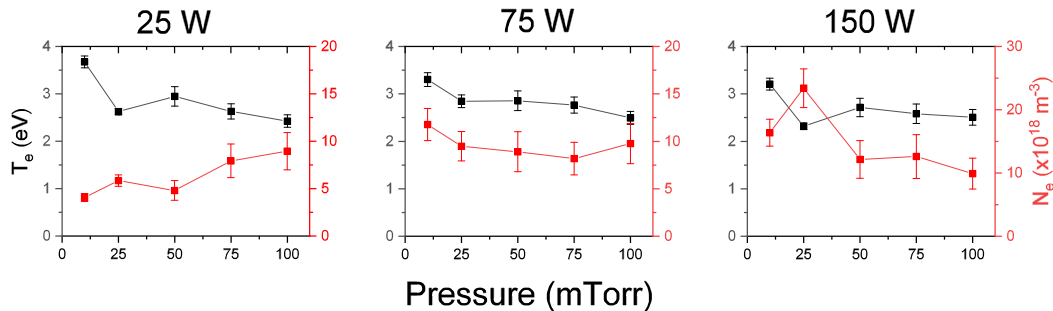
Figure 64: T_e and n_e vs. Pressure for discharges without added DC bias. Solid lines are visual guidelines.

As a whole, there doesn't seem to be any relationship between the pressure and T_e/n_e. The expectation is that as one of the parameters trend in one direction, the other parameter would trend in the opposite direction, much like those results for positive biases. While this can be seen in small instances, they are well within the statistical error and are therefore inconclusive. The explanation for the lack of variation with pressure remains unknown.

8.5 THE CALCULATION OF n_e USING THE COMBINATION METHODS

The results for n_e as a function of the external parameters are presented for the multiple measurement/calculation sources outlined at the beginning of the chapter. The combination methods are labeled in the format N_R/T_e throughout this section as according to Table 6. When the CRM was used as the T_e input source, n_e was calculated for each spectral line and averaged in the same way as the self-consistent CRM. In the cases where the n_e results from the Langmuir Probe are included, they are presented without error only for comparative purposes. In the case of the combined treatment utilizing 1s densities from TDLAS and T_e from the Langmuir Probe, the data is presented with error bars of $\pm$ 30 %.

The electron density as a function of the RF power are shown for 50 and 75 mTorr in Figure 65 and 66 respectively.
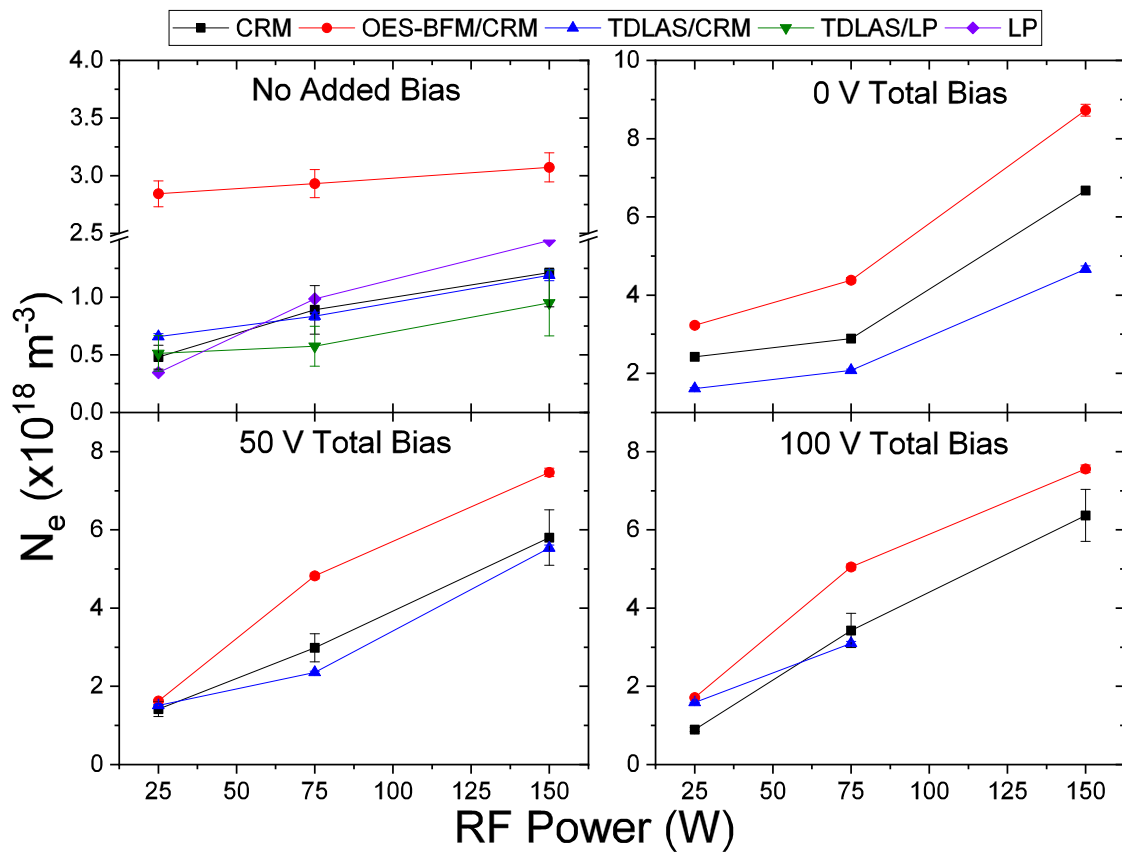
Figure 65: n_e vs. RF power at 50 mTorr for each DC bias configuration. Solid lines are visual guidelines.
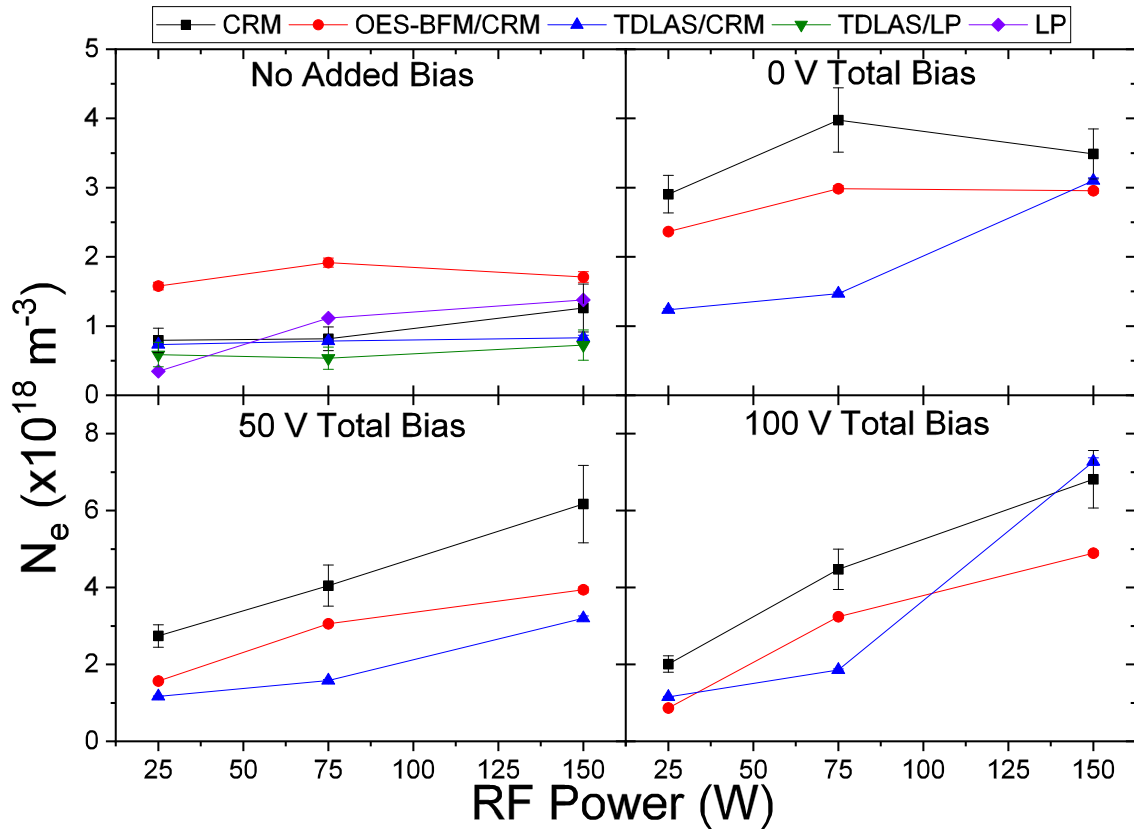
Figure 66: n_e vs. RF power for a pressure of 75 mTorr in each DC bias configuration. Solid lines are visual guidelines.

In general, all of the different methods show the same general trends as a function of RF power. It is noteworthy that the self-consistent CRM and the OES-BFM/CRM combination, which both use the same $1s_4$ and $1s_5$ densities, typically overestimate n_e compared to the other methods. The self-consistent CRM has the largest statistical error, while the TDLAS/CRM combination has the lowest statistical error. This is not surprising as TDLAS is the more accurate method in measuring the 1s state densities.

The electron density as a function of the DC bias for 50 and 75 mTorr is shown in Figure 67.
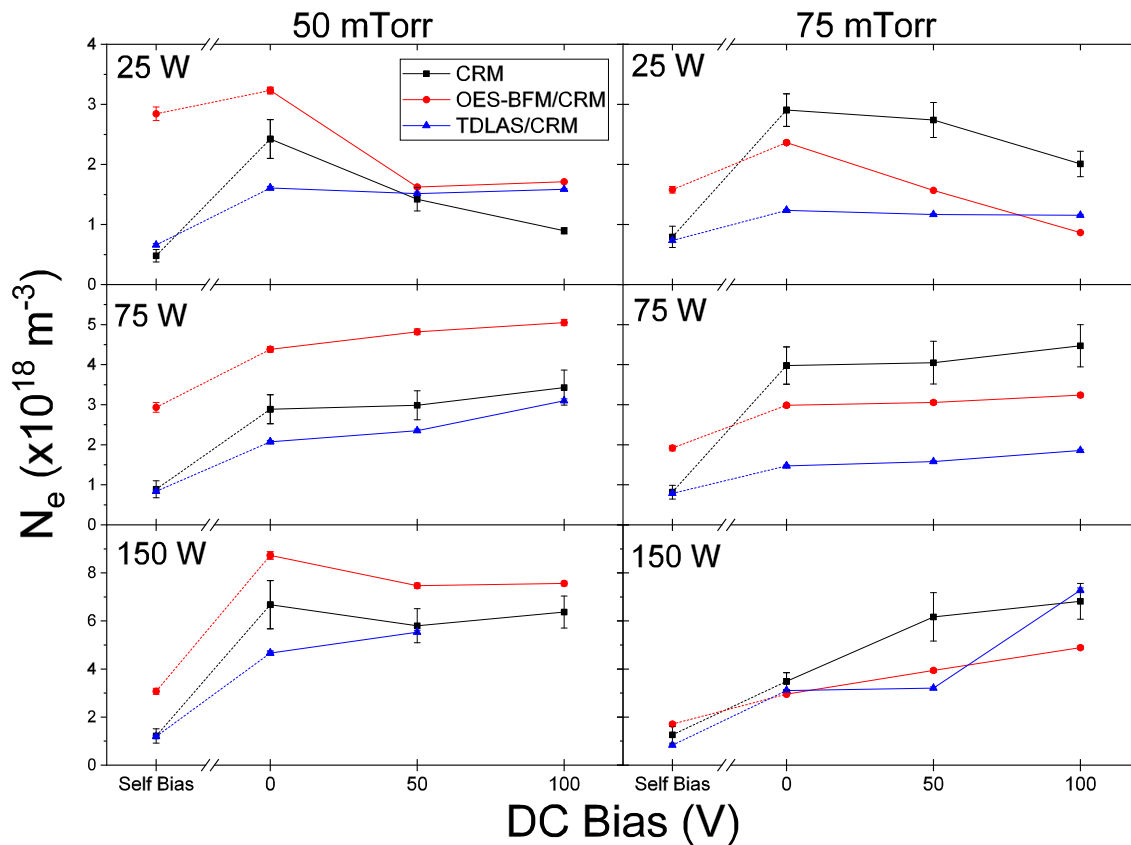
Figure 67: n_e vs. DC bias for each RF power with discharge pressures 50 and 75 mTorr. The dashed lines indicate the negative bias region outlined in Section 7.4.3.

All of the n_e calculation methods show an increase as a function of DC bias as was presented in the previous section. This is encouraging as the effect transcends the N_R measurement source. As the TDLAS/CRM combination show the most consistent trends with the lowest error, this combination is shown for a greater array of experimental conditions in Figure 68.
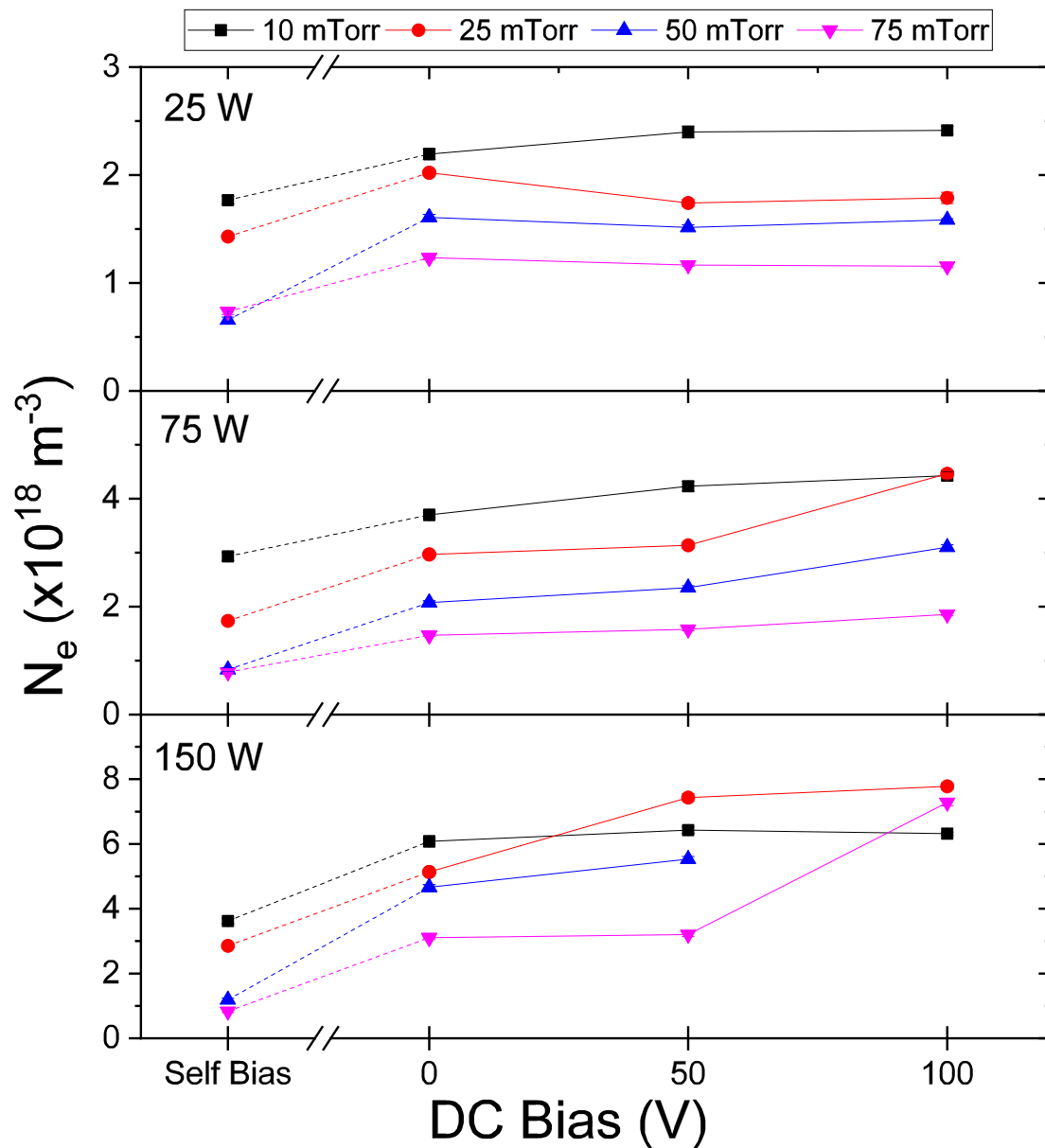
Figure 68: n_e vs. DC bias for different discharge pressures. All data was calculated using the TDLAS/CRM N_R/T_e combination.

The results from the TDLAS/CRM combination show similar trends and densities as those presented in Figure 62, but with even more consistency. Additionally, the effect of increasing the discharge pressure remains consistent for a greater range of parameters, including the results without added bias. A similar reverse of the trend occurs for the higher power and DC bias, but to a much lesser extent than was seen previously.

8.6 Ar/Cl$_2$ RESULTS

The application of the CRM to Ar/Cl$_2$ is challenging due to the inability to find the 1s densities using the OES-BFM diagnostic method (see Section 7.2). Additionally, TDLAS was used to find the 1s$_5$ density in Ar/Cl$_2$ mixtures, but the 1s$_4$ density was not. Therefore, the direct application of a fully self-consistent CRM is not feasible. However, Figure 59 in Section 7.4.4 shows the relationship between the 1s$_5$ density and the Cl$_2$ concentration of the discharge. In each case, there is a consistent trend with the increase of Cl$_2$ that closely follows the relationship found by Scheller *et al.* [97]. By applying this same relationship to the other 1s state densities measured in pure Argon, the CRM can be used just as before to calculate T_e and n_e. This can also be applied to the 1s$_4$ densities measured by TDLAS, so that the TDLAS/CRM combination method can be used as well. We believe this approximation is appropriate as the collisional quenching rate between Ar and Cl$_2$ atoms is the same for the metastable and resonant levels $(71 \times 10^{-17} \mathrm{m}^3/\mathrm{s})$. Additionally, due to the large reduction in densities with the introduction of Cl$_2$, photon reabsorption is negligible as the photon escape factor approaches 1 (see Eq. (65)). Therefore, it stands to reason that all of the densities would follow the same general trend with an increase in Cl$_2$ concentration.

An example of the application of this approximation is shown for an Ar/Cl$_2$ discharge with 90% Argon and 10% Cl$_2$ at 75 mTorr in Figure 69.
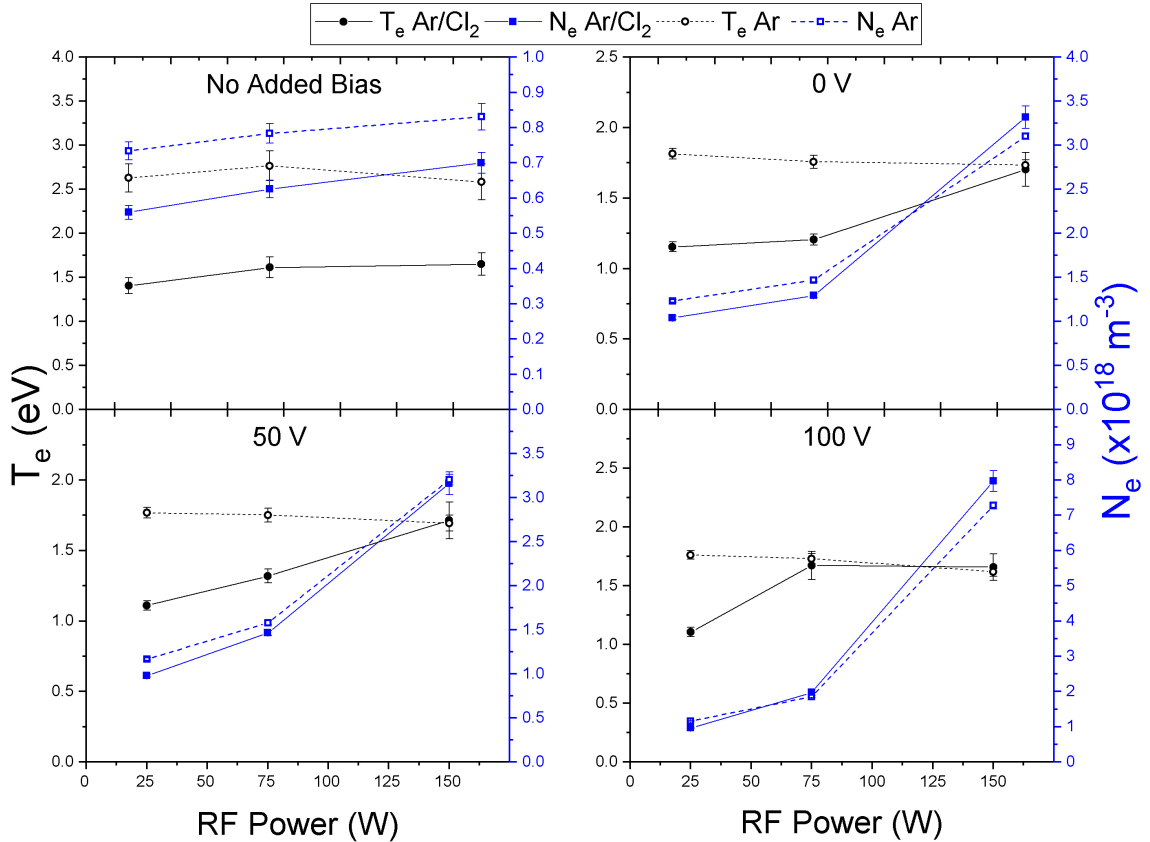
Figure 69: T_e and n_e vs. RF power for pure Argon (solid symbols) and Ar/Cl$_2$ (90/10 %) for each DC bias configuration at 75 mTorr. T_e was found using the CRM, while n_e was found using the TDLAS/CRM combination method. Lines are visual guidelines.

It is first important to point out that the n_e results calculated by the CRM and the OES-BFM/CRM combination methods are not shown as these methods, particularly the CRM, overestimate the electron density by a great deal. As the calculation of the electron temperature was not dependent on n_e (n_e is canceled in the ratio method Eq. (74)), these values were not considered inaccurate. However, this means that the only difference between the calculation of n_e in Ar and Ar/Cl$_2$ is the input T_e as the ratio N_R is the same. Therefore, the ratio of the pure Ar n_e and Ar/Cl$_2$ mixture is strictly dependent on the ratio of the electron temperatures. Due to the addition of Cl$_2$, the discharge becomes electronegative, meaning that there is an additional negative species (Cl$^-$) in the discharge. Naturally, this means that the electron density should decrease to maintain quasineutrality. The experimental work in an ICP by Fleddermann indeed shows a decrease in n_e as the Cl$_2$ concentration

is increased, but there are two distinct regions for low and high concentrations [93]. Below 40% Cl_2, the electron density is much higher than expected, with n_e only decreasing by a factor of 2 from 0 to 10 %Cl_2. Additionally, measurements by the same group show that the electron temperature does not change significantly between Ar and Ar/Cl_2 discharges at lower Cl_2 concentrations [92]. Due to these discrepancies, additional work must be done to fully understand the Ar/Cl_2 discharge in our context.

8.7 GENERAL CONCLUSIONS

The electron temperature and density for a pure Argon discharge in a coaxial CCP have been measured as a function of a number of external parameters pertinent to RIE using a collisional radiative model. Particularly, the relationship between T_e/n_e and DC bias is consistent with both experimental and theoretical works for parallel-plate CCPs [41, 42, 94–96]. A decrease in T_e and increase in n_e is seen as the DC bias on the driven electrode switches from negative to positive. This nicely explains the trends seen in the previous chapter as the 1s state densities decrease in the same manner as T_e. This indicates that the ionization of the 1s states increases with this transition in bias, contributing to a higher n_e. A positive DC bias also forces an increase in the plasma potential which encourages ionization processes by confining electrons in a tighter region between the electrodes. A combination of a positive DC bias, high pressure, and higher powers shows a transition region in which the EEDF deviates from a Maxwellian distribution. This can be useful when determining operating conditions for a plasma etching experiment.

Additional to the CRM, the electron density was calculated in multiple ways by utilizing a simple relationship developed by Li *et al.* [61, 81]. The ratio of the $1s_5$ and $1s_4$ densities calculated from the diagnostic methods outlined in Chapter 5 was used as an input parameter in conjunction with the electron temperature measured by the CRM and Langmuir Probe. In general, all of the various methods show consistent trends and results as a function of the external parameters. The combination of the density ratio from TDLAS and T_e from the CRM show the most consistency.

The CRM and TDLAS/CRM combination method were applied to an Ar/Cl_2 discharge in a similar manner as the pure Argon discharge. However, approximate values for the $1s_2, 1s_3$, and $1s_4$ densities were used based on the relationship between the $1s_5$ density and Cl_2 concentration found in the previous chapter. While this approximation seems appropriate, further work is required to confirm the results

found using this relationship.

8.8 COMPARISONS TO TRADITIONAL REACTORS AND CONNECTIONS TO REACTIVE ION ETCHING

At this point, it is pertinent to outline particularly interesting results and make appropriate connections of the plasma parameters to the mechanisms of RIE. Among the most surprising and intriguing results of this work are those pertaining to the electron density. In particular, the high value of the 1s states and n_e for the conditions of this work illuminate the benefits of this reactor. Among the types of low temperature discharge sources, the CCP typically has the lowest plasma density in the range of $10^{15} - 10^{17}$ m^{-3}. Higher densities are reached by using ICP's or helicon based electron cyclotron resonance (ECR) sources with typical values in the range of $10^{16} - 10^{18}$ m^{-3} or higher [2]. The astute reader will notice that the plasma density measured in this work is *very* high for a CCP as the values are consistently in the range of $10^{17} - 10^{18}$ m^{-3}. Indeed, this remains true when comparing the 1s state and electron densities to the works that are frequently cited throughout this dissertation, regardless of the plasma source [11, 57, 58, 60, 65, 68, 74, 76, 77, 98]. The 1s$_4$, 1s$_5$ and electron densities are typically 1-2 orders of magnitude higher compared to these outside works. It it important to emphasize that this is true while many of the basic relationships that have been well understood between the plasma and external parameters remain. The consistency of the results in this work between the various diagnostic methods firmly establishes that, at the very least, the order of magnitude of these densities are undeniable.

These higher densities at the comparable RF powers and discharge pressures of the other works is a significant boon to the etching mechanisms of RIE. The higher ion density (due to quasineutrality) is an obvious benefit as they are the 'fuel' of the etching process. Additionally, in the case of pure Argon discharges, there are no external parameters that lead to the quenching of electron/ion pairs, at least below 100 mTorr. The simple relationship between the electron temperature/density with DC bias, while expected, is useful as the amount of change is quantifiable and constant with the increase of positive DC bias. This can provide someone with the means to establish a more sophisticated model of this discharge as a function of the external parameters with the goal of understanding the *ion* energy distribution. It was also shown that the operation at a lower pressure is quite beneficial, especially

when a positive DC bias is involved, as the plasma density is certainly high enough to facilitate RIE processes while the plasma remains simple in characterization. This is particularly useful for experimentalists as considerations regarding the experimental apparatus and its longevity are always a concern, especially when halogen gases are involved. While results including Cl_2 remain elusive for the time being, it is important to keep in mind that the addition of Cl_2 at these lower concentrations are not expected to decrease the electron density in a significant manner. Thus, the important energy providing electrons remain abundant in an Ar/Cl_2 discharge. These conclusions are not only important for the RIE of Nb cavities, but for the technology of RIE as a whole as the unique reactor geometry/style could provide a solution to processes that require a high plasma density at lower pressures and RF powers.

CHAPTER 9

SURFACE CHARACTERISTICS OF PLASMA ETCHED

Nb SAMPLES

The empirical study of Reactive Ion Etching (RIE) parameters in the previous work by Upadhyay (see Chapter 4) provided a great deal of insight into the effectiveness of using RIE for the processing of SRF cavities. Additionally, a more complete understanding of the physical and chemical etching mechanisms of the RIE process was established, particularly as it pertained to the amount of material removal. However, missing from that work is the effect of the external etching parameters on the final surface roughness profile of the processed Nb. A smoother, more uniform surface is desired to reduce losses in the cavities, particularly in the case of cavities with a high amount of grain boundaries (see Section 3.4). Among the external parameters to study in this aim, the most important are the surface temperature of the substrate and the added DC bias. The surface temperature of the substrate is directly related to the chemical etching component (see Section 4.1.4) while the DC bias is necessary for the physical etching component (see Section 4.1.2). Understanding the effects of varying these parameters on the surface roughness of Nb is the next logical step in the development of RIE technology for SRF cavities.

Throughout the development of this technology, material and engineering limitations have been found that must be addressed before it can be considered viable for the processing of SRF cavities. Some of these limitations were described by Upadhyay [1], which in turn led to a great deal of experimental modifications for this work (see Chapter 6). Many of these alterations were indeed beneficial, but also illuminated further material/engineering roadblocks that hinder the technology's development. However, much of the study required to fully address these issues are beyond the scope of this work and, in the author's opinion, require the expertise of chemists and material scientists. Nonetheless, qualitative observations of particularly important issues are outlined in this chapter with the goal of aiding those in the future who would look to improve upon this technology.

9.1 THE Nb COUPON ETCHING EXPERIMENT

In order to study the final surface roughness profile of RIE processed Nb, small coupon samples were placed in various locations of the chamber. The complete details of this experimental setup are given in Section 6.5. Four coupon samples were plasma etched simultaneously in the locations given in Figure 51. This was done because the distribution of the discharge throughout the chamber is still unclear. The studies outlined in Chapters 7 and 8 were only conducted in one local region, in this case corresponding to the location in front of S3 (see Figure 51). Comparing the etch rates of each sample under the same conditions can provide a better understanding of the plasma's spatial profile and the most effective etching location, particularly in relation to the driven electrode. The samples were placed in 'staggered' locations to avoid the possible loading that may occur for samples placed on the same side of the chamber (see Section 6.1.2 for more details about the loading effect).

9.2 SAMPLE ETCH RATE

Although the primary purpose is to study the surface profile of the samples, the nature of the experiment has the added benefit of studying the etch rate with the variation of experimental parameters. This can be used as a simple comparison to the previous work by Upadhyay [1], with the added caveat that the experimental apparatus has a number of different components. The etch rate for each sample is calculated from the time rate of change of the sample mass per density per sample area, or more simply

$$\text{etch rate} = \frac{\Delta m}{DAt}. \tag{100}$$

The change in mass Δm is found simply by measuring the mass before and after the processing and the time t is the total time of Ar/Cl_2 exposure. Each sample has a surface area of 1.814 cm^2 and the density of Nb is 8.57 g/cm^3. Before the samples were exposed to the Ar/Cl_2 discharge, a pure Ar discharge was created in the chamber to clean the system and to maintain a constant temperature when transitioning to an Ar/Cl_2 discharge. Table 8 presents a summary of each experiment.

The etch rate for each position versus temperature for all configurations in Table 8 is shown in Figure 70.

Table 8: Summary of the Nb coupon sample experiments. The identifier is used for reference in the text and figures. In each case, the discharge conditions are 150 W, 75 mTorr, and 85/15 % Ar/Cl_2. For T1-T5 the total DC bias is 100 V.

Identifier	Sample	T (K)	Etch Rate (nm/min)	Material Removed (μm)
T1	S1	645 ± 10.25	30.02	6.30
	S2	471 ± 7.56	49.32	10.36
	S3	667 ± 10.40	131.74	27.66
	S4	625 ± 0.82	43.20	9.07
T2	S1	609 ± 2.20	12.25	2.57
	S2	493 ± 6.30	40.44	8.49
	S3	590 ± 6.96	33.09	6.95
	S4	576 ± 0.90	21.45	4.50
T3/B1	S1	517 ± 12.04	8.94	1.61
	S2	525 ± 1.54	28.59	5.15
	S3	500 ± 7.00	14.65	2.64
	S4	468 ± 5.18	6.43	1.16
T4	S1	659 ± 11.19	45.75	8.24
	S2	681 ± 2.69	184.79	33.26
	S3	640 ± 7.59	29.67	5.34
	S4	588 ± 4.18	44.68	8.04
T5	S1	455 ± 7.78	6.43	1.16
	S2	422 ± 3.42	21.09	3.80
	S3	484 ± 2.15	12.15	2.19
	S4	475 ± 4.50	7.15	1.29
B2	S1	536 ± 4.81	-	-
	S2	493 ± 3.28	32.17	5.79
	S3	594 ± 1.08	57.19	10.29
	S4	537 ± 4.56	38.24	6.88
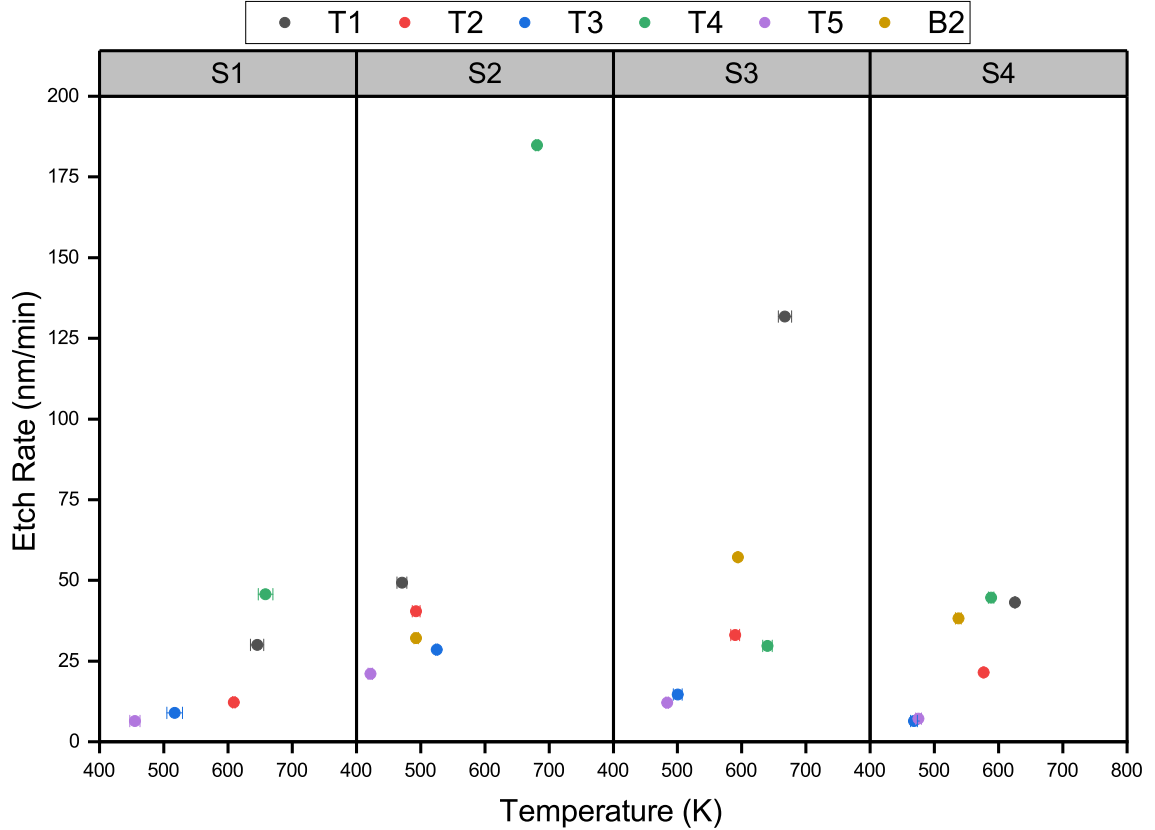
Figure 70: The etch rate vs. temperature for each sample position. Each configuration is further labeled by their respective identifier from Table 8.

In general, there is very little difference in etch rate for each position. The two large outliers for S2 and S3 happen at those experiments with the highest temperatures. However, S1, S3, and S4 show a slight increase in etch rate with temperature. This relationship will be explored further in the next section.

9.2.1 ETCH RATE VS. SUBSTRATE TEMPERATURE

As was explained in Section 4.1.4, an Arrhenius relationship between the etch rate and surface temperature is indicative of a strong chemical etching component. The Arrhenius curve has the form

$$k = Ae^{-E_a/k_B T}, \tag{101}$$

where k is the reaction rate coefficient (etch rate in this case), A is a pre-exponential constant, k_B is the Boltzmann constant, T is the temperature, and E_a is the activation energy, or the energy required to facilitate the chemical reaction. The desire

is to find E_a, and thus the value for A is not important. Figure 71 shows the etch rate plotted as a function of inverse temperature for each sample across all etching experiments.
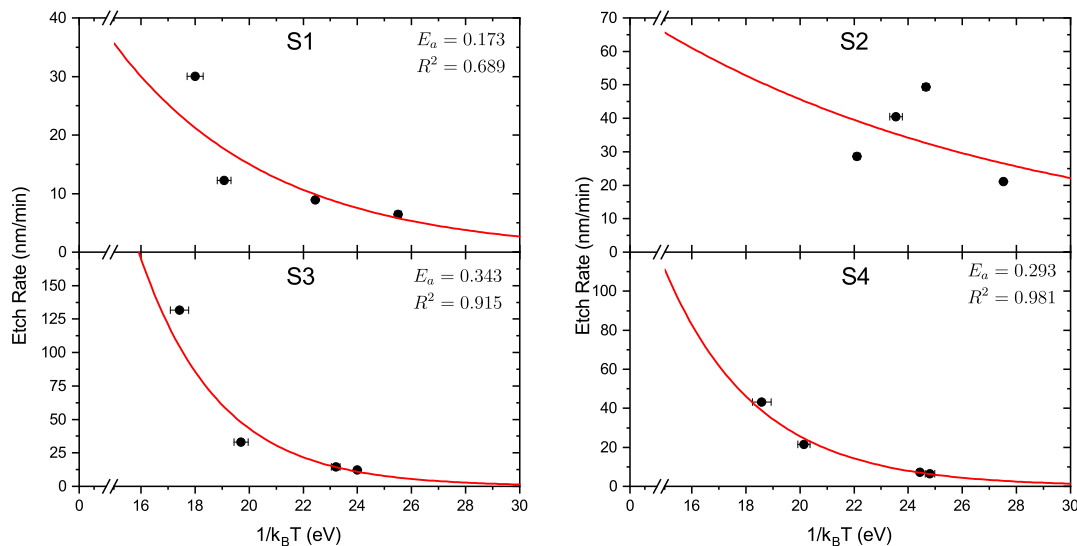
Figure 71: Etch rate vs. $1/k_B T$ and corresponding Arrhenius function fit for each sample as labeled in the top of each pane.

Each sample location in Figure 71 show interesting artifacts of their particular location in the chamber. S1 shows a large increase in etch rate below 20 eV, so much so that Eq. (101) cannot adequately fit the whole set of data. The measurements of S2 leave a lot to be desired, but it is important to recognize the absence of measurements between 18-22 eV, which seems to be the region in which the exponential takes shape. This is due to experimental limitations regarding the uniform temperature delivery to the chamber (see Section 6.5). S3 yields a curve that is indicative of strong chemical etching in this location. This sample is located closest to the gas inlet and is the first to encounter Cl radicals, so a significant loading effect (see Section 6.1.2) is probable. S4 also shows a relationship indicating significant chemical etching, although it is important to point out the magnitude of etch rates between S3 and S4. The chemical etching is much higher in the location closest to the gas inlet, while the physical etching is going to be highest at S2 and S4 where they are closest to the driven electrode. It also seems that the region between 18-22 eV is important to the Arrhenius fit and must be studied further.

The data from T4 has been omitted from each fit as this experiment corresponds

to the highest average temperature of all four samples, which lead to a significantly higher chemical etching component as a whole. This high temperature, combined with the experimental configuration (see 9.3.3 and Table 8) consisting of no gas feed with all Ni gaskets, seemed to modify the chemical etching component of all the samples so much so that the results were inconsistent. It seems that the increase in chemical reactions at such high temperatures can hinder the etching of Nb as other byproducts and impurities are created and deposited on the surfaces of the samples. The effect of these byproducts on the etch rate of each sample cannot be easily quantified in the current experimental setup. However, qualitative observations illuminate the limitations imposed by these byproducts as seen in Figure 72.

Figure 72: Example of a sample after plasma etching. The color indicates chlorine contaminants on the surface.

Depending on the experimental conditions the deposits on the samples varied in amount and type, but were almost always present on each sample. It is unknown when the deposits occur, but their presence is expected to have detrimental effects to etching. The efforts to mitigate these deposits by using more durable materials is discussed in Section 9.3.3.

Figure 71, particularly S3 and S4, indicate that the activation energy E_a is in the range of 0.29-0.35 eV. In a study of Nb etching using a CF_4/O_2 plasma, Chen *et al.* found that the activation energy for Nb was 0.22 eV [99]. While the activation energy will indeed be different for different chemical reactions, the closeness of these values when regarding the chemical similarity of fluorine and chlorine is encouraging. It is also important to point out that the activation energy found in this work is around 2 times the value (0.15 eV) found by Upadhyay [1] (see Section 4.1.4). This discrepancy may be due to the difference in the accuracy of the temperature measurement for

the Nb samples. In the previous case ([1, 7]) the temperature was measured by a thermocouple in contact with the outside of the etching chamber and the temperature was considered constant in all locations. In this case, each sample's temperature was measured individually with thermocouples placed inside the vacuum chamber in direct contact with each sample. The details of this configuration is given in Section 6.5. Thus, it is expected that the previous value is an underestimate of the true activation energy. Regardless, the Arrhenius relationship of S3 and S4 give evidence of a chemical etching component.

9.3 SURFACE MEASUREMENT SYSTEMS

The surface roughness profile was measured for each sample using an atomic force microscope (AFM) and PHENOM scanning electron microscope (SEM) imaging systems. The AFM provides 2D and 3D images of the sample surface at the nanometer scale. Additionally, AFM measures the physical values of the surface roughness in a given image including the maximum roughness (distance between highest and lowest point), the average roughness, and the root mean square (RMS) roughness (quadratic mean). In general, the RMS roughness is the best figure of merit as it inherently includes the standard error. The SEM system also provides high quality 2D images on a micron scale. The SEM does not provide more than qualitative information regarding the surface roughness, but rather yields surface composition information in both large areas (≈ 270 micron^2) and specific spots on the surface. This is very useful for identification of impurities on the sample after the etch process. The results from the AFM system is used in the following section to describe the surface roughness profiles of RIE etched samples, while results from the SEM are presented in Section 9.3.3 to outline specific material and experimental limitations.

9.3.1 SURFACE PROFILES

A side-by-side example of the difference in surfaces before and after RIE is shown in Figure 73.
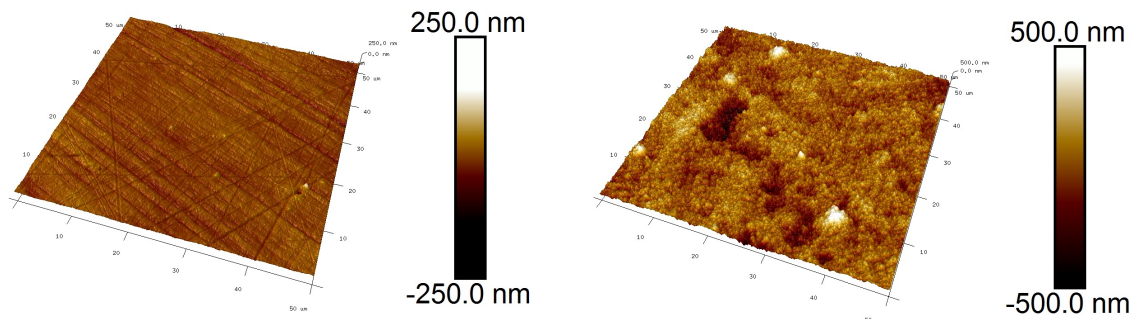
Figure 73: 3D AFM images of Nb samples. Left: Polished (1 micron) unetched sample. Right: Etched sample from experiment T4 in location S3. The sample location description can be found in Figure 51.

The effects of RIE on the sample roughness is obvious from Figure 73. On the left, the grooves left by the polishing process can be clearly seen, while the surface on right is much more chaotic with many peaks and valleys. To compare the effect of surface temperature on the sample profile, AFM scans are shown in Figure 74 for the same sample location for each experimental configuration outlined in Table 8.
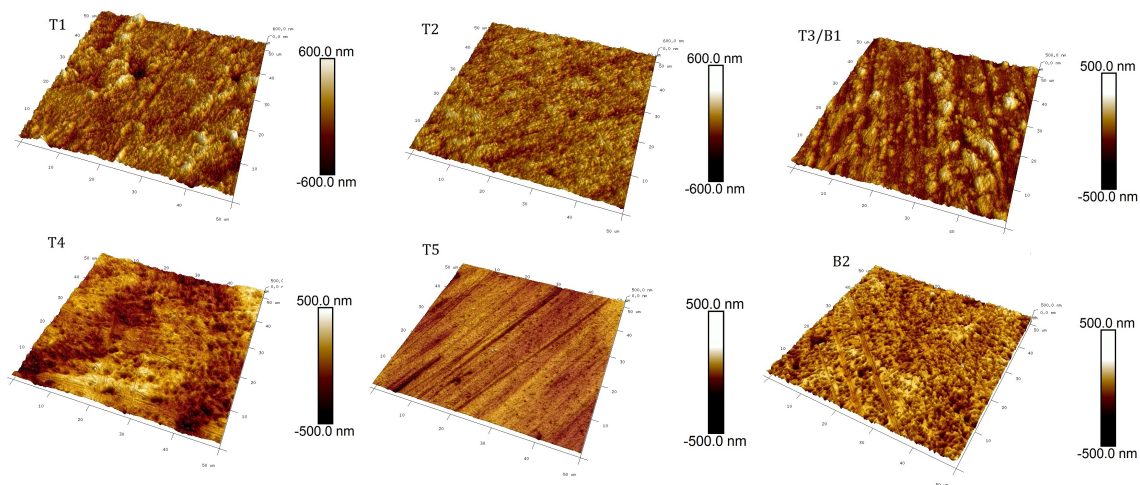
Figure 74: Comparison of surface roughness profiles for S4 in each experimental configuration. Sample location description can be found in Figure 51.

In general, an increase in the substrate temperature leads to a rougher surface with pits and uneven looking surface structures. At lower temperatures (T5) there is very little difference in the surface structure compared to the unetched sample in Figure 73. With the expectation that increased temperature leads to an increased

etch rate, this general trend is not surprising. Furthermore, the temperature for this particular sample is $\approx$ 200 ^{o}C, whereas the boiling point of NbCl$_5$, the desired volatile product, is 250 ^{o}C. Thus, we would not expect much etching of this sample and indeed the etch rate was among the smallest at 7.15 nm/min. In the same vein, an increase in the DC bias (B2) shows an even further increase in the pit-like structure. This is likely due to the increased physical etching aided by the higher bias potential, and therefore a higher ion energy. Further verification of this hypothesis can be seen in Figure 75, which corresponds to sample 1 in experiment B2.
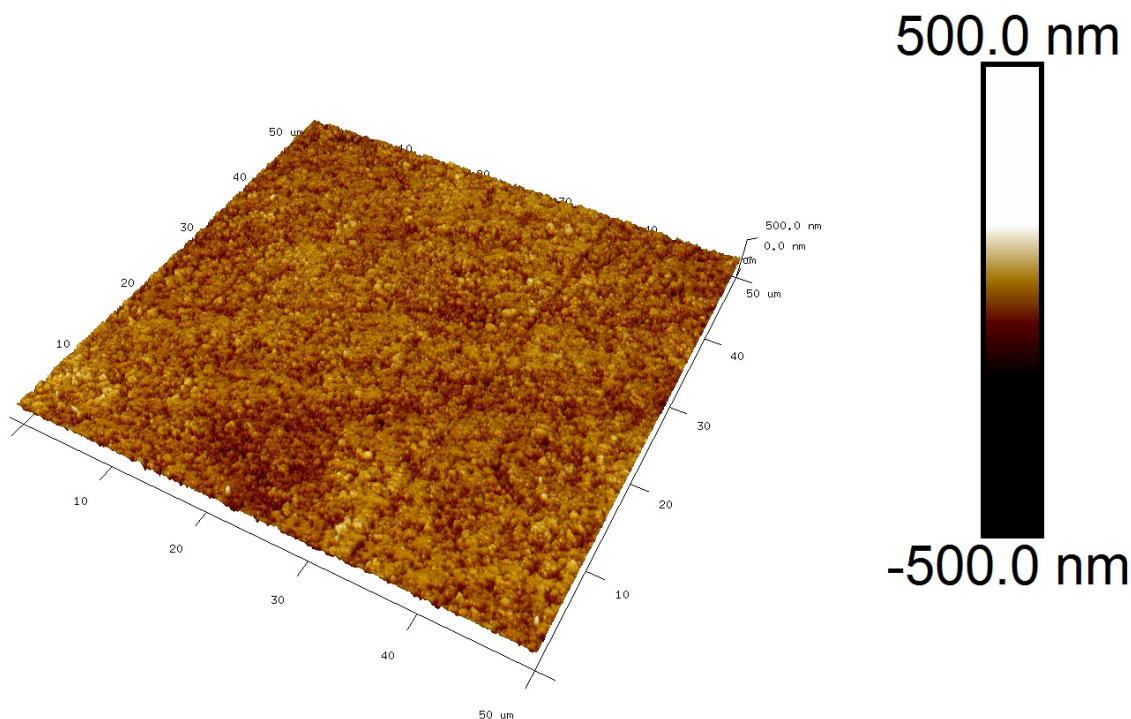
Figure 75: AFM scan of S1 in configuration B2. This sample was found to have a negligible etch rate. The sample location description can be found in Figure 51.

This is a particularly interesting example as the etch rate was measured to be approximately 0, even though the surface temperature should have been sufficient for chemical etching. Regardless, one can see that with minimal to no chemical etching, the surface still shows significant pitting and uneven characteristics that are indicative of purely physical, sputtering type interactions.

9.3.2 RMS SURFACE ROUGHNESS

The RMS surface roughness for each sample is presented in Table 9 and in Figure 76.
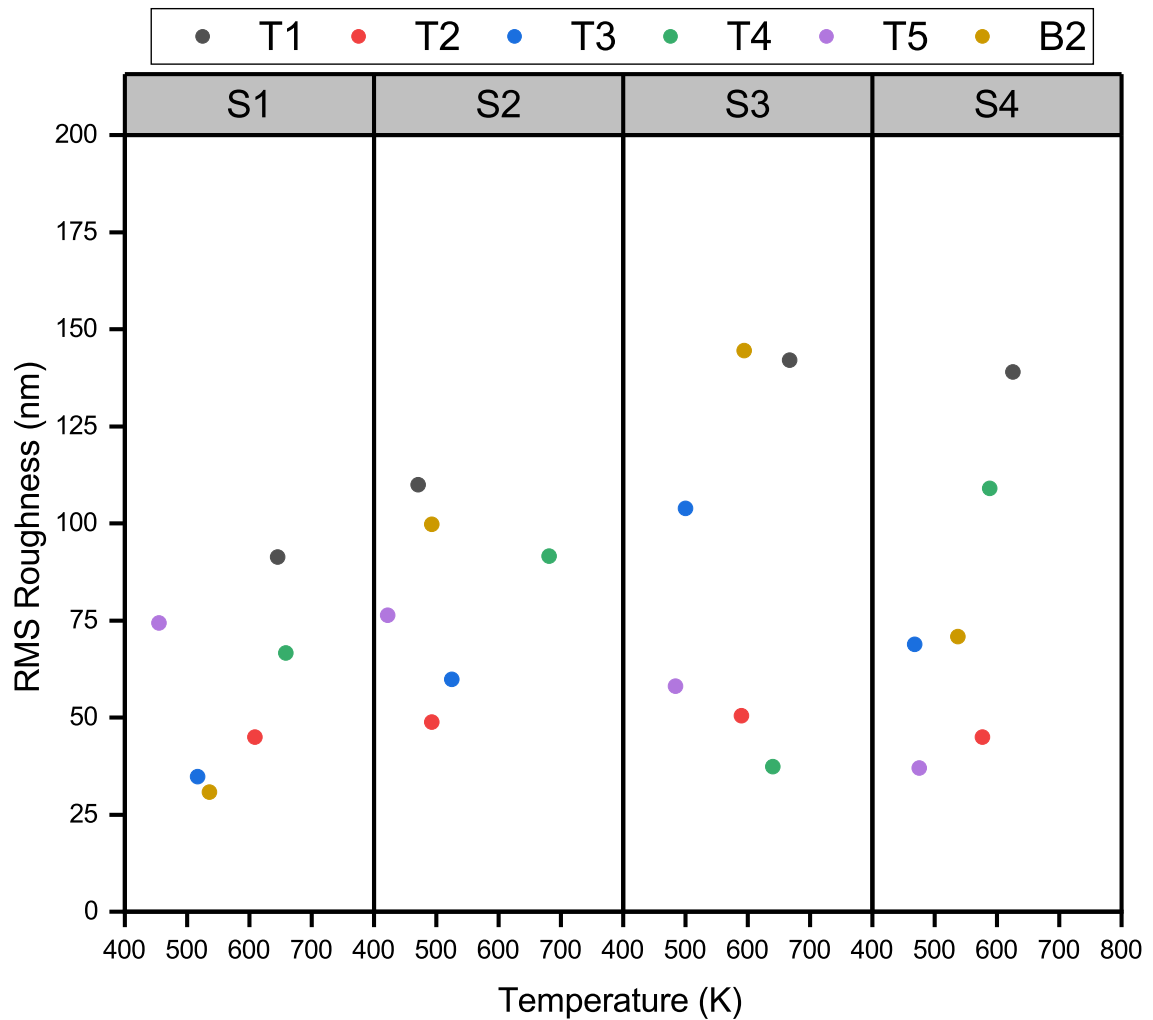
Figure 76: RMS surface roughness vs. surface temperature for each sample position. The raw data and identifier can be found in Table 9. Data is presented without error bars for clarity.

Interestingly, there is no discernible connection between the substrate temperature and the RMS surface roughness. The same can be said in regards to the sample position as no trend appears to exist. The effects of temperature and DC bias discussed in the previous section seem to only apply at very small scales, rather than a macroscopically.

It is important at this point to compare the RMS surface roughness of the plasma etched Nb samples to the typical surface roughness of traditional cavity processing

Table 9: RMS results for each sample and experimental configuration. In all cases, the scan area was 50 μm $\times$ 50 μm. There were two polished and unetched samples with RMS roughness < 30 nm.

Identifier	Sample	T (K)	RMS Roughness (nm)
	S1	645 ± 10.25	91.35
	S2	471 ± 7.56	110.00
T1	S3	667 ± 10.40	343.00
	S4	625 ± 0.82	139.00
	S1	609 ± 2.20	44.95
	S2	493 ± 6.30	48.80
T2	S3	590 ± 6.96	50.45
	S4	576 ± 0.90	44.95
	S1	517 ± 12.04	34.75
	S2	525 ± 1.54	59.85
T3/B1	S3	500 ± 7.00	103.90
	S4	468 ± 5.18	68.90
	S1	659 ± 11.19	66.65
	S2	681 ± 2.69	91.55
T4	S3	640 ± 7.59	37.40
	S4	588 ± 4.18	109.00
	S1	455 ± 7.78	74.40
	S2	422 ± 3.42	76.40
T5	S3	484 ± 2.15	58.05
	S4	475 ± 4.50	37.00
	S1	536 ± 4.81	30.80
	S2	493 ± 3.28	99.75
B2	S3	594 ± 1.08	144.50
	S4	537 ± 4.56	70.90

techniques. The typical resulting RMS surface roughness for the Buffered Chemical Polished (BCP) chemical process is about $1.6 \pm 0.42\,\mu$m [100], while Electropolishing (EP) can achieve better results with a typical value of about $0.34 \pm 0.11\,\mu$m [101] for a 50 μm $\times$ 50 μm scan area [102]. As seen in Table 9, the highest RMS surface roughness is $\approx$ 150 nm. Additionally, these samples did not undergo any additional processing or cleaning other than simple hand cleaning with methanol and isopropyl alcohol. These results are certainly promising, but the inhomogeneity of the final sample surface is a concern.

9.3.3 SURFACE COMPOSITION AND IMPURITIES

The experimental requirements for RIE of the inner surface of a cylindrical surface inherently introduces the samples to potential impurities through the experimental components. Ideally, all of these individual pieces would be made of specialized highly corrosive resistant materials, but this is monetarily infeasible, especially for a developmental technology still in its adolescence. Therefore, the introduction of foreign impurities on the surface of the samples is inevitable, especially with the necessary use of chlorine for the RIE process. However, identifying the source and amount of impurities as they are related to the experimental parameters can aid in the development of tactics for their mitigation. In this aim, the Phenom SEM is particularly useful as atomic and weight concentrations of elements on a material surface can be explicitly measured. The most significant sources of experimentally detrimental impurities and suggestions for their reduction are outlined in this section.

In the case of this particular experiment, the most obvious source of impurities is carbon, which can be embedded into the surface from the polishing process. To a lesser extent, trace amounts of silicon can be found in some instances due to the fiberglass insulation on the thermocouple wires. Additionally, etching of the stainless steel components of the chamber can occur, especially at higher temperatures and Cl_2 concentrations. These impurities have indeed caused issues in previous works [1, 38] and efforts were made to reduce them by constructing the gas and power delivery components out of niobium or nickel based alloys as they are constantly exposed to the reactive discharge (see Section 6.1). The complete elimination of stainless steel in the system is impractical as it is the standard material used in the production of commercial vacuum chamber components. However, the material change of the gas and power greatly reduced the amount of impurities as a whole.

Certainly an increased temperature can help alleviate these issues in some cases as the impurities would remain volatile enough to be pumped out of the system. However, the temperatures of the system, particularly when the chamber is heated further from the outside to increase the substrate temperature, can facilitate reactions with the stainless steel chamber walls and the copper gaskets used for the vacuum seal. Indeed, impurities related to these materials were found on local regions of samples in the T1 configuration as seen in Figure 77.

Element	Atomic Conc.	Weight Conc.
Oxygen	63.86	29.88
Copper	16.36	30.4
Niobium	10.98	29.83
Chlorine	7.39	7.66
Iron	0.71	1.16
Chromium	0.71	1.07
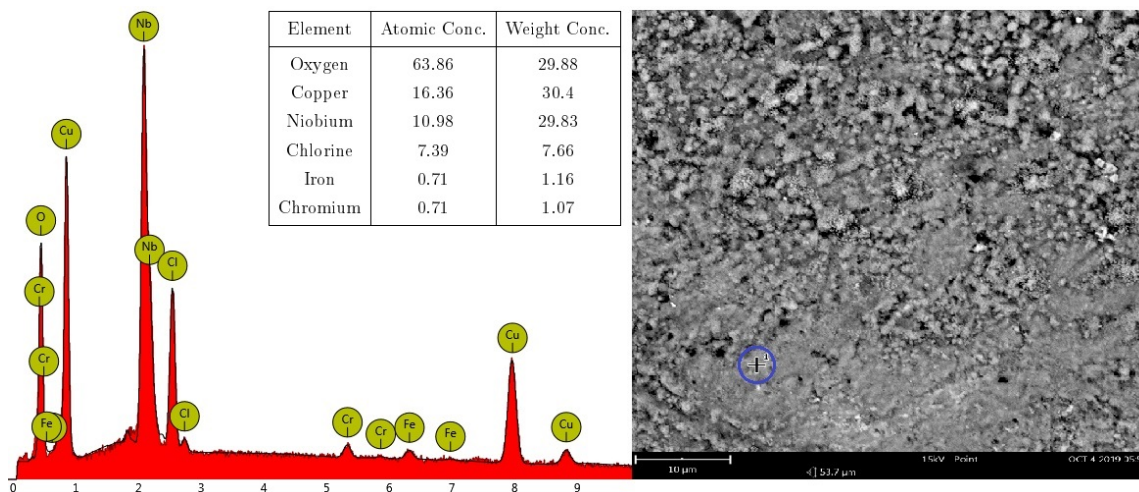
Figure 77: Material spectrum, spot image, and composition table for sample 1 in the T1 experimental configuration. The location corresponding to the material spectrum is circled in blue. Configuration information can be found in Table 9 and sample location description can be found in Figure 51.

It seems that this is the first instance of the formation of Cu impurities in any of the related RIE studies at Old Dominion University. This is due to the high temperatures used in this experiment (T1 in particular) compared to the previous work as discussed in Section 9.2.1 [1]. It seems that the temperature was high enough to create copper chlorides, which were quickly deposited on the surfaces of the apparatus. Additionally, chromium from the stainless steel parts, and more specifically the nuts used to compression fit the thermocouples (see Figure 50), reacted with chlorine to make chromic chloride ($CrCl_3$) which is discernible by its distinct purple color. In addition, the Nb conical gas inlet (shown in Figure 32) was destroyed during the etching experiment. This gas feed was used throughout the studies outlined in Chapters 7 and 8 which used comparable experimental conditions with the exception of the surface temperature. The higher surface roughness of the samples in the T1

experiment are attributed to these effects. Thus, it was necessary to explore possible options to eliminate the production of copper impurities and the destruction of the gas feed components.

The commercially available replacements for Cu gaskets include silver, gold, and nickel. Among these, only nickel can withstand the combination of high temperatures and corrosiveness of Cl_2. As the price of the solid Ni gaskets were exorbitant (roughly 48 times more expensive per gasket) we elected to instead have Cu gaskets electrolytically Ni plated by a local metal plating business. It was expected that these would work in the same manner as the solid Ni gaskets as the only requirements were that no copper was exposed and sufficient vacuum can be achieved. This study was conducted in tandem with the surface roughness and etch rate experiments to utilize the SEM measurements and see the effects of these material changes on these surface studies. In addition, the destruction of the gas feed led to the development of the laminar showerhead gas inlet shown in Figures 33 and 34. The laminar showerhead was constructed of a nickel alloy (Inconel^{TM} 600) that has particularly high corrosion resistance. The different gasket material and gas feed configurations are listed in Table 10 for each sample experiment.

Table 10: Gasket material and gas feed configuration for each sample experiment.

Identifier	Gasket Material/Gas Feed Configuration
T1	Conical niobium gas feed (destroyed). Copper gaskets only.
T2	No gas feed. Single 6" Ni plated gasket in reaction region.
T3/B1	No gas feed. All Ni plated gaskets for chamber components.
T4	No gas feed. All Ni plated gaskets for chamber components.
T5	Laminar flow gas feed. Two 6" Ni plated gaskets in reaction region.
B2	Laminar flow gas feed. Two 6" Ni plated gaskets in reaction region.

The 'reaction region' in Table 10 refers to the gaskets located on either side of the cavity structure shown in Figures 29 and 31. There are a couple of general comments that can be made for all of the samples for experiments T2-5 and B2. In all samples, even those that were not plasma etched, there exists a small fraction of phosphorus on the surface. The inclusion of this element on the sample surface is puzzling and there is no known reason for its existence. However it is possible that the SEM is mistaking an artifact of the Nb peak in the spectrum as P. Regardless, the concentration of P

is ignored when considering the surface concentration of impurities. Secondly, there are no measured traces of Cu on any sample in any of these configurations. This is an encouraging development as the use of nickel or nickel plated pieces could be an effective, experimentally feasible, and relatively inexpensive method of preventing Cu and other stainless steel impurities. It is evident that at these high temperatures it is imperative that durable anti-corrosive materials be used when possible to reduce byproducts and increase the longevity of the apparatus.

In terms of impurity concentration, carbon is by far the most abundant across all samples and experimental configurations. The amount of carbon has a large variation in general, but it seems that samples at lower temperatures retain higher amounts of carbon impurities, which is not particularly surprising. The second highest would be nickel impurities, which were almost explicitly located on samples 2 and 3. Other impurities include Cr, Fe, and trace amounts of Si which are all typically found indiscriminately in small amounts. Examples of surface locations with high concentrations of impurities can be seen in Figure 78.
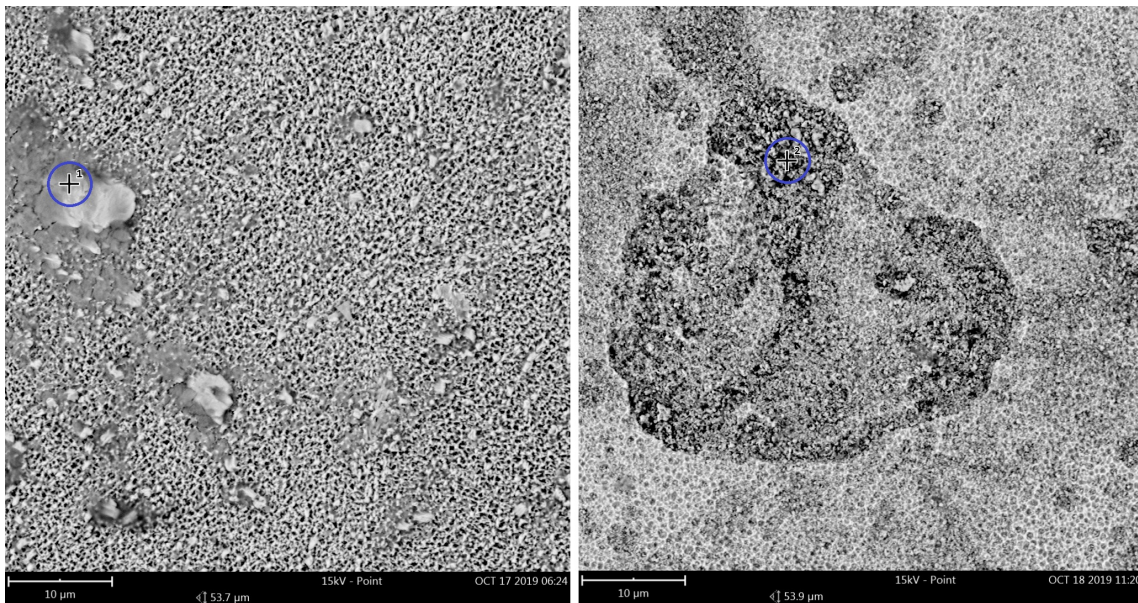
Figure 78: Left: Example of a location with high carbon deposit (C: 38.83%). Right: Example of a location with high stainless steel impurity deposits (Ni: 59.06 % Cr: 2.13 % Fe: 0.92 %).

It is evident that the reduction of chemical byproducts and embedded impurities through improved material design, uniform cavity heating, and the development of an

in situ cleaning process are some of the most significant limitations of this technology at its present state, and therefore require further study.

Relative Nb and O Concentration

Niobium naturally oxidizes instantaneously due to the large bonding energy between the Nb and O atoms [22]. For the purposes of superconductivity, the metallic interface has a thin NbO layer that acts as a protective barrier for the superconducting bulk Nb below the surface. However, the oxidation is often dominated by the production of crystalline Nb_2O_5 which creates strains and basically 'eats' into the bulk Nb [22, 103]. Measuring the relative concentration between Nb and O on the surface can indicate whether the surface is composed of NbO or Nb_2O_5. The atomic masses of Nb and O are 41 and 8 amu, respectively, so an atomic concentration of 67 % Nb and 33 % O is indicative of a Nb_2O_5 surface layer.

The vast majority of the samples indeed show atomic concentrations that are indicative of a Nb_2O_5 surface layer. However, there are cases in which a higher Nb concentration is seen in a macroscopic region, or a higher O concentration is seen in a macroscopic region. Examples of two such regions are shown in Figure 79.
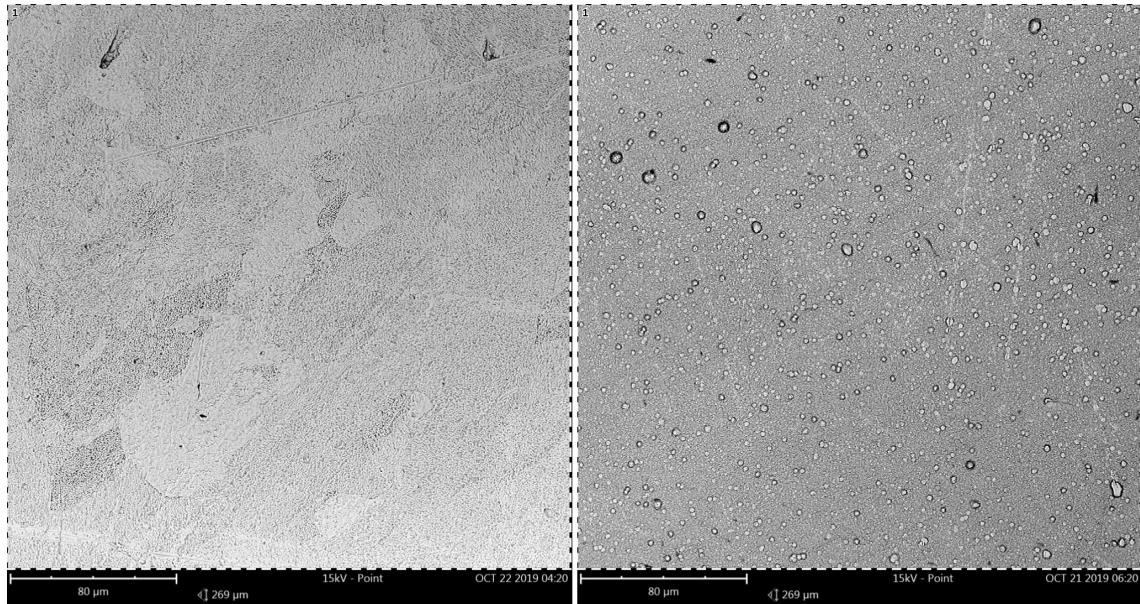
Figure 79: Left: Example of a region scan with high Nb concentration (Nb: 71.94 % O: 24.06 %). Right: Example of a region scan with high O concentration (O: 62.14 % Nb: 35.08 %).

The difference in surface structures can be seen clearly as the O heavy sample region has a great deal of blemishes. According to corresponding spot scans (not pictured) the darker regions around the blemishes are local areas of high relative O. As these two particular cases are exceptions, further study is required to fully understand how these surfaces came to be.

9.4 SUMMARY

Experiments were conducted on small Nb coupon samples to study the effect of the substrate surface temperature and driven electrode DC bias on their respective etch rate and surface roughness profiles. Four samples were etched simultaneously for each set of external parameters at different locations within the chamber corresponding to different local regions of the discharge. As a function of temperature, the etch rates of samples corresponding to the same location show an Arrhenius type dependence that corresponds to a strong chemical etching component of the process. This confirms previous measurements and observations by Upadhyay [1] where a similar relationship was found, although with a lower activation energy. At similar temperatures, an increase in the positive DC bias seems to increase the etch rate, but more data is required in order to substantiate this claim.

The surface roughness of each sample was measured using an atomic force microscope (AFM) for each sample. The AFM is capable of producing 2D and 3D images of the surface profile, while also providing the RMS surface roughness in a specific scan region. While an increase in temperature seems to cause pit-like defects on the surface based on qualitative observations of the images, the RMS surface results show no direct correlation between the two parameters. An increase in the positive DC bias also seems to modify the surface to a more 'bumpy' structure indicative of an increase in the physical sputtering of the sample, but once again the RMS roughness shows no correlation between the two parameters.

A scanning electron microscope (SEM) was used to provide high definition optical images of the surface and measure the atomic composition of the surface. The nature of the experiment introduces a great deal of potential surface impurities that could be detrimental to the surface characteristics and superconducting properties of Nb. The SEM is used to investigate the sources of surface impurities that are embedded during plasma etching under various conditions. The intention is to use this information to develop material and engineering solutions for the mitigation of these problematic

impurities. Among the most significant source of impurities are the copper gaskets that are used to seal the vacuum chamber, particularly at high temperatures. The solution to this issue was to plate the gaskets with nickel as it has a much higher threshold for corrosive reactions. The gaskets can be plated and implemented with no concerns for the sealing effectiveness, while copper impurities were completely avoided. It is suggested that this also be applied to a great deal of the other vacuum components used for the plasma etch process as stainless steel impurities can be problematic, and nickel plating is a relatively straightforward and cheap process, especially compared to the production of the same pieces using solid nickel.

Due to the highly destructive nature of the discharge at high temperatures the conical gas feed delivery system was destroyed in the first sample etching experiment. Therefore, a replacement gas feed was designed and produced with particular considerations given to the material and uniform gas delivery. The final product was a laminar flow showerhead made of highly corrosive resistant nickel alloys. While quantitative comparisons cannot be made at this time, it is the opinion of the author that this design is far superior to the previous design in both longevity and uniform gas delivery considerations.

CHAPTER 10

CONCLUSION

This dissertation presents work that is a continuation of the development of a Reactive Ion Etching (RIE) technology for the processing of superconducting radio-frequency (SRF) cavities. Reactive Ion Etching, or plasma etching, is a dry etch process that could serve as a beneficial addition to or possible replacement of the current wet etch cavity processing routines. The previous work on this front established empirical relationships between the user controlled external parameters and the removal of surface layers of the niobium cavity. However, missing from that study, and a focus of this one, is the connection of these external etching parameters to the physical description of the plasma. The measurement and understanding of these plasma parameters are particularly important for the future of the technology. A more complete understanding of the process at large would allow for the development of computer "jelly models" that aid in the physical description of the etching system as a whole. A computer model, in conjunction with the experimental results herein, would aid in the development of an effective and controllable etching routine. In order to etch the inner surface of a cavity, the plasma must be created within the cavity, meaning that a powered electrode must be placed in the center. This type of configuration creates a coaxial plasma instead of a flat parallel plate plasma commonly used in industrial applications. This offers the opportunity to study the physics of a plasma configuration of which very little is known.

The plasma parameters of particular interest for this work include the densities of the first four excited states of Argon (1s states in Paschen notation), the electron density (n_e), and the electron temperature (T_e) in both Argon and Ar/Cl$_2$ plasmas. The 1s states of Argon are useful as they are involved in a majority of the higher energy (>10 eV) excitation and radiative decay processes, as well as ionization from collisions of excited atoms. Additionally, there exist a large array of spectral lines that correspond to transitions from the next ten excited levels of Argon (2p levels in Paschen notation) that are easily measurable with basic spectroscopic equipment. Information about the significant kinetic processes of these excited states can be measured from these transitions and applied to a collisional radiative model (CRM)

to find information about the distribution of electrons in the respective discharge. Electrons are the primary source of energy transfer in the discharge due to their high mobility in the oscillating electric fields. Electrons provide energy to the Ar and Cl atoms through collisions causing ionization and excitation. Thus, knowledge of n_e and the average electron energy T_e as functions of the external is imperative for the development of a consistent discharge model.

The densities of the first four excited states in Argon were measured using two distinctly different optical spectroscopy techniques. These excited state densities were measured for both Ar and Ar/Cl_2 mixtures of varying concentrations as the Ar/Cl_2 mixture is necessary for etching of SRF cavities. The two measurement techniques, tunable diode laser absorption spectroscopy (TDLAS) and the optical emission spectroscopy branching fraction method (OES-BFM), were conducted as pertinent external parameters were varied to develop a working model to describe the discharge. TDLAS is used to measure the Doppler broadened profile of a spectral line by sweeping a tunable diode laser across the resonant frequency of the transition. The absorption profile is representative in the velocity distribution of the absorbing species, and can be used to calculate the population density. OES-BFM uses the relationship between the optical emission of spectral lines and the density of the final state. In particular, the connection between the resonant reabsorption of photons traveling through the plasma and the absorbing species is utilized, therefore circumventing the need for any *a priori* knowledge of the energy distribution. As a direct comparison, TDLAS is much more effective than OES-BFM at measuring the excited state densities with accuracy and consistency, while OES-BFM has the significant advantage of being a more robust method capable of measuring all four excited states simultaneously. The results of this work show agreement between the two methods up to a factor of three for the vast majority of the external parameters studied.

The results from the optical spectroscopy studies were then applied to a collisional radiative model (CRM) to calculate pertinent information about the electron energy and density in the discharge. The CRM uses the balancing of the population and depopulation processes of excited states (2p levels of Argon in this case) to calculate unknown quantities involved in the transitions. In this case, the 1s state densities are among the major population channels of the 2p levels, and their densities measured from the diagnostic methods can be used to find the electron temperature and density. Additionally, an alternative method found in the literature for calculating

the electron density using the ratio of the $1s_5$ metastable level and $1s_4$ resonant level was explored. We have established significant relationships between the etching and plasma parameters that are very useful for the future design of computer "jelly models" and etching experiments. Among the most surprising and exciting results is the magnitude of the electron density which is in the order of 10^{18} m^{-3}. Densities of these magnitudes are not typically found in capacitively coupled discharges and require higher power or magnetic sources. This fact alone suggests that the simple geometrical change from typical parallel plate to coaxial configurations could provide the same benefits for etching processes that would normally require a significant increase in power.

As an extension to the etching studies performed in previous works, the effect of RIE on the final surface structure of niobium was studied. The surface roughness and composition of bulk niobium is directly related to its inherent superconducting properties. In this aim niobium coupon samples were plasma etched to study the effects of substrate temperature and the driven electrode DC bias on the final surface as these are understood to be directly related to the chemical and physical etching components, respectively. Four samples were etched simultaneously for each set of external parameters at different locations within the chamber corresponding to different local regions of the discharge. An atomic force microscope (AFM) was used to measure the surface roughness characteristics of each sample, while a scanning electron microscope (SEM) was used to measure the surface composition. In general, plasma etched niobium samples show an RMS surface roughness lower than the standard wet chemical etch processes typical of cavity processing. The experimental requirements of this plasma etch process forces the introduction of the etching substrate to potential impurities that may arise from the experimental chamber, particularly when corrosive halogen gases are used. The SEM measurements were used to help identify and eliminate significant sources of impurities related to the construction of the apparatus. It was found that using nickel and nickel alloys provide significant benefits in the reduction of detrimental impurities that would otherwise be unavoidable.

To conclude, we have measured the plasma parameters as a function of external etching parameters of a cylindrical coaxial capacitively coupled plasma designed for the processing of Nb SRF cavities. The plasma parameters are important inputs for computational models that can more effectively model the discharge chamber

as a whole. Surface properties and roughness profiles were studied as functions of parameters that pertain to the etching mechanisms of the Ar/Cl_2 plasma. Basic relationships between the external parameters and the etch rate, surface roughness, and impurity deposition have been established. These investigations were the next logical steps in the advancement of RIE technology for the processing of Nb SRF cavities and provide a framework for the establishment of effective, consistent, and controllable plasma etching routines that could significantly improve the operation of superconducting particle accelerators around the world.

REFERENCES

[1] Janardan Upadhyay. *Plasma Processing of Superconducting Radio Frequency Cavities*. PhD thesis, Old Dominion University, 2016.

[2] Allan J. Lichtenberg Michael A. Lieberman. *Principles of Plasma Discharges and Materials Precessing*. John Wiley & Sons Inc., 1994.

[3] A von Keudell and V Schulz von der Gathen. Foundations of low-temperature plasma physics—an introduction. *Plasma Sources Science and Technology*, 26(11):113001, oct 2017.

[4] M Nikolic. *Characterization of Microwave Discharge Plasmas for Surface Processing*. PhD thesis, Old Dominion University, 2013.

[5] H. R. Koenig and L. I. Maissel. Application of rf discharges to sputtering. *IBM Journal of Research and Development*, 14(2):168–171, March 1970.

[6] Janardan Upadhyay, Svetozar Popović, Leposova Vušković, Do Im, Anne-Marie Valente, and H Phillips. Plasma processing of large surfaces with application to srf cavity modification. Technical report, Thomas Jefferson National Accelerator Facility, Newport News, VA (United States), 2013.

[7] Janardan Upadhyay, Do Im, S Popović, A-M Valente-Feliciano, L Phillips, and L Vušković. Etching mechanism of niobium in coaxial ar/cl$_2$ radio frequency plasma. *Journal of Applied Physics*, 117(11):113301, 2015.

[8] Janardan Upadhyay, Do Im, Svetozar Popović, Leposava Vušković, Anne-Marie Valente-Feliciano, and Larry Phillips. Reversal of the asymmetry in a cylindrical coaxial capacitively coupled ar/cl$_2$ plasma. *Journal of Vacuum Science & Technology A: Vacuum, Surfaces, and Films*, 33(6):061309, 2015.

[9] J. Upadhyay, J. Peshl, S. Popović, A.-M. Valente-Feliciano, and L. Vušković. Effect of self-bias on cylindrical capacitive discharge for processing of inner walls of tubular structures–case of srf cavities. *AIP Advances*, 8(8):085008, 2018.

[10] V. A. Godyak, R. B. Piejak, and B. M. Alexandrovich. Probe diagnostics of non-maxwellian plasmas. *Journal of Applied Physics*, 73(8):3657–3663, 1993.

[11] John B Boffard, RO Jung, Chun C Lin, and AE Wendt. Optical emission measurements of electron energy distributions in low-pressure argon inductively coupled plasmas. *Plasma Sources Science and Technology*, 19(6):065001, 2010.

[12] J T Gudmundsson. On the effect of the electron energy distribution on the plasma parameters of an argon discharge: a global (volume-averaged) model study. *Plasma Sources Science and Technology*, 10(1):76–81, jan 2001.

[13] M. J. Druyvesteyn and F. M. Penning. The mechanism of electrical discharges in gases of low pressure. *Rev. Mod. Phys.*, 12:87–174, Apr 1940.

[14] John B Boffard, Garrett A Piech, Mark F Gehrke, LW Anderson, and Chun C Lin. Measurement of electron-impact excitation cross sections out of metastable levels of argon and comparison with ground-state excitation. *Physical Review A*, 59(4):2749, 1999.

[15] John B Boffard, Chun C Lin, and Charles A DeJoseph Jr. Application of excitation cross sections to optical plasma diagnostics. *Journal of Physics D: Applied Physics*, 37(12):R143, 2004.

[16] John B Boffard, B Chiaro, Tobin Weber, and Chun C Lin. Electron-impact excitation of argon: Optical emission cross sections in the range of 300–2500 nm. *Atomic Data and Nuclear Data Tables*, 93(6):831–863, 2007.

[17] John B Boffard, RO Jung, LW Anderson, and CC Lin. Electron-impact excitation of rare-gas atoms from the ground level and metastable levels. *Advances in Atomic Molecular and Optical Physics*, 54:320, 2007.

[18] J Ethan Chilton, John B Boffard, R Scott Schappe, and Chun C Lin. Measurement of electron-impact excitation into the 3 p 5 4 p levels of argon using fourier-transform spectroscopy. *Physical Review A*, 57(1):267, 1998.

[19] O Zatsarinny and K Bartschat. B-spline breit–pauli r-matrix calculations for electron collisions with argon atoms. *Journal of Physics B: Atomic, Molecular and Optical Physics*, 37(23):4693–4706, nov 2004.

[20] Oleg Zatsarinny, Yang Wang, and Klaus Bartschat. Electron-impact excitation of argon at intermediate energies. *Phys. Rev. A*, 89:022706, Feb 2014.

[21] Arati Dasgupta, M Blaha, and JL Giuliani. Electron-impact excitation from the ground and the metastable levels of ar i. *Physical review A*, 61(1):012703, 1999.

[22] Gianluigi Ciovati. *Investigation Of The Superconducting Properties Of Niobium Radio-Frequency Cavities*. PhD thesis, Old Dominion University, 2005.

[23] Hasan S Padamsee. Superconducting radio-frequency cavities. *Annual review of nuclear and particle science*, 64:175–196, 2014.

[24] B. Aune, R. Bandelmann, D. Bloess, B. Bonin, A. Bosotti, M. Champion, C. Crawford, G. Deppe, B. Dwersteg, D. A. Edwards, H. T. Edwards, M. Ferrario, M. Fouaidy, P.-D. Gall, A. Gamp, A. Gössel, J. Graber, D. Hubert, M. Hüning, M. Juillard, T. Junquera, H. Kaiser, G. Kreps, M. Kuchnir, R. Lange, M. Leenen, M. Liepe, L. Lilje, A. Matheisen, W.-D. Möller, A. Mosnier, H. Padamsee, C. Pagani, M. Pekeler, H.-B. Peters, O. Peters, D. Proch, K. Rehlich, D. Reschke, H. Safa, T. Schilcher, P. Schmüser, J. Sekutowicz, S. Simrock, W. Singer, M. Tigner, D. Trines, K. Twarowski, G. Weichert, J. Weisend, J. Wojtkiewicz, S. Wolff, and K. Zapfe. Superconducting tesla cavities. *Phys. Rev. ST Accel. Beams*, 3:092001, Sep 2000.

[25] Walther Meissner and Robert Ochsenfeld. Ein neuer effekt bei eintritt der supraleitfähigkeit. *Naturwissenschaften*, 21(44):787–788, 1933.

[26] Heike Kamerligh-Onnes. The superconductivity of mercury. *Comm. Phys. Lab. Univ. Leiden*, 122:122–124, 1911.

[27] C Jo Gorter and HBG Casimir. The thermodynamics of the superconducting state. *Z. tech. Phys*, 15:539–42, 1934.

[28] Fritz London and Heinz London. The electromagnetic equations of the supraconductor. *Proceedings of the Royal Society of London. Series A-Mathematical and Physical Sciences*, 149(866):71–88, 1935.

[29] Alfred Brian Pippard and William Lawrence Bragg. An experimental and theoretical study of the relation between magnetic field and current in a superconductor. *Proceedings of the Royal Society of London. Series A. Mathematical and Physical Sciences*, 216(1127):547–568, 1953.

[30] VL Ginzburg and LD Landau. Phenomenological theory. *J. Exp. Theor. Phys. USSR*, 20:1064, 1950.

[31] A. Gurevich. Nonlocal josephson electrodynamics and pinning in superconductors. *Phys. Rev. B*, 46:3187–3190, Aug 1992.

[32] John Bardeen, Leon N Cooper, and John Robert Schrieffer. Theory of superconductivity. *Physical review*, 108(5):1175, 1957.

[33] Hasan Padamsee, Jens Knobloch, Tom Hays, et al. *RF superconductivity for accelerators*, volume 2011. Wiley Online Library, 2008.

[34] Ralph Howard Fowler and Lothar Nordheim. Electron emission in intense electric fields. *Proceedings of the Royal Society of London. Series A, Containing Papers of a Mathematical and Physical Character*, 119(781):173–181, 1928.

[35] Ari Palczewski. R & d progress in srf surface preparation with centrifugal barrel polishing (cbp) for both nb and cu. Technical report, Thomas Jefferson National Accelerator Facility, Newport News, VA (United States), 2013.

[36] J Upadhyay, Do Im, S Popović, A-M Valente-Feliciano, L Phillips, and L Vušković. Plasma processing of large curved surfaces for superconducting rf cavity modification. *Physical Review Special Topics-Accelerators and Beams*, 17(12):122001, 2014.

[37] Janardan Upadhyay, Do Im, J Peshl, M Bašović, S Popović, A-M Valente-Feliciano, L Phillips, and Leposova Vušković. Apparatus and method for plasma processing of srf cavities. *Nuclear Instruments and Methods in Physics Research Section A: Accelerators, Spectrometers, Detectors and Associated Equipment*, 818:76–81, 2016.

[38] J Upadhyay, A Palczewski, S Popović, A-M Valente-Feliciano, Do Im, HL Phillips, and L Vušković. Cryogenic rf test of the first srf cavity etched in an rf ar/cl$_2$ plasma. *AIP Advances*, 7(12):125016, 2017.

[39] M. A. Lieberman and S. E. Savas. Bias voltage in finite length, cylindrical and coaxial radio frequency discharges. *Journal of Vacuum Science & Technology A*, 8(3):1632–1641, 1990.

[40] E. Kawamura, M. A. Lieberman, A. J. Lichtenberg, and E. A. Hudson. Capacitive discharges driven by combined dc/rf sources. *Journal of Vacuum Science & Technology A*, 25(5):1456–1474, 2007.

[41] E Kawamura, A J Lichtenberg, and M A Lieberman. Secondary electrons in rf and dc/rf capacitive discharges. *Plasma Sources Science and Technology*, 17 (4):045002, aug 2008.

[42] Wei Jiang, Xiang Xu, Zhong-Ling Dai, and You-Nian Wang. Heating mechanisms and particle flow balancing of capacitively coupled plasmas driven by combined dc/rf sources. *Physics of Plasmas*, 15(3):033502, 2008.

[43] Vincent M Donnelly and Avinoam Kornblit. Plasma etching: Yesterday, today, and tomorrow. *Journal of Vacuum Science & Technology A: Vacuum, Surfaces, and Films*, 31(5):050825, 2013.

[44] M Rašković, J Upadhyay, L Vušković, S Popović, AM Valente-Feliciano, and L Phillips. Plasma treatment of bulk niobium surface for superconducting rf cavities: Optimization of the experimental conditions on flat samples. *Physical Review Special Topics-Accelerators and Beams*, 13(11):112001, 2010.

[45] CJ Mogab. The loading effect in plasma etching. *Journal of the Electrochemical Society*, 124(8):1262–1268, 1977.

[46] VM Donnelly, DL Flamm, CW Tu, and DE Ibbotson. Temperature dependence of inp and gaas etching in a chlorine plasma. *Journal of The Electrochemical Society*, 129(11):2533–2537, 1982.

[47] SJ Pearton, AB Emerson, UK Chakrabarti, E Lane, KS Jones, KT Short, Alice E White, and TR Fullowan. Temperature dependence of reactive ion etching of gaas with ccl2f2: O2. *Journal of Applied Physics*, 66(8):3839–3849, 1989.

[48] H. M. Mott-Smith and Irving Langmuir. The theory of collectors in gaseous discharges. *Phys. Rev.*, 28:727–763, Oct 1926.

[49] VA Godyak and VI Demidov. Probe measurements of electron-energy distributions in plasmas: what can we measure and how can we achieve reliable results? *Journal of Physics D: Applied Physics*, 44(23):233001, 2011.

[50] Francis F. Chen. Langmuir probe analysis for high density plasmas. *Physics of Plasmas*, 8(6):3029–3041, 2001.

[51] J E Allen, R L F Boyd, and P Reynolds. The collection of positive ions by a probe immersed in a plasma. *Proceedings of the Physical Society. Section B*, 70(3):297–304, mar 1957.

[52] Bernstein Ira B. and Rabinowitz Irving N. Theory of electrostatic probes in a low density plasma. *The Physics of Fluids*, 2(2):112–121, 1959.

[53] M. J. Druyvesteyn. Der niedervoltbogen. *Zeitschrift für Physik*, 64(11):781–798, Sep 1930.

[54] Nancy L. Bassett and Demetre J. Economou. Effect of cl2 additions to an argon glow discharge. *Journal of Applied Physics*, 75(4):1931–1939, 1994.

[55] Ramamurti Shankar. *Principles of quantum mechanics*. Springer Science & Business Media, 2012.

[56] A. Kramida, Yu. Ralchenko, J. Reader, and and NIST ASD Team. NIST Atomic Spectra Database (ver. 5.6.1), [Online]. Available: `https://physics.nist.gov/asd` [2019, May 31]. National Institute of Standards and Technology, Gaithersburg, MD., 2018.

[57] M Schulze, A Yanguas-Gil, A von Keudell, and P Awakowicz. A robust method to measure metastable and resonant state densities from emission spectra in argon and argon-diluted low pressure plasmas. *Journal of Physics D: Applied Physics*, 41(6):065206, feb 2008.

[58] John B Boffard, RO Jung, Chun C Lin, and AE Wendt. Measurement of metastable and resonance level densities in rare-gas plasmas by optical emission spectroscopy. *Plasma Sources Science and Technology*, 18(3):035017, 2009.

[59] V. P. Sushkov, H. T. Do, and R. Hippler. Application of the escape factor method for determination of excited states densities in a low-pressure argon radio-frequency discharge. *Contributions to Plasma Physics*, 53(7):549–559, 2013.

[60] Marcel Fiebrandt, Bastian Hillebrand, Stefan Spiekermeier, Nikita Bibinov, Marc Böke, and Peter Awakowicz. Measurement of ar resonance and metastable level number densities in argon containing plasmas. *Journal of Physics D: Applied Physics*, 50(35):355202, aug 2017.

[61] Jiang Li, Fei-Xiang Liu, Xi-Ming Zhu, and Yi-Kang Pu. The spatially resolved measurements of the atomic densities in argon paschen 1s levels by OES in a capacitively coupled plasma. *Journal of Physics D: Applied Physics*, 44(29): 292001, jul 2011.

[62] T. Holstein. Imprisonment of resonance radiation in gases. *Phys. Rev.*, 72: 1212–1233, Dec 1947.

[63] R.W.P. McWhirter. In R. H. Huddlestone and S. L. Leonard, editors, *Plasma Diagnostic Techniques*, page 201, 1965.

[64] Yu Golubovskii, S Gorchakov, and D Uhrlandt. Transport mechanisms of metastable and resonance atoms in a gas discharge plasma. *Plasma Sources Science and Technology*, 22(2):023001, feb 2013.

[65] Xi-Ming Zhu, Zhi-Wen Cheng, Yi-Kang Pu, and Uwe Czarnetzki. Escape factors for paschen 2p–1s emission lines in low-temperature ar, kr, and xe plasmas. *Journal of Physics D: Applied Physics*, 49(22):225204, may 2016.

[66] R Mewe. Relative intensity of helium spectral lines as a function of electron temperature and density. *British Journal of Applied Physics*, 18(1):107–118, jan 1967.

[67] R. Mewe. Simplified model for ionization and recombination in a hydrogenic plasma with resonance radiation trapping. *Zeitschrift für Naturforschung A*, 25(12), 1970.

[68] Xi-Ming Zhu, Zhi-Wen Cheng, Emile Carbone, Yi-Kang Pu, and Uwe Czarnetzki. Determination of state-to-state electron-impact rate coefficients between ar excited states: a review of combined diagnostic experiments in afterglow plasmas. *Plasma Sources Science and Technology*, 25(4):043003, jul 2016.

[69] Xi-Ming Zhu and Yi-Kang Pu. A simple collisional–radiative model for low-temperature argon discharges with pressure ranging from 1 pa to atmospheric

pressure: kinetics of paschen 1s and 2p levels. *Journal of Physics D: Applied Physics*, 43(1):015204, dec 2009.

[70] J T Gudmundsson and E G Thorsteinsson. Oxygen discharges diluted with argon: dissociation processes. *Plasma Sources Science and Technology*, 16(2): 399–412, apr 2007.

[71] Chun C Lin. Measurements of electron-impact excitation cross sections out of the ground and metastable levels of rare gases with applications to low-temperature plasmas. *Contributions to Plasma Physics*, 44(5-6):405–412, 2004.

[72] J Vlcek. A collisional-radiative model applicable to argon discharges over a wide range of conditions. i. formulation and basic data. *Journal of Physics D: Applied Physics*, 22(5):623–631, may 1989.

[73] M C Bordage, S F Biagi, L L Alves, K Bartschat, S Chowdhury, L C Pitchford, G J M Hagelaar, W L Morgan, V Puech, and O Zatsarinny. Comparisons of sets of electron–neutral scattering cross sections and swarm parameters in noble gases: III. krypton and xenon. *Journal of Physics D: Applied Physics*, 46(33): 334003, aug 2013.

[74] Sarah Siepa, Stephan Danko, Tsanko V Tsankov, Thomas Mussenbrock, and Uwe Czarnetzki. On the oes line-ratio technique in argon and argon-containing plasmas. *Journal of Physics D: Applied Physics*, 47(44):445201, 2014.

[75] Xi-Ming Zhu, Tsanko Vaskov Tsankov, Dirk Luggenhölscher, and Uwe Czarnetzki. 2d collisional-radiative model for non-uniform argon plasmas: with or without 'escape factor'. *Journal of Physics D: Applied Physics*, 48(8):085201, feb 2015.

[76] Xi-Ming Zhu and Yi-Kang Pu. Optical emission spectroscopy in low-temperature plasmas containing argon and nitrogen: determination of the electron temperature and density by the line-ratio method. *Journal of Physics D: Applied Physics*, 43(40):403001, sep 2010.

[77] Shicong Wang, Amy E. Wendt, John B. Boffard, Chun C. Lin, Svetlana Radovanov, and Harold Persing. Noninvasive, real-time measurements of plasma parameters via optical emission spectroscopy. *Journal of Vacuum Science & Technology A*, 31(2):021303, 2013.

[78] John B Boffard, RO Jung, Chun C Lin, LE Aneskavich, and AE Wendt. Argon 420.1–419.8 nm emission line ratio for measuring plasma effective electron temperatures. *Journal of Physics D: Applied Physics*, 45(4):045201, 2012.

[79] Zhi-Wen Cheng, Xi-Ming Zhu, Fei-Xiang Liu, and Yi-Kang Pu. Determination of the rate coefficients of the electron-impact excitation from the metastable states to 2p states of argon by the emission line ratios in an afterglow plasma. *Journal of Physics D: Applied Physics*, 47(27):275203, jun 2014.

[80] Zhi-Wen Cheng, Xi-Ming Zhu, Fei-Xiang Liu, and Yi-Kang Pu. Determination of the rate coefficient of the electron-impact excitation from the argon resonance states (1s2 and 1s4) to 2p states by the emission line ratio in an afterglow plasma. *Plasma Sources Science and Technology*, 24(2):025025, mar 2015.

[81] Jiang Li, Xi-Ming Zhu, and Yi-Kang Pu. The population distribution of argon atoms in paschen 1s levels in an inductively coupled plasma. *Journal of Physics D: Applied Physics*, 43(34):345202, 2010.

[82] Sandra Schröter, Hendrik Bahre, Marc Böke, and Jörg Winter. The role of argon metastables in an inductively coupled plasma for treatment of pet. *Plasma Processes and Polymers*, 11:239–246, 2014.

[83] S. Hübner, N. Sadeghi, E. A. D. Carbone, and J. J. A. M. van der Mullen. Density of atoms in ar* (3p^{5}4s) states and gas temperatures in an argon surfatron plasma measured by tunable laser spectroscopy. *Journal of Applied Physics*, 113(14):143306, 2013.

[84] N Beverini, G Cicconi, G L Genovesi, and E Piano. Metastable level density and temperature measurement in a low-density argon plasma. *Plasma Sources Science and Technology*, 6(2):185–188, may 1997.

[85] Michael G. Littman and Harold J. Metcalf. Spectrally narrow pulsed dye laser without beam expander. *Applied Optics*, 17(14):2224–2227, Jul 1978.

[86] S. Charles Doret. Simple, low-noise piezo driver with feed-forward for broad tuning of external cavity diode lasers. *Review of Scientific Instruments*, 89(2): 023102, 2018.

[87] Francis F Chen, John D Evans, and Wade Zawalski. Calibration of langmuir probes against microwaves and plasma oscillation probes. *Plasma Sources Science and Technology*, 21(5):055002, aug 2012.

[88] L. Oksuz, F. Soberón, and A. R. Ellingboe. Analysis of uncompensated langmuir probe characteristics in radio-frequency discharges revisited. *Journal of Applied Physics*, 99(1):013304, 2006.

[89] B M Annaratone and N S J Braithwaite. A comparison of a passive (filtered) and an active (driven) probe for RF plasma diagnostics. *Measurement Science and Technology*, 2(8):795–800, aug 1991.

[90] JE Velazco, JH Kolts, and DW Setser. Rate constants and quenching mechanisms for the metastable states of argon, krypton, and xenon. *The Journal of Chemical Physics*, 69(10):4357–4373, 1978.

[91] V. M. Donnelly and M. V. Malyshev. Diagnostics of inductively coupled chlorine plasmas: Measurements of the neutral gas temperature. *Applied Physics Letters*, 77(16):2467–2469, 2000.

[92] G. A. Hebner and P. A. Miller. Behavior of excited argon atoms in inductively driven plasmas. *Journal of Applied Physics*, 87(12):8304–8315, 2000.

[93] C. B. Fleddermann and G. A. Hebner. Negative ion densities in chlorine- and boron trichloride-containing inductively coupled plasmas. *Journal of Vacuum Science & Technology A*, 15(4):1955–1962, 1997.

[94] P Diomede, S Longo, D J Economou, and M Capitelli. Hybrid simulation of a dc-enhanced radio-frequency capacitive discharge in hydrogen. *Journal of Physics D: Applied Physics*, 45(17):175204, apr 2012.

[95] Paola Diomede, Doosik Kim, and Demetre J. Economou. Particle-in-cell simulation of electron and ion energy distributions in dc/rf hybrid capacitively-coupled plasmas. *AIChE Journal*, 59:3214–3222, 2013.

[96] Michael Zeuner, Horst Neumann, and Jürgen Meichsner. Ion energy distributions in a dc biased rf discharge. *Journal of Applied Physics*, 81(7):2985–2994, 1997.

[97] Geoffrey R. Scheller, Richard A. Gottscho, T. Intrator, and D. B. Graves. Nonlinear excitation and dissociation kinetics in discharges through mixtures of rare and attaching gases. *Journal of Applied Physics*, 64(9):4384–4397, 1988.

[98] John B Boffard, RO Jung, Chun C Lin, LE Aneskavich, and AE Wendt. Optical diagnostics for characterization of electron energy distributions: argon inductively coupled plasmas. *Plasma Sources Science and Technology*, 20(5): 055006, 2011.

[99] Mao-Min Chen and Young H Lee. Heating effects in reactive etching of nb and nb2 o 5. *Journal of The Electrochemical Society*, 131(9):2118–2123, 1984.

[100] Lilje L. PhD thesis, University of Hamburg, Hamburg, Germany, 2001.

[101] Tian H. PhD thesis, The College of William & Mary, Williamsburg, Virginia, USA, 2008.

[102] Gianluigi Ciovati, Hui Tian, and Sean G. Corcoran. Buffered electrochemical polishing of niobium. *Journal of Applied Electrochemistry*, 41(6):721–730, Jun 2011. ISSN 1572-8838.

[103] J. Halbritter. On the oxidation and on the superconductivity of niobium. *Applied Physics A*, 43(1):1–28, May 1987. ISSN 1432-0630.

VITA

Jeremy J. Peshl
Department of Physics
Old Dominion University
Norfolk, VA 23529

EDUCATION

- **Dec 2019 Ph.D.**, Physics, Old Dominion University

- **Aug 2015 M.S.**, Physics, Old Dominion University

- **May 2013 B.S.**, Physics, Grand Valley State University

PUBLICATIONS IN REFEREED JOURNALS

- J. Peshl, R. McNeill, C.I. Sukenik, M. Nikolić, S. Popović and L. Vušković, "Argon metastable and resonant level densities in Ar and Ar/Cl2 discharges used for the processing of bulk niobium", Journal of Applied Physics, **126**, 103302 (2019)

- J. Peshl, A.-M. Valente-Feliciano, J. Upadhyay, S. Popović, and L. Vušković, "The Effect of Process Parameters on the Surface Properties of Niobium during Plasma Etching," Proceedings of 18th International Conference on RF Superconductivity, Lanzhou, China, ISBN: 978-3-95450-191-5 (2018).

- J. Upadhyay, Do Im, J. Peshl, M. Bašović, S. Popović, A.-M. Valente-Feliciano, L. Phillips, and L. Vušković, "Apparatus and method for plasma processing of SRF cavities," Nuclear Inst. And Methods in Physics Research, A **818**, 76-81 (2016).

Typeset using LaTeX.